Cranfield University

ARYAN HOROUFI

CAR ENGINE BREATHER ICING

School of Engineering

Ph.D. Thesis

Cranfield University

School of Engineering
Department of Power and Propulsion

PhD Thesis

Academic Years: 2008-2012

ARYAN HOROUFI

CAR ENGINE BREATHER ICING

Supervisor: Dr. David W. Hammond

November 2012

This thesis is submitted in partial fulfilment of the requirements for the degree of Doctor of Philosophy.

Dedication

I would like to dedicate this doctoral dissertation to my mother and father for their love and encouragement throughout my life. This dissertation is further dedicated to my beloved brothers Arya and Arash whose love and patience is always a source of inspiration and encouragement. They always offering me support and help. I would like to thank my uncles, Arash, Abel and my aunties, Eithne and Wendy who endured this long process with me and always support me.

Aryan Horoufi

Acknowledgements

The author gratefully acknowledges Dr. David W. Hammond for his kind guidance and supervision throughout this work and his extensive assistance in setting up my test rig and reading my numerous revisions. The author's deepest gratitude is extended to my industrial supervisor Dr Steven Pierson, Principal Technical Specialist at Jaguar Landrover, and his significant support with my CFD analysis. The author further greatly acknowledges the assistance of Mr. Brian Stapleton, Technician at Cranfield University, for his valuable technical support and suggestion throughout running my experiments. The author further greatly acknowledges the assistance of the following individuals: Cranfield Icing group members, Jafar Alzaili (PhD candidate), Marie-Laure Pervier (PhD Candidate), who helped me with calibrating the Icing Tunnel, Mr Satish Paluri, CAE Engineer at Jaguar Landrover, UK for fruitful discussions and assistance in carrying out the CFD analysis, Mr Rodolfo Piccioli, Support engineer at CD Adapco, and Mr Valerio Magri, support engineer at CD Adapco, for their time and invaluable efforts for resolving my problems with Star CCM+ software. The author's deepest gratitude is extended to Mr Reza Moloudi and all my friends who supported me in any respect during the completion of the project.

Finally, the author gratefully acknowledges the Jaguar Landrover Ltd for complete funding in support of the author's doctoral studies.

Abstract

Icing in an engine breather system can block the engine breather pipe, cause excessive crankcase pressure and degrade the engine performance. In this project, a numerical study, experimental tests and CFD analysis are employed in order to understand condensation and the extent of freezing inside a vertical pipe, a horizontal pipe and a T-joint pipe which are exposed to an external convective cooling. The pipe internal flow is assumed to be a vapour/air mixture. This study has led an evaluation of freezing in an engine breather pipe. The finding in this project highlighted the effects of the pipe internal flow condition (vapour mass fraction, relative humidity, mixture gas flow rate, and inlet relative humidity), the pipe external cooling condition (temperature and air velocity) and pipe thermal conductivity on condensation and extents of ice formation in the pipe. In the experimental study, a test rig has been designed and the condensation and freezing in the pipe have been tested at the Cranfield Icing Tunnel. The local pipe temperatures are measured to validate the numerical and the CFD analysis. The numerical study has led to develop a one dimensional code which used heat and mass analogy to model condensation and freezing in a vertical pipe exposed to a cold air flow (-20C). This code satisfactory predicts the trend and magnitude of the local temperatures and heat transfer coefficient along the vertical pipe at available test condition within an acceptable uncertainty of 25%. This study proposes an empirical correlation based on a degradation factor to evaluate heat transfer coefficient inside a vertical pipe. Its results fit with the experimental data within 15% uncertainty. The CFD methodology developed in this study is capable of predicting condensation rates, local temperatures, heat transfer coefficients and extent of freezing in the pipes with good agreement with the experimental results. The CFD model over predicts the breather pipe ice blockage time due to disparities between an actual engine operating condition and the CFD model. Therefore, an adjustment factor of 1.7 is proposed in this study to correlate the predicted blockage time. The results of this study can help Jaguar to establish guideline for future design of engines breather pipes.

Table of Contents

List of Figures

List of Tables

Nomenclature

A	Surface area [m^2]
c_p	Specific heat at constant pressure [J kg^{-1} K^{-1}]
C_{emp}	Empirical condensation constant
C_g	Concentration of vapour in air
C_s	Saturation concentration of vapour in air
D	Diffusivity [m^2 s^{-1}]
d_i	Inner wall diameter [m]
d_o	Outer wall diameter [m]
f	Friction factor
h	Heat Transfer Coefficient [W m^{-2} K^{-1}]
h_{fg}	Latent heat of vaporization [J kg^{-1}]
q_{wall}	Heat flux through the wall [W m^{-2}]
q_{cv}	Convective Heat flux [W m^{-2}]
Ja	Jakob Number
k_c	Condensation Thermal Conductivity [W m^{-1} k^{-1}]
k_f	Thermal conductivity of the film [W m^{-1} k^{-1}]
K_w	Wall thermal conductivity [W m^{-1} k^{-1}]
K_l	Liquid film thermal conductivity [W m^{-1} k^{-1}]
L	Characteristic length
L_f	Latent heat of fusion, [J kg^{-1}]
$\dot{m}$	Mass flow rate [kg s^{-1}]
m''	Mass flux [kg m^{-2} s^{-1}]
M_g	Molecular weight of gas
M_v	Molecular weight of vapour
$\overline{M}_m$	Average mixture molecular weight
Nu	Nusselt number
Pr	Prandtl number
P	Total pressure [Pa]
r	pipe radius [m]
R	Universal gas constant [J K^{-1} mol^{-1}]

Ra	Rayleigh number
Re	Reynolds number
Sc	Schmidt number
Sh	Sherwood number
T	Temperature [°C]
T^*	Normalized temperature ($T^* = \frac{T - T_{solidus}}{T_{liquidus} - T_{solidus}}$)
u	Longitudinal velocity [m s^{-1}]
U	Overall heat transfer coefficient [W m^{-2} K^{-1}]
w	film waviness
W	Mass fraction
x	Volume fraction

Abbreviations

AIS	Air Intake Stub
CCM	Computational Continuum Mechanics
CFD	Computational Fluid Dynamics
CO_2	Carbon Dioxide
H_2O	Water
HTC	Heat Transfer Coefficient
NO	Nitric Oxide
O_2	Oxygen
PCCS	Passive Contaminant Cooling System
PCV	Positive Crankcase Ventilation
PPM	Part per million
RH	Relative Humidity
RTD	Resistance Temperature Detector
SLM	Standard Litre per Minute
SCCM	Standard Cubic Centimetre per Minute

Subscripts

a	Air
ave	Arithmetic average
b	Gas bulk
c	External cooling air
cv	Convection
i	Two-phase interface
in	Pipe inlet
g	Mixture gas
f	Condensate film
T	Air Tank
l	Laminar flow
t	Turbulent flow
v	Vapour
w	Wall
wi	Inner wall
wo	Outer wall

Greek

α_s^*	Relative solid volume fraction
ρ	Density [kg m^{-3}]
μ	Dynamic viscosity of liquid
ν	Kinetic viscosity
δ_{cond}	Condensate film thickness
θ_t	Suction factor
τ_I	Interfacial shear stress
ΔT	Incremental temperature [°C]
Δz	Incremental length [m]
∞	Free stream

Chapter 1 Introduction

1.1 Overview

When a car engine is started up in cold conditions its intake system can be prone to icing. Recent tests conducted at the Jaguar Research Centre indicate that ice formation in an engine intake system can restrict airflow and significantly degrade the engine performance. In fact, in freezing conditions the temperature of the engine breather pipe can be less than the dew point temperature of the breather gas mixture. In this situation, the vapour in the mixture condenses inside the breather pipe which can result in blockage and crankcase over pressurisation.

The current PhD study is sponsored by Jaguar Land Rover Ltd. with the goal of modelling condensation and evaluating ice formation in an engine breather pipe. The results of this study will help Jaguar to establish new guidelines for future design of engines.

Jaguar XK engine is shown in Figure (1-1). According to the Jaguar icing tests, the critical region for breather icing is at the connection of the breather pipe to the air manifold, as shown in Figure (1-1).

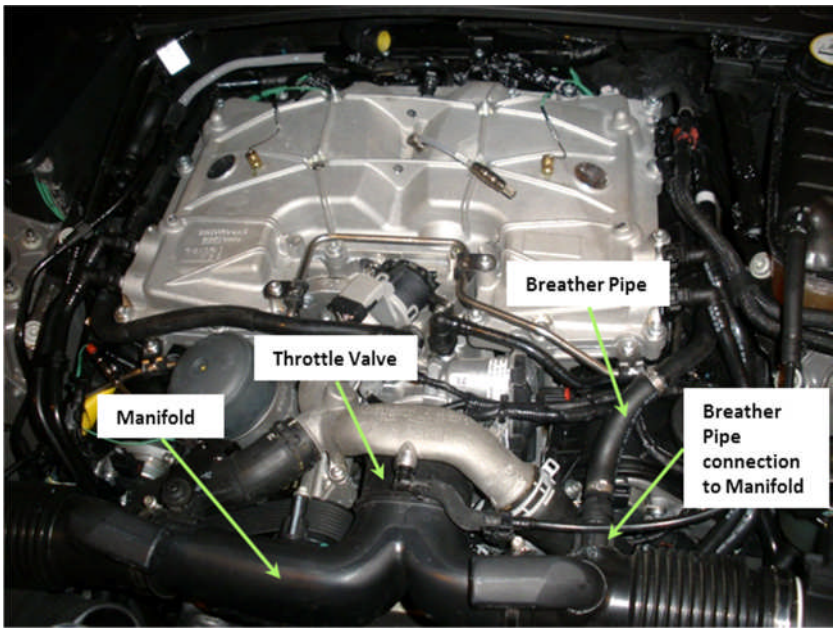

Figure 1-1 Jaguar XK engine indicating breather pipe connection to the air manifold

The icing test results show that ice starts to build up at this junction and eventually can block the breather pipe. This can lead to an increase in crankcase pressure which in a long engine run can blow out the crankcase gasket. Also some of the ice can be ingested to the air manifold and stick to the engine throttle valve, shown in Figure (1-2).

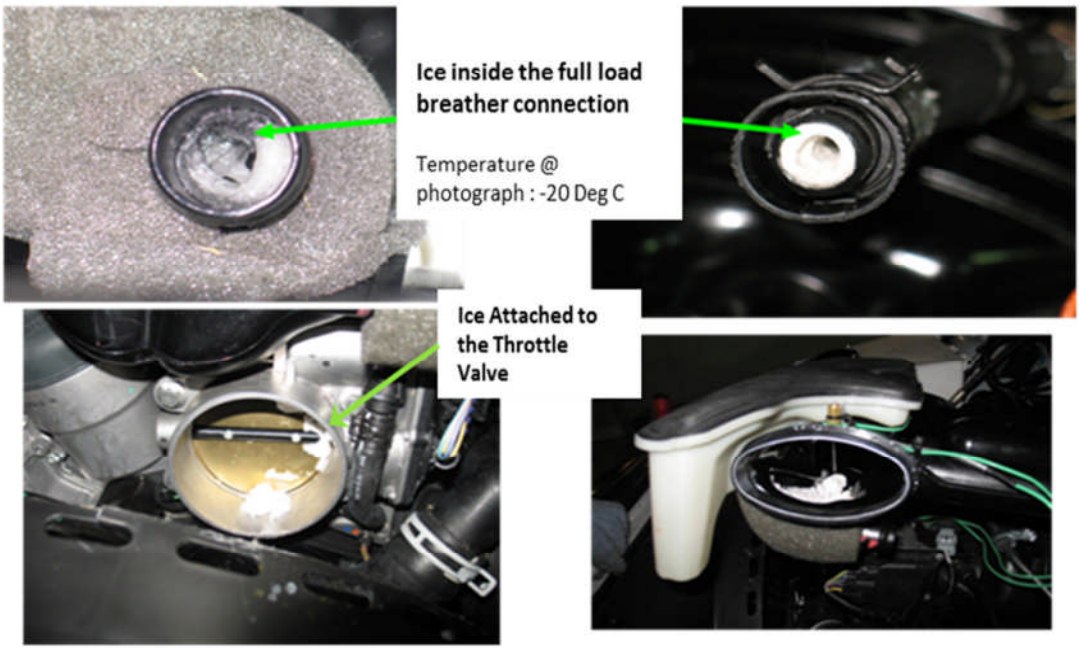

Figure 1-2 Ice inside the breather pipe and affects the throttle valve

The most important key which researchers at Jaguar are looking for in this project is an understanding of the parameters which can affect icing in pipes in a flow of cool air. Also they aim to obtain a CFD model which can model condensation and freezing in the breather pipe and estimate the total time in which the pipe become blocked by ice. The case study in this project is on the Jaguar Engine X250 V8 n/a.

1.2 Project objectives

The aim of the current research is to provide Jaguar with a CFD model which can be applied to model freezing in the engine breather pipe and evaluate the pipe blockage time. Beyond this, assessing the process of condensation and freezing in the pipes exposed to external convective cooling through experimental and numerical study, understanding the heat and mass transfer phenomena during condensation in the pipes are the focus in this study.

1.3 Methodology

The objectives of this study are fulfilled by employing a numerical study, CFD analyses and experimental tests.

To model and simulate ice formation inside the breather pipe, firstly condensation should be addressed. To simplify the case, condensation is studied in the vertical pipe through numerical analysis. In the numerical studies a one dimensional code is developed for a vertical pipe which applies heat and mass transfer equations and can predict the condensation rate and ice formation inside the vertical pipe. This analysis has led to a better understanding of heat and mass transfer in reflux condensation of steam in vertical pipe.

In the experimental part, a test rig is designed and constructed to evaluate the numerical results. All the experiments have been conducted at the Cranfield Icing Tunnel. The Icing Tunnel is used to blow cold air around the pipe and simulate external forced convection and a test rig is designed to supply vapour/air mixture. The choice of employing the Icing Tunnel and the test rig provide more flexibility on changing the boundary conditions and making observation of condensation and freezing process in the pipe compared to the tests done at the Jaguar Icing facilities.

In the experiments condensation and icing are evaluated in horizontal, vertical and a T-joint pipe and have been conducted in two phases. Even though, conducting icing tests on these pipes may not be fully representative of an icing test on an actual engine breather pipe, they can provide useful information about the process of condensation and freezing inside the pipe which can be used as a validation tool to investigate the result of the numerical study and the CFD model. The results of the vertical tests have been used to validate the 1D-code.

CFD analysis is another useful tool which has been employed in this research to evaluate condensation and freezing. Star CCM + is a commercial CFD software which is used by Jaguar LandRover Ltd and has also been applied to this study.

In CFD studies a defogging model has been developed to be able to compute condensate flux along the pipe. A Java script is also written and implemented to be used with the software to take into account the freezing heat flux in every iteration. The model is validated by results of the horizontal pipe tests.

In the last stage of this research, the CFD model is applied to the actual breather pipe and the breather pipe blockage time is estimated.

In the diagram presented in Figure (1-3) the phases of this research are shown and are highlighted as follows.

- Understand condensation and freezing in a pipe via a numerical study.
- Develop a one dimensional code which can model condensation and apply freezing heat flux.
- Conduct experimental analysis to observe condensation and ice formation at different input conditions. The first phase of the experiments is conducted with the goal of evaluating the hydrodynamics of condensation and ice formation inside a vertical pipe. In the second series of experiments the pipe temperatures are measured and the experimental heat transfer is evaluated. The experimental results can be employed as a validation tool to evaluate the numerical study and the CFD model.
- Perform CFD Analysis of condensation and freezing in horizontal pipe and develop a model to predict risk of Ice formation. The software used is StarCCM+ .
- Apply the model on actual breather pipe and validate it by using Jaguar Engine test results.
- Provide the model to Jaguar LandRover Ltd.

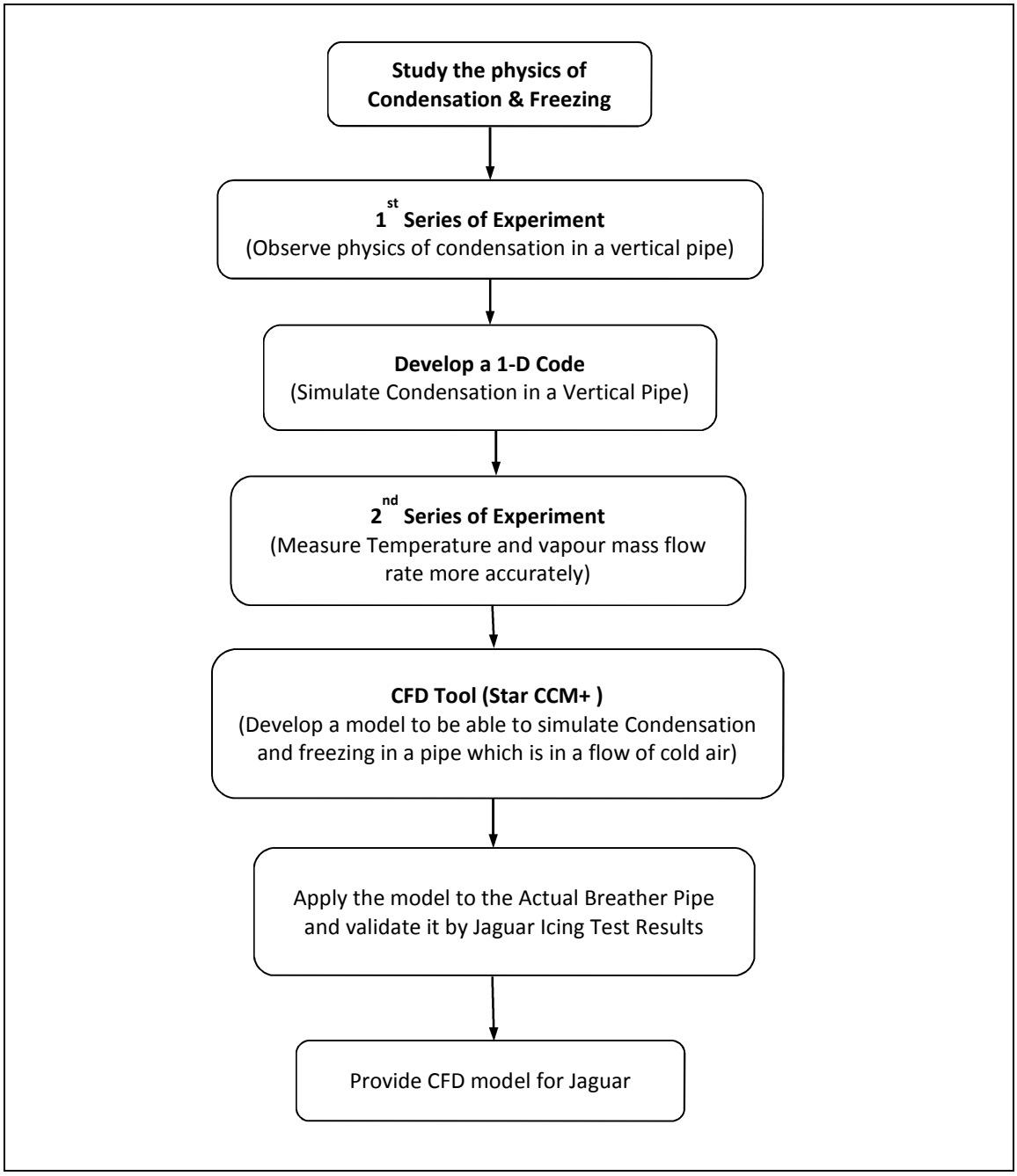

Figure 1-3 Stages of Research

1.4 Thesis Structure

The thesis has been divided in to nine chapters as follows:

Chapter 2 presents the literature review and explains the car engine icing and Positive Crankcase Ventilation (PCV) system. A physical model of condensation and freezing in a pipe and its formulation is developed and discussed in this chapter. Also available models for modelling condensation and Ice formation in Star CCM+ software are presented.

Chapter 3 explains the test rig which has been used in the experimental study. This test rig has been designed to study condensation and freezing in pipes which are exposed to a flow of cool air. This chapter focuses on explaining components of the test rig as well as test procedure and calibration.

Chapter 4 provides more discussion on experimental results. These results are referred in chapter 5 and chapter 6 for validation process.

Chapter 5 explains the solution method of a one dimensional code written to model condensation in a vertical pipe. The solution procedure of this model and its result are presented in this chapter.

Chapter 6 explains CFD simulation which has been done in Star CCM+ software to model condensation and predicts ice formation in a horizontal pipe. The results of the CFD model are presented and validated, with experimental data.

Chapter 7 applies the CFD model on an actual engine breather pipe and predicts ice accretion and risk of ice in the engine breather pipe. The results of the model are correlated with experimental test results conducted at Jaguar Landrover test facilities.

Chapter 8 gathers all the conclusions and recommendations which have been arrived at the findings of the present study.

Chapter 9 explains several aspects of this study which are subjected to further investigation.

1.5 General Comments

This study was started in October 2008. All the experimental tests have been conducted at the Cranfield University Icing Tunnel. A test rig has been designed and employed for conducting the tests with extensive help and support of Dr David W. Hammond.

The first series of experiments was performed in April 2009 with the main purpose of observing the hydrodynamics of condensation and icing in a vertical Perspex pipe. Then in January 2010 the test rig was modified and more instruments were employed to achieve higher measurement accuracy. Tests on a vertical pipe, a horizontal pipe and a T-Joint pipe were conducted. The CFD part of the project has been undertaken by using Jaguar Land Rover Research Centre computer facilities at Coventry, UK.

1.6 Application software and programming languages

The test rig components in the current project are designed by using the AUTOCAD (2007)[1]. The one-dimensional numerical code has been written by using Matlab Script File (7.10)[2]. A commercial CFD package (Star CCM+ 7.02[3]) was used for developing the computational solution in the breather pipe. This CFD package gives the ability to model condensation using the defogging model. Post processing the results was done in this software. Also a code written in Java and implemented within StarCCM+ to take into account the freezing heat flux in every iteration. N.I Compact Field Point interface connected to a PC and controlled by using Labiew (7.1)[4].

[1] AutoCAD is a software application for computer-aided design (CAD) and drafting which is developed and sold by Autodesk, Inc.; www.autodesk.com

[2] MATLAB is a programming language developed by MathWorks. www.mathworks.co.uk

[3] Star CCM+ is a package for CFD simulation developed by CD Adapco. www.cd-adapco.com.

[4] Compact Field Point & Labview are trade names for products made by National Instruments; www.ni.com

Chapter 2 Literature Review

In this literature review, first the background of engine icing is investigated. The engine breather system and the flow conditions in this system are reviewed. The freezing process in the breather pipe starts from the condensation of vapour. Therefore, evaluating condensation and heat transfer in the pipe is the main focus in this literature review. A theoretical model of reflux condensation of steam-air mixture in a vertical pipe is developed by the author for this specific project, based on the formulation of the previous works, and is presented in this section. The theoretical model is used to develop a one dimensional code which is explained in chapter 5.

In the last section of this literature review the formulation of condensation and freezing models in StarCCM+ software are reviewed. StarCCM+ is used as a CFD tool in this study.

2.1 Car engine icing

Car engine icing is the term for a condition where ice accumulates inside of a piston engine air intake or ventilation system. The source of this icing is water vapour contained in the ambient air, crankcase gases or the fuel. Ice formation in the car engine can occur typically in four different zones and categorized as carburettor icing, fuel icing, impact icing and breather icing accordingly.

2.1.1 Carburettor icing

The effects of both “carburettor icing” and “breather icing” are similar in terms of restricting flow in the engine manifold. However carburettor icing is the most common and serious amongst the types of icing in carburettor engines. The cause of this icing is the sudden temperature drop due to fuel vaporization and pressure reduction at the carburettor

venturi which cause the water vapour in the air to condense. When the carburettor temperature is at or below freezing, some of this water freezes and ice forms on the internal surfaces of the carburettor and it can extend up to the throttle valve. In Figures (2-1) and (2-2) ice formation around the throttle valve and in the venture are shown.

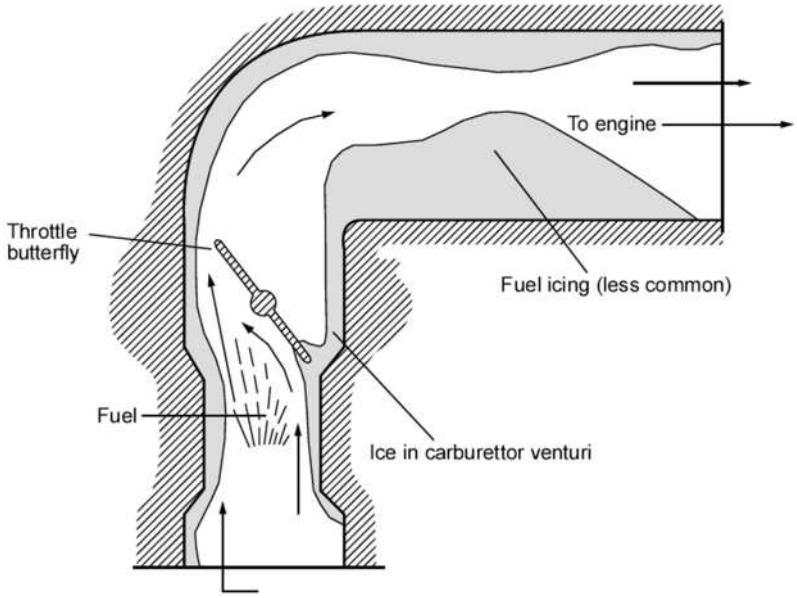

Figure 2-1 Restricting the airflow in engine manifold due to ice formation (www.caa.co.uk)

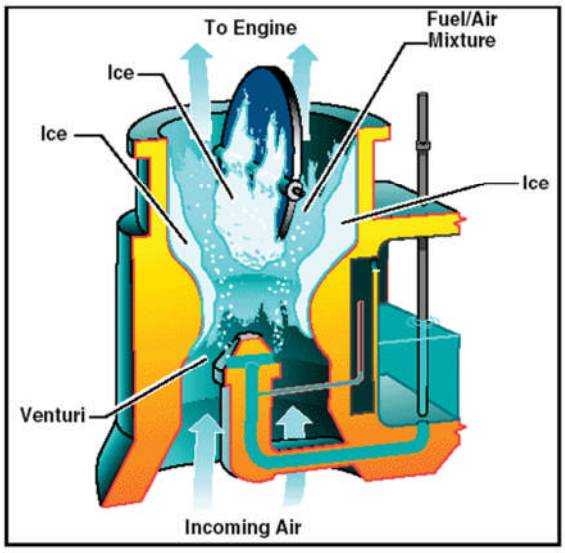

Figure 2-2 Ice formation in Carburettor (www.free-online-private-pilot-ground-school.com)

Carburettor icing degrades engine performance and in extreme conditions it can stop the engine and the engine may not even re-start and if it does, it may be with a delay.

Whilst, in this study the focus is to investigate breather icing, studying several aspects of carburettor icing helps to understand how ice formation is addressed in the engine.

It can be inferred from the literature that carburettor icing is common in aircraft piston engines. Gardner (1998) conducted a study of carburettor icing on aircraft piston engines in warm conditions at the Fuels and Lubricants Laboratory of the National Research Council of Canada. According to his report, carburettor icing in aircraft engines is not restricted to cold weather, and will occur in warm days if the humidity is high enough, especially at low power settings when the throttle butterfly is only partially open.

Sleezer et al (2004) used a chart to indicate the icing probability of carburettor engine of light aircraft (Fig 2-3). As it is illustrated in this chart the serious risk of icing occurs at the range of -4 °C to 16 °C. Moderate risks will happen between temperatures of -7 °C to 25°C.

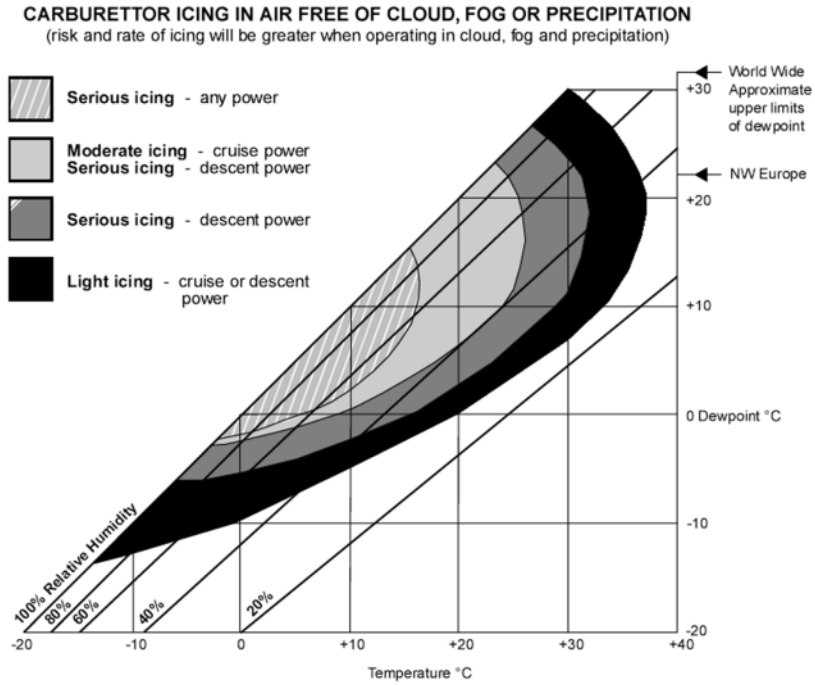

Figure 2-3 Carburettor Icing probability chart (Sleezer et al, 2004)

This way of presenting the risk of ice formation gives an idea of a possible way to develop a similar chart to evaluate breather icing risk in this study.

In Figure (2-4) the number of accidents caused by carburettor icing in aircraft piston engines per month in 1999 is shown. It illustrates that the critical time is unexpectedly in the warm months, because the water vapour content of the air in warm days is more than cold days.

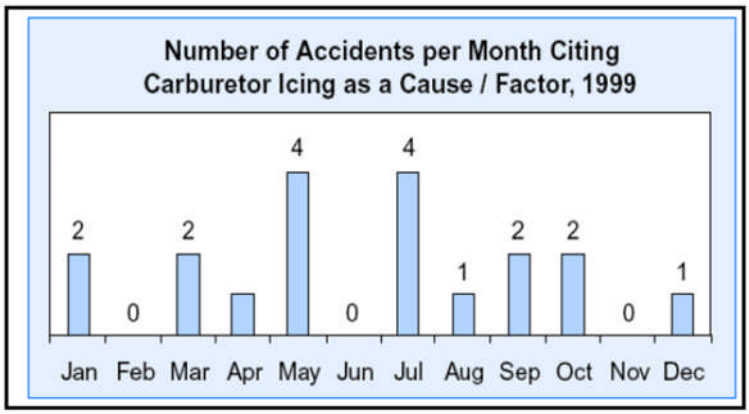

Figure 2-4 Number of accident per month citing Carburettor as cause in Northern hemisphere (Sleezer et al, 2004)

In general, the conditions favouring carburettor icing in aircraft piston engines include:

- Temperature range -3C to 15 C at any power
- High relative humidity (RH) e.g. 60-100%
- Increasing altitude lowers dew point temperature and causing more condensation and increases risk of freezing in cold condition
- Increasing speed (wind chill effect)

In order to identify the risk of carburettor icing the majorities of aircraft piston engines are equipped with a carburettor temperature gauge, ice light or similar instruments. carburettor heating system are the most common system used to prevent carburettor icing.

2.1.2 Fuel icing

Fuel icing is the result of water, held in suspension or solution in the fuel, precipitating and freezing in the induction piping and even in fuel tank. This sort of icing is most likely to occur in aircraft engines. In order to avoid fuel icing, fuel heaters as well as anti-icing agents are used which stop the ice crystal formation in the fuel.

2.1.3 Impact icing

The ice which builds up on an engine air box and air filters causes what is referred to as intake or impact icing. This type of icing occurs when ice particles or water droplets impact on engine air box and block the intake air filter. This typically happens in the snow, sleet, sub-zero cloud or even in rain, if either the rain or car body are below 0°C. This type of icing can affect fuel injection systems as well as carburettor based systems and can be more hazardous for turbocharged engines since some of the ice particles can be ingested in the engine manifold and can impinge on the turbocharger blades. Engines at reduced power

settings are more prone to Impact Icing because the partially closed throttle valve can more easily be restricted by the ice.

2.1.4 Breather icing

Breather icing is the term for a condition where ice accumulates inside a piston engine breather system. The source of this icing is mostly water vapour in blow-by gas which is circulated by the Positive Crankcase Ventilation (PCV) system. Blow-by gas and the PCV system are explained in section (2-2).

The warm blow-by gas carried by the PCV system brings a lot of moisture and fuel to the manifold tube. As this vapour passes through the breather tube, under some conditions it may condense and if the breather pipe surface is at or below freezing, the water freezes before it can pass out of the breather pipe. This can then restrict the airflow, increase the crankcase pressure and causes rough engine running. The pressure rise also may blow up the crankcase sealing and results in oil leaks.

Some of the knowledge obtained from Carburettor Icing can help to identify the parameters which may affect breather icing as listed as follows:

- Air flow condition inside the breather pipe such as temperature, relative humidity and pressure which affect the dew point
- Blow-by composition (see section 2-2-1)
- Air conditions around the breather pipe (under bonnet airflow) which may be affected by vehicle speed and ambient conditions
- Geometry of the breather tube
- The pipe thickness and material (thermal conductivity)

All the terms such as PCV system, breather pipe, and blow by gas are explained in the next section.

2.2 PCV System

The crankcase is the enclosed space at the bottom end of an internal combustion engine which includes the crankshaft, pushrods, piston cylinders, pistons, connecting rods, and timing gears that connect to the front cover. Most of these components are moving and are in contact with engine lubrication oil.

A Positive Crankcase Ventilation system (PCV system) is used to circulate the crankcase gases to the engine intake and prevent the crankcase gas from being expelled to the environment. Crankcase gases are mixture of blow-by gas[5], soot from the engine combustion mixed with oil mist and oil vapour.

If the crankcase gases are allowed to accumulate in the crankcase compartment due to the flow of blow-by gas, it would result in considerable pressure and cause the crankcase seals and gaskets to leak. Thus, the crankcase gases must be properly vented from the engine by a check valve. The check valve, which typically is a conventional reed type valve, vents the crankcase gases through a pipe to the engine air intake to reduce air pollution .This pipe is called a "Breather Pipe". In another word, crankcase gases are returned into the cylinder for combustion and eventually the resulting fumes are taken to a catalytic converter where they are treated for release to the atmosphere.

According to a Racor Technical Report[6] (2006), restrictions on environmental pollutants were not in place until the first legislation on car passenger pollution in 1960's. In the 1970's emissions caused by blow-by gas on heavy-duty diesel engines were a small portion of the total emissions emanating from the engine and there were no regulations on diesel crankcase emissions, so crankcase gases were vented directly to the atmosphere. By the 1990's, diesel emissions had been reduced to the point where blow-by emissions became a more significant part of the overall engine emissions. In 2007, the US EPA (Environmental Protection Agency) required engine manufacturers to include crankcase emissions for all diesel engines and PCV systems are broadly used nowadays in most of vehicles. The EPA Emission Standard for heavy duty Diesel Engines from 1998 to 2007 is listed in Table (2-1).

[5] Blow-by gas is the term used for gases which escape through the piston rings during engine operation. See section (2.2.1) for more information.

[6] www.parker.com/racor

Table 2-1 EPA Emission Standards for Heavy-Duty Diesel Engines (g/bhp.hr) (www.parker.com/racor)

Heavy Duty Diesel Truck Engines				
Year	HC	CO	NO_x	PM
1988	1.3	15.5	10.7	0.6
1990	1.3	15.5	6	0.6
1991	1.3	15.5	5	0.25
1994	1.3	15.5	5	0.1
1998	1.3	15.5	4	0.1
2004 option 1		15.5	2.4 NHHC+NOx	0.1
2004 option 2	0.5 NMHC only	15.5	2.5 NHHC+NOx	0.1
2007	0.14	15.5	0.2	0.01

2.2.1 Blow-by gas composition

During engine operation the compressed fuel and air mixture burns in the cylinder on the top of the pistons. When the piston rings become worn and even, to some extent, when they are new they allow some of this compressed and burning mixture to escape and leak past into the crankcase (Fig. 2-5). This flow is called "blow-by gas".

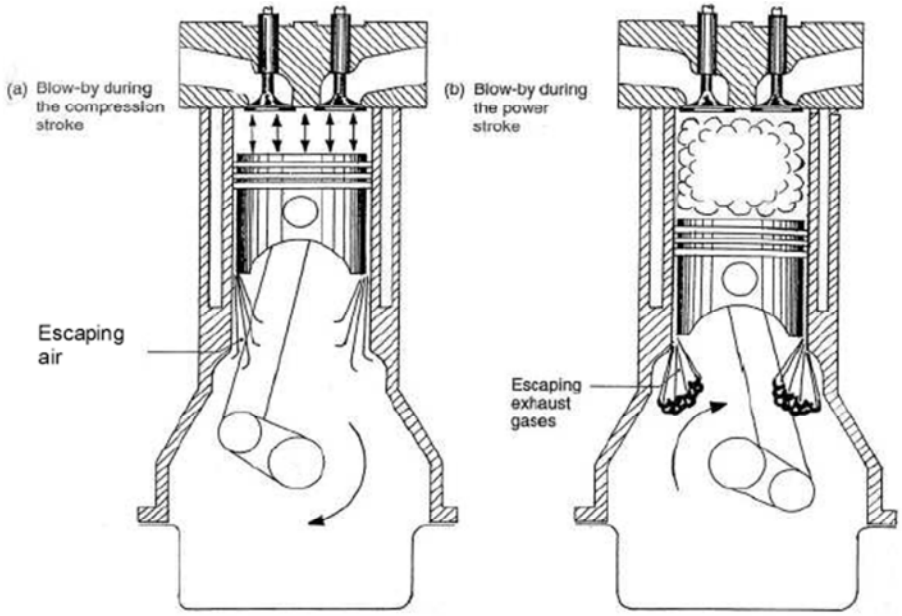

Figure 2-5 Blow-by gas during compression and expansion stroke (Heisler 1995)

As illustrated in Figure 2-6, most of the blow-by gas passes through the piston ring contact surfaces and the cylinder wall. A small amount of blow-by escapes in to the crankcase along the sides of the groove behind the piston ring. A third part of the blow-by escapes through the rings gap.

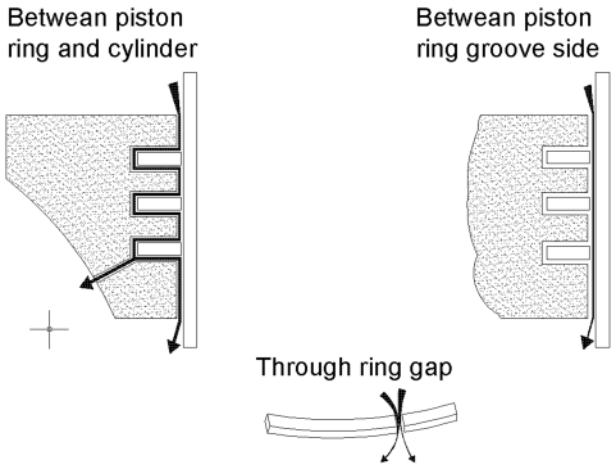

Figure 2-6 Blow-by gas scape through cylinder rings (Heinz et al 1998)

Avergard and Lindstrom (2004) mentioned that the blow-by gas originates not only from the combustion chamber, but it can also be from other sources in the whole engine system. He stated that around 60 % originates from the combustion process and the remaining 40 % comes from other sources such as the air compressor and turbocharger. All these blow-by sources have a connection to the crankcase. Either their own crankcase is directly connected or they have lubricating channels that are connected to the oil sump.

2.2.2 Blow-by gas flow rate

The blow-by gas flow rate depends on different engine parameters such as load, engine speed, whether or not the air compressor is charging etc., but it also increases with the engines total operating time and it can vary a lot between different manufactures and models. The amount of blow-by is measured in a variety of ways and the values of measured blow-by are very different. Heinz (1995) stated that the blow-by increases with engine speed and in particular as the piston rings and cylinder bore wear, the blow-by becomes more noticeable in the upper speed range, (Fig 2-7). In charged engines, leaks in the turbo charger can have a considerable effect on the measured blow-by volume as well.

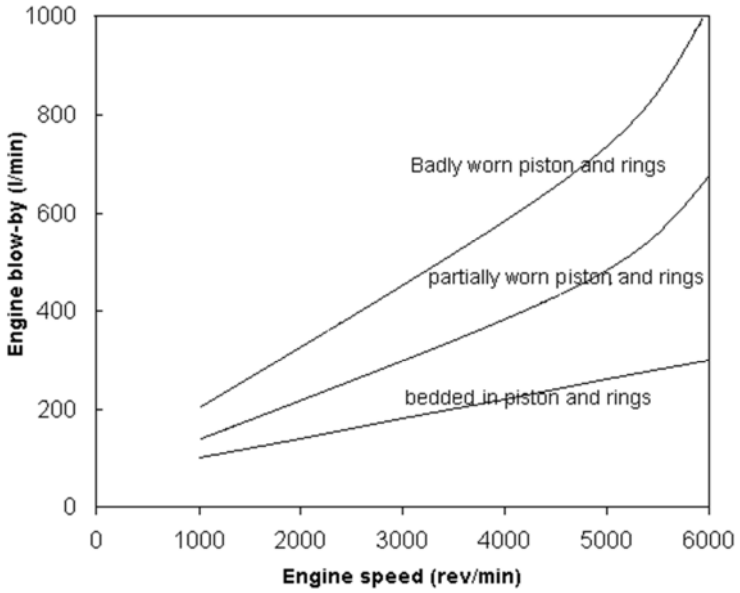

Figure 2-7 Effect of engine speed on piston and ring blow-by (Heinz , 1995)

Heinz et al (1998) stated that the most common method used for indicating the blow by flow rate is by expressing it as a percentage of the intake volume. In this form, the blow-by can be compared between different engine types. The amount of blow-by can only be determined through direct measurement but good rule-of-thumb is that figures are 0.5% in new engine, 1% in design target for breather sizing and a maximum of 2.5% to 3% for a worn engine, or with poor piston ring sealing.

Heinz et al (1998) measured the blow-by in a 1.6 litre, 4 cylinder petrol engine and compared it with a 2.0 litre 4-cylinder diesel engine. The characteristic map of the petrol engine shows at low speeds, the ratio of blow-by to intake air is about 1% to 6.8% and at high speed and high load the value falls to about 0.9%. A similar pattern can be observed for the diesel engine. It is because of the fact that at high load and high cylinder pressures, the gas pressure is high enough to press the piston ring's contact surfaces into the distortion recesses. At low pressure, the rings skip over these gaps and open space for blow-by gas. Therefore the blow-by may be greater at partial load and low cylinder pressure. Avergard and Lindstrom (2004) called this phenomena "ring flutter" which would happen when the pressure difference between the combustion chamber and the crankcase is not high enough to push the piston ring tightly onto the piston ring groove and cause the piston ring to flutter in the groove. He also showed that blow-by is a pulsating gas with partial backflow or, if a crankcase breather is fitted, even flow reversal. He tested a specific engine, a 1.3 litre, 4-cylinder petrol engine with liquid cooling, as an example and reported that blow by gas

pulses heavily with time with peaks at 85 l/min and -50 l/min. In Table (2-2) different values of blow-by gas are shown by Avergard and Lindstrom (2004).

Table 2-2 Different measurements of blow-by. The measurements have been done on engines with an output between 300-600 horsepower (Avergard and Lindstrom (2004))

Measured value	Reference
10 - 30 l/min per cylinder	Marty (2003)
140 - 300 l/min	Batram et al (2000)
1120 l/min on a worn engine	Batram et al (2000)
0.5 l/min per rated engine horsepower	Batram et al (2000)

2.2.3 Crankcase gas content

The gas mixture which goes through the breather pipe is crankcase gas which is mixture of blow-by gases, soot from the engine combustion mixed with oil mist and oil vapour.

Blow-by gases are composed of unburned air fuel mixture or partially burnt products of combustion plus oil aerosol, (e.g. CO_2, CO, O_2, NO_x and H_2O). As with the blow-by mass flow rate, which varies from one engine to another, its composition differs according to engine speed, load and other engine components such as air compressor.

Lopez (2004) showed that leaking blow-by through the piston rings atomized the oil in to droplets and entrained them to the flow (Fig 2-8a). He postulated that approximately 50 % of the oil aerosol in crankcase gases forms around the piston rings and the cylinder wall. Components of the engine oil with low boiling points vaporize and likewise lead to the formation of aerosols by condensation. In addition, the high piston temperature and the action of other rotating-parts such as crankshaft, which is constantly rotating, cause the oil to evaporate, splash and break up into different droplet sizes. The mixture then mixes with blow-by gases and passes through PCV system (Fig 2-8b).

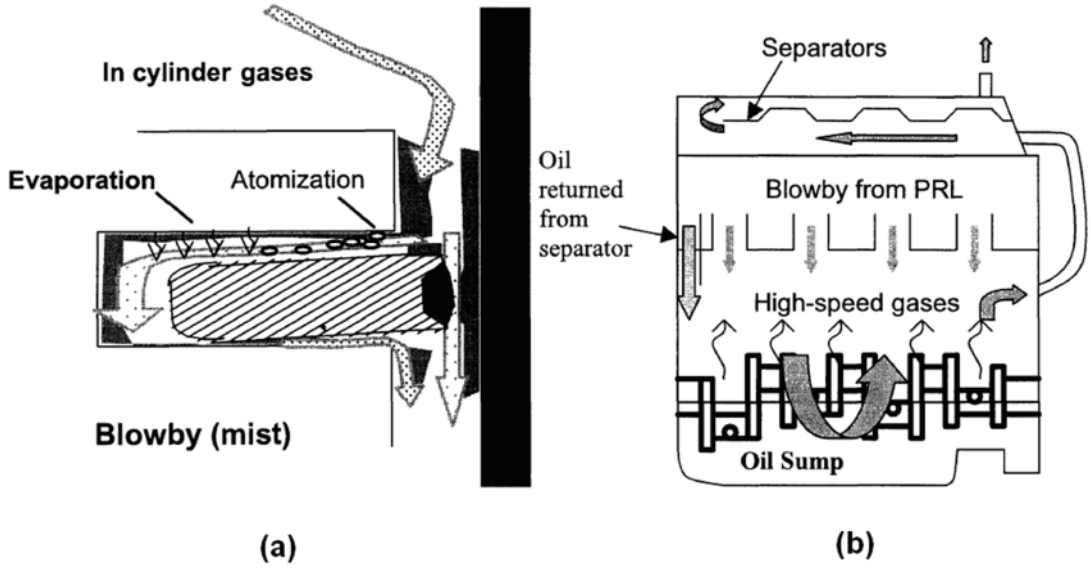

Figure 2-8 Oil entrainment in blow-by flow through the piston-ring liner (Lopez, 2004)

Heinz et al (1998) examined the composition of the blow-by gas and its condensate and expressed the results in terms of volume fraction relative to that present in unburnt gasoline. He showed that the amount of high boiling point compounds in blow by condensate is more than that of low boiling point compounds. He also mentioned that 10 to 40 percent of the condensates consisted of lube components (Fig 2-9).

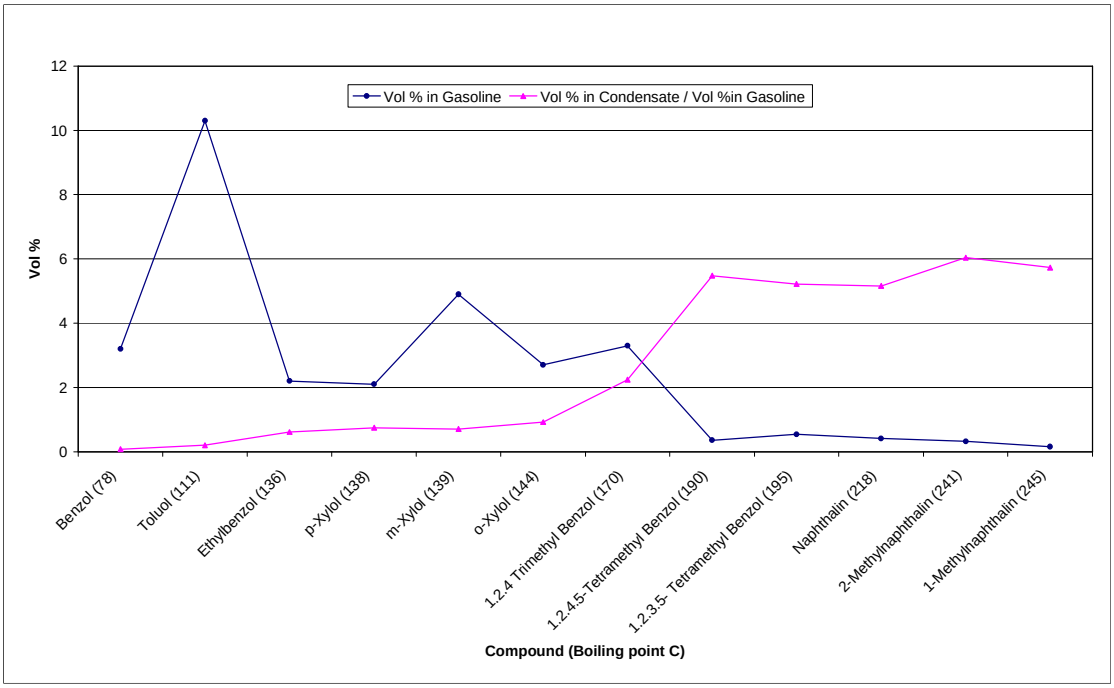

Figure 2- 9 Analysis results of blow-by condensates, Heinz et al (1998)

In general the crankcase vapours are normally comprised of fuel, moisture, unburnt hydrocarbons, and combustible materials such as atomized oil, diesel fuel, and heavy

particulate resulting from engine operation. Some are gaseous, some are liquid, and some are particulate matter.

Heinz et al (1998) describes the crankcase gases as follows:

- Soot Particles; 0.3 to 0.5 µm
- Oil Aerosol Particles; 0.1 to 10 µm
- Gasses; CO, CO_2, NOx , O_2 , H_2O
- Gaseous Hydro-Carbons (HC)
- Water Vapour (H_2O)

2.2.3.1 Filtering Crankcase blow-by gas

Since, the crankcase gases contain fine oil particles in the form of oil mist they may cause engine malfunctions if they return to intake section of the combustion engine. Thus, these gases are filtered by the PCV system with at least one separator.

Mostly labyrinth or cyclone separator and textile fibre filters are used to filter the mixture. Steffan (2003) investigated the fluid and droplet dynamics in cyclone and disc stack centrifuges and showed that the cyclones have better overall separation performance. Reitze (2001) stated that filters and separators only remove particulate material, liquid droplets, liquid mist and submicron sized droplets, but allow vapour to pass through. If this vapour condenses in the breather pipe it may turn to ice in cold condition and can cause Breather Icing.

In the next section, condensation and freezing of water in vertical pipe is studied.

2.3 Film condensation inside of a vertical pipe

Condensation is considered here to be as an isothermal phase change phenomena which involves an abrupt discontinuity of properties at constant dew point temperature. The study of condensation is very important in many industrial applications. Some typical examples of these applications are in nuclear power generation industry, chemical processing, thermal power generation and refrigeration industries.

Around one century back Nusselt (1916), for the first time[7], studied condensation of steam analytically. In his research, he studied the condensation of steam on a vertical cooled isothermal flat plate maintained below the dew point temperature. The condensation starts at the top of the plate and forms a liquid film which flows downward due to gravity. Nusselt derived condensate mass flow rate from the momentum equation and balanced his energy equation at the gas/liquid interface. He made several assumptions to simplify his model such as: negligible shear stress at the film/gas interface, negligible momentum transfer across the film, constant fluid properties and laminar fluid film and calculated the film heat transfer coefficient and film velocity as a function of local film thickness. The results of Nusselt work has been widely referred in lots of books.

Since Nusselt's pioneering analytical study, there have been considerable research works on external and internal condensation on various geometrical configurations such as channels and tubes in both horizontal and vertical orientations.

An intensive detailed review of in-tube condensation is given by Dalkili and Wongwises (2009). The in-tube condensation process of steam in a vertical pipe is classified by gas mixture type (containing non-condensable gas or pure steam), flow regime (whether it is laminar or turbulent) and direction of gas (whether it is co-current or counter current to the liquid film motion).

The methods of evaluating the condensation in vertical pipe can be categorized as analytical and experimental.

In analytical methods, the governing equations which are derived from condensation models are solved numerically with using mostly an iterative procedure. Some typical works of this kind are Liao et al (2009), Park and No (1999) and Dehbi and Guentay (1997).

In the experimental studies, test rigs were set up to generate and measure condensation. The typical measured parameters are: inlet gas mixture temperature, inlet mixture mass flow rate, inlet pressure and temperature variation along the pipe. From this test data, the

[7] According to the best of the author's knowledge

experimental heat transfer coefficient in the pipe is evaluated by balancing heat and mass transfer equations or performing an empirical correlation. Some of these types of works are Kuhn et al (1997), Lee and Kim (2008) and Moon et al (2000).

It is important to note that most of the studies of condensation of steam in vertical tubes have dealt with condensation in absence of noncondensable gases. However, in practise there is always a small amount of noncondensable gas present in the condensing tube due to atmospheric operating conditions encountered in many of these applications. Theoretical and experimental research studies have consistently indicated that noncondensable gases have a strong influence on steam condensation in the vertical pipe (Dehbi and Guentay 1997). As a general rule, the greater the noncondensable mass fraction the greater resistance to the condensation.

The scope of the numerical study in this thesis is to study reflux film condensation of a steam-air mixture in a vertical pipe considering the effect of noncondensable gas and to develop a correlation to quantify the parametric effects of nondimensional parameters on the experimental heat transfer coefficient. Therefore, numerical analyses and empirical correlations of film condensation from steam-air mixture in vertical pipes are reviewed in this section.

2.3.1 Analytical models

Colburn and Hougen (1934) analysed condensation of vapour-air mixtures in a vertical pipe. They proposed a theory that the condensation mass transfer is controlled by diffusion across a diffusion layer. This diffusion layer is a thin layer of air near the condensate film layer. Their theory is based on balancing heat transfer through the vapour-air mixture side with the heat transfer through the liquid film at the gas/film interface. In their model the overall heat transfer conduction between the condenser tube and the vapour-air mixture is comprised of conduction through the gas boundary layer and condensate film. The heat transfer through the gas boundary layer includes of sensible and latent heat transfer. The latent heat is evaluated by using heat and mass analogy. This calculation requires an iterative process, extensive iterations, to converge two unknown variables which are air mole fraction and gas/film interface temperature.

It should be noted that in the heat and mass analogy, heat and mass transfer equations are solved for the gas boundary layer and liquid film and are balanced at liquid/gas interface.

Peterson et al (1993) developed a diffusion layer theory by introducing the concept of a "condensation thermal conductivity (k_c)". By this model the overall gas side conductivity is a

combination of condensation thermal conductivity for latent heat transfer and the standard thermal conductivity for the sensible heat. The advantage of the diffusion layer theory is quick convergence in numerical calculations as the condensation thermal conductivity is just a function of interface temperature. The condensation thermal conductivity in Peterson's diffusion theory is derived from the formulation of mass diffusion by using the Fick's law of diffusion[8] on a molar basis.

Liao and Vierow (2007) extended the Petrson et al's (1993) diffusion layer model on a mass basis. This formulation is more elaborate than Peterson et al's model and it is appropriate for use when condensation thermal conductivity is linked with the heat and mass analogy to evaluate latent heat transfer. They also showed that the mass based diffusion model can predict the experimental data better than the molar-based model.

Moon et al (2000) proposed a heat and mass analogy model for reflux condensation in presence of non-condensable gas. They evaluated the condensate film heat transfer coefficient based on the liquid film model derived from condensation of vapour co-current to liquid film. They developed an iterative model to evaluate the condensation and assumed that the vapour is condensed completely in the pipe. They didn't make serious attempts to quantify uncertainty in their model.

Liao et al (2009), used the heat and mass analogy approach to evaluate local heat transfer coefficients in reflux condensation of a flowing steam-air mixture flowing counter-current to a laminar condensate film in a vertical pipe. In contrary to Moon et al (2000), they anticipated that vapour might not necessarily condense completely in the pipe. They developed an iterative solution method which marches from the bottom of the pipe to the top of the pipe and calculate the local gas/film temperature and the vapour mass flow rate at the tube outlet within two iterations. The inner wall temperature is determined in this process. In their model condensate film movement is coupled to both gas mixture motion and vapour condensation. Hence, the local condensate film behaviour must be treated differently between co-current and counter current condensation.

2.3.2 Empirical Correlations

The empirical correlations are mostly used to compute the local or average heat transfer coefficient, local or average Nusselt number and condensate film thickness. These correlations are developed from iterative numerical solutions correlated with the experimental data and mostly are a function of the following parameters:

[8] Fick Law of diffusion is explained in Appendix A

- Condensate Film Reynolds Number (Ref)
- Gas mixture Reynolds Number (Reg)
- Gas Mass Fraction (Wg)
- Jakob Number (Ja)

The main drawbacks with these correlations are their validity range and their accuracy. The simple correlations are not sensitive to their local variables and the variable range. There are some accurate correlations but mostly require an elaborate solution.

Revankar et al (2010), developed a correlation for a vapour and air mixture in a vertical tube based on the heat and mass analogy model for various operating parameters of a passive condenser system. He used an alternating conditional regression (ACE) to correlate the local heat transfer coefficient with the noncondensable gas mass fraction (W_b), the mixture gas Reynolds number (Re_g) and the Jakob number (Ja). A total of 102,600 experimental data points was used as input to the ACE. His correlation is valid for $0<Re_g<40{,}000$, $0<W_b<0.5$, and $0.002<Ja<160$. The operating pressure in his experiment was 100 to 400 kPa.

Hasanein et al (1995) conducted an experimental and theoretical investigation to correlate local mixture Nusselt number in terms of Re_g, Ja and W_g or mixture Schmidt Number (Sc). The correlation including Schmidt number is better in representing the condensation in presence of noncondensable gases. In his experiments, condensation is studied inside a vertical pipe with 46mm internal diameter and length of 2.44m. The range of parameters in his investigation was ($825<Re_g<24460$, $0.238<Sc<1.187$, $0.007<Ja<0119$, and Gas temperature between 100°C to 130°C). This correlation predicts the experimental data very well. He also developed a theoretical model and solved the diffusion equation to obtain steam mass flux at the interface between the condensate film and the gas mixture. He showed that the thermal resistance of the condensate film is significant when the gas mixture Reynolds number is high ($Re_g>6000$) and mass fraction of noncondensable gases of the mixture is low ($W_g<0.2$).

Moon et al (2000), studied reflux condensation and conducted experiments with variations of three main parameters: inlet steam flow rate, inlet air mass fraction and system pressure. He used his test data to make an empirical correlation for local heat transfer coefficient. He nondimensionlized local heat transfer coefficient by introducing a degradation factor (F) as the ratio of local experimental heat transfer coefficient to the film heat transfer coefficient. He used 165 data points of local heat transfer coefficients and correlated the degradation factor with four nondimensional parameters namely the gas mass fraction (W_g), the mixture gas Reynolds number (Re_g), the Jakob number (Ja,) and the film Reynolds number (Re_f). His

correlation is applicable in the range of $6119<Re_g<66586$, $0.14<W_g<0.972$, and $0.03<Ja<0.125$. The root mean square error of his correlation is 17.7% compared with experimental data.

Vierow and Schrock (1991) proposed a degradation factor defined as the ratio of local experimental heat transfer coefficient to the Nusselt Number. He correlates F with the enhancing factor (f_1) which relates to Reynolds Number (Re) and the degradation factor, f_2 which is related to gas mass fraction W_g. Their condensing tube length and inner diameter was 2.1m and 0.022m, respectively. This correlation in the case of pure vapour becomes too simple to be effective as f_2 become unity. The mass fraction of the mixture is between 0 to 14% with operating pressure of 30 to 450 kPa.

Kuhn et al (1997), continued the work of View and Schrock (1991) and defined f1 to include the effect of interfacial shear stress and the film waviness as $f_1=f_{1shear} \times f_{1other}$. The factor f_2 defined as a function of film Reynolds number. The simplicity of this correlation makes it easy to be used in computer codes, but its accuracy depends on the condensation mass flux and shear stress. His condensing tube was 2.4m length and 0.0475m diameter. The operating pressure was 100 to 500 Kpa.

Shah (1979, 2009) presents a correlation for heat transfer during film condensation inside of vertical, horizontal and inclined pipes in co-current condensation. He used 1189 data points from 39 different studies. Shah (1979, 2009) applied his correlation for co-current condensation and assumed that the heat transfer coefficient at the tube entrance is zero and is equivalent to a tube full of saturated liquid at the end of the pipe. However in many situations at the end of condensation there is not enough water to fill the pipe.

Siddique (1993) correlated local Nusselt number as a function of Sc, Re_g ,W_g and Ja. In order to find the coefficients for the correlation, he used a logarithmic transformation and linear regression analysis. He reported that as the Schmidt number is small for the steam air mixture it can be removed from the correlation. He used a condensing tube with the length of 2.54m and diameter of 0.046m in his experiments. He used air and helium with gas mass fractions of 10% to 35% as noncondensable gases in his experiments.

Most of the research works on condensation in vertical pipe have focused on condensation in the passive containment cooling system (PCCS) of a nuclear reactor (Kuhn et al (1997), Maheshwari et al. (2004) Kim et al (2009)) in which the steam flows co-current to the condensate film. However, only few experimental investigations were found on reflux or counter current condensation.

From the above, empirical correlations and the analytical works, a number of conclusions can be drawn:

1) Analytical works have been based on the governing equations for momentum and energy. They use a diffusion layer method and based on heat and mass analogy the condensation mass in the pipe is calculated. The four most difficult quantities to calculate in these analyses are: interfacial shear stress, interfacial temperature, gas and film velocity profile and turbulence. They all require iterative solution procedure.

2) Empirical correlations which are simple in solution are not very accurate. More complicated solutions are better in terms of accuracy but they require an iterative solution procedure.

3) The developed methodologies for co-current condensation are not generally applied to counter-current condensation due to following reasons:
   - While gas concentration increases along the pipe, condensate film thickness decreases under counter-current condensation whereas in co-current condensation it increases.
   - Shear stress at the interface of gas/liquid tend to accelerate film flow and make the condensate film thinner in co-current flow while it thicken the film for counter current condensation
   - The numerical solution in co-current condensation marches from the top to the bottom of the pipe. This scenario is not suitable for counter current condensation, since the condensate film thickness is usually unknown in counter current condensation.

In the next section a physical model for reflux condensation of a steam-air mixture in a vertical pipe which is exposed to external cold airflow is explained. The formulation applied in this model comes from the analytical works done in the literature and are explained in the next section. An iterative procedure is developed based on this model which is explained in Chapter 5.

2.3.3 Physical model of reflux condensation of a steam-air mixture

Models developed so far have evaluated condensation in condensing tubes exposed to external cooling water and require the specification of wall temperature. However, in this study the external cooling is caused by external cross air flowing at velocity of V_c and temperature of T_c. Here, the detail formulation and methodology used for modelling reflux condensation in a vertical pipe, exposed to a cold air flow, which is developed for this specific project by the author is described.

In the current model, gas phase heat transfer is modelled by employing the heat and mass transfer analogy and using the diffusion layer theory proposed by Liao and Vierow (2007) due to its good performance. The liquid film heat transfer is approximated using the liquid film model derived from condensation of vapour in counter-current flow used by Liao et al (2009). The heat and mass transfer equations for liquid and gas phase are balanced with gas mass fraction, temperature and shear stress at the liquid/gas interface. The unknowns are local heat transfer coefficients, tube wall temperatures and gas/liquid film interface temperature which are solved iteratively, as explained in Chapter 5.

The problem being studied here is shown schematically in Figure (2-10).

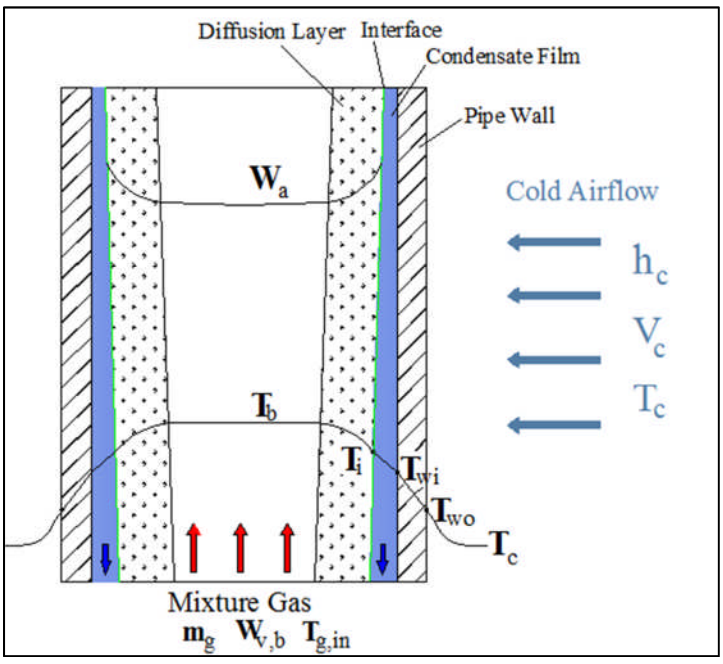

Figure 2-10 Schematic illustration of reflux condensation in vertical tube in presence of non-condensable gas

With forced in-tube condensation, the vapour condenses on the inner side of the pipe wall as droplets which can eventually flow down as a liquid film in the vertical pipe. The direction

of gas flow has an important role on shear stress and the governing equations which are explained in this section. In reflux condensation, the condensed liquid flows downward as an annular film adjacent to the cooled pipe wall, while the uncondensed gas mixture flows upward in the core of the tube, as shown in Figure (2-10). The high density difference between the condensed liquid and the gaseous core together with the shear force of the gas mixture maintain an annular flow pattern over the most of the condensing length.

In this study both the gas mixture and the film are assumed to be in the laminar regime. It should be noted that both Moon et al (2000), Vierow et al (2003) reported that when the condensate film is in laminar film, the turbulence effect of counter current flow is insignificant. With the condensation of pure vapour, the condensate film provides the only heat transfer resistance to the condensation (Kim (2000)). Whereas, if small amounts of non-condensable gas is presented, the main resistance to the heat transfer will lie in the gas/vapour boundary layer. In fact, the concentration of the non-condensable gas increased near to the liquid films as it becomes excluded from the condensate film and it forms a boundary layer as shown in Fig (2-10). The boundary layer is called a diffusion layer because the vapour in the gas core region must diffuse through this layer to condense at the interface. This diffusion layer acts as a thermal resistance. The heat transfer coefficient in the diffusion layer includes condensation and convection terms. While, both depend on the mixture flow dynamics, the condensation heat transfer also depends on mass diffusion through the diffusion layer. Therefore, to model condensation both of the heat and mass transfer equations must be solved for the gas boundary layer and the liquid film and balanced at the liquid/gas interface.

Figure (2-10) illustrates schematically the control volume of the model considered for the analysis. Mixture gas enters the vertical pipe with a given mixture mass flow rate (m_g), vapour mass fraction ($W_{v,b}$) and bulk temperature $T_{g,in}$. The pipe has been exposed to the external cold air cross flow at temperature of T_c and velocity of V_c. The inside wall of the tube is at a prescribed temperature $T_{w,i}$, lower than the saturation temperature of the gas mixture, and therefore condensation takes place on the inner wall surface to begin with. The interface between the liquid and the vapour/gas region is at saturation ($T_i = T_{sat}$). T_{sat} is the saturation temperature at the corresponded partial pressure. W_a is the air mass fraction.

This condensate flows downward as a film because of gravity. The condensate film thickness δ_f, is a function of position along the flow direction.

2.3.4 Heat and Mass Analogy

The overall heat transfer from the gas-vapour mixture to outside of pipe includes convective (q_{cv}) and condensate heat (q_{cd}) through the diffusion layer, convective heat in the liquid film (q_f), conduction heat through the wall and convection to the external flow as shown in Figure (2-11).

The condensate heat is the latent heat due to condensation of the vapour.

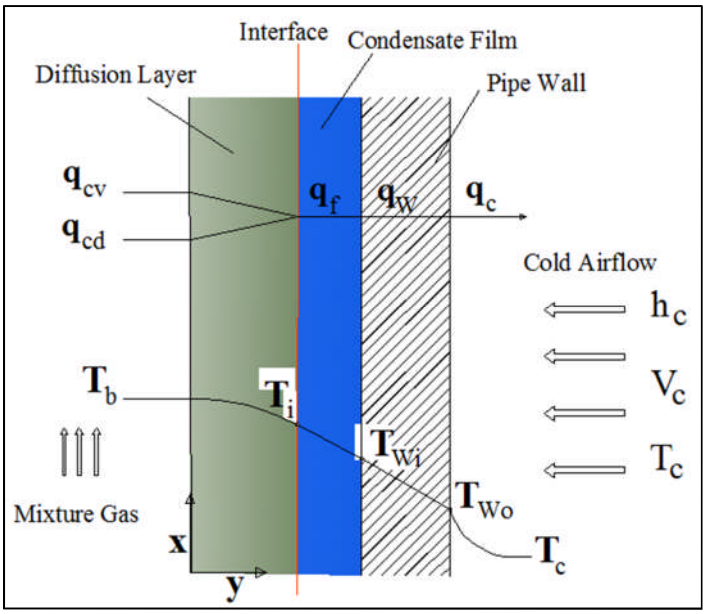

Figure 2-11 Schematic illustration of the model

The total heat flux form the gas side to the interface is given as:

$$q'' = q''_{cv} + q''_{cd} \tag{2.2}$$

$$q'' = h_{cv}(T_b - T_i) + m''_{cond} h_{fg}$$

T_b : Gas bulk temperature of the core flow

h_{cv}: Convective heat transfer coefficient from the gas phase to the liquid film

m''_{cond}: Interfacial mass flux (kg/m^{2}s)

This must be equal to the heat flux through the liquid film as

$$q'' = h_f (T_i - T_{wi}) \tag{2.3}$$

After equating Eq. (2.2) and Eq. (2.3), (heat balance at the interface) we get:

$$h_f (T_i - T_{wi}) = h_{cv}(T_b - T_i) + m''_{cond} h_{fg} \tag{2.4}$$

h_f: condensate film heat transfer coefficient

The condensation heat flux, q''_{cd}, can be defined as the following equation.

$$m''_{cond} h_{fg} = h_{cd}(T_b - T_i) \tag{2.5}$$

h_{fg} is the latent heat of vaporization of water vapour in the diffusion layer temperature $h_{fg}=h_{fg}(T_{ave})$, T_{ave} is the arithmetic average of the gas bulk temperature (T_b) and the interface temperature (T_i).

Substituting Eq. (2.5) in Eq. (2.4) gives:

$$h_f (T_i - T_{wi}) = (h_{cv} + h_{cond})(T_b - T_i) \tag{2.6}$$

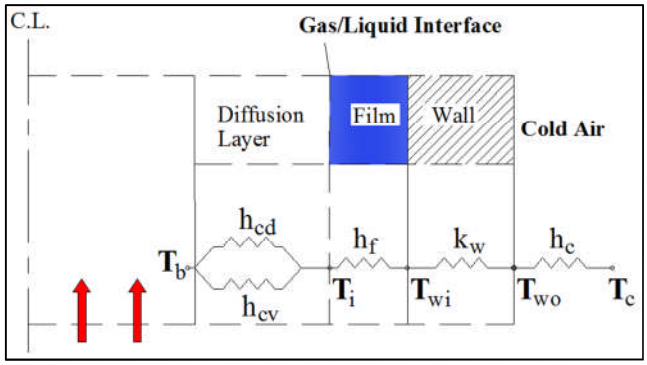

Figure 2-12 Equivalent heat transfer resistance circuit

The equivalent thermal resistance circuit is shown in Figure (2-12). Based on this circuit the overall heat transfer coefficient (U) can be decomposed in to the following equation.

$$U = \left[\frac{1}{h_{cd} + h_{cv}} + \frac{1}{h_f} + \frac{d_i}{2k_w} \ln\left(\frac{d_o}{d_i}\right) + \frac{d_i}{d_o}\frac{1}{h_c} \right]^{-1} \tag{2.7}$$

k_w : is the conductivity of the wall

d_i and d_o are inner wall diameter and outer wall diameter, respectively. h_c is the external cooling heat transfer coefficient.

The overall heat transfer is then given as.

$$Q_{w,i} = U\ A_i\ (T_b - T_c) \tag{2.8}$$

Where A_i is the inner surface of the pipe, T_c is the external coolant temperature.

All the heat transfer coefficients (h_{cd}, h_{cv}, h_f, h_c) must be calculated and the procedure to calculate these are presented as follows.

2.3.4.1 Condensate film heat transfer

The motion of the liquid film is specified by neglecting the acceleration terms in the momentum equations. The thickness of the condensate film is also assumed to be so thin relative to the radius of the pipe so that the curvature of the layer can be neglected. Therefore,

the simplifying assumption is made that the effect of the pipe curvature can be neglected in the evaluation of the thickness of the condensate film.

Then the momentum equation for the liquid film is simplified as follows.

$$\frac{\partial^2 u_f}{\partial y^2} = \frac{1}{\mu_f}\frac{dp}{dx} - \rho_f g \tag{2.9}$$

The liquid velocity profile is determined by integrating Eq. (2.9) twice with respect to y, and considering the following boundary conditions as Eq. (2.10).

$$(\mu_f \frac{\partial u_f}{\partial y})_{y=\delta} = \tau_I \quad , \quad (u_f)_{y=0} = 0 \tag{2.10}$$

$$u_f(y) = \frac{1}{\mu_f}(\frac{dp}{dx} - \rho_f g)(\frac{1}{2}y^2 - \delta y) + \frac{\tau_i}{\mu_f} y \tag{2.11}$$

Where the longitudinal pressure gradient (dp/dx) is equal to that for the gas phase and is balanced by the interfacial shear and the gradient momentum flux as follows.

$$\frac{dp}{dx} = -\left[\frac{4\tau_i}{d} + \frac{d(\rho_g u_g^2)}{dx}\right] \tag{2.12}$$

Seban and Hodgson (1982) recast Eq. (2.9) as the following equation and defined G as Eq. (2.14).

$$\frac{\mu_f}{\rho_f g}\frac{\partial^2 u_f}{\partial y^2} = \left(1 + \frac{1}{\rho_f g}\frac{dp}{dx}\right) \tag{2.13}$$

$$G = 1 + \frac{1}{\rho_f g}\frac{dp}{dx} \tag{2.14}$$

Considering the G and the liquid velocity profile, Eq. (2.11) can be rearranged as follows.

$$u_f(y) = G(\frac{g}{2\nu_f} y^2 - \frac{g\delta}{\nu_f} y) + \frac{\tau_I}{\rho_f \nu_f} y \tag{2.15}$$

This velocity distribution can be used to derive the liquid Reynolds number as a function of film thickness.

$$\mathrm{Re}_f = \frac{m_f}{\pi D_i \mu_f} = \frac{1}{\mu_f}\int_0^{\delta} \rho_f(-u_f)dy = \left(\frac{{\rho_f}^2 g}{{\mu_f}^2}\right)\left[G\frac{\delta^3}{3} - \frac{\tau_I}{\rho_f g}\frac{\delta^2}{2}\right] \tag{2.16}$$

With the charectristic length L

$$L = \left(\frac{v_f^2}{g} \right)^{1/3} \tag{2.17}$$

the dimensionless gas shear stress, τ^*

$$\tau_I^* = \frac{\tau_I}{\rho_f \, g \, L}, \tag{2.18}$$

and dimensionless film thickness δ^*,

$$\delta^* = \frac{\delta}{L}, \tag{2.19}$$

Eq. (2.16) can be normalized as follows.

$$\mathrm{Re}_f = G\frac{(\delta^*)^3}{3} - \frac{\tau_I^*(\delta^*)^2}{2} \tag{2.20}$$

Recasting Eq. (2-20), the dimensionless film thickness δ^*, can be calculated as a function of G and the film Reynolds number as follows. (Liao et al (2009)).

$$\delta^* = \frac{1}{2}\left(24\frac{\mathrm{Re}_f}{G} \right)^{1/3} + \frac{1}{2}\frac{\tau_I^*}{G} + \frac{1}{2}\left(24\frac{\mathrm{Re}_f}{G} \right)^{-1/3}\left(\frac{\tau_I^*}{G} \right)^2 + \frac{1}{3}\left(24\frac{\mathrm{Re}_f}{G} \right)^{-2/3}\left(\frac{\tau_I^*}{G} \right)^3 \tag{2.21}$$

Eq. (2-21) shows that the laminar film thickness increases with the interfacial shear stress. In the cases when vapour shear stress is negligible compared to gravity, (G=1, $\tau_I^* = 0$) , Eq (2.20) can be simplified to give Eq. (2-22).

$$\delta^* = \left(3\mathrm{Re}_f\right)^{1/3} \tag{2.22}$$

This equation is the Nusselt's classical solution for evaluating film thickness for zero shear stress.

For a laminar film, the temperature distribution in the film is almost linear. Therefore the film heat transfer coefficient can be expressed as:

$$h_f = \frac{k_f}{\delta} = \frac{k_f}{\delta^* L} \tag{2.23}$$

Where, k_f is the thermal conductivity of the film. This theoretical film heat transfer coefficient is based on a smooth laminar film. However the actual film surface includes waviness. Chun et al, (1971) considered the effects of waviness and corrected the film heat transfer coefficient for co-current condensation by an empirical factor as follows when Re_f is greater than 4.

$$h_{f,w} = \frac{h_f}{1.33(4\mathrm{Re}_f)^{-0.11}} \tag{2.24}$$

The subscript, w, denotes the waviness. The above equation is derived for co-current condensation but Thumm et al (2001) reported that it can be applied for counter current condensation as well.

2.3.4.2 Two-phase interfacial stress in counter-current condensation

The liquid film velocity (u_f) at the interface is defined in terms of the interfacial shear stress τ_I exerted by the gas/vapour mixture on the condensate film, as expressed in Eq. (2-11). The interfacial shear stress for counter-current condensation was expressed by Liao et al (2009) as:

$$\tau_I = \frac{1}{2}\rho_g \, f (u_g - u_f)^2 + \dot{m}_c (u_g - u_f) \tag{2.25}$$

The first term on the right hand side of the Eq. (2.25), relates to the shear stress at zero mass transfer and the second term results from the momentum transferred by the condensation mass flux. In this equation, ρ_g is the mixture density, f is a friction factor, u_g is the bulk steam-gas mixture velocity. It should be noted that both the velocities of the gas and the film can be expressed as average velocities here. In this study the approximation $u_g << u_f$ is made, therefore Eq. (2.25) can be expressed as.

$$\tau_I = \frac{1}{2}\rho_g \, f \, u_g^2 \tag{2.26}$$

The friction factor (f) for the upward flowing gas is given in modified form by Seban and Hodgson (1982) for the counter-current flow. This friction factor is defined as follows.

$$\left(\frac{f}{2}\right) = \left(\frac{f}{2}\right)_0 \left(1 + 1400 \frac{\sqrt{2}\,\mathrm{Re}_f^{0.5}}{\mathrm{Re}_g^{0.9}} \frac{v_f}{v_g} \left(\frac{\rho_f}{\rho_g}\right)^{0.5} \left[1 - \exp\left(-\frac{\tau_I}{\rho_f g \delta}\right)\right]\right) \tag{2.27}$$

Where $\left(\frac{f}{2}\right)_0$ is the single phase friction coefficient and is defined in terms of the gas Reynolds number as follows,

$$\left(\frac{f}{2}\right)_0 = \frac{8}{\mathrm{Re}_g} \qquad \mathrm{Re}_g < 2000 \tag{2.28}$$

$$\left(\frac{f}{2}\right)_0 = \frac{0.04}{(\mathrm{Re}_g)^{0.25}} \qquad \mathrm{Re}_g > 4000$$

$$\left(\frac{f}{2}\right)_0 = \frac{(\mathrm{Re}_g)^{0.33}}{3050} \qquad 2000 < \mathrm{Re}_g < 4000$$

Thumm (2001), adopted a method to calculate the friction factor as follows.

$$\left(\frac{f}{2}\right)=\frac{1}{8}\left(\frac{258}{\Omega^2}+\frac{0.205}{\Omega^{0.25}}\right) \tag{2.29}$$

$$\Omega = c\frac{\mathrm{Re}_g}{\mathrm{Re}_f}\left(\frac{\rho_f}{\rho_g}\right)^{0.4}\left(\frac{\mu_g}{\mu_f}\right)^{0.67}\left[\frac{2\delta_0^*(v_f^2/g)^{1/3}}{d}\right]^{0.5}$$

Where the constants c and n are evaluated from Eq (2.30) and the δ_0^* is expressed in Eq (2.31).

$$c=1.31 \quad , \quad n=0.25 \quad for \quad \mathrm{Re}_f < 40 \tag{2.30}$$
$$c=4.76 \quad , \quad n=0.60 \quad for \quad \mathrm{Re}_f \geq 40$$

$$\delta_{l,0}^* = (3\,\mathrm{Re}_f)^{1/3} \qquad for \qquad \mathrm{Re}_f \leq 513 \tag{2.31}$$
$$\delta_{t,0}^* = (0.303\,\mathrm{Re}_f)^{0.583} \qquad for \qquad \mathrm{Re}_f > 513$$

The above suggested correlations are applied for counter-current condensation and are quite different from the correlations applied to co-current condensation ([Kim and Corradini, 1990] and [Dehbi and Guentay, 1997]).

2.3.4.3 Diffusion Layer Model (Condensation heat transfer coefficient)

The condensation heat transfer in the presence of non-condensable gases can be evaluated by the generalized diffusion layer model (Liao and Vierow, 2007), in which a condensation thermal conductivity is introduced on mass basis to facilitate formulation of the mass transfer.

As expressed in Eq. (2.5) the condensation heat flux can be expressed as: $(q''_{cd} = m''_{cond} h_{fg})$. To find m''_{cond}, the mass balance at the interface is applied. Considering the steady state diffusion equation in the radial direction y, the condensation mass flux at the interface is evaluated as the following equation (See Appendix A-1 for more details).

$$m''_{cond} = \frac{\rho D}{\delta_g}\ln\left(\frac{1-W_{v,i}}{1-W_{v,b}}\right) \tag{2.32}$$

Where δ_g is the effective diffusion layer thickness, D is diffusivity, $W_{v,b}$ and $W_{v,i}$ are vapour mass fraction at the bulk and the interface, respectively. Using Eqs. (2.32), (2.5) the condensation heat transfer coefficient (h_{cd}) can be calculated as follows.

$$h_{cd} = \frac{m''_{cond} h_{fg}}{(T_b - T_i)} = \frac{\rho\, D\, h_{fg}}{\delta_g (T_b - T_i)}\ln\left(\frac{1-W_{v,i}}{1-W_{v,b}}\right) \tag{2.33}$$

The condensation heat transfer h_{cd} can be evaluated using Sherwood number as

$$Sh = \frac{h_{cd}L}{k_c} = \frac{L}{\delta_g} \tag{2.34}$$

The Sherwood number in the above equation can be recast by substituting δ_g from Eq. (2.34) as.

$$Sh = \frac{h_{cd}L(T_b - T_i)}{h'_{fg}\rho D} \frac{1}{\ln\left((1-W_{v,i})/1-W_{v,b}\right)} = \frac{h_{cd}L}{k_c} \tag{2.35}$$

Therefore the condensation thermal conductivity (k_c) derived on the basis of mass as follows.

$$k_c = \frac{h_{fg}\rho D}{(T_b - T_i)} \ln\left(\frac{1-W_{v,i}}{1-W_{v,b}}\right) \tag{2.36}$$

Liao and Vierow (2007) recast the above equation by using the Clausius-Clapeyron equation and ideal gas law as:

$$k_c = \frac{\phi_2}{\phi_1} \frac{h_{fg}h^{/}_{fg}PDM_vM_g}{R^2T^3_{ave}} \tag{2.37}$$

$$\phi_1 = \frac{\ln\left[(1-m_{g,b})/(1-m_{g,i})\right]}{\ln(m_{g,i}/m_{g,b})}$$

$$\phi_2 = \frac{\overline{M}^2_m}{M_{mb}M_{mi}}$$

In the above equation:

- R is the ideal gas constant. ϕ_1 accounts for the non-condensable gas and suction effects and ϕ_2 accounts for the effect of variable mixture composition across the condensation boundary layer.
- P is the gas total pressure and D is the vapor mass diffusivity (See Appendix-B for more details)
- $\overline{M}_m$ is the average mixture molecular weight and is calculated as $\overline{M}_m = \bar{x}_v M_v + (1-\bar{x}_v)M_g$ which $\bar{x}_v$ is the vapour log mean mole fraction and given as $\bar{x}_v = (x_{v,b} - x_{v,i})/\ln(x_{v,b}/x_{v,i})$.
- $h^{/}_{fg}$ is defined as $h^{/}_{fg} = h_{fg} + cp_v(T_b - T_i)$ and c_{pv}: is the specific heat of the vapour species.

The condensation thermal conductivity in Eq. (2.37) differs from the ones in the previous studies ([Kageyama et al., 1993], [Kuhn et al., 1997] and [Herranz et al., 1998]) in that it has a more rigorous technical derivation.

Using the condensation thermal conductivity (k_c) in Eq. (2.37) the condensation heat transfer coefficient (h_{cd}) can be evaluated by using the Sherwood number from the following equation.

$$Sh = \frac{h_{cd} d}{k_c} = \begin{cases} 48/11 \quad , \quad \mathrm{Re}_g < 2300 \\ 0.023 \mathrm{Re}_g^{0.8} \, Sc_g^{0.35} \quad , \quad \mathrm{Re}_g > 10000 \end{cases} \tag{2.38}$$

The Sherwood number in the transition regime ($2300 < \mathrm{Re}_g < 10000$) is taken to be a linear interpolation between the Sherwood numbers at the two ends of the transition regime.

2.3.4.4 Convective heat transfer coefficient

The gas phase sensible heat transfer is evaluated with the standard forced convection formulation for flowing vapour and non-condensable gases. Similar to the condensation heat transfer, the sensible heat transfer coefficient comes from Nusselt number (Nu) as follows.

$$Nu = \frac{h_{cv} d}{k_g} \tag{2.39}$$

Invoking the heat and mass transfer analogy, the Nusselt number can be evaluated using Eq. (2.40), where the Sherwood number is replaced with the Nusselt number and the Prandtl number is replaced with the Schmidt number [$Sh\ (Sc) = Nu(\mathrm{Pr})$]. The gas phase convective heat transfer coefficient h_{cv} is then given as follows.

$$Nu^* = \frac{h_{cv} d}{k_G} = \begin{cases} 48/11 \quad , \quad \mathrm{Re}\, g < 2300 \\ 0.023 \mathrm{Re}_g^{0.8} \, \mathrm{Pr}_g^{0.35} \quad , \quad \mathrm{Re}_g > 10000 \end{cases} \tag{2.40}$$

2.3.4.5 External Heat Transfer Coefficient

Cross-flow over a pipe exhibits complex flow patterns depending on the Reynolds number defined as the following Eq.

$$\mathrm{Re} = \frac{\rho V D}{\mu_g} \tag{2.41}$$

In which D, is the outer diameter of the pipe, V is the flow velocity, ρ is density and μ_g is the dynamic viscosity.

At very low upstream velocities (Re<1), the fluid completely wraps around the pipe, however at higher velocities the boundary layer detached from the surface and a separation region behind the cylinder is formed, as shown in Figure (2-13).

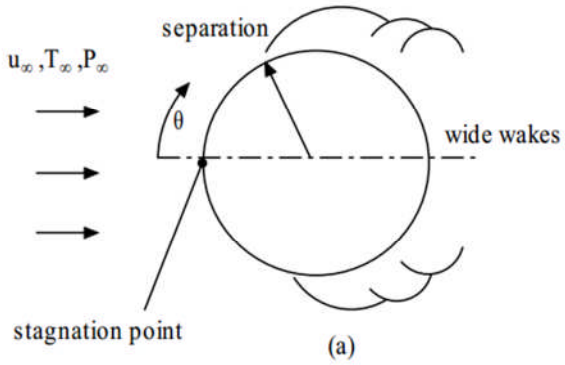

Figure 2-13 Flow over cylinder, (Holman, 2002)

Because of complexity of the flow pattern, only correlations for the average heat transfer coefficient have been developed. These correlations are generally appropriate only over a certain range of conditions.

In forced convection flow conditions around the pipe, Knudsen and Katz s (H.J Holman 1997) proposed an empirical relation given in Equation (2-42) which is widely used, where constants C and n are given in Table (2-3).

$$\overline{Nu_g} = C(\mathrm{Re}_g)^n \, \mathrm{Pr}_g^{1/3} \tag{2.42}$$

Table 2-3 Constants for use with Eq. (2-42) (Holman, 2002)

Re_g	C	n
0.4-4	0.989	0.33
4-40	0.911	0.385
40-4000	0.683	0.466
4000-40000	0.193	0.618
40,000-400,000	0.0266	0.805

All properties are evaluated at film temperature (T_f), Holman (2002). T_f is arithmetic mean of the free stream temperature (T_∞) and the pipe outer surface Temperature (T_{wo}) as follows:

$$T_f = \frac{T_\infty + T_{wo}}{2} \tag{2.43}$$

For all values of Re_g, as well as wide range of Prandtl numbers, Holman (1997) proposed the following correlation.

$$\overline{Nu_g} = 0.3 + \frac{0.62\,\mathrm{Re}_g^{1/2}\,\mathrm{Pr}_g^{1/3}}{\left[1+\left(\frac{0.4}{\mathrm{Pr}_g}\right)^{2/3}\right]^{1/4}} + \left[1+\left(\frac{\mathrm{Re}_g}{282{,}000}\right)^{5/8}\right]^{4/5} \quad (2.44)$$

Holman (2002) expressed that this equation is pretty accurate, and thus has been preferred to be used in study.

Churchill and Chu (1975), give a correlating equation for natural convection from a long isothermal horizontal cylinder which is the most reliable for Rayleigh number (Ra). Rayleigh number is the product of Grashof (Gr) and Prandtl number (Pr) and is defined as:

$$Ra = Gr\,.\,\mathrm{Pr} \quad (2.45)$$

The Grashof number (Gr), can be interpreted as dimensionless number representing the ratio of buoyancy forces to the viscous forces in the free-convection flow system. This number plays a similar role to that played by the Reynolds number in forced convection. It is defined as

$$Gr = \frac{D^3 \rho_g^{\,2} g\,\Delta T\,\beta}{\mu^2} \quad (2.46)$$

Where d is the pipe diameter, g is gravity acceleration, β is the volumetric thermal expansion coefficient which is equal to $1/T_f$, ΔT is the difference between the pipe outer surface temperature (T_{wo}), and ambient temperature (T_∞) and μ is the dynamic viscosity. Natural convection Nusselt number is given as:

$$Nu = \left(0.6 + \frac{0.387\,Ra^{1/6}}{\left[1+(0.599/\mathrm{Pr})^{9/16}\right]^{8/27}}\right)^2 \quad (2.47)$$

2.3.4.6 Partial properties

Variables or properties related to the condensate film, vapour and non-condensable gas are respectively denoted with subscript f, v, g.

The physical properties of the gas mixture are evaluated at the arithmetic mean of the gas core (bulk) temperature and interface temperature as follows:

$$T_{ave} = \frac{T_b + T_i}{2} \quad (2.48)$$

Water film physical properties are evaluated at the film temperature (T_f) which is derived from Eq. (2.49).

$$T_f = T_{wi} + 0.31\left(T_i - T_{wi}\right) \quad (2.49)$$

The air and vapour mass fraction are calculated according the following equations.

$$W_v = \frac{m_v}{m_v + m_a} = \frac{\rho_v}{\rho_v + \rho_a} = \frac{M_v}{M}\frac{P_v}{P} \quad (2.50)$$

$$W_a = 1 - W_v \quad (2.51)$$

Where M_v is the vapor molecular weight, P is the gas total pressure, and M is the mixture molecular weight given by.

$$\frac{1}{M} = \frac{W_v}{M_v} + \frac{W_a}{M_a} \quad (2.52)$$

The density of water vapor, ρ_v and the density of air ρ_a are respectively given by:

$$\rho_v = \frac{P_v}{R_v T} \qquad \rho_a = \frac{P - P_v}{R_a T} \quad (2.53)$$

Where R_a= 287 Nm/kg K and R_v= 462 Nm/kg K. The density of the gas mixture is then given by

$$\rho_g = \rho_v + \rho_a = \frac{\rho_v}{1 - W_a} \quad (2.54)$$

Vapour partial pressure (P_v) at interface or bulk can be calculated by Gibbs-Dalton ideal gas mixture equation from the gas total pressure (P) and dry air mass fraction (W_a) as follows.

$$P_v = P\frac{1 - W_a}{1 - (1 - M_v / M_g)W_a} \quad (2.55)$$

By re-arranging the above equation, one can calculate the non-condensable gas (dry air) mass fraction with vapour partial pressure as follows.

$$W_a = \frac{P - P_v}{P - (1 - M_v / M_g)P_v} \quad , \quad W_v = 1 - W_a \quad (2.56)$$

The molecular weight of dry air is M_a =0.0289644 (kg/mol) and molecular weight of water vapour is M_v =0.01802 (kg/mol)

The vapour mole fraction, x_v and air mole fraction, x_a are defined as follows.

$$x_v = \frac{P_v}{P} \quad , \quad x_a = \frac{P_a}{P} = 1 - x_v \quad (2.57)$$

The gas mixture molecular weight M_g (kg/mol) is then derived as follows

$$M_g = x_v M_v + (1 - x_v)M_a \quad , \quad W_v = \frac{x_v M_v}{M} \quad (2.58)$$

The molecular transport properties of gas mixture, such as viscosity and thermal conductivity can be calculated as follows (Bird 1960).

$$\mu_g = \sum_{i=1}^{n} \frac{x_i \mu_i}{\sum_{j=1}^{n} x_j \phi_{ij}} \quad , \quad k_g = \sum_{i=1}^{n} \frac{x_i k_i}{\sum_{j=1}^{n} x_j \phi_{ij}} \tag{2.59}$$

$$\phi_{ij} = \frac{1}{\sqrt{8}} \left(1 + \frac{M_i}{M_j}\right)^{-0.5} \left[1 + \left(\frac{\mu_i}{\mu_j}\right)^{0.5} \left(\frac{M_j}{M_i}\right)^{0.25}\right]^2 \tag{2.60}$$

If we assume air as species 1, and saturated vapour as species 2 the above equation can be recast as follows.

$$\mu_g = \frac{x_a \mu_a}{x_a \phi_{aa} + x_v \phi_{av}} + \frac{x_v \mu_v}{x_a \phi_{va} + x_v \phi_{vv}} \tag{2.61}$$

$$k_g = \frac{x_a k_a}{x_a \phi_{aa} + x_v \phi_{av}} + \frac{x_v k_v}{x_a \phi_{va} + x_v \phi_{vv}} \tag{2.62}$$

It should be noted that ϕ_{aa} and ϕ_{vv} are equal to 1.The specific heat capacity for the gas mixture is simply calculated by mass fraction weighted average.

$$c_{p,g} = W_a c_{p,a} + (1 - W_a) c_{p,v} \tag{2.63}$$

2.3.5 Energy balance equation

The heat transfer through the gas/boundary layer can be expressed with reference to convection and conduction as follows:

$$q'' = q''_{conv} + q''_{cond} \tag{2.64}$$

Considering q''_{conv} and q''_{cond} the heat flux can be rewritten as:

$$q'' = h_{cv}(T_b - T_i) + h_{cd}(T_b - T_i) \tag{2.65}$$

Where h_{cv} is the forced convection heat transfer coefficient in the condensate film due to sensible heat, h_{cd} is the condensation heat transfer coefficient.

The temperature at the interface, inner and outer wall can be calculated by using the heat balance equations.

First, the gas phase sensible and latent heat flux transferred to the two-phase interface must be balanced by the heat flux transferred from the interface to the liquid film in steady state as:

$$(h_{cv} + h_{cond})(T_b - T_i) = h_f (T_i - T_{wi}) \tag{2.66}$$

Second, in steady state condition, the heat flux transferred from the liquid film to the wall inside surface must be equal to the heat flux transferred from the wall inside surface through the wall:

$$h_f (T_i - T_{wi}) = \frac{k_W}{d_i \ln(d_o / d_i)/2}(T_{wi} - T_{wo}) \quad (2.67)$$

Where T_{wi} and T_{wo} are respectively the temperatures at the inside and outside surfaces of the tube; D_i and D_o are respectively the inside and outside diameters of the tube. Finally, the heat flux transferred from the tube wall outside surface to the coolant must be removed by the cooling air flowing around the pipe, external air flow:

$$\frac{k_W}{d_o \ln(d_o / d_i)/2}(T_{wi} - T_{wo}) = h_c (T_{wo} - T_c) \quad (2.68)$$

Where the heat transfer coefficient for the external air flow (h_c) is evaluated considering the relative importance of the forced convection.

2.4 Condensation and Ice formation in CFD Software (Star CCM+)

Although the numerical study and the theoretical model developed in this study can help to model condensation and predict freezing regions in the pipe, the Jaguar interest is to use a CFD model to simulate condensation and predict the extend of freezing in the pipe. StarCCM+ is the current CFD software being used at Jaguar. Therefore, current models in this software which can be used to model condensation and freezing in the pipe are investigated.

Star CCM+ can model condensation using a model referred to as the "Thin Film Defogging model". For modelling freezing there are two models available in this software which are Thin Film DeIcing and VOF Solidification models.

The Thin Film Defogging model allows for condensation, but not for deposition of ice. This model is based on solving an additional scalar transport equation that represents the mass fraction of water vapour. A source term for the scalar is considered for condensation of the gas mixture. The vapour content in the air does not affect the thermal properties of the vapour-air mixture and this need to be specified separately. The water vapour mass is neglected with respect to the total mass in a cell.

The Thin film De-icing model allows melting but not solidification. VOF Melting and Solidification is the only model available in the software which can be used for simulating ice formation in free surface cases. This model is available for VOF phases and enables a liquid to turn into a solid, and vice versa, within one VOF phase. Currently there is no mechanism for deposition of a condensate film directly on to walls from the water vapour.

2.4.1 Defogging Model in StarCCM+

The defogging model is a simplified approach to simulate condensation inside a cabin windshield or other surfaces.

In this model, the mass fraction of vapour is obtained by solving an additional scalar transport equation. A source term for the scalar is considered for condensation of the fog layer as well as the latent heat required for transition. Condensation rate is also calculated when there is a difference between the water vapour content in the gas mixture and the cell

next to the surface. In this model the fog layer is modelled by a function and it is not represented as a phase in the inner volume mesh. Thus the fog layer does move or flow

It is advised by Star CCM+ manual (Ver 7.02) to run the simulation in steady state to initialize the flow field.

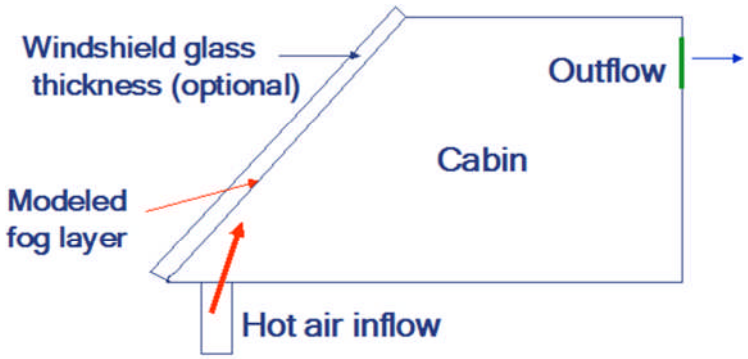

Figure 2-14 Boundaries in a windshield application (Star CCM+ User Guide)

Since the fog layer does not affect the flow field, it is advised to select a large time step during the transient run.

The rate of mass transfer per unit surface (kg/s-m^2) in this model is computes as:

$$\dot{m} = \rho_g \beta_g CG \ln \frac{CG(1-C_s)}{CG(1-C_g)} \tag{2.69}$$

Where, β_g is given by:

$$\beta_g = C_{emp} \cdot D_v / L \cdot 0.045 \cdot \mathrm{Re}^{0.8} Sc^{0.43} \tag{2.70}$$

- C_{emp} is the empirical constant used for calibration (0.05-0.9)
- L is characteristic length (cubic root of cell volume adjacent to fog layer boundary
- D_v is diffusion of vapour in air (m^2/s) and constants CG and CS are given

$$CG=0.622+0.378C_g \tag{2.71}$$

$$CS=0.622+0.378C_s$$

- C_g is the concentration of vapour in air
- C_s is the saturation concentration of vapour in air
- Sc is Schmidt Number

The saturation pressure is calculated from the following equation

$$p_s(T) = 611.85 e^{\frac{17.502(T-273.15)}{T-32.32}} \tag{2.72}$$

The amount of condensation in every time step is

$$d\dot{m} = \dot{m} \cdot dt \tag{2.73}$$

and the thickness of the liquid film is calculated by

$$s = s_{t-1} + dm/\rho_l \tag{2.74}$$

2.4.2 Solidification model (general enthalpy method)

In order to model Ice formation in Star CCM+ software, an enthalpy method is used. This model does not track the liquid-solid interface explicitly but instead it uses an enthalpy formulation and determines the solidified portion of the liquid-solid which can be converted to ice [StarCCM+].

In this case the enthalpy of the liquid-solid phase h_{ls}^* is defined as function of the sensible enthalpy of water (h_{ls}) and the relative solid volume fraction (α_s^*), defined as:

$$h_{ls}^* = h_{ls} + (1-\alpha_s^*)h_{fusion} \tag{2.75}$$

α_s^* is the relative solid volume fraction and it is defined as the portion of the volume occupied by the liquid-solid phase which is the solid state and h_{fusion} is the latent heat of fusion.

In this model the relative solid volume fraction is calculated by:

$$\alpha_s^* = \begin{cases} 1 & if \quad T^* < 0 \\ f(T^*) & if \quad 0 < T^* < 1 \\ 0 & if \quad 1 < T^* \end{cases}$$

Where, T^* is the normalized temperature defined as:

$$T_l^* = \frac{T - T_{solidus}}{T_{liquidus} - T_{solidus}} \tag{2.76}$$

$T_{solidus}$: The temperature at which a material completely solidifies.

$T_{liquius}$: The temperature at which a material becomes completely liquid

Chapter 3 Experiment

3-1 Introduction

The main purpose of conducting the experimental study is to assess condensation and ice formation in a vertical, a horizontal and a T-Joint pipe exposed to external convective cooling. Specifically, evaluating the main test parameters like vapour mass fraction, external heat transfer and surface coating on heat flux is the main focus in this study

In order to generate an air/steam mixture at a predetermined humidity, a test rig has been designed and constructed which is able to provide a steady air-steam mixture at a given vapour concentration to flow in to the pipe. To simulate external convective cooling, the Cranfield icing tunnel has been utilized to blow cold air around the pipe at different air speeds and temperatures.

In this section, the test rig design and its components are described. Test conditions, test procedures, and the calibration of tunnel are explained and in the last section the evaluation of the heat transfer from temperature measurement will be studied. The experimental analysis is described in chapter 4.

3-2 Cranfield icing tunnel

The Cranfield icing tunnel is a closed–circuit wind tunnel with of 760mm square working section (Fig. 3-1). Its wind speed range and total temperature range are from 30m/s to 100m/s and from 30°C to -30°C, respectively.

Figure 3-1 Convergent entry (left) to 760mm square working section (right), Luxford (2005)

It is also equipped with a multi-channel video monitoring and surveillance system, a National Instruments Field Point based flexible 16 bit signal monitoring and recording installation for temperatures, pressures and other electrical signals. The schematic of the tunnel is shown in Fig. (3-2).

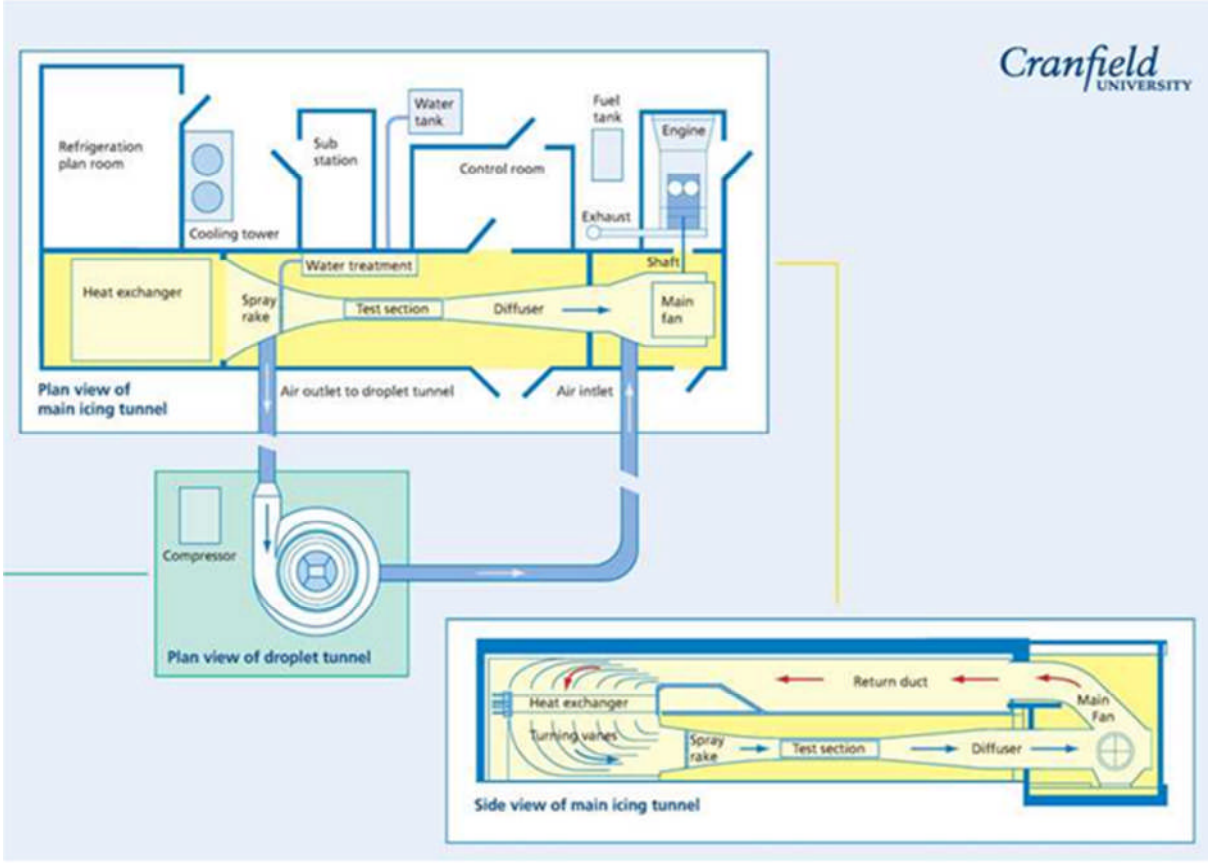

Figure 3-2 Schematic of Cranfield Icing Tunnel

3-3 Test rig design

The test rig comprises of a vapour/air source, a Perspex pipe, a data acquisition system and picture/video cameras. The air/steam mixture producer supply a steady mixture of air-steam at a specific vapour mass fraction and guide it to the Perspex pipe at a constant mass flow rate and temperature. The Perspex pipe is installed inside the icing tunnel test section. The main components of the test rig are:

- Air compressor and air tank
- Air dryer
- Pressure regulator and needle valve
- Air mass flow rate controller
- Boiler (Steam Generator)
- Rubber Hose
- Gas manifold
- Three-way valve
- Flange
- Condensate container
- Perspex pipe
- Clamps and connections
- Temperature probes (RTD, Thermocouples)
- Temperature controller
- Data acquisition box (Labview software is used for collecting and analysing data in the system).
- Video/photo camera

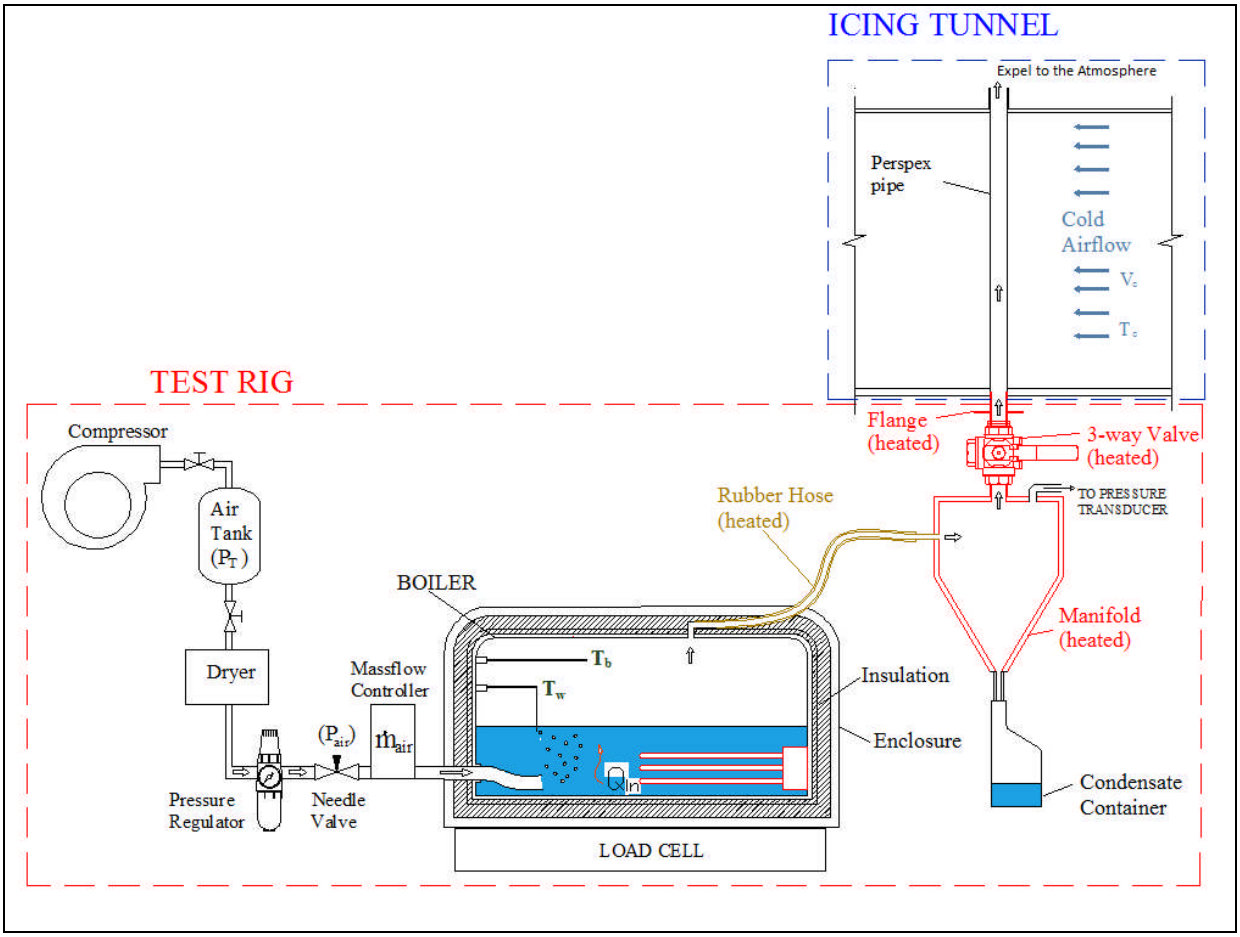

Figure 3-3 Schematic diagram of the test rig

The schematic of the test rig has been shown in Figure (3-3), dry air is supplied by a compressor and it is stored in an air tank to minimize air pressure fluctuations and keep the air pressure constant (P_T). Then the compressed air goes in to a dryer and passes through a pressure regulator, a needle valve, a mass flow rate controller (Omega-FMA5528) and finally it is injected in to the boiler. The dry air is mixed with the water vapour and a steady air-steam mixture at a given mass concentration is generated. The mixture then passes through a heated rubber hose, a heated manifold, a heated three-way valve, a heated flange and flows into the Perspex pipe from its bottom and eventually is expelled in to the Atmosphere from the outlet of the pipe.

The pipe is installed in the test section and exposed to the cold airflow inside the tunnel. (The flow direction of the gas mixture is shown in Figure (3-3)). The length of the pipe is 80 cm, which is 4 cm longer than the size of the test section. This allows the gas mixture to be expelled to the atmosphere at the end of the pipe. The pipe material is Perspex which permits visual observation of condensation and ice formation in the pipe. One HD Sony video

recorder and three Nikon cameras (500D) have been used to capture video and pictures during the tests.

In order to prevent the steam from condensing before entering the Perspex pipe, all of the component of the test rig which come to contact with the gas mixture have been insulated and heated up to 2-5 degree Celsius above the saturation temperature of the gas mixture.

3.3.1 Mass flow rate controller

The dry air mass flow rate is measured by an electronic mass flow rate controller (OMEGA-FMA5528). This device can control the airflow from 10 SCCM (standard cubic centimetre per minute) up to 50 SLM (standard litre per minute). The FMA5528 measures the air mass flow rate directly, without needing to compensate for variations in gas temperature or pressure (within stated limits). It can also maintain a constant flow regardless of variation in inlet or outlet pressure through a built-in electromagnetic valve. The set-point is controlled locally via a potentiometer. It also produces a digital output and sends digital data through a 9 pin serial port connected to computer.

The reading of the mass controller is shown on its built-in screen (shown in Figure (3-4)) in standard litres per min. The standard condition is 20 °C and 1 atm absolute. Knowing the temperature and pressure of the actual flow, the actual mass flow rate can be calculated by using the following formula.

$$Actual\ Mass\ Flow\ Rate\ \left(\frac{litre}{\min}\right) = Reading\left(\frac{litre}{\min}\right) \times \frac{1}{Actual\ Pressure\ (atm)} \times \frac{Actual\ Temperature(K)}{293\ (K)} \quad (3.1)$$

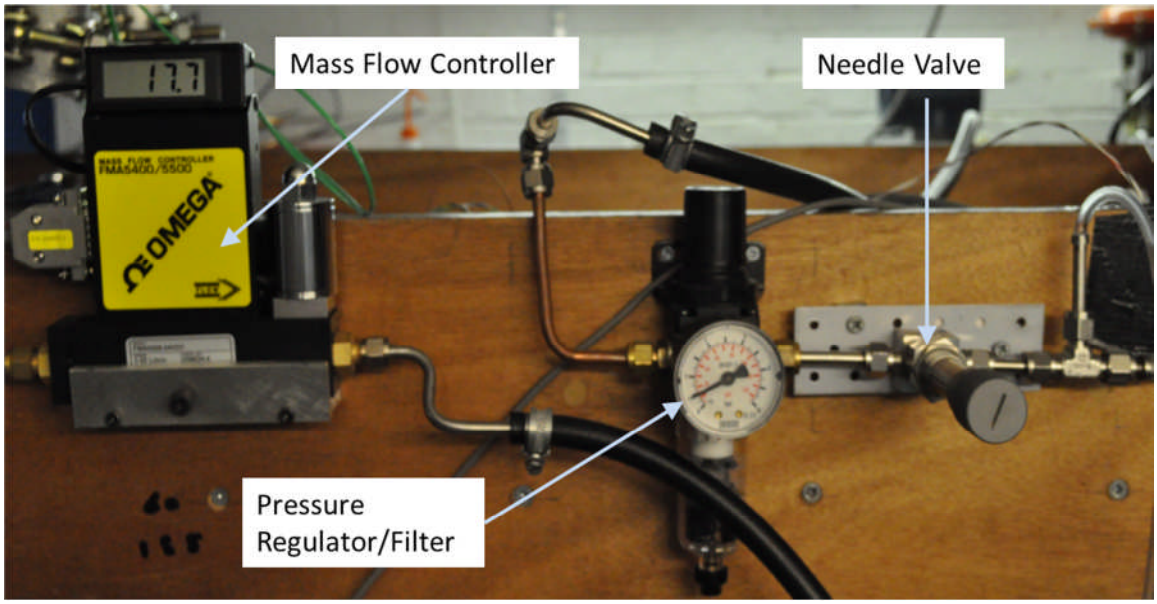

Figure 3-4 Mass Flow Rate Controller (OMEGA-FMA5528), Pressure regulator and a Needle Valve

An air pressure regulator and a needle valve have been used upstream of the mass flow rate controller to reduce the air pressure from 8 bar (P_T) to 2 bar which is the operating pressure of the mass flow controller, as shown in Figure (3-4). There is a built-in filter in the air regulator which can separate water from the air before it reaches the mass flow rate controller.

3.3.2 Steam Generator (Boiler)

There are two methods for mixing dry air with steam. In the first approach dry air and steam are mixed via a nozzle after the boiler. However, in the second method dry air is injected directly to water in the boiler. Tanrikut (2000) showed that the steam behaviour in the second method, i.e. injection to the boiler, is more stable compared to the first method especially when air mass flow rate is increasing. Moreover, this method avoids local condensation and entrainment due to possible inadequate thermal control of incoming air. In this test rig, the second approach has been utilized. The air connection to the boiler is shown in Figure (3-5).

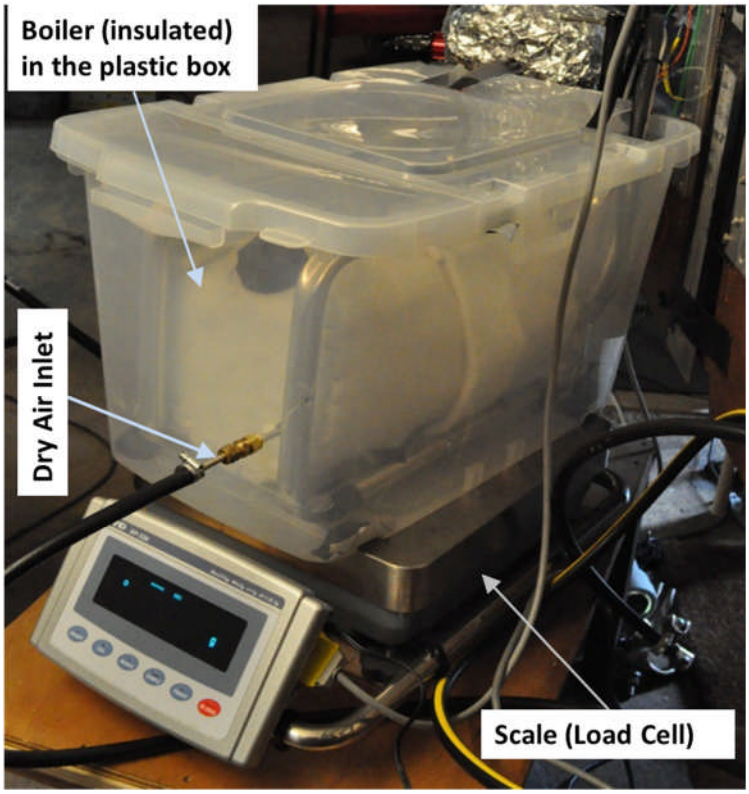

Figure 3-5 Boiler (steam generator) and Scale

The boiler has been insulated and secured in a plastic box to reduce thermal loss, as illustrated in Figure (3-5). The boiler was based on a steam generator for stripping wall paper. In order to measure vapour mass flow rate, evaporation rate, the boiler has been placed on a

scale. This scale measures the weight of the boiler during the tests and sends the data through a 9 pin connector to a computer in frequency of 20milliseconds. Water in the boiler is heated up by an immersion type electrical heater mounted at the bottom of the boiler. The steadiness of the water evaporation primarily depends on the constancy of heat supply to the evaporator which is easily achieved by constant electric heating at a calculated wattage and at a steady evaporator pressure (P_B) which in this case is at atmospheric pressure. The boiler power is set by using a power controller (Variac) as shown in Figure (3-6). It generates a constant electrical heating which helps to generate the steam at a constant rate. The power (wattage) is measured by a digital multi meter connected to the Variac as shown in Figure (3-6).

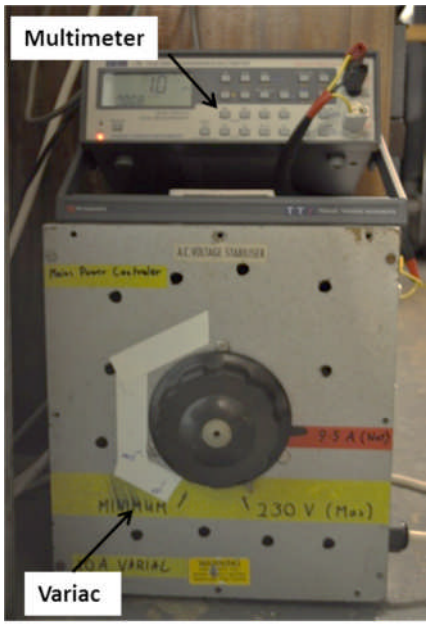

Figure 3-6 Boiler Power Controller (Variac)

3.3.3 Gas manifold, three-way valve and flange

After the boiler the gas mixture passes through a flexible hose and thereafter it flows through a manifold, a three-way valve and a flange until it reaches the Perspex pipe which is installed in the icing tunnel test section. In Figure (3-7), the way which the manifold, the three-way valve and the flange are connected is shown. They are held by a stand from the bottom and bolted to test section from the top. They are all insulated and heated up to 2 to 5 degrees above the saturation temperature of the gas mixture.

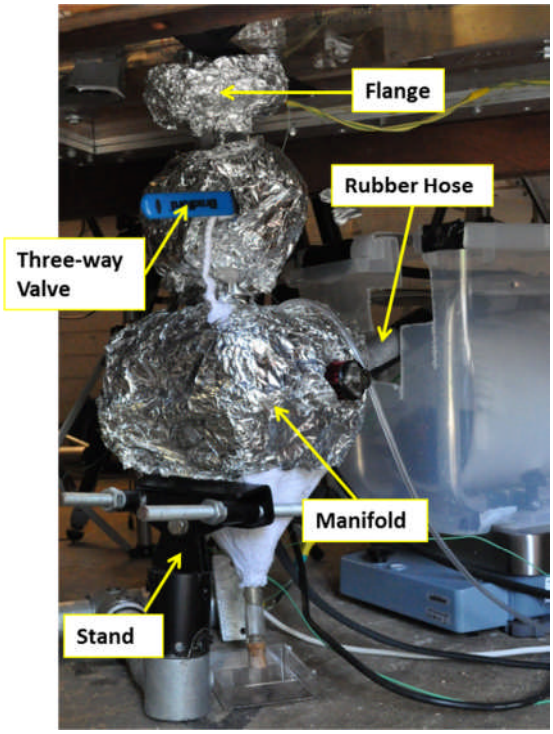

Figure 3-7 Position of Boiler, Hose Pipe, Manifold, T-Valve, Flange

3.3.3.1 Gas manifold

The main reason to use the gas manifold is to guide the condensate liquid toward the condensate container mounted at the bottom of the manifold. Hence the bottom of the manifold has been shaped like a pyramid shown in Figure (3-8). Moreover it provides space to insert a temperature probe (RTD). The manifold was made to be large enough to accommodate a dew point humidity measuring device as shown in Figure (3-8). However, the humidity measuring device failed during the first test. Therefore, the humidity of the mixture was evaluated by measuring the weight of the boiler during the tests as shown in Figure (3.5).

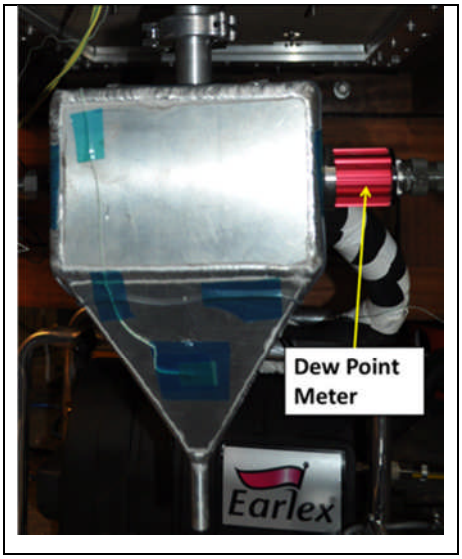

Figure 3-8 Gas Manifold

The manifold is heated to prevent the gas mixture from condensing on its inner walls. It is made of aluminium plates with thickness of 6mm.

Six electrical resistors have been attached to its surfaces, 4 on the top and 2 on the sides, shown in Figure (3-9a).

A temperature controller is used to control the temperature by applying voltage through the resistors. This was a convenient way to produce heat to the structure. A thermocouple is also installed on its top surface to give feedback to the temperature controller. (See Section 3.3.4 for more details on the temperature controller).

The direction of the mixture gas through the manifold is illustrated in Figure (3-9b). As shown the gas mixture enters from the side and leaves the manifold from the top. To measure the gas temperature a RTD (PT 100) probe has inserted inside the manifold which is perpendicular to the gas-mixture flow. The pressure of the gas mixture is measured by using a pressure transducer.

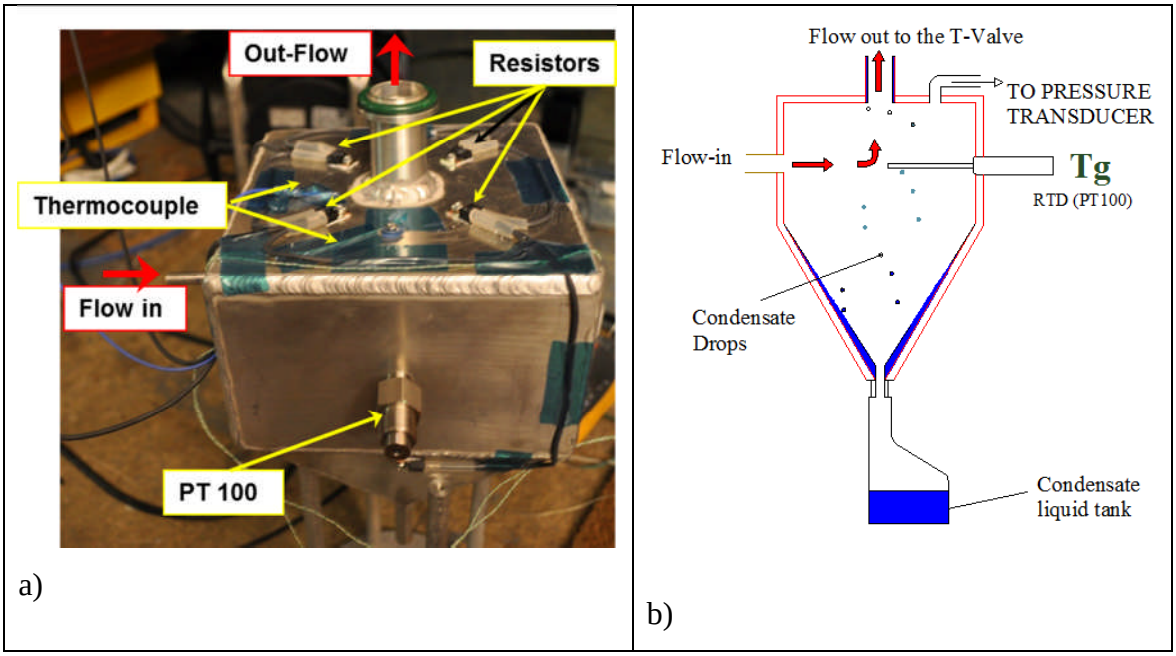

Figure 3-9 Gas Manifold, a) Electrical resistors attached b) Direction of the flow in the manifold

3.3.3.2 Three-way valve

A three-way valve (L type), has been used in order to control the gas mixture and guide the mixture to the Perspex pipe when the tunnel velocity and temperature become steady. It expels the mixture to the atmosphere before reaching the steady condition. The schematics of the two different combinations of the flow direction are shown in Figure (3-10).

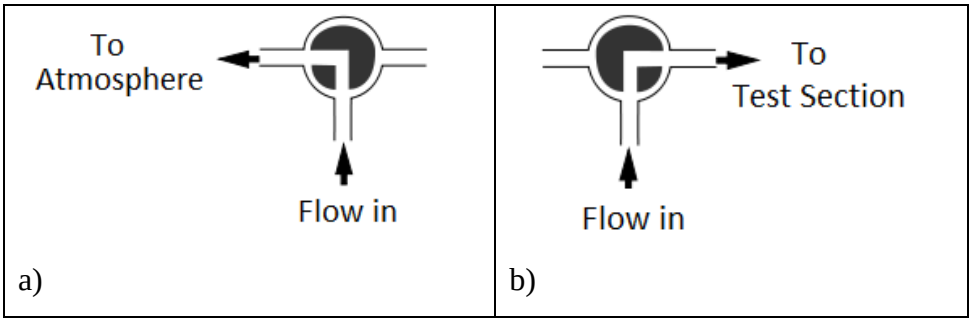

Figure 3-10 Schematic of flow in a L-Type Valve

The valve has been heated with three resistors and insulated as illustrated in Figure (3-11). A thermocouple has been also mounted on the cold spot of the valve to give feedback to the temperature controller.

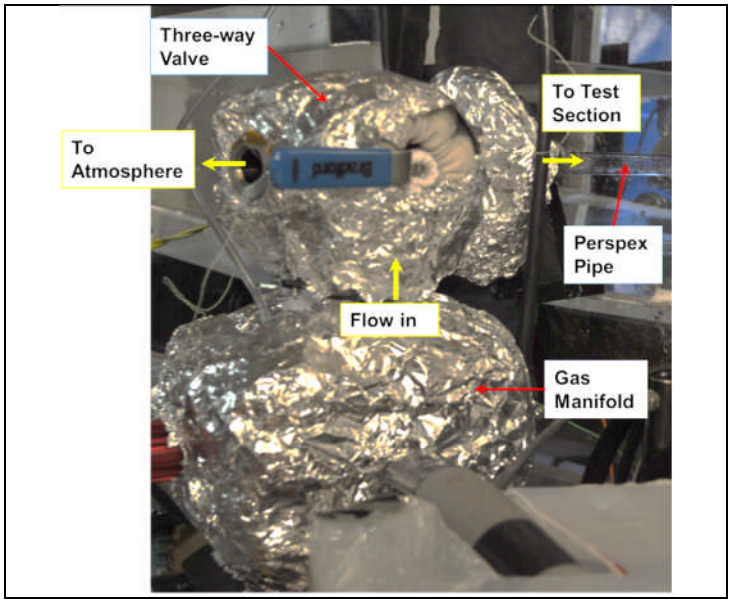

Figure 3-11 T-Valve insulated and installed

3.3.3.3 Flange

A flange has been designed to connect the valve to the test section and also hold the Perspex pipe in the test section. In other words, it is attached to the three-way valve from its bottom, with metal clamp, and supports the perspex pipe from its top. It is bolted to the bottom of the test section with 4 adjustable screws (Fig. (3-12)).

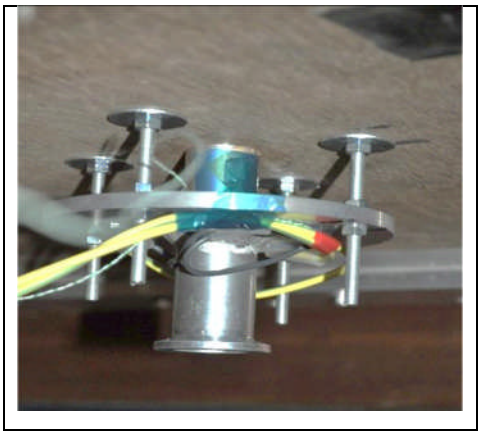

Figure 3-12 Flange Connected to the test section through four bolts

The flange is heated with three electrical resistors (4 amps) and also insulated as shown in Figure (3-13b).

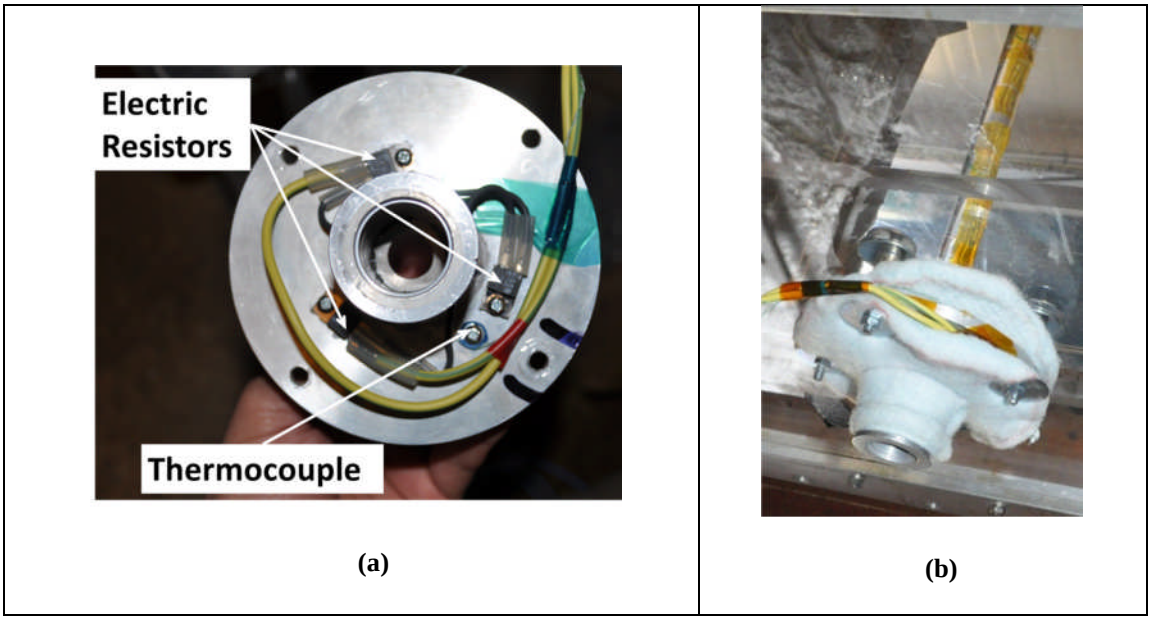

Figure 3-13 Flange a) electrical resistors attached to the flange (top view), b) insulated flange bolted to the test section

3.3.4 Temperature Controller

A controller has been made to regulate the temperature of each separate zone through the gas path and keep the temperatures above the saturation temperature of the gas mixture. This would prevent the gas mixture from condensing before it reaches the perspex pipe. This device controls temperature by comparing the process temperature with its adjustable set value.

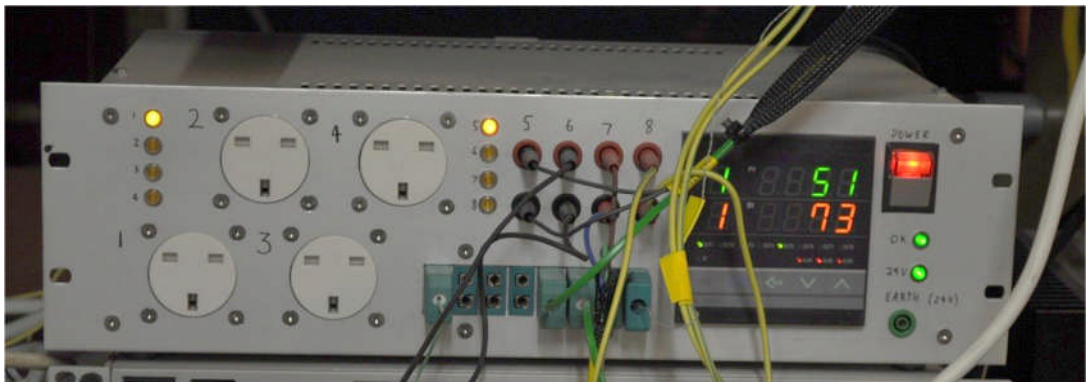

Figure 3-14 Temperature Controller Diagram

The temperature controller includes of eight independent channels and four of them have been used to control the temperature of the rubber hose, the manifold, the three-way valve and the flange. To reduce the chance of short circuit and electric shock, a 24 volts supply is used to drive the controller. This is shown in Figure (3-16).

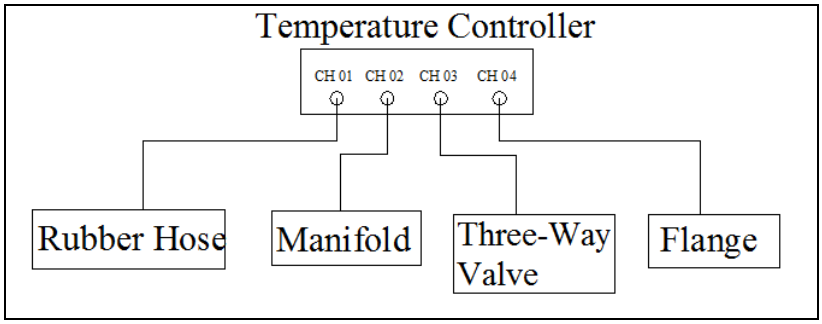

Figure 3-15 Schematic of the temperature controller channels in used

Figure 3-16 Flange preheater controllers

3.3.5 Diffuser Box

Cranfield icing tunnel minimum steady speed is about 35 m/s. This air speed had to be reduced to a desirable range of 3.5m/s to 5m/s in the test section where the Perspex pipe is installed. To achieve this, a diffuser box has been designed to be installed inside the tunnel and reduce the air velocity to approximately one tenth of the tunnel speed. The shape of this box is like a diffuser with an approximate total length of 1443 mm and diffusion angle of 5 degrees drawn in Figure (3-18).

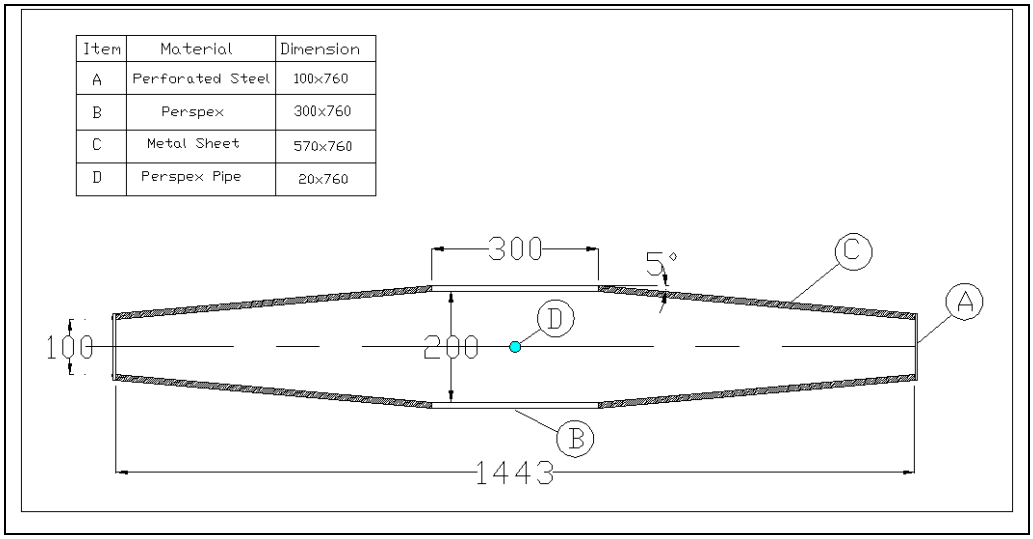

Figure 3-17Diffuser Box Dimensions

A perforated sheet (gauze) has been welded to both inlet and outlet of the box in order to restrict the air going through the box (Fig 3-18). Both sides of the box are made of plexiglass for visual observation. The box is installed and bolted in the middle of the test section shown in Figure (3-19a). The air speed inside the box has been measured and calibrated at different tunnel speed as explained in section (3-6).

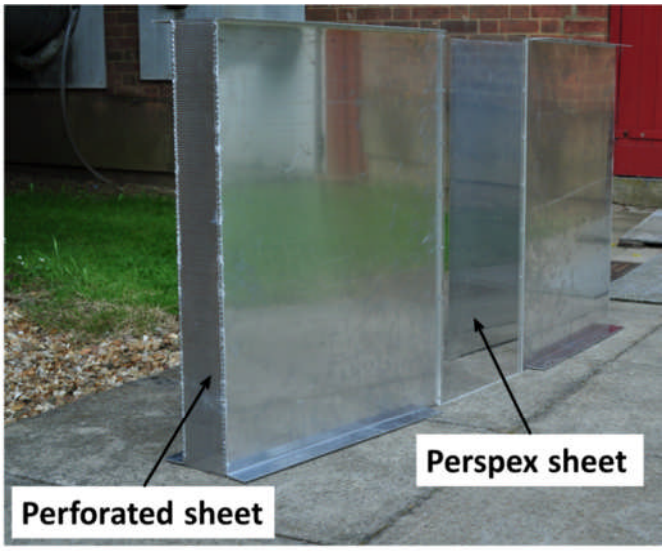

Figure 3-18 Air Box after construction

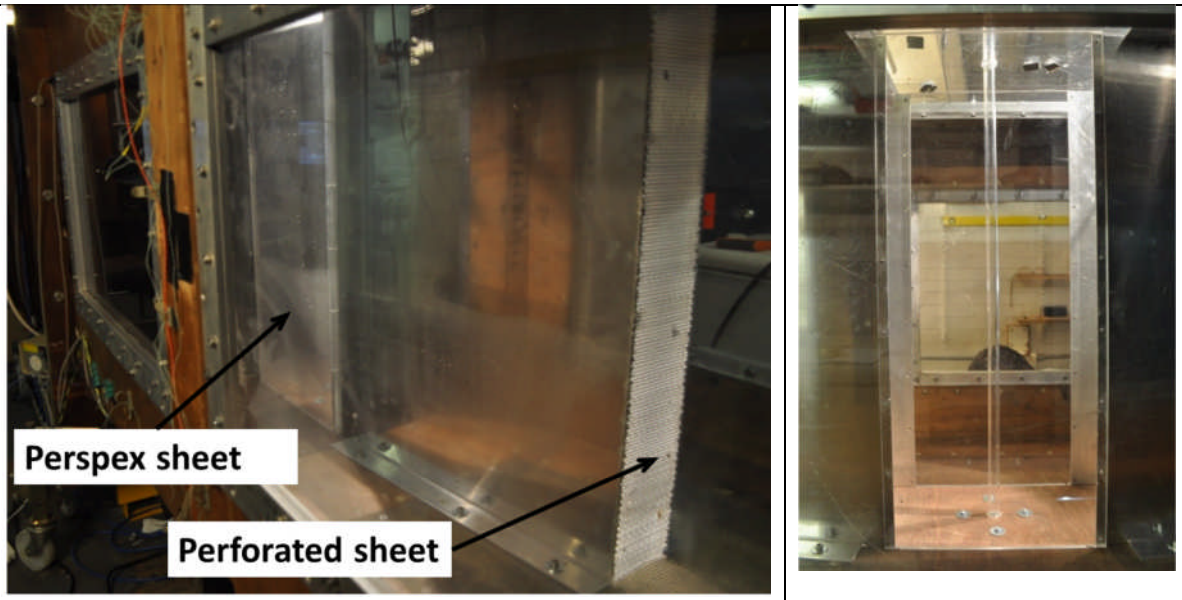

(a) **(b)**

Figure 3-19 Diffuser Box (a) Bolted inside the test section (b) Perspex pipe installed in the middle of the box

3.3.6 Instrumentation

In this experiment, data has been measured in two common ways of visual observation and gathering electric signals by Data Acquisition System (DAS).

A total of 30 different parameters have been measured which 25 of them are temperatures at different places. The temperatures have been measured by using K-type thermocouples. Tunnel air speed, dry air pressures, boiler power and dry air mass flow rate are the other measured parameters. Some of these variables were measured to control the test rig and the rest for observing and recording purposes which all are presented in Table (3-1). Their positions are also marked in the schematic of the test rig, Figure (3-20).

Table 3-1 Instruments on the component of facility

Component	Parameter	Identifier	Instrument	Purpose
Compressor	Pressure	P_T	Barometer	Controlling
Pressure Regulator	Pressure	P_{air}	Gauge Pressure	Controlling
Mass Flow rate Controller	Dry air mass flow rate	m_{air}	Mass Flow meter Controller (Omega-FMA 5528)	Recorded
Boiler	Steam Temperature	T_s	K-type Thermocouple	Recorded
	Water Temperature	T_w	K-type Thermocouple	Recorded
	Power	W	Multi Meter	Recorded
Flexible Hose	Surface Temperature	T_{hose}	K-type Thermocouple	Controlling
Air Manifold	Gas Temperature	T_{gas}	PT 100	Recorded
	Gas Pressure	P_{gas}	Micro manometer	Recorded
	Hot Spot Temperature	$T_{man,c}$	K-type Thermocouple	Controlling
	Cold Spot Temperature	$T_{man,h}$	K-type Thermocouple	Controlling
Flange	Surface Temperature	$T_{flanger}$	K-type Thermocouple	Controlling
T-Valve	Hot Spot Temperature	$T_{man,c}$	K-type Thermocouple	Controlling
	Cold Spot Temperature	$T_{man,h}$	K-type Thermocouple	Controlling
Perspex Pipe	Wall Temperatures	T_1 - T_9	K-type Thermocouple	Recorded
	Core Temperature	$T_{b,1} - T_{b,5}$	K-type Thermocouple	Recorded
Icing Tunnel	Velocity	V_c	Static tapping	Recorded
	Temperature	T_c	K-type Thermocouple	Recorded

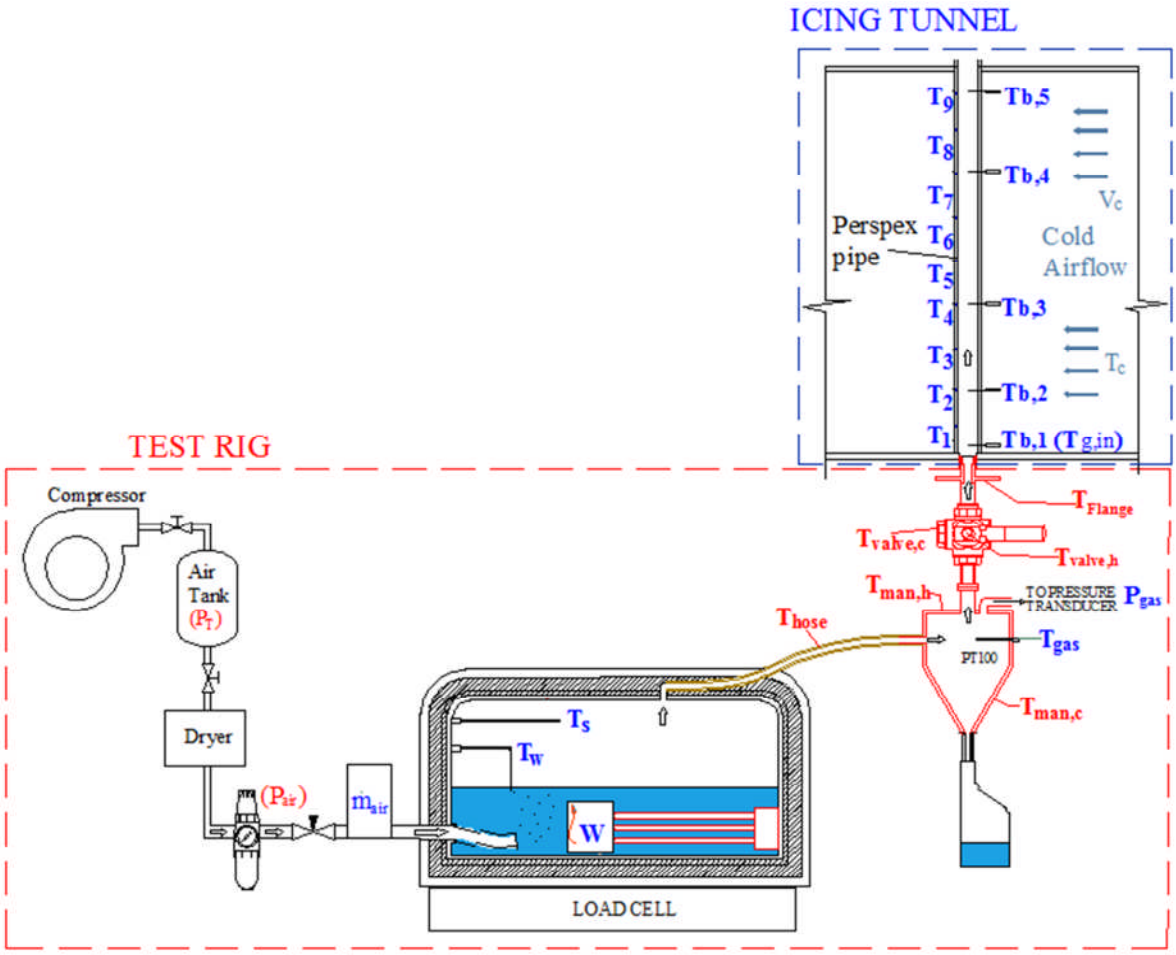

Figure 3-20 Schematic of the test rig showing the measured parameters

The data acquisition boxes are shown in Figure (3-21).

Figure 3-21 Data Acquisition Boxes (16 channels for T/C and 1 RTD)

The growth, coalescence, motion, and detachment of the condensate droplets are observed by three video recorders which were located at different positions to cover the whole length of the pipe and monitored by three screens, Figures (3-22) and (3-23). Pictures were taken

with reasonable resolution from different angels in every 5 seconds by using two Nikon 500D cameras.

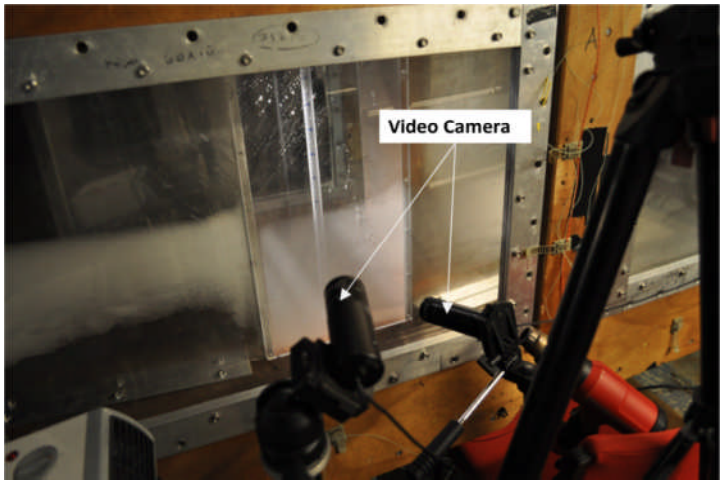

Figure 3-22 Location of three video cameras

Figure 3-23 Three screens used for monitoring the videos during tests

Most of the parameters including all of the temperatures and the Icing Tunnel data are measured using a “Compact Field Point” interface connected to a computer and controlled using Labiew (7.1)[9]. In Figure (3-24) a print screen of the Labview front panel is presented.

[9] Compact Field Point & Labview are trade names for products made by National Instruments; www.ni.com

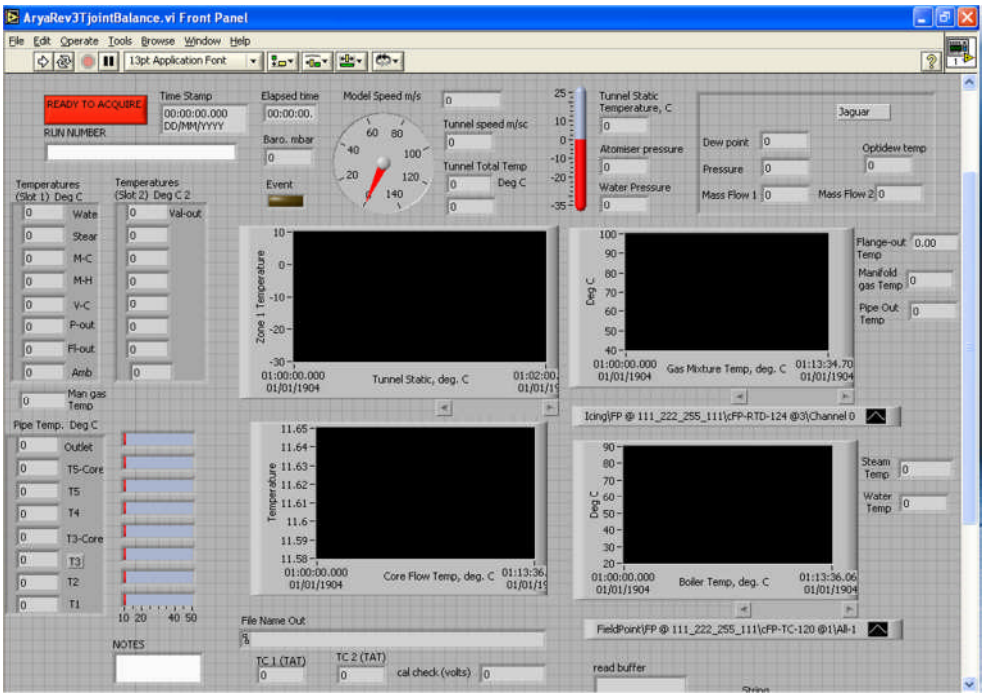

Figure 3-24 Labview front panel used for data monitoring

3.4 Test condition

Conducting the experiments from the design of the test rig to running of the tests took about 7 months. This includes 1 month to design the test rig, 4 months for preparation and making the parts and finally 2 months for calibration and running the tests.

Condensation and freezing have been investigated in three different test cases of a horizontal, a vertical and a T-Joint pipe. In the case of horizontal and T-Joint pipe the diffuser box has been installed horizontally inside the tunnel. However, in the case of the vertical pipe it has been turned in to a vertical position. See Figure (3-25).

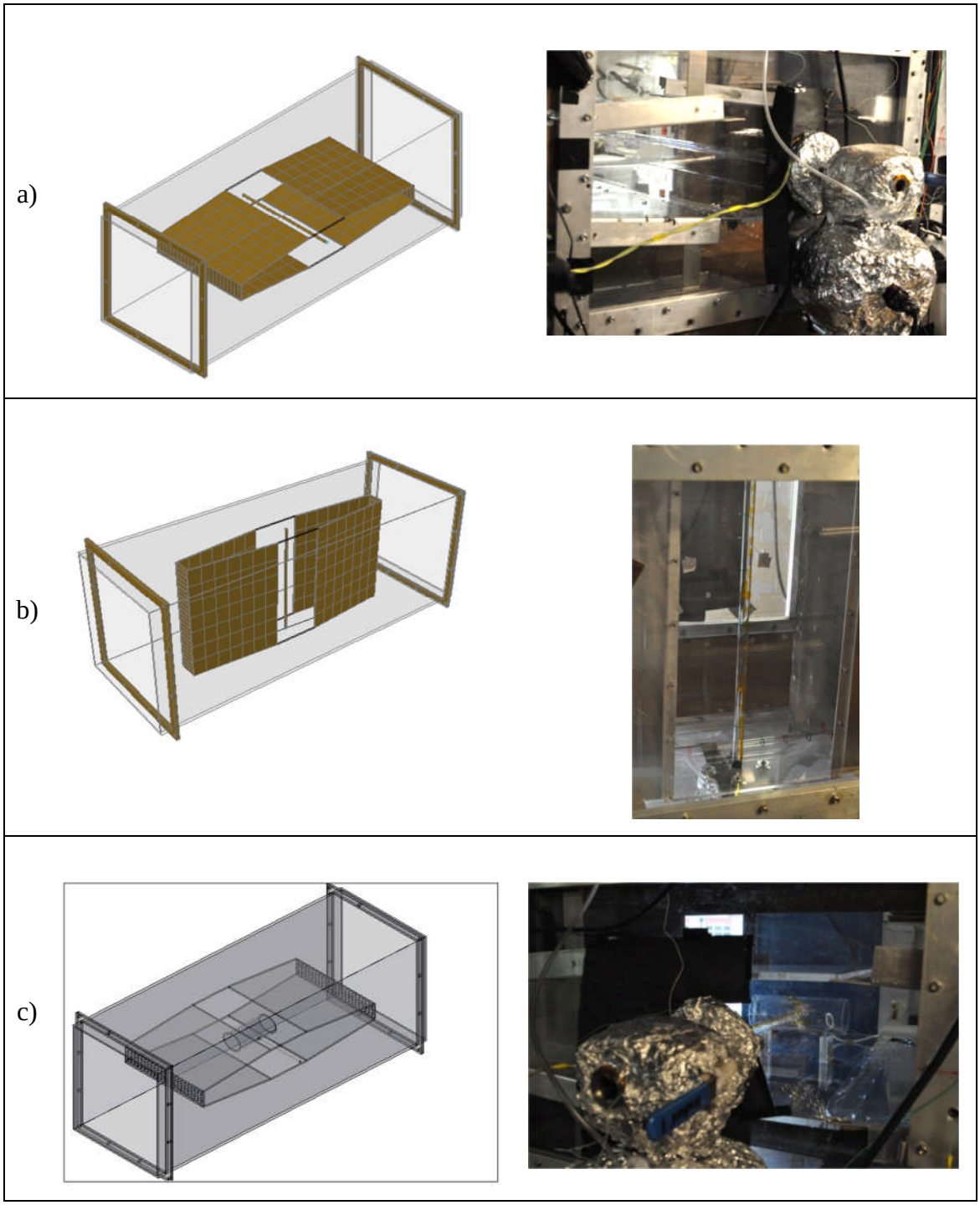

Figure 3-25 Pipe and diffuser box positions inside the test section a) Horizontal Pipe b) Vertical Pipe c) T-joint Pipe

The inner diameter of the Perspex pipe has been selected to be 15mm, which is equal to the actual engine breather pipe, with thickness of 2mm. The choice of the wall thickness allows inserting thermocouple through the pipe wall and also it is nearly equal to the actual engine breather pipe thickness which is 1.5mm to 2mm. The length of the pipe is 80 cm which is 4 cm longer than the test section width which goes out of the test section.

The objective of performing the tests on the horizontal and vertical pipes is to observe the way condensation occurs and determine experimental data to underpin the determination of effective heat transfer coefficient.

The results of vertical pipe are used to validate a one dimensional code which models condensation and freezing in a vertical pipe (explained in Chapter 5). Horizontal pipe test has been run to validate the CFD study, is explained in Chapter 6.

The actual engine breather pipe is connected to the engine air manifold at its outlet (See Figure 1-1). According to the Jaguar icing tests, this connection point is the critical region in terms of ice blockage. The main purpose of conducting test on the T-joint pipe was to evaluate ice formation at the junction of the two pipes. A schematic of the T-joint pipe is shown in Figure (3-26). This T-joint pipe is made of a 15 mm pipe (equal to the breather pipe diameter) connected perpendicular to a 75mm pipe (equal to the manifold pipe diameter), presented in Figure (3-26). Both of the pipes are perspex and their dimensions are listed in Table (3-2). Although testing the T-joint pipe may ne be fully representative of the actual breather pipe, it provides good indication of movement of condensate film and ice growth at the junction. The ice growth rate at the junction is also investigated in this study in chapter 4.

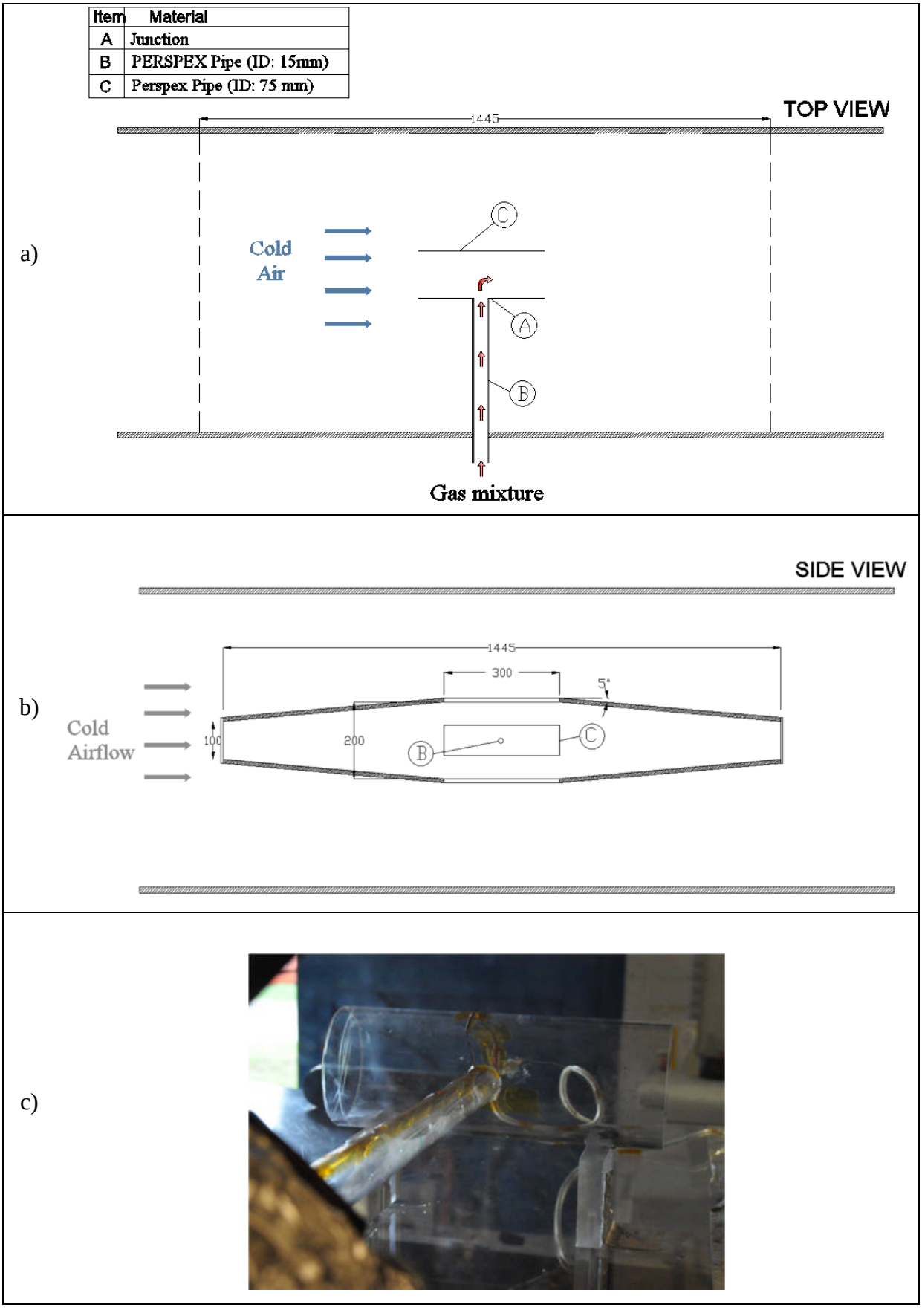

Figure 3-26 Schematic of T-joint pipe installed inside the Icing Tunnel, a) Side View b) Top View c) Actual T-joint pipe installed inside the test section (side view)

Table 3-2 Dimension of the T-Joint Pipe

	Inner Diameter (mm)	Length (mm)	Thickness (mm)
Pipe B	15	340	2
Pipe C	70	200	3

3.4.1 Test Matrix

A total number of 28 tests have been conducted in three categories of horizontal pipe, vertical pipe and T-Joint pipe. These runs have been conducted at various inlet conditions. The main parameters are vapour mass flow rate, dry air mass flow rate, mixture inlet temperature and tunnel air velocity which have been varied to evaluate their influences on hydrodynamics of condensation and ice formation. The ranges of the main parameters are given in Table (3-3) and the test matrix is presented in Table (3-4).

Table 3-3 Experimental ranges

Parameter	Units	Range
Dry Air Mass Flow rate	Kg/hr	0.5 – 1.44
Vapour Mass Flow Rate	gr/min	0.38 - 5.55
Tunnel Velocity	m/s	40 , 50
Inlet Gas Temperature	C	43.2 - 86

Table 3-4 Test Matrix for Condensation and Ice formation inside the Vertical pipe

Pipe Type	Case	Test Duration (minutes)	Tunnel Speed (m/s)	$T_{g,in}$ (°C)	Boiler Power (W)	m_a (kg/hr)	m_v (g/min)	m_g (kg/hr)	W_v
T-Pipe	**Run 1**	42:00	40	86.1	322	0.9	5.55	1.26	0.26
T-Pipe	**Run 2**	36:00	40	62.0	115	1.0	2.13	1.39	0.11
T-Pipe	**Run 3**	27:00	40	62.2	161	1.0	2.74	1.20	0.14
T-Pipe	**Run 4**	29:00	50	62.0	161	1.0	2.74	1.20	0.14
T-Pipe	**Run 5**	27:00	50	62.1	161	0.8	2.29	0.98	0.14
T-Pipe	**Run 6**	16:00	40	62.4	161	1.2	2.77	1.20	0.14
T-Pipe	**Run 7**	20:00	0	63	165	1.0	2.8	1.22	0.14
T-Pipe	**Run 8**	20:00	0	63	165	1.0	2.8	1.21	0.14
T-Pipe	**Run 9**	20:00	0	62.4	167	1.38	3.46	1.59	0.13
T-Pipe	**Run 10**	39:20	0	48.0	97	1.0	1.5	1.1	0.1
T-Pipe	**Run 11**	24:00	50	52.0	97	1.0	1.6	1.1	0.1
T-Pipe	**Run 12**	32:00	50	61.0	99	0.5	1.4	0.6	0.13
T-Pipe	**Run 13**	26:00	50	43.5	99	1.4	1.2	1.4	0.05
T-Pipe	**Run 14**	41:00	50	43.2	62	0.5	0.6	0.6	0.06
Horizontal	**Run 15**	14:00	50	46.0	63	0.54	0.56	0.58	0.06
Horizontal	**Run 16**	37:00	50	43.5	63	0.55	0.59	0.58	0.06
Horizontal	**Run 17**	16:00	50	46.9	157	1.44	3.27	1.64	0.11
Horizontal	**Run 18**	35:00	50	58.4	157	0.55	3.0	0.73	0.25
Horizontal	**Run 19**	18:00	50	59.1	154	0.55	3.0	0.71	0.25
Horizontal	**Run 20**	20:00	50	59.6	154	0.49	3.0	0.66	0.27
Horizontal	**Run 21**	13:00	50	60.9	154	0.56	3.1	0.73	0.25
Vertical	**Run 22**	21:00	50	49.9	62	1.40	0.38	1.43	0.02
Vertical	**Run 23**	12:00	50	49.2	168	1.39	3.12	1.39	0.12
Vertical	**Run 24**	21:00	50	53.9	165	0.82	3.12	1.01	0.19
Vertical	**Run 25**	21:00	50	60.2	240	0.81	3.62	1.09	0.25
Vertical	**Run 26**	18:00	40	53.0	158	0.63	3.66	0.85	0.26
Vertical	**Run 27**	12:00	40	51.8	158	0.68	3.55	0.89	0.24
Vertical	**Run 28**	12:00	40	52.8	158	0.72	3.55	0.93	0.23
Vertical	**Run 29**	12:00	40	52.8	158	0.74	3.55	0.95	0.22

3.5 Test procedure

To carry out the tests the following procedure has been conducted.

(1) Fill the boiler with 5 litre of water at boiling temperature

(2) Set the three-way valve to its vent position which expel the mixture to the Atmosphere

(3) Adjust the boiler power and the dry air mass flow rates to the given values (for instance P=100Watt, m_a=0.74 kg/hr)

(4) Adjust the temperature controller to control the temperature of the rubber hose, the manifold, the Three-way valve and the flange 2 degrees above the gas saturation temperature.

(5) Start the icing tunnel and set its velocity (V_c) and temperature (T_c)

(6) After allowing a sufficient time to reach a quasi-steady state the three-way valve is set to the open position which allows the air/steam mixture to go in to the perspex pipe. From this point the observation and the data measurement are started.

Duration of each test is different and depends on the condensation performance and rate of ice formation. After each test the perspex pipe was taken out for taking pictures.

3.6 Temperature measurements of Perspex pipe

The perspex pipe wall temperatures have been measured at 9 locations (T_1 to T_9) along the pipe shown in Figure (3-27a). To measure the temperatures, 9 holes have been drilled through the middle of the pipe and the thermocouples have been inserted in to the holes. A cross section of the pipe wall is shown in Figure (3-27b). As the pipe thickness is 2 millimetres, miniature thermocouples with diameter of 0.25 mm have been utilized, Fig. (3-28).

The gas core temperatures have been measured at 5 different points (T_{C1} to T_{C5}) along the pipe as shown in Figure (3-27). The thermocouples have been inserted to the pipe half way across up to the centre of the pipe, shown in Figure (3-29).

All the thermocouples are sealed with silicon and fixed with heat resistant self-adhesive tape shown in Figure (3-30).

In the case of the T-joint pipe, 5 wall temperatures and 3 core temperatures have been measured, as shown in Figure (3-27c).

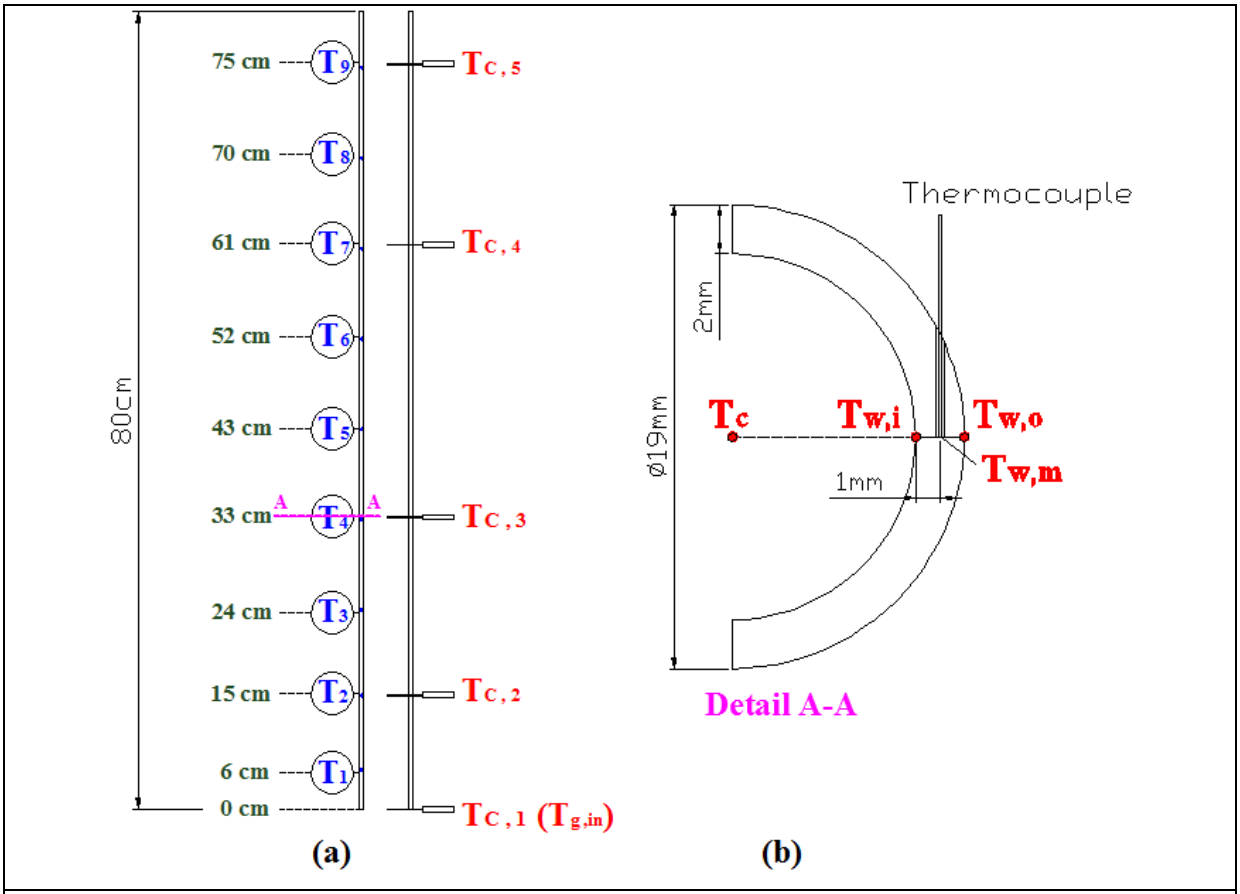

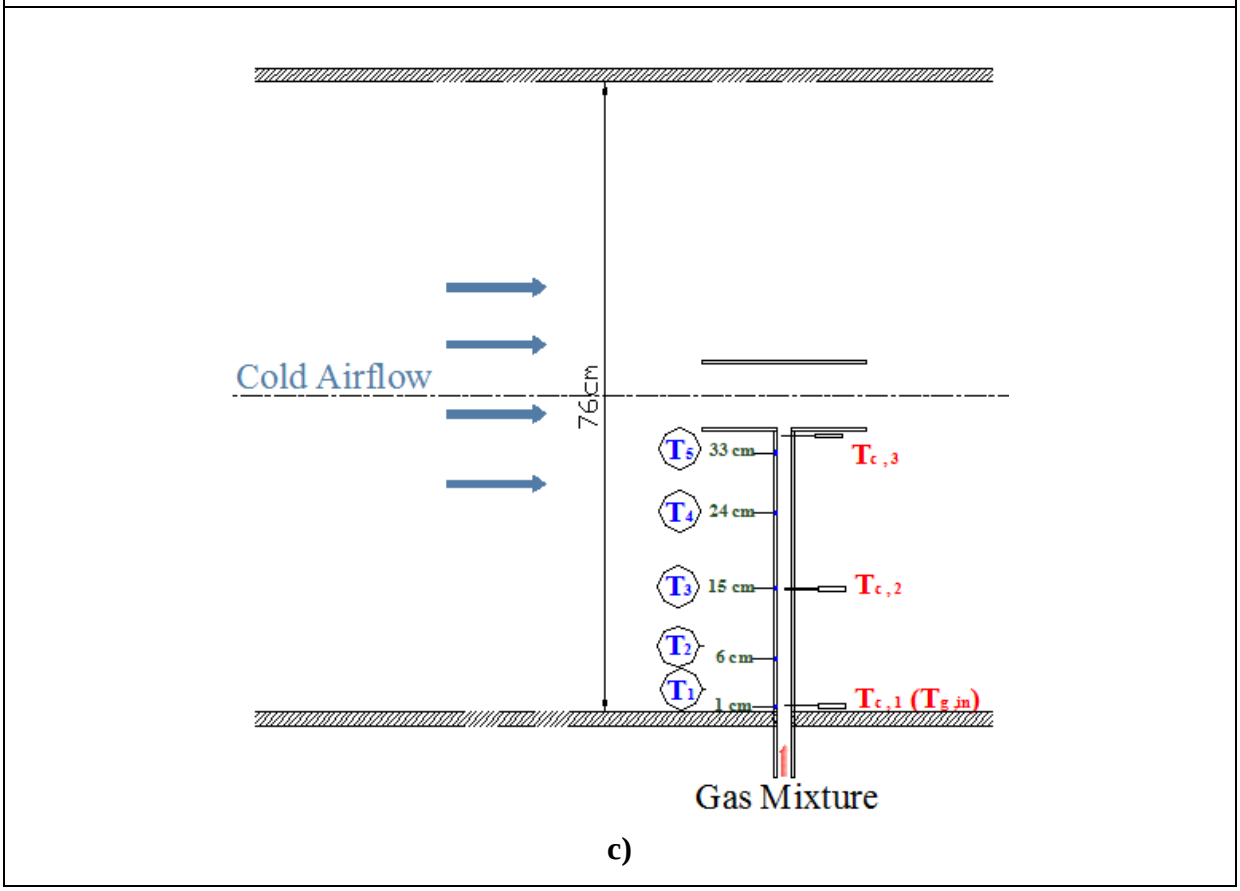

Figure 3-27 Temperature measuring points, a) Perspex pipe, b) cross section of Perspex pipe, c) T-joint Pipe

Figure 3-28 Miniature TC Direct K-type Thermocouple (Diameter: 0.25 mm)

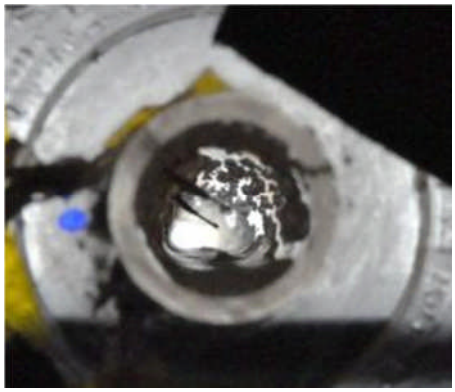

Figure 3-29 Thermocouples inserted to the middle of the horizontal pipe, Condensate droplets were formed on the inner surface of the pipe and large droplets slide down and accumulate at the bottom of the pipe

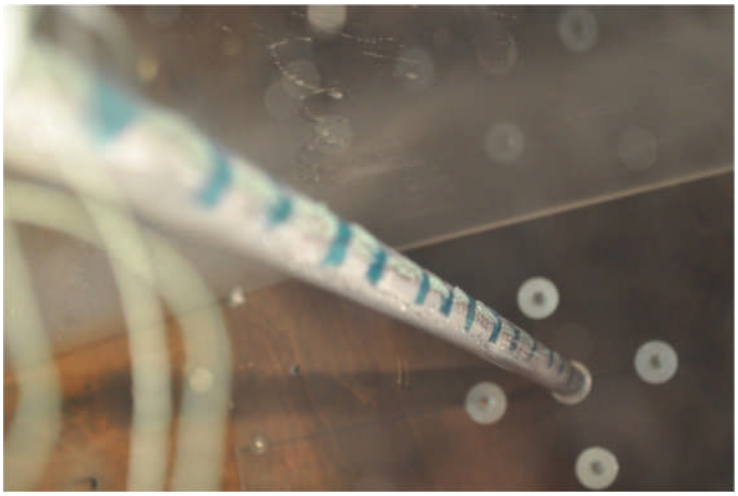

Figure 3-30 Thermocouples embedded in the vertical pipe and fixed with heat resistance self-adhesive tape. (The pipe is installed inside the test section)

3.7 Tunnel calibration

Taking measurements with any instruments or devices needs calibration to ensure the accuracy of the data. In order to calibrate the air velocity across the diffuser box in the tunnel a standard pitot-static tube has been used.

Figure 3-31 Pitot-Static Tube

The probe was traversed across the test section perpendicular to the direction of airflow at 15 different locations shown in Figure (3-32). The difference between the static and total pressure has been measured at each of these locations. Air velocity was then calculated by applying Bernoulli Equation as follows.

$$V = \sqrt{2(P_{total} - P_{static})/\rho} \qquad (3\text{-}2)$$

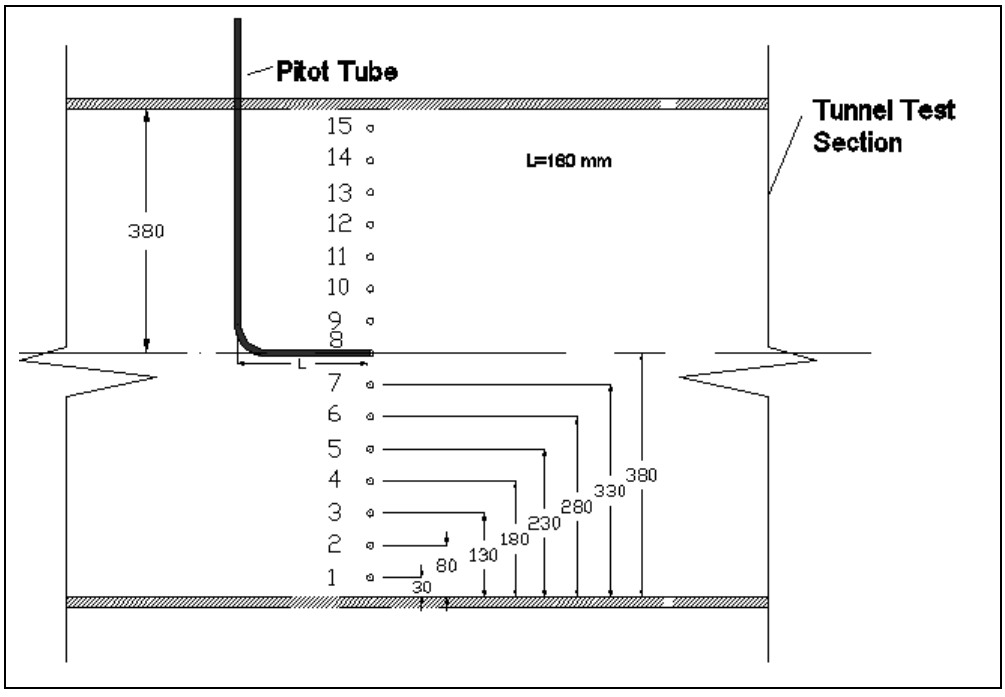

Figure 3-32 Positions of measuring tunnel air velocity across the tunnel test section

The target air velocity in the diffuser box is between 3.5 to 6 m/s which is around the air speed under bonnet of a typical Jaguar car. To achieve this velocity, three different tunnel

speeds of 40m/s, 45m/s and 50 m/s have been tested and air velocities in the test section have been measured. The maximum and minimum values of pressure difference ($\Delta P = P_{total} - P_{static}$) at each of the points have been measured by using the pitot-static tube and presented in Table (3-5). Referring to these values and applying Eq. (3-2) the maximum and minimum value of the velocities can be evaluated and the arithmetic mean can be calculated which are given in Table (3-5).

Table 3-5 Pressure difference and air velocity at different positions across the test section at tunnel velocity of 50 m/s

Position	Position cm	ΔP(min) Pa	ΔP(max) Pa	V (min) m/s	V (max) m/s	V (ave) m/s
1	3	16	22	5.1	6.0	5.5
2	8	15	29	3.9	6.9	5.9
3	13	25	37	6.4	7.8	7.1
4	18	21	27	5.8	6.6	6.2
5	23	8	16	3.6	5.1	4.4
6	28	11	18	3.2	5.4	4.8
7	33	15	28	3.9	6.7	5.8
8	38	16	29	5.1	6.9	5.9
9	43	36	48	7.7	8.8	8.2
10	48	17	27	5.3	6.6	5.9
11	53	8	6	3.6	3.6	3.4
12	58	8	8	3.6	3.6	3.6
13	63	5.5	6.5	3.0	3.3	3.1
14	68	4	7	2.6	3.4	3.0
15	73	2	10	1.8	4.0	2.9

The local averaged air velocities at each of the locations have been plotted at different tunnel velocities in Figure (3-33). As shown, the air velocity variations in all three different cases have followed a similar pattern which has two rises around 10cm and 45cm.

a)

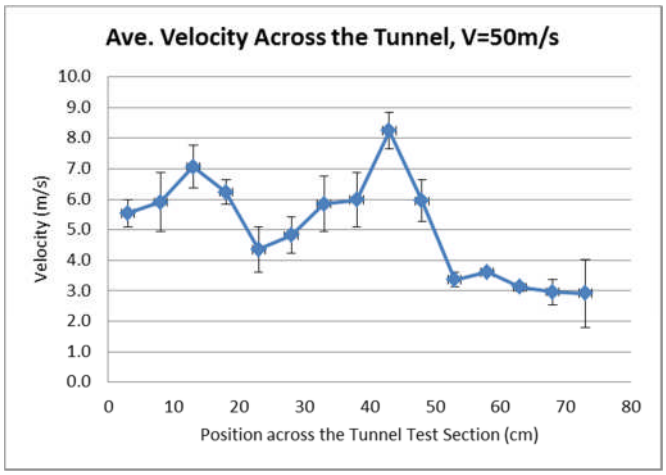

b)

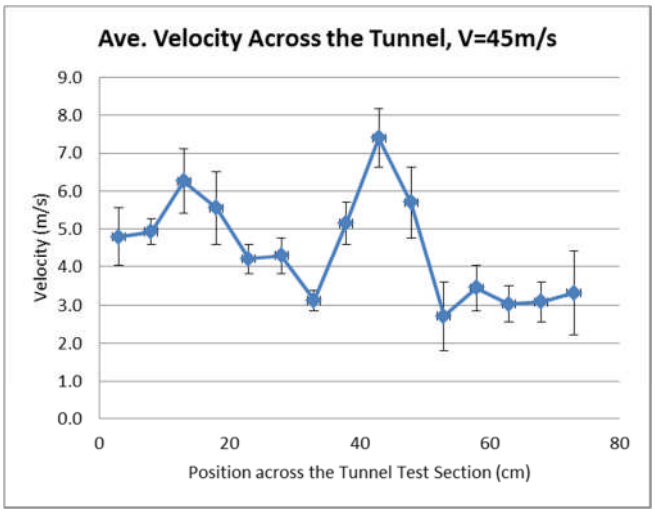

c)

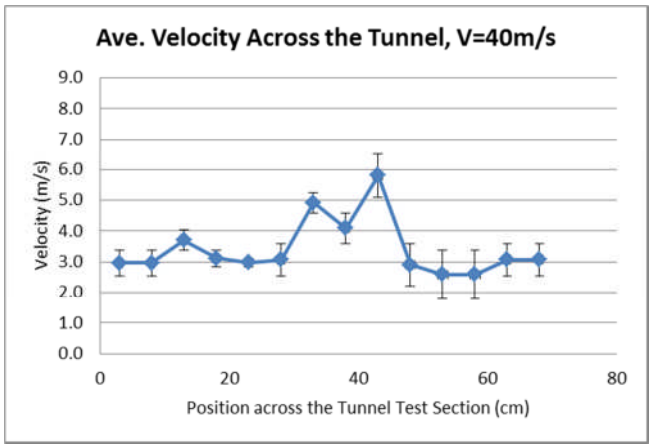

Figure 3-33 Air Velocity in the diffuser box along the cross section of the tunnel a) tunnel velocity= 50 m/s, b) tunnel velocity= 45m/s, c) tunnel velocity= 40m/s

3.8 External heat transfer coefficient

The averaged heat transfer coefficient in cross flow over a cylinder is given by Eq. (3.3) External heat transfer coefficient at different points along the pipe can be calculated by Eq. (3-4). (See section 2-3-2 for more details).

$$h = \frac{\overline{Nu_a} k_a}{d} \tag{3.3}$$

$$\overline{Nu_g} = 0.3 + \frac{0.62 \mathrm{Re}_a^{1/2} \mathrm{Pr}_a^{1/3}}{\left[1+\left(\frac{0.4}{\mathrm{Pr}_a}\right)^{2/3}\right]^{1/4}} + \left[1+\left(\frac{\mathrm{Re}_a}{282{,}000}\right)^{5/8}\right]^{4/5} \tag{3.4}$$

Note that, d, is the characteristic length which in this case is the outer diameter of the pipe (d=19mm). k_a is the gas thermal conductivity. The Reynolds number (Re_a) is calculated based on the measured velocity given in Figure (3-33). Pr, is Prandtl number and calculated by applying Eq. (3-5).

$$\mathrm{Pr} = \frac{\mu C_p}{k} \tag{3-5}$$

μ: Dynamic viscosity, (N s/m^2)

c_p: Specific heat, (J/kg K)

k: Thermal Conductivity (W/m k)

The air density is calculated by applying ideal gas equation ($\rho = \frac{P}{R_a T}$) at the tunnel temperature (T= -20°C), Atmospheric pressure and R_a=287J/Kg K.

The Nusselt number and external heat transfer coefficient at tunnel velocity of 50 m/s and 40 m/s have been calculated and presented in Table (3-6) and Table (3-7), respectively.

In the event of natural convection, the heat transfer coefficient is evaluated by Eqs. (2.45) (2.46) and (2.47).

Table 3-6 External heat Transfer Calculation at Tunnel Velocity of 50m/s

Location (cm)	Velocity (m/s)	Reynolds Number	Nusselt Number	HTC (W/m2K)
3	5.5	9205	49	57
8	5.9	9806	51	60
13	7.1	11739	57	67
18	6.2	10357	52	62
23	3.4	7232	42	49
28	3.8	8007	45	53

33	5.8	9707	50	59
38	6.0	9941	51	60
43	8.2	13693	62	73
48	5.9	9871	51	60
53	3.4	5590	36	42
58	3.6	5992	37	44
63	3.1	5184	34	40
68	3.0	4921	33	39
73	2.9	4847	33	39

Table 3-7 External heat transfer Calculation at Tunnel Velocity of 40m/s

Location (cm)	Velocity (m/s)	Reynolds Number	Nusselt Number	HTC (W/m2K)
3	3.0	4921	33	39
8	3.0	4921	33	39
13	3.7	6152	38	45
18	3.1	5171	34	40
23	3.0	4963	33	39
28	3.1	5114	34	40
33	3.9	8186	45	53
38	3.1	6815	41	48
43	5.8	9637	50	59
48	2.7	4494	31	37
53	2.6	4300	30	36
58	1.7	2802	23	27
63	3.1	5114	34	40
68	1.8	2996	24	29
73	2.4	3953	29	34

a)

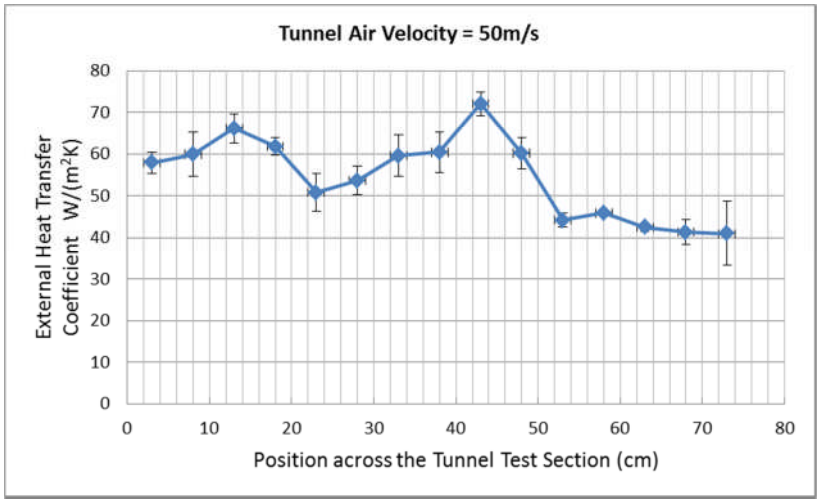

b)

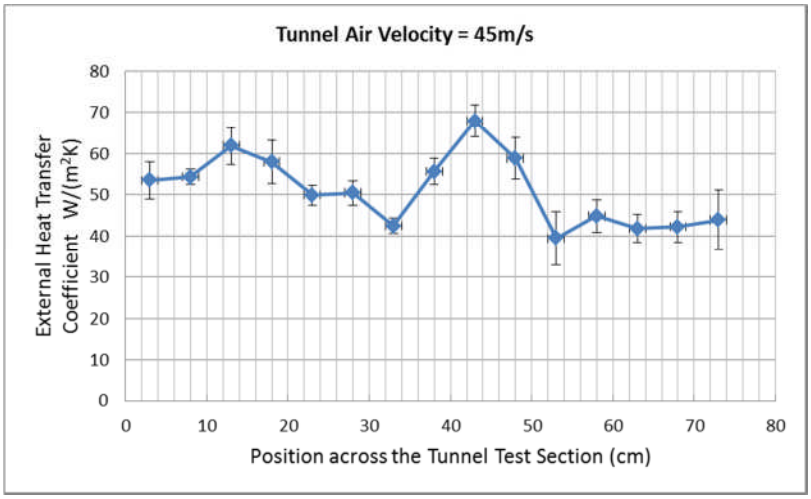

c)

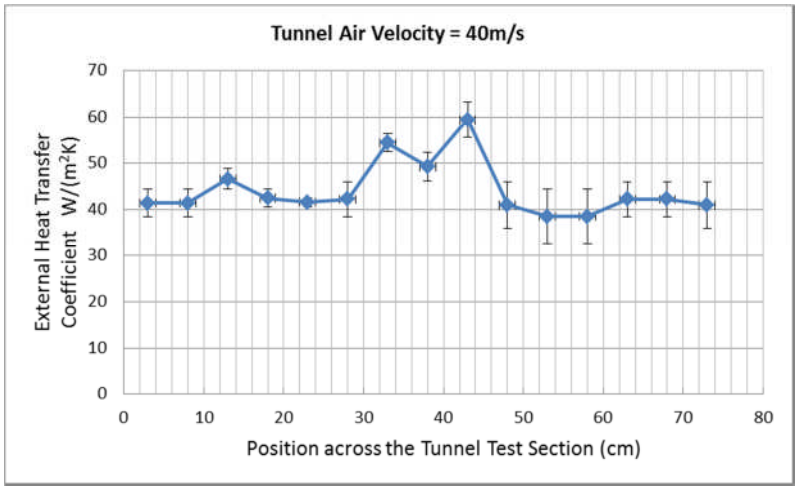

Figure 3-34 External heat Transfer Coefficient, a) at Tunnel Velocity of 50m/s, b) at Tunnel Velocity of 45m/s, c) at Tunnel Velocity of 40m/s

Chapter 4 Experimental Results and Analysis

In chapter 3, the design of the test rig has been explained and also the measurement techniques, test conditions and the test procedure have been described. Here, in this chapter the results of the tests are investigated.

Studying the hydrodynamics and heat transfer associated with condensation and freezing of the air/steam mixture is a focus in this chapter.

The experiments have been conducted separately on the horizontal pipe, the vertical pipe and the T-joint pipe. Here, in this chapter, the results are analysed separately in each of these test cases. In each section, first condensation rate and ice formation are studied and then the temperature measurement results are addressed to evaluate heat transfer. Variation of the main test parameters like vapour mass fraction, external heat transfer and surface coating on heat flux are investigated and heat transfer coefficient is evaluated by addressing the temperature results.

4.1 Vertical pipe

The vertical pipe tests have been conducted to validate a one dimensional numerical study. This numerical code and its results are discussed in chapter 5. The test matrix of the vertical pipe has been shown in Table (4-1). All the variables in this table are averaged over the 12 minutes of the runs. A total number of 8 tests have been run on the vertical pipe at different inlet mass flow rate ranges of 0.84kg/hr to 1.58kg/hr with an inlet vapour mass fractions of 0.02 to 0.36. The operating pressure was at atmospheric pressure.

Table 4-1 Vertical Pipe Test Matrix

Pipe Type	Run Number	Time (Minutes)	Tunnel Speed (m/s)	Tg,in (°C)	Boiler Power (W)	Ma (kg/hr)	Mv (g/min)	Mg (kg/hr)	Wv
Vertical	**Run 22**	12:00	50	49.9	62	1.43	0.38	1.45	0.02
Vertical	**Run 23**	12:00	50	49.2	168	1.39	3.12	1.58	0.13
Vertical	**Run 24**	12:00	50	53.9	165	0.81	3.12	1.00	0.23
Vertical	**Run 25**	12:00	50	60.2	240	0.82	4.62	1.1	0.34
Vertical	**Run 26**	12:00	40	54.0	158	0.62	3.66	0.84	0.36
Vertical	**Run 27**	12:00	40	51.8	158	0.68	3.55	0.89	0.31
Vertical	**Run 28**	12:00	40	52.8	158	0.72	3.55	0.93	0.30
Vertical	**Run 29**	12:00	40	52.8	158	0.74	3.55	0.95	0.29

In this section, condensation rate is investigated by exploring pictures and recorded videos during the test. Also the effects of vapour mass fraction on pipe temperature and condensation rate are investigated.

4.1.1 Observing condensation

When gas mixture goes through the perspex pipe, vapour starts to condense on the inner surface of the pipe and the condensate film flows down inside the pipe as a film because of gravity forces. A container was used at bottom of the manifold to collect the condensate water, shown in Figure (4-1).

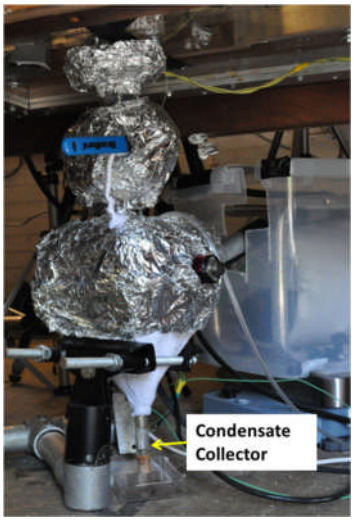

Figure 4-1 Condensate collector for Vertical pipe

Observation in this study shows that the whole process of the condensation can be divided in three phases.

The first phase begins immediately when the mixture starts to go up through the pipe (t=0), the inner surface of the pipe is completely bare, after a time interval droplets nucleate and begin growing by direct condensation at specific locations called nucleation sites which

are usually pits and surface scratches. These droplets are called primary droplets and as their critical sizes are much smaller than the average distance between nucleation sites, they are too far from one another to coalesce. (Figure 4-2 b)

In the second phase, coalescence between adjacent drops takes place. In this phase droplets grow due to direct condensation and random coalescences. They move about as a result of coalescence and can be located at virtually any points on the solid surface. Therefore, their physical locations are no longer limited to their nucleation sites on the surface. (See Figure 4-2 c). As the drops grow they reach a size, departure size, in which they are ready to fall off. (See Figure 4-2 d)

In the third phase, the droplets slide down and sweep other droplets on their path. New droplets start to grow again by direct condensation and then by coalescence and direct condensation until the drop size distribution becomes identical with the un-swept region. This region is swept by another departing droplet and the cycle continues repetitively.

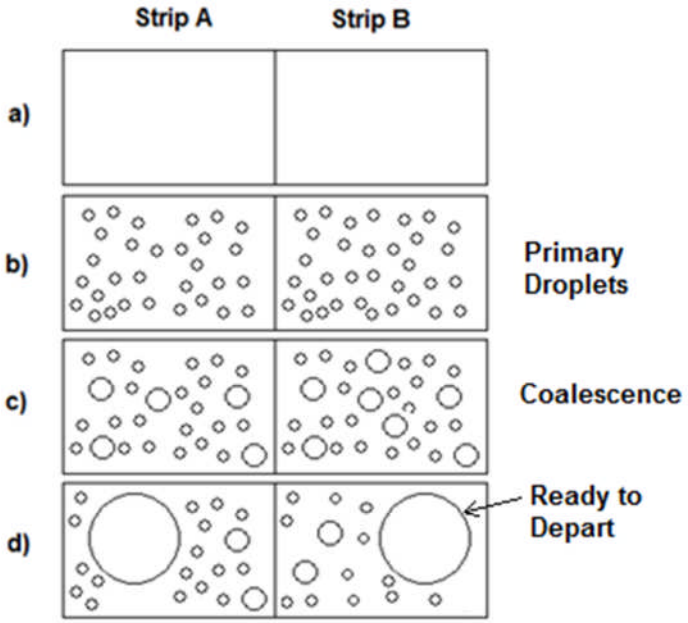

Figure 4-2 Typical growth behaviour of droplets in condensation

In Figure (4-3) and Figure (4-4) the condensation process at the beginning of the perspex pipe (up 5 cm from the pipe inlet) and middle of the pipe (at 35cm) are shown. These two figures show the condensation process at three different moments in time (1min, 3min, 5min) during the Run22. Comparing these pictures indicates that at time=3 min droplets at the beginning of the pipe are in the coalescing mode (Figure 4-3b), but the upper part of the pipe

(35 cm) is still in the primary phase (Figure 4-4b). This comparison shows that the condensation rate decreases along the pipe.

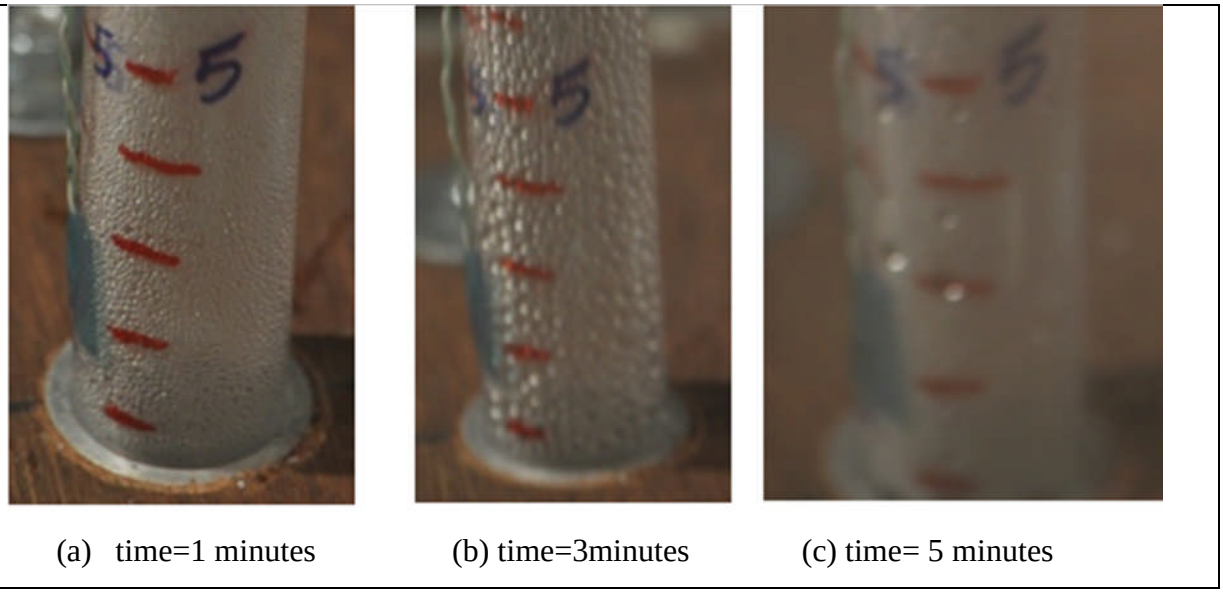

(a) time=1 minutes (b) time=3minutes (c) time= 5 minutes

Figure 4-3 Serial photograph of condensation at the beginning of the pipe in Run 22 (a) Primary Droplets (b) Coalescence (c) Sweeping

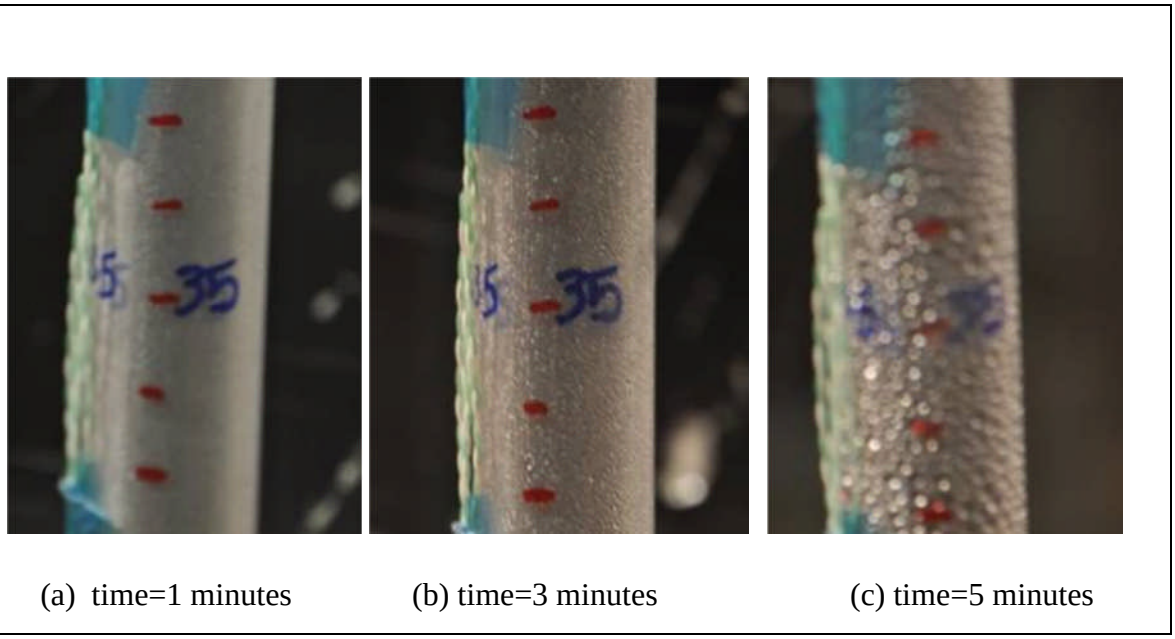

(a) time=1 minutes (b) time=3 minutes (c) time=5 minutes

Figure 4-4 Serial photograph of condensation at location of 35 cm in Run 22 (a) Start of the test at 1 minute (primary droplets) (b) Start of the test at 3 minutes (primary droplets) (c) Start of the test at 3 minutes (coalescence)

4.1.2 Condensation Rate

The other way to investigate condensation rate is measuring droplet departure time and their departure position. This has been evaluated in 5 different regions (A,B,C,D,E) along the pipe, identified in Figure (4-5).

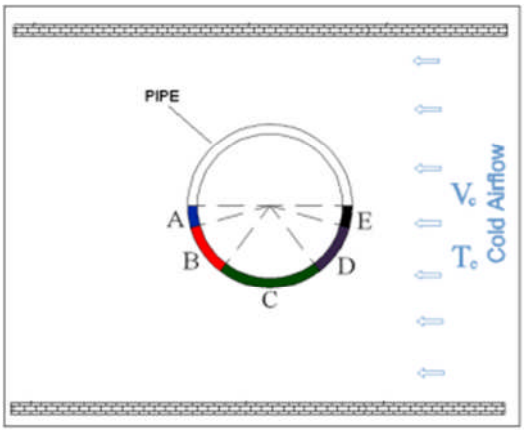

Figure 4-5 Top view of the vertical pipe in the test section (Divided in 5 different Section)

Videos of Run 22 have been investigated for 14 minutes and the locations and the departure time of droplets have been measured and listed in Table (4-2). This Table presents that the first droplet departed after 3:39 minutes from region "E" at the height of 1.5cm from the bottom of the pipe. Then second droplet departed from the same height (h=1.5 cm) but after 4:09 minutes from region "B".

Table 4-2 Time and height of droplets departure inside the pipe at different regions

Time (min)	Height of Departure (cm)				
	A	B	C	D	E
00:00					
03:39					1.5
04:09		1.5			
04:16			3		
04:43	2				
04:49		2			
04:57			4		
05:10				5	
05:30	3				
05:34		6.5			
05:38			5		
05:57			9		
06:03				5	
06:07	45				
06:14	7				
06:24					8

Time	Height of Departure (cm)				
	A	B	C	D	E
06:30			10		
06:51	8				
06:58					12
07:09		11			
07:18	11				
07:25				16	
07:43	11.5				
08:08					18
08:22				18	
08:31					16
08:36	15				
08:41					19.5
09:01		19			
09:11				23	
09:15					20
09:29					25
09:44	15				

Time	Height of Departure (cm)				
	A	B	C	D	E
09:51	21				
09:52			23		
10:25	23				
11:03				28	
11:06				7	
11:09	6.5				
11:28		22.5			
11:27					30
11:44	23				
11:55		28			
12:16	28				
12:43		32			
13:05	31				
13:15			32.5		
13:30					
13:38			35		

The time and the locations of the droplets departures in each of the five regions (A,B,C,D,E) over 14 minutes (840 seconds) of the test are shown in Figure (4-6). This figure clearly shows as the gas mixture goes up through the pipe, it takes longer for droplets to grow and fall off.

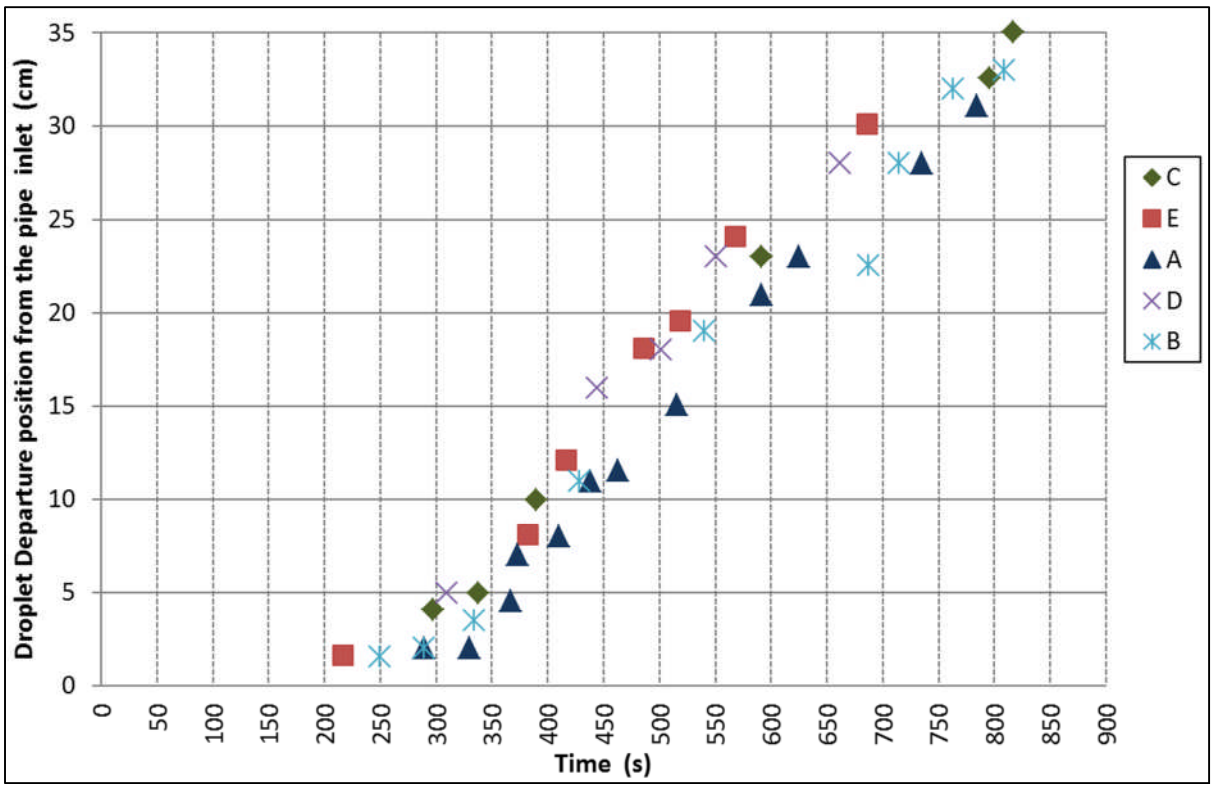

Figure 4-6 Height of departure versus the time in different region inside the pipe

It is shown in Figure (4-6) that droplets from region E have dropped quicker than region A. This can be due to greater heat transfer at the front of the pipe compared to the back of the pipe.

The droplet departure position in respect to non-dimensional departure frequency is illustrated in Figure (4-7). The non-dimensional frequency is defined as the frequency of the droplet departures divided by the frequency of the first departure $f(y)/f(y_1)$.

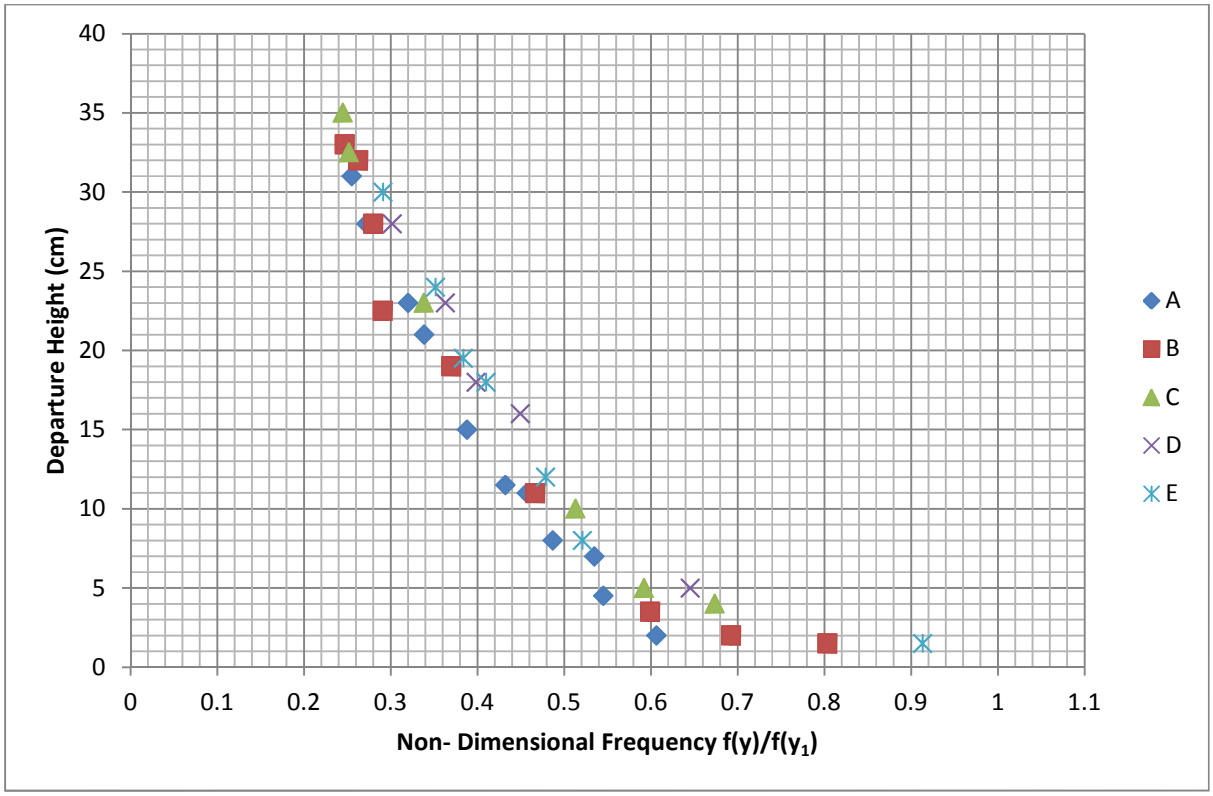

Figure 4-7 Variation of departure position in respect to the non-dimensional departure frequency

4.1.3 Temperature variation along the pipe

The Perspex pipe wall temperature distribution (T_1 to T_9) and core temperatures (T_{c1} to T_{c5}) are measured along the pipe, explained in section (3.6). Variations of these temperatures over the 12 minutes of Run 24 are shown in Figure (4-8).

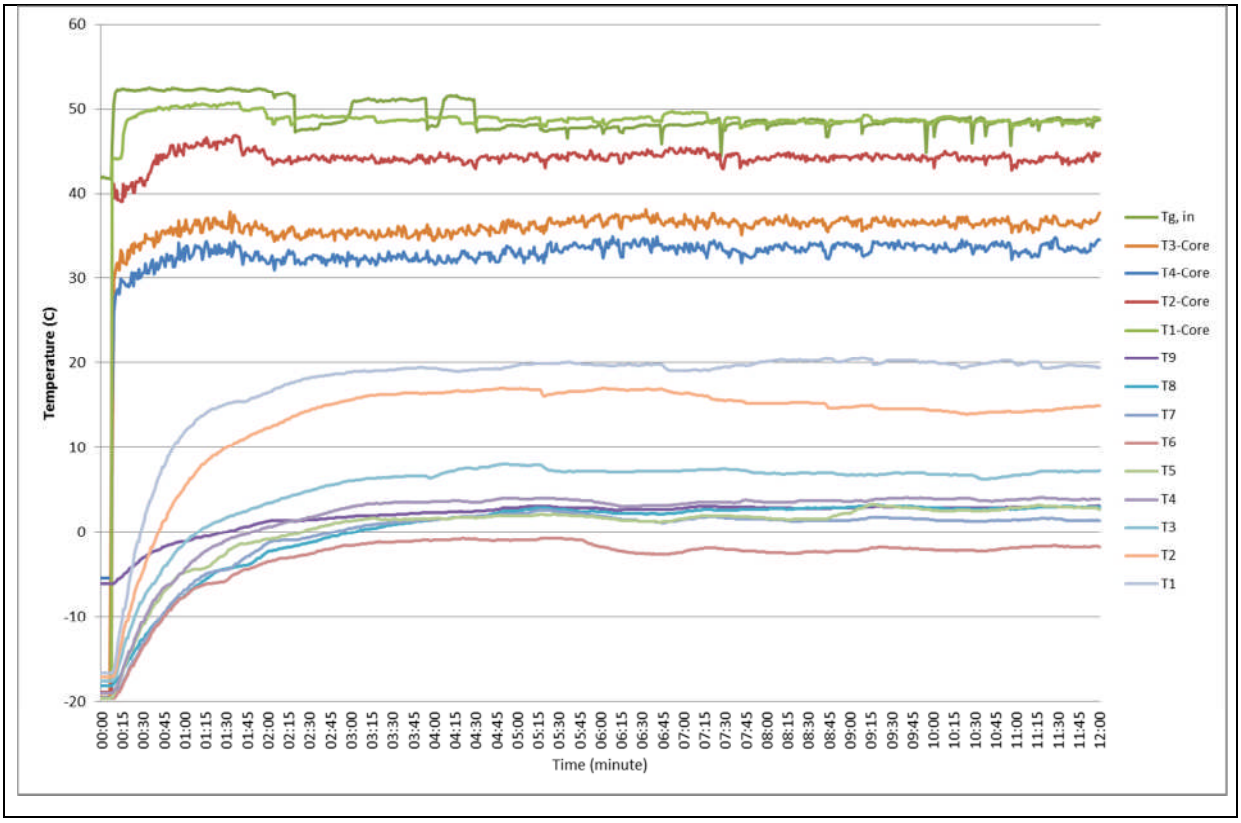

Figure 4-8 Temperature variation of the Perspex pipe at different location along the pipe over the time for Run 24.

As illustrated, in the beginning of the test (time=0) mostly the temperatures are around -20°C. This is due to the fact that the pipe is exposed to the cold air (-20C) inside the tunnel before the gas mixture flows in. When the gas mixture enters the pipe it induces the temperatures to increase and after about 3 minutes they appear to become mostly steady. As it is shown in Figure (4-8), there are few decreases and increases in the pipe temperature graphs (T_1 to T_9) which can be related to the movement and the growth of the droplets in the pipe. To investigate this better, the temperature variation at the height of 6cm (T_1) is investigated separately in Figure (4-9). As it is shown, once the air/steam mixture enters the pipe (at time=00:15min), the wall temperature increases quickly in the first minute and then it gradually becomes steady after about 4 minutes. Comparing the temperature variation with the recorded videos of this run, confirms that the temperature measurement is influenced by progress and movement of droplets in the pipe. Droplet growth on the inner surface of the pipe imposes additional resistance to the heat transfer which can be the cause of the gradual increase of the pipe temperature at (01:15 < t < 04:15). When the droplets fall off, they sweep the inner surface and this may produce a decrease in the surface temperature. The sweeping effect on the temperature graph can be recognizable by sudden drops shown in Figure (4-9).

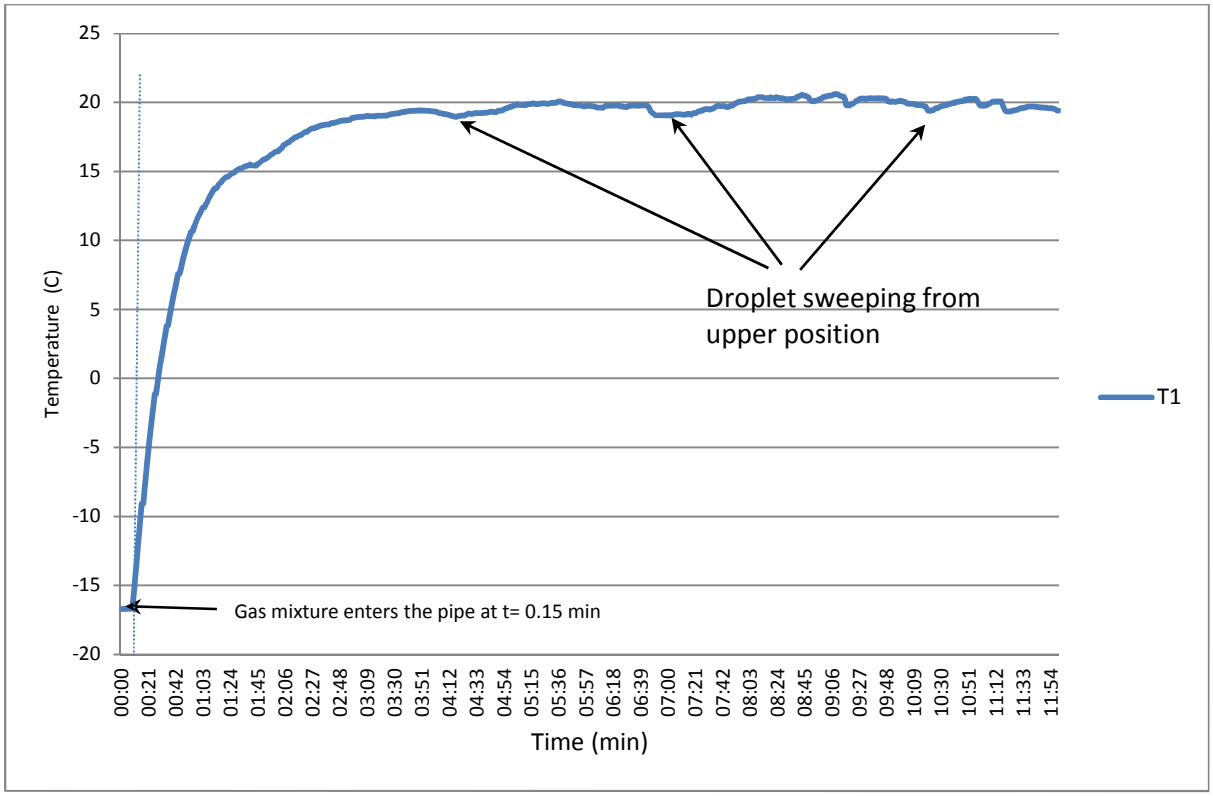

Figure 4-9 Pipe temperature at 6cm from the pipe inlet over 20 minutes

In order to make general comparisons between the test cases, all the temperatures were averaged between 4 to 12 minutes in which they are mostly steady.

Standard deviation values at each of the data points is calculated and presented in Table (4-3). The standard deviation gives a measuring tool to put a probability value on the difference of the data points and the averaged value. The standard deviation is referred here as a potential uncertainty. In Table (4-3), both the local temperature averaged value with its attributed uncertainty at each of the measuring points at different runs are presented.

Table 4-3 Vertical pipe wall temperature and uncertainty at different locations

		T1	T2	T3	T4	T5	T6	T7	T8	T9
		6	15	24	33	43	52	61	70	75
Run22	Temp. ©	11.0	10.4	1.0	-2.5	-3.4	-4.0	-2.4	-4.0	-1.5
	Uncertainty	0.966	0.555	0.769	0.450	0.564	0.876	0.010	0.585	0.432
Run23	Temp. ©	19.8	15.6	7.1	3.7	2.1	-1.8	1.6	2.6	2.8
	Uncertainty	1.027	0.360	0.258	0.577	0.565	0.328	0.008	0.375	0.175
Run24	Temp. ©	9.6	4.9	-3.3	-6.3	-7.7	-10.5	-9.7	-7.7	-2.1
	Uncertainty	2.358	0.779	0.515	0.191	0.147	0.096	0.005	0.958	0.138
Run25	Temp. ©	23.4	19.2	9.0	2.6	1.9	-3.2	-1.7	0.9	0.9
	Uncertainty	1.674	1.332	0.583	0.614	0.615	0.540	0.004	0.674	0.717
Run26	Temp. ©	9.5	4.3	-1.4	-6.7	-7.9	-9.5	-7.3	-5.6	-2.7
	Uncertainty	0.599	0.837	0.505	0.434	0.674	0.921	0.005	0.599	0.198

Pipe wall temperature distribution and gas core temperature distribution have been plotted in Figure (4-10) and Figure (4-11), respectively. The local uncertainty at each of the data point is illustrated as an error bar. These figures show that the temperatures decrease along the pipe. This is due to latent and convection heat transfer from the vapour mixture to the cold wall. The latent heat is released due to condensation of vapour and the convection heat transfer is due to temperature difference between the gas mixture and cold wall.

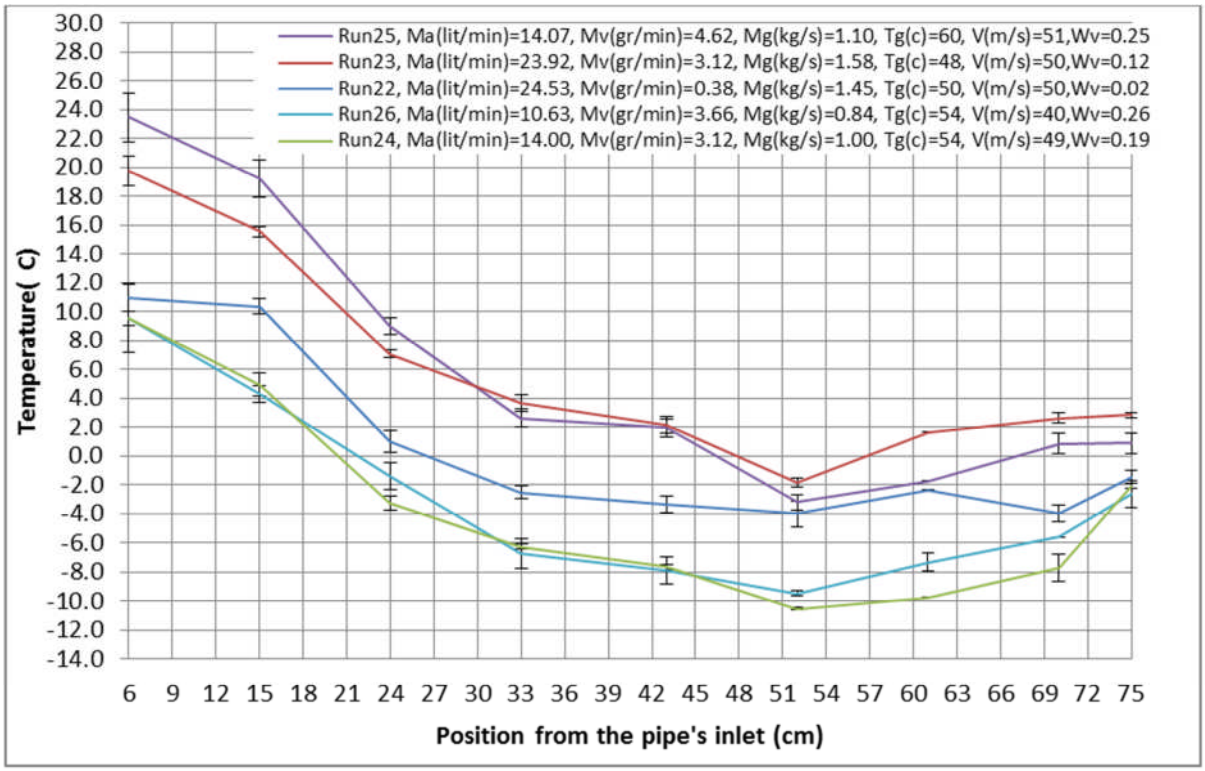

Figure 4-10 Pipe wall temperature for Run 22 to Run 26 on vertical pipe

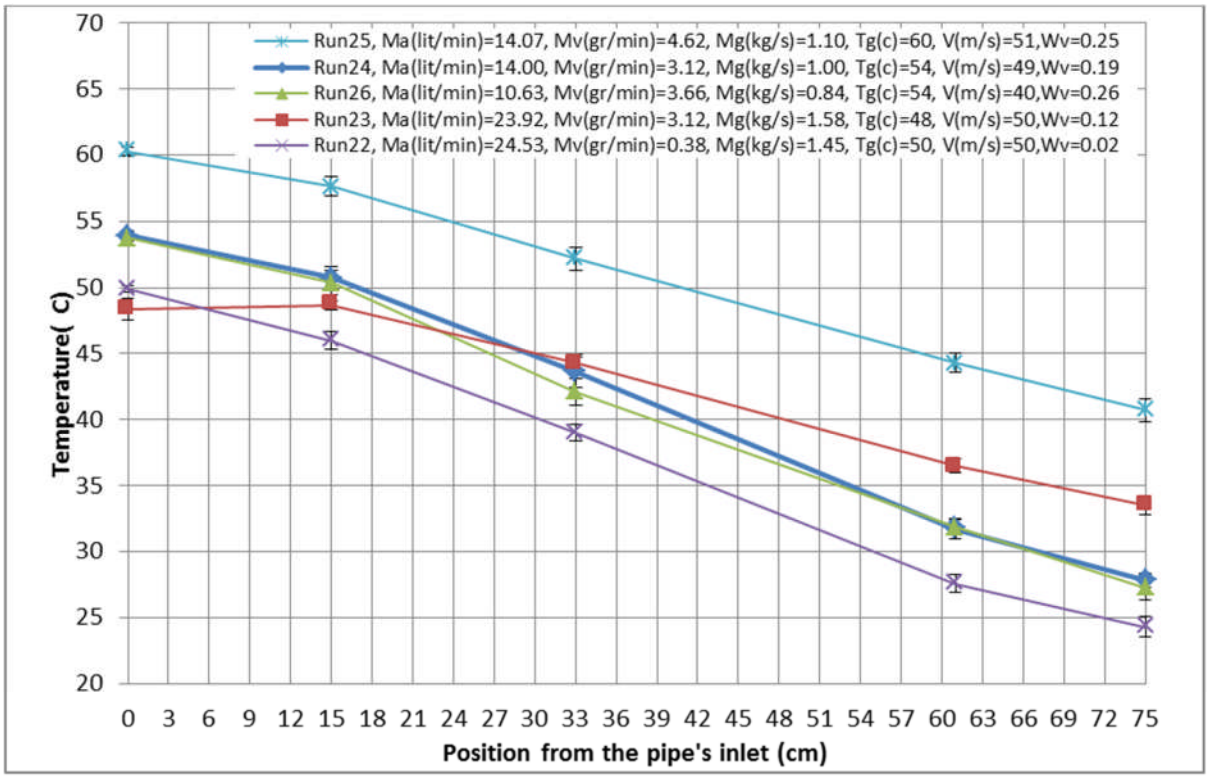

Figure 4-11 Gas Core Temperature for Run 22 to Run 26 on Vertical Pipe

4.1.4 Heat Transfer Coefficient

Here, the process of evaluating the local in-tube heat transfer coefficient based on the experimental temperature is described.

Figure (4-12), shows a schematic of condensation process and temperature measurement points in the vertical pipe.

For local condensation, in-tube heat transfer coefficient at any axial locations (x) along the pipe can be expressed by Eq. (4-1).

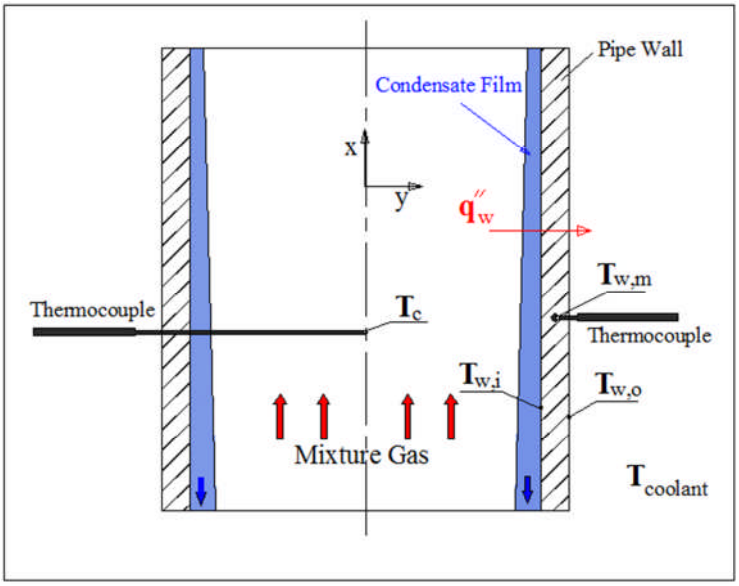

Figure 4-12 Control Volume for reflux condensation

$$HTC = \frac{q''_w}{T_c(x) - T_{w,i}(x)} \tag{4-1}$$

Where, HTC is the local in-tube experimental heat transfer coefficient and it is deducted from the measured heat flux (q''_w), gas core temperature (T_c) and pipe inner wall temperature (T_{wi}) at any x along the pipe.

The heat flux through the tube wall at any axial position is calculated by applying heat conduction through the wall and external convection from a cylindrical geometry, as presented by Eq. (4-2).

$$q''_{w,o} = U\,(T_{W,m} - T_{coolant}) \tag{4-2}$$

Where U, is the external overall heat transfer coefficient which is a function of conduction and convection heat transfer coefficients.

$$U = \left[\frac{\ln(r_o / r_m) r_o}{k_w} + \frac{1}{h_c}\right]^{-1} \tag{4-3}$$

r_o: external diameter of the pipe (m)

k_w: conduction heat transfer coefficient of the pipe (W/m.K)

h_c: external heat transfer coefficient (W/m.K)

Where subscripts “m” denotes the radial position at which the thermocouple is installed.

Since, the thermocouples were inserted to the middle of the pipe wall ($T_{w,m}$), shown in Figure (3-27), the temperature at the tube inner wall ($T_{w,i}$), can be deduced from the heat flux equation as Eq. (4-4).

$$T_{W,i} = T_{W,m} + q''_{w,o} \frac{r_o \ln(r_m / r_i)}{k_w} \qquad (4\text{-}4)$$

$T_{w,m}$: middle pipe wall temperature

r_i: internal diameter of the pipe (m)

The thermal conductivity of the pipe wall (k_W) is given as 0.18 W/(m.K) which is for the Perspex material.

The following procedure is proposed to evaluate the experimental heat transfer coefficient.

1- Calculate the overall heat transfer coefficient (U) from Eq. (4-3)
2- Calculate heat flux from Eq. (4-2) based on the measured temperatures
3- Calculate the inside wall temperature ($T_{w,i}$) from Eq. (4-4)
4- Calculate the heat transfer coefficient (HTC) from Eq. (4-1).

The above procedure was applied and the experimental heat transfer coefficient (HTC) has been evaluated at different locations along the pipe. In Table (4-4), the inner wall temperature T_{wi} , the calculated heat fluxes and finally the calculated HTCs are listed at four different locations (15cm, 33cm, 61cm and 75cm) along the pipe.

Table 4-4 Heat Transfer Coefficient for Vertical Pipe

Case	Location (cm)	15.00	33.00	61.00	75.00
Run22	Tcore (°C)	45.97	39.00	27.57	24.29
	Twall (°C)	10.38	-2.55	-2.35	-1.46
	External HTC (W/m2.K)	64.01	59.63	44.21	20.51
	Overall Heat Transfer Coeffcient (W/m2.K)	45.62	43.35	34.58	18.16
	Heat Flux (W/m2)	1385.78	756.72	610.24	245.90
	Twi (°C)	13.16	-1.02	-1.13	-0.97
	HTC (W/m2.K)	42.24	18.91	21.27	9.74
Run23	Tcore (°C)	45.97	39.00	27.57	24.29
	Twall (°C)	15.55	3.70	1.64	2.85
	External HTC (W/m2.K)	64.01	59.63	44.21	20.51
	Overall Heat Transfer Coeffcient (W/m2.K)	45.62	43.35	34.58	18.16
	Heat Flux (W/m2)	1621.85	1027.29	748.36	324.12
	Twi (°C)	18.81	5.76	3.15	3.50
	HTC (W/m2.K)	59.72	30.91	30.64	15.59
Run24	Tcore (°C)	50.81	43.68	31.73	27.86
	Twall (°C)	4.94	-6.27	-9.73	-2.07
	External HTC (W/m2.K)	64.01	59.63	44.21	20.51
	Overall Heat Transfer Coeffcient (W/m2.K)	45.62	43.35	34.58	18.16
	Heat Flux (W/m2)	1137.88	595.36	355.07	325.69
	Twi (°C)	7.23	-5.07	-9.02	-1.41
	HTC (W/m2.K)	26.11	12.21	8.71	11.13
Run25	Tcore (°C)	57.60	52.20	44.32	40.73
	Twall (°C)	19.22	2.65	-1.74	0.89
	External HTC (W/m2.K)	64.01	59.63	44.21	20.51
	Overall Heat Transfer Coeffcient (W/m2.K)	45.62	43.35	34.58	18.16
	Heat Flux (W/m2)	1789.36	981.78	631.42	379.43
	Twi (°C)	22.82	4.62	-0.47	1.66
	HTC (W/m2.K)	51.45	20.63	14.10	9.71
Run26	Tcore (°C)	50.39	42.09	31.85	27.29
	Twall (°C)	4.26	-6.73	-7.31	-2.67
	External HTC (W/m2.K)	44.51	54.33	37.03	18.41
	Overall Heat Transfer Coeffcient (W/m2.K)	34.76	40.48	30.02	16.50
	Heat Flux (W/m2)	843.52	537.38	381.03	285.92
	Twi (°C)	5.96	-5.64	-6.54	-2.10
	HTC (W/m2.K)	18.99	11.26	9.93	9.73

In order to estimate the uncertainty attributed to the heat transfer coefficient, the classical method of Kline and McClintock (1953) has been applied. In this approach, the uncertainty in a given function is due to the combined effects of uncertainties in all the variables, according to the well-known root-sum-square method. Therefore, the uncertainty of the heat transfer coefficient (HTC) to be due to the uncertainty of the heat flux exchanged at the surface (q''_w) and to the uncertainties associated to the measurements of the pipe inner wall (T_{wi}) and gas core temperature (T_c). Moreover, the heat flux (q''_w) accounts for the external overall heat transfer coefficient and uncertainties of wall ($T_{w,m}$) and tunnel external temperature (T_c), Eq.

(4-2). Thus, from Eqs. (4-1), (4-2) and (4-3), the uncertainty associated with the heat transfer coefficient can be given by:

$$\frac{\sigma h}{h} = \sqrt{\left(\frac{\sigma q''}{q''}\right)^2 + \left(\frac{\sigma(T_c - T_{wi})}{(T_c - T_{wi})}\right)^2}$$
$$= \sqrt{\left(\frac{\sigma U}{U}\right)^2 + \left(\frac{\sigma(T_{w,m} - T_C)}{(T_{w,m} - T_C)}\right)^2 + \left(\frac{\sigma(T_c - T_{wi})}{(T_c - T_{wi})}\right)^2} \qquad (4.5)$$

The variables r_i, r_o, k_w are assumed to be error free. Uncertainty of the external overall heat transfer coefficient (U) is assumed to be just dependent on the coolant heat transfer coefficient. The uncertainty of the coolant heat transfer coefficient was evaluated in the section (3-7).

The K type Thermocouples were calibrated within $\pm 0.1\ ^{\circ}C$ error limit. This standard error has been added to the temperature standard deviations, given in Table (4-3).

In Figure (4-13) the uncertainties of the heat transfer coefficient at different runs have been plotted as a percentage.

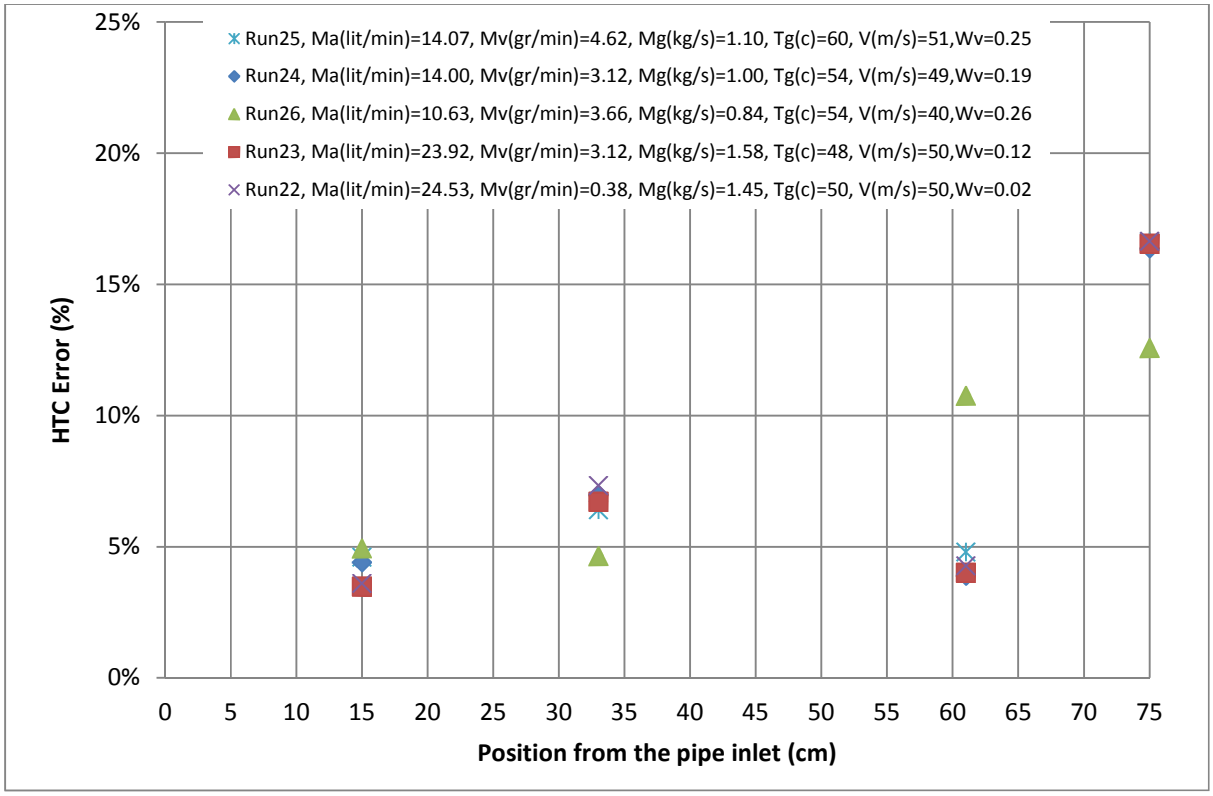

Figure 4-13 Heat Transfer error for Vertical pipe

The maximum error of the heat transfer coefficient is 17% at the end of the pipe (75 cm). This large error may be due to disturbances of external flow. This has happened because the air from the outside of the icing tunnel has been sucked in to the tunnel test section through the gap between the outlet of the Perspex pipe and the test section (shown in Figure 4-14). This can affect the external convective cooling and introduce an error in the determination of heat transfer coefficient. Despite several attempt to seal this gap, due to practical restriction, air leakage hasn't been stopped during the tests.

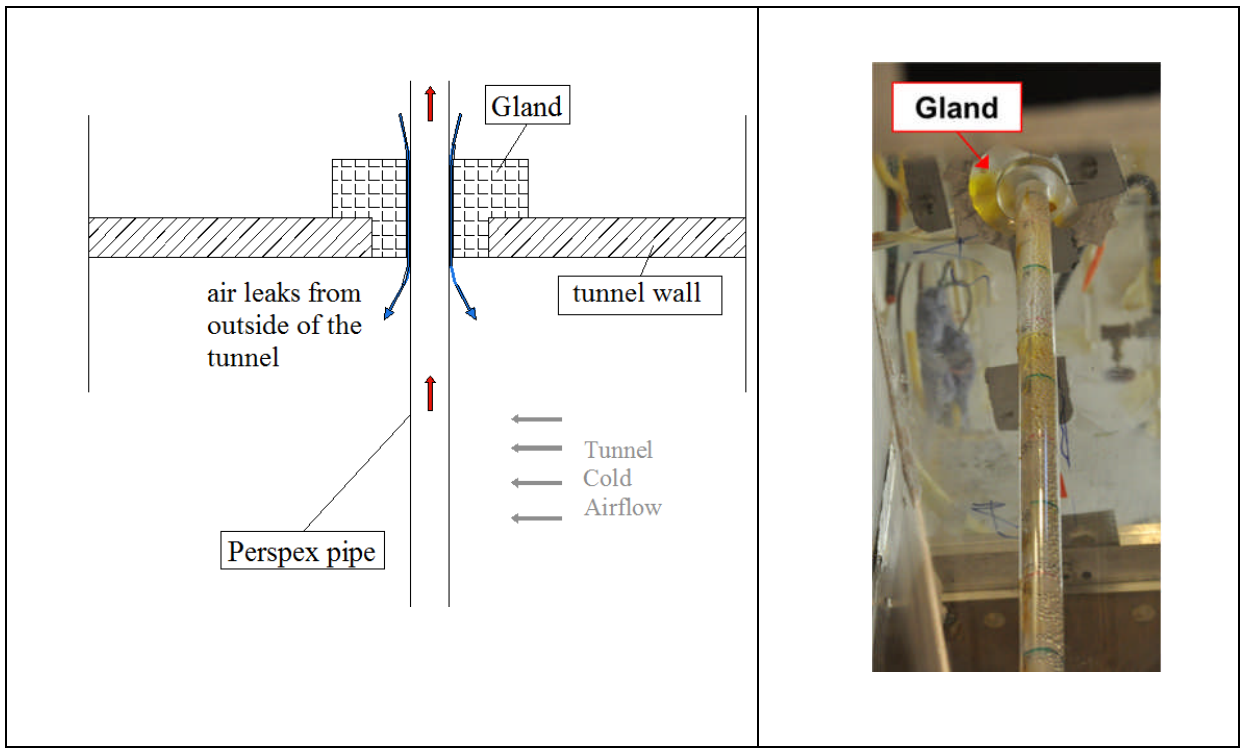

Figure 4- 14 Suction of air from outside of the tunnel test section

The heat transfer coefficients (HTC) for Run 22 to Run 26 are plotted in Figure (4-15).

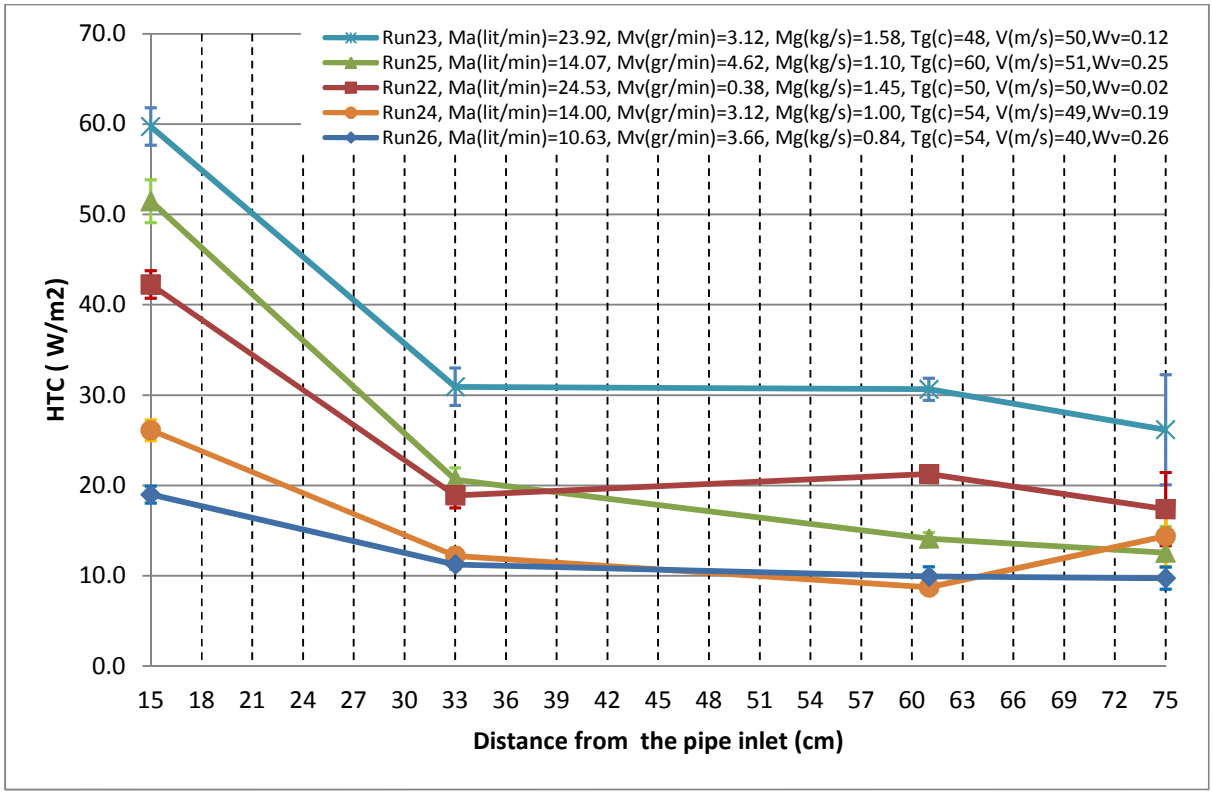

Figure 4-15 Heat Transfer Coefficients (HTC) for Run 22 to Run 26 (Vertical Pipe)

The heat transfer from the gas mixture during condensation depends on two interdependent parameters which are sensible heat and latent heat. Sensible heat transfer is due to the temperature difference between the gas mixture and the wall. Latent heat transfer is due to vapour mass flow rate (moisture content of the air). Therefore increasing the vapour mass flow rate and the mixture temperature increases the heat transfer coefficient in the pipe.

Figure (4-15), shows that heat transfer coefficient decreases sharply at the initial length of the pipe and then slowly as the vapour mass fraction decreases along the length. This can be due to the fact that most of condensation in the pipe happens in the beginning of the pipe up to 33cm.

4.1.5 Vapour Mass Fraction

In Figure (4-16), two test cases (Run 22 and Run 23) with similar inlet gas temperatures and dry mass flow rate but with different vapour mass fractions (W_v=0.02 and W_v= 0.12) are presented. The purpose of this comparison is to evaluate the effects of vapour mass fraction on heat transfer coefficient. As it is presented, increasing the vapour mass flow rate from 0.38 g/min (Run21) to 3.12 g/min (Run23) increases the local heat transfer coefficients approximately by 50% all along the pipe. This means vapour content plays an important role

on heat transfer resistance. In the event of higher vapour mass fraction, more water vapour can be condensed and more latent heat is released.

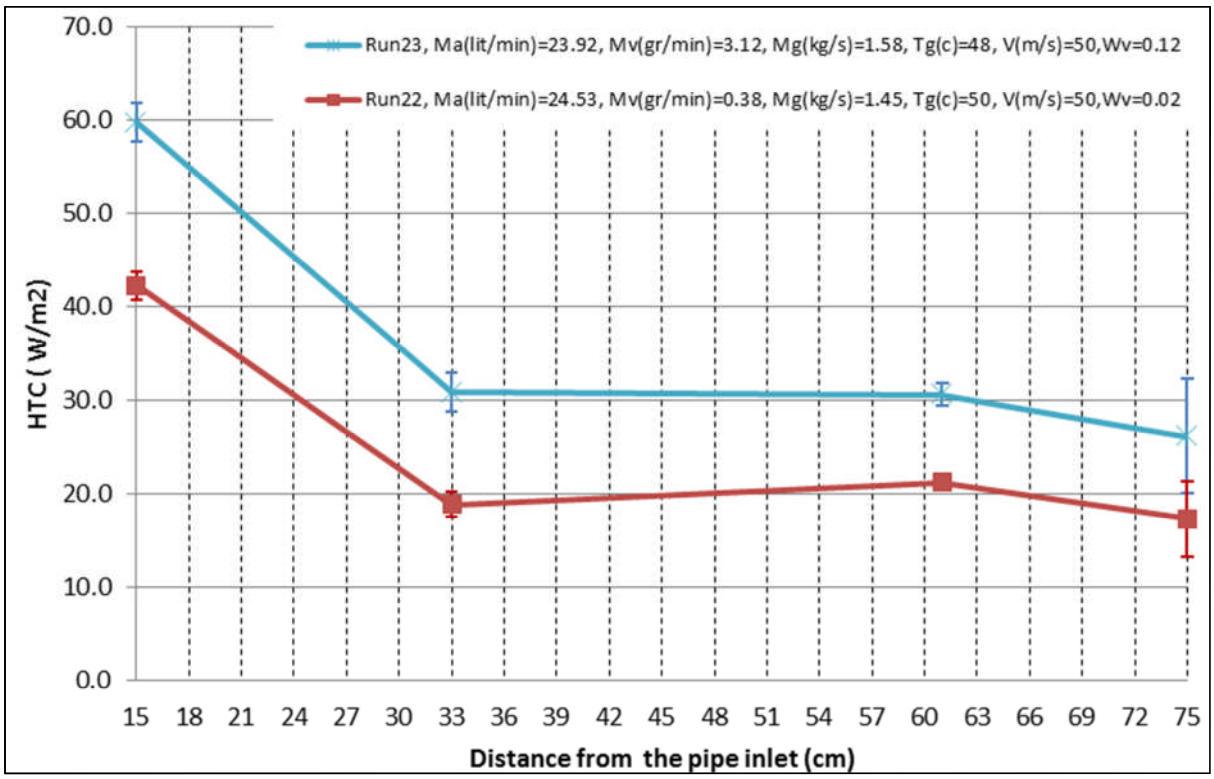

Figure 4-16 Pipe wall temperature for Run 22 and Run 23

4.1.6 Ice formation in vertical pipe

Ice formation inside the pipe can be assessed by monitoring pipe wall temperature. The temperature plot for Run 22 at 18 minutes is shown in Figure (4-17). This graph shows that condensate film in the pipe starts to freeze from 26cm. The wall temperature distribution rises gradually after 52cm. This can be due to the external flow disturbances which have been explained earlier in the section (4.1.3). This rise of temperature can be recognized in all the runs.

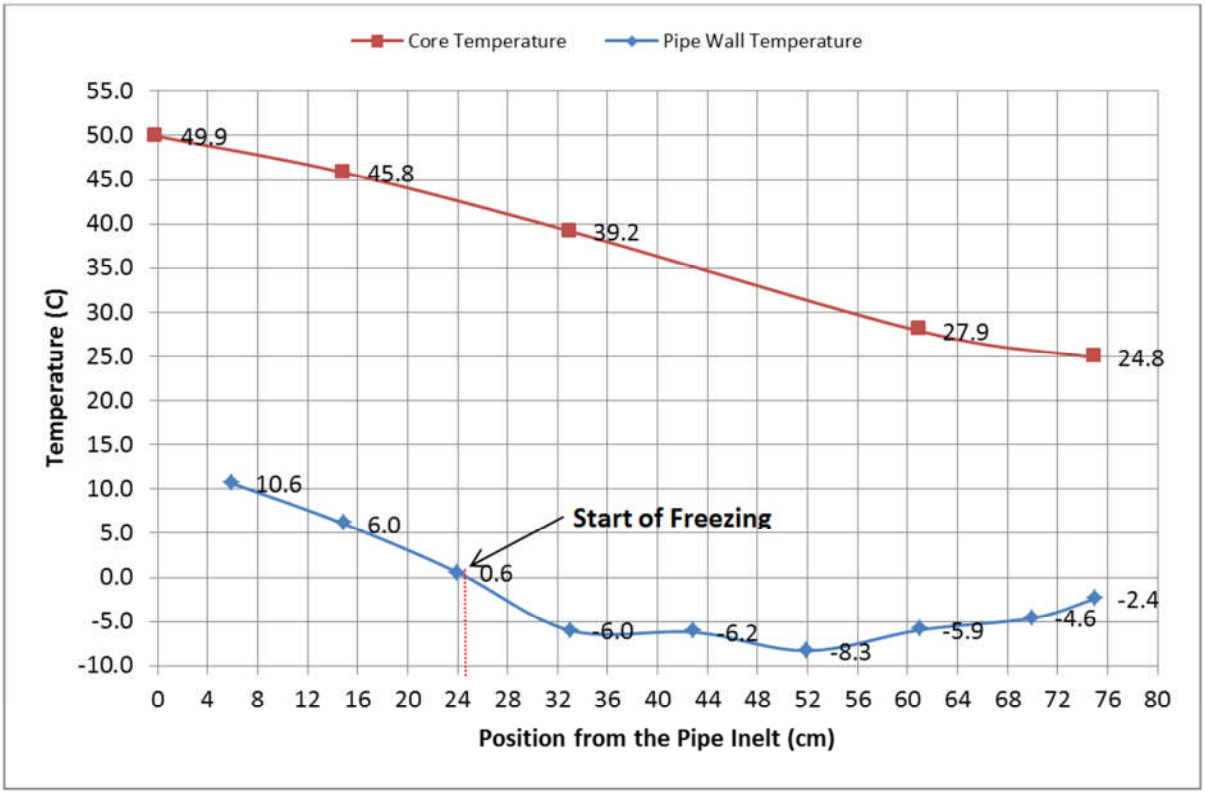

Figure 4-17 Pipe temperature for Run 22 at 18 minutes

In Figure (4-18) ice formation inside the pipe is shown. After the test, the weight of the ice was measured which was 2.04 g.

Figure 4-18 Ice layer inside the pipe in Run 22 at the end of the test. The direction of internal airflow is from left to right

4.2 Horizontal Pipe

The purpose of conducting an experiment on a horizontal pipe was to evaluate a CFD study which is explained in the Chapter 6. In this experiment a total number of 7 runs have been conducted. The test matrix of the horizontal pipe has been shown in Table (4-5). All the variables in this table are averaged over the 12 minutes of the runs. The inlet mixture mass flow rate varies from 0.58 kg/hr to 1.63 kg/hr with an inlet vapour mass fractions of 0.06 to 0.26. The operating pressure was at atmospheric pressure. The effects of moisture content, gas inlet temperature and pipe coating on condensation and ice formation is evaluated.

Table 4-5 Horizontal Pipe Test Matrix

Pipe Type	Case	Time (Minute)	Tunnel Speed (m/s)	Tg,in (°C)	Boiler Power (W)	Ma (kg/hr)	Mv (g/min)	Mg (kg/hr)	Wv
Horizontal	Run 15	12:00	50	46	63	0.54	0.56	0.58	0.06
Horizontal	Run 16	12:00	50	44	63	0.55	0.58	0.58	0.06
Horizontal	Run 17	12:00	50	48	157	1.44	3.12	1.63	0.12
Horizontal	Run 18	12:00	50	58	157	0.55	3	0.73	0.25
Horizontal	Run 19	12:00	50	59	154	0.54	3	0.71	0.23
Horizontal	Run 20	12:00	50	60	154	0.47	3	0.63	0.26
Horizontal	Run 21	12:00	50	61	154	0.56	3.1	0.73	0.23

4.2.1 Observing Condensation

When the air-steam mixture enters the Perspex pipe, it starts to condense on the inner surface of the pipe. The whole procedure of the condensation in the horizontal pipe can be divided in to four phases. The first two phases are similar to the vertical pipe which are as, primary droplet and coalescence. In the third phase, droplets fall off, drain downwards and accumulate gradually on the bottom of the pipe up to a certain thickness (Figure (4-19)). This phase is called slip down. In the fourth phase, called flow out, the condensate pool flows out axially toward the end of the pipe due to shear forces between the core gas and the condensate film. (Figure (4-20)).

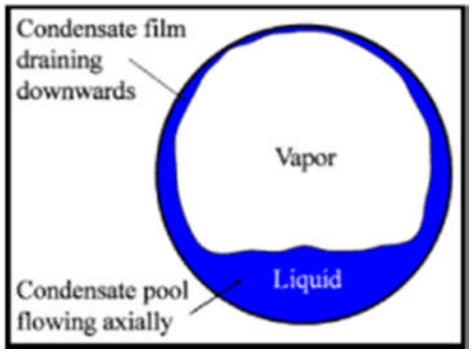

Figure 4-19 Cross section of the pipe showing the flow of the condensate film draining down

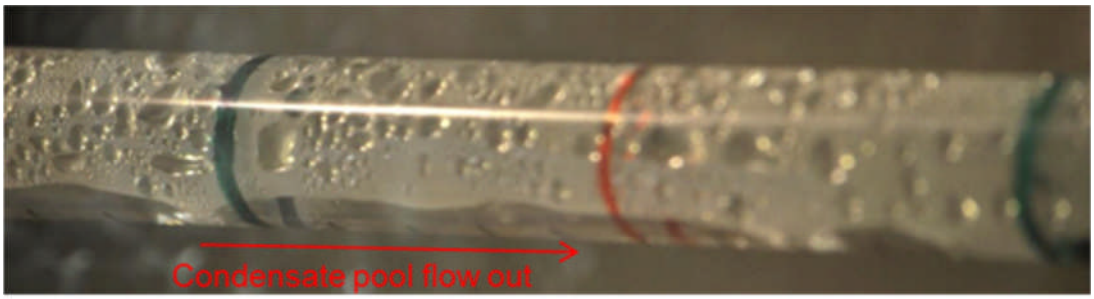

Figure 4-20 Condensation in a horizontal pipe

4.2.2 Effects of thermocouple and coating on condensation rate

As an engine breather pipe becomes older, its inner surface may be affected by oil or any other particles in the breather gas. Here, it has been tried to evaluate the effects of the nature of pipe inner surface on condensation rate. Hence, a hydrophobic coating (Nikwax) has been used. Nikwax is a soap based cleaner which can be used to clean equipment. This product produces a durable water repellent coating with elastic water-repellent molecules. It can also withstand temperature up to 50-60 °C.

In order to coat inner surface of the pipe, Nikwax liquid has been poured in to the pipe and soaked for 20 minutes. The purpose of producing this coating was to evaluate effects of hydrophobicity on condensation rate.

Run 21, has been repeated once with a coated pipe (Run19) and once without coating (Run 20). Both the runs were conducted without thermocouples. In Table (4-6) the test conditions of these three runs (Run19, Run20 and Run21) have been listed.

Table 4-6 Test Condition of Run19, Run20, Run21

Run Number	Condition	Tunnel Speed (m/s)	Tg,in (°C)	Boiler Power (W)	Ma (kg/hr)	Mv (g/min)	Mg (kg/hr)	Wv
Run 19	Without Coating- Without T/C	50	59.1	154	0.55	2.77	0.71	0.23
Run 20	With Coating- Without T/C	50	59.6	154	0.49	2.77	0.66	0.25
Run 21	Without Coating- With T/C	50	60.9	154	0.56	2.77	0.73	0.23

Comparing the results of Run 21 with Run 20 helps to assess the effects of attaching thermocouple to the pipe on condensation rate.

As occurred in the previous section, the rate of condensation has been evaluated by visualizing the recorded videos and monitoring droplet departure time and departure positions. The position and time of droplet departures in these three cases are presented in Figure (4-22). The droplet departure time in the horizontal pipe is defined as the time when droplets reach the bottom of the pipe (region C shown in Figure (4-21)).

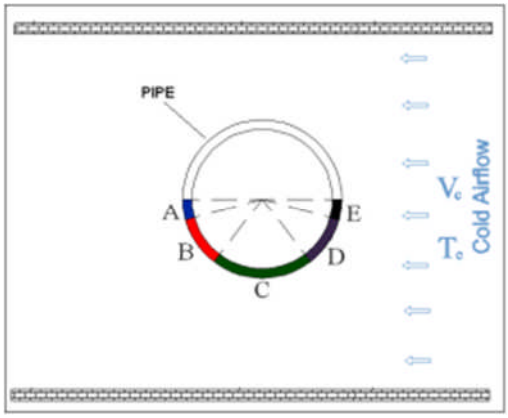

Figure 4-21 Side view of the horizontal pipe installed in the test section

Figure (4-22) clearly shows that the hydrophobic coating increases the departure time. This is due to the fact that the hydrophobic coating decreases the surface energy and therefore the droplets are kept on the surface longer. Using the coating has nearly doubled the departure time.

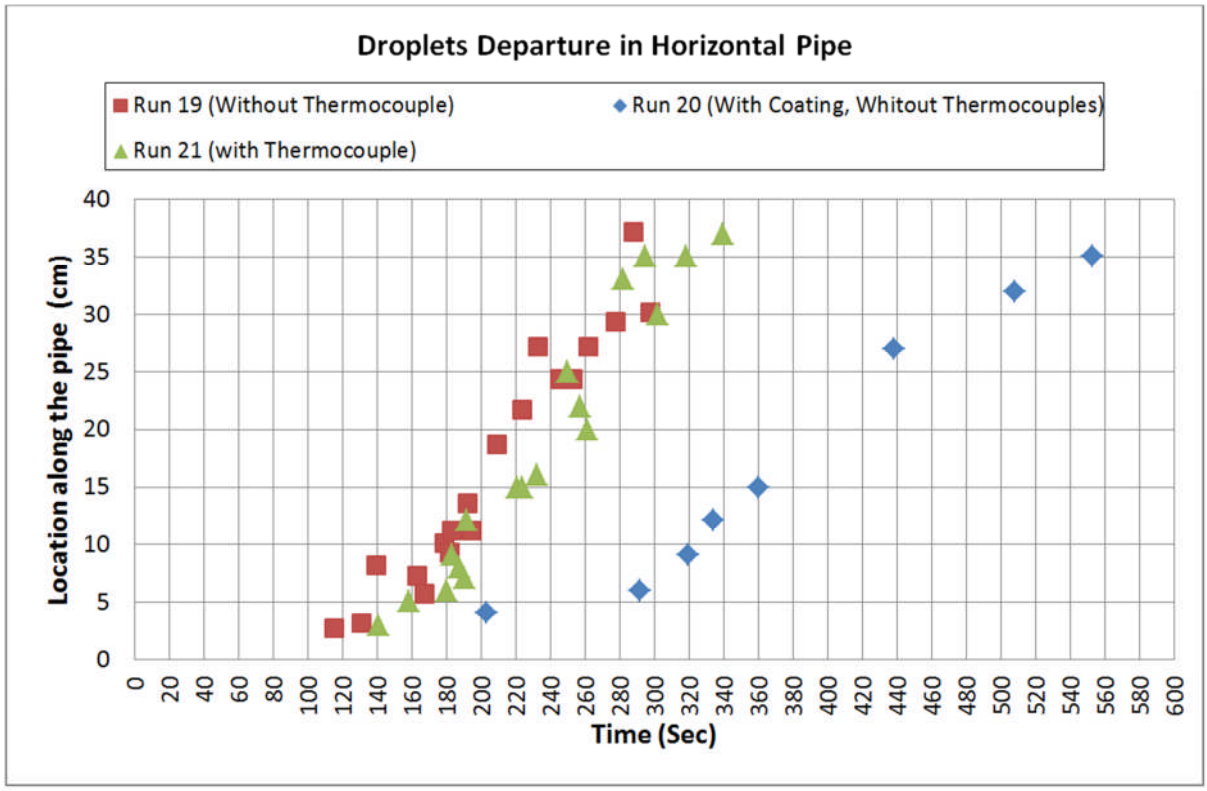

Figure 4-22 Time of droplet departure in horizontal pipe

In order to assess the condensation further, accumulation of condensate film at the bottom of the horizontal pipe in Run 19, Run 20 and Run 22 are compared at two moments in time (3

minutes and 5 minutes) in Figure (4-23) and Figure (4-24). The pictures have been taken from beneath the pipes and show condensate accumulation at the bottom of the pipe.

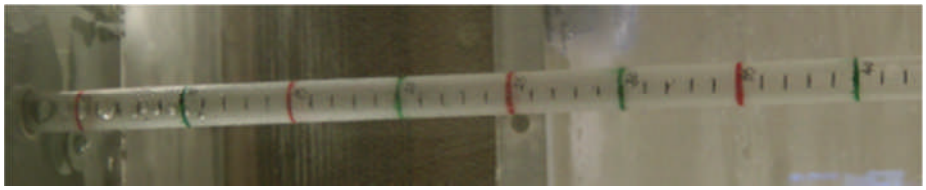

a) Pipe without coating- without Thermocouple (Run19)

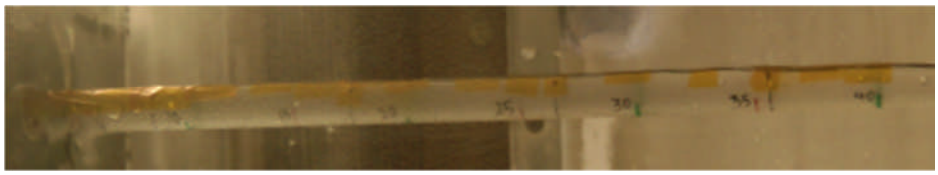

b) Pipe without coating- with Thermocouple (Run21)

c) Pipe with hydrophobic coating- without Thermocouple (Run20)

Figure 4-23 Effects of Thermocouple and Coating on Condensation Rate at 3 minutes

a) Pipe without coating- without Thermocouple (Run19)

b) Pipe without coating- with Thermocouple (Run21)

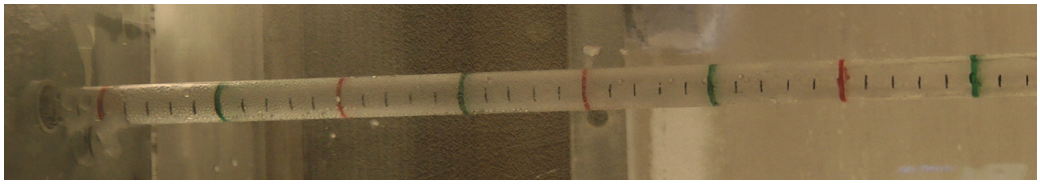

c) Pipe with hydrophobic coating – without Thermocouple (Run20)

Figure 4-24 Effects of Thermocouple and Coating on Condensation Rate after 5 minutes

This comparison suggests that attaching thermocouples to the pipe does not affect the condensation rate or in other words the heat transfer.

4.2.3 Temperature and heat transfer coefficient

Variation of the measured temperatures along the pipe for Run 21is illustrated in Figure (4-25), this includes 9 wall temperatures $T_1$to T_9 and 5 gas core temperatures T_{gin} and T_{1core} to $T_{4,core}$ over 13 minutes of the test.

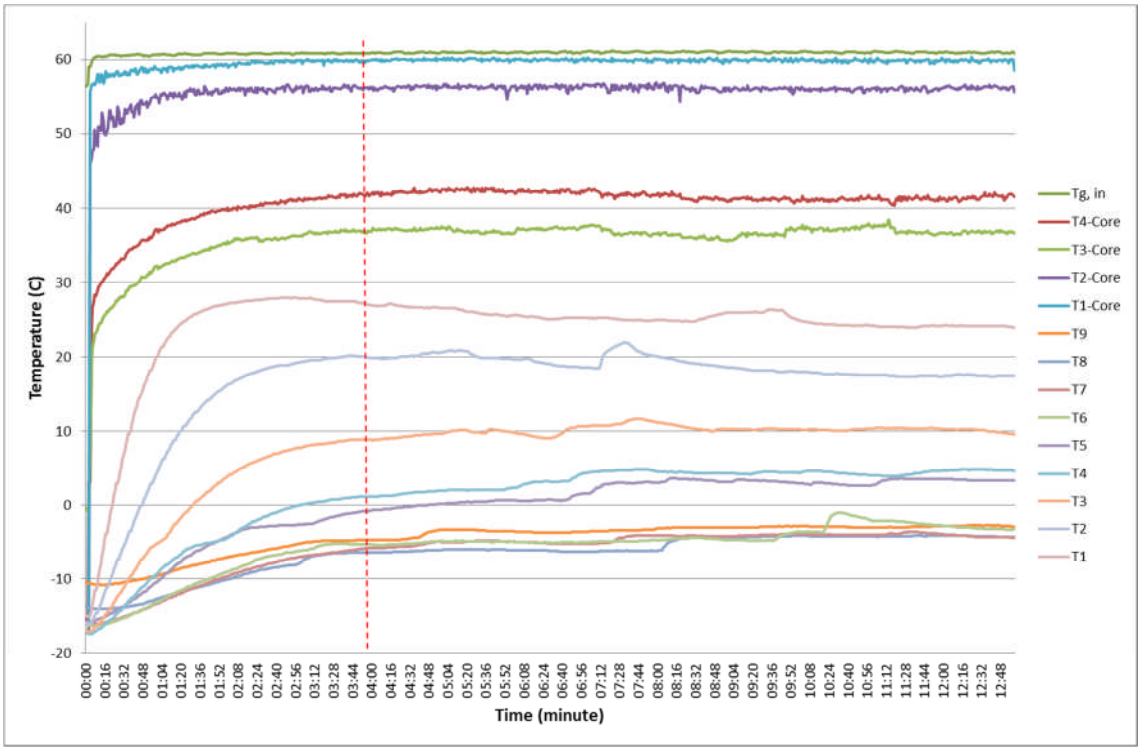

Figure 4-25 Temperature variation of the Perspex pipe at different locations along the pipe over the time for Run 21.

According to the test procedure, (see section 3.5), when the tunnel velocity and temperature become steady at 50m/s and -20C, respectively, the gas mixture enters the perspex pipe. Here, in Figure (4-25), it is clearly shown that at the beginning of the test (time=0) all the temperatures are between -20C to -10C. When the gas mixture enters the pipe the temperatures increase and they all become mostly steady after about 4 minutes. The local average temperatures of gas core flow and pipe wall are presented in Table (4-7) and Table (4-8). The temperature values are averaged value between 4 to 12 minutes. Standard deviation from the mean value at each of the measurement points have been calculated and presented as an uncertainty in Tables (4-7) and (4-8).

Table 4-7 Horizontal pipe wall temperature at different locations along the pipe

	Location	6	15	24	33	43	52	61	70	75
Run15	Uncertainty ©	0.4	0.3	0.3	0.1	0.1	0.2	0.1	0.2	0.2
	Temperature ©	6.5	-2.9	-8.0	-13.2	-14.1	-14.3	-14.4	-15.1	-11.6
Run16	Uncertainty ©	0.15	0.20	0.09	0.10	0.45	0.15	0.27	0.17	0.19
	Temperature ©	11.43	-0.14	1.89	-0.13	-1.74	-3.82	-5.49	-8.96	-8.07
Run17	Uncertainty ©	1.41	2.79	0.66	1.17	2.01	1.74	0.66	0.14	0.31
	Temperature ©	22.89	16.14	14.44	9.02	9.81	5.86	8.23	3.50	4.95
Run18	Uncertainty ©	1.15	0.62	1.65	0.08	2.31	1.86	0.56	0.37	0.15
	Temperature ©	24.62	13.16	3.32	-5.20	-5.78	-8.37	-9.80	-11.45	-6.81
Run21	Uncertainty ©	0.86	1.21	0.59	1.16	1.43	1.20	0.60	0.95	0.49
	Temperature ©	25.3	19.1	10.2	3.6	2.1	-4.2	-4.5	-5.3	-3.3

Table 4-8 Horizontal pipe gas core temperature at different locations along the pipe

	Location	0	15	33	61	75
Run15	Uncertainty (°C)	0.2	0.4	0.4	0.5	0.5
	Temperature (°C)	46.2	43.7	35.6	18.0	16.0
Run16	Uncertainty (°C)	0.1	0.4	0.8	0.5	0.9
	Temperature (°C)	44.3	40.8	21.8	13.1	10.3
Run17	Uncertainty (°C)	0.2	0.3	0.8	0.3	0.3
	Temperature (°C)	47.2	46.5	40.8	32.4	28.7
Run18	Uncertainty (°C)	0.1	0.2	0.4	0.4	1.0
	Temperature (°C)	57.7	55.7	49.6	30.7	26.9
Run21	Uncertainty (°C)	0.1	0.2	0.3	0.5	0.5
	Temperature (°C)	61.0	59.9	56.2	41.7	36.9

The in-tube heat transfer coefficient (HTC) in the horizontal pipe is evaluated by applying procedure given in the section (4-1-4). In Table (4-9) the HTC is listed at 4 different locations along the pipe.

Table 4-9 Heat Transfer Coefficients (HTC) in Horizontal Pipe

Location (cm)	15	33	61	75
Run15	16.81	6.06	6.04	4.91
Run16	22.24	39.73	27.05	10.84
Run17	54.59	39.81	40.58	18.38
Run18	35.73	11.77	8.77	6.59
Run21	43.81	19.61	11.62	7.11

Applying the method of Kline and McClintock (1953) explained in the section (4.1.4), the uncertainty of heat transfer coefficient in the Horizontal pipe has been evaluated for all the runs as given in Figure (4-26).

The maximum uncertainty of the heat transfer coefficient was 23% at the end of the pipe (75 cm). This large uncertainty at the end of the pipe was due to disturbances of external flow (explained in section 4-1-4).

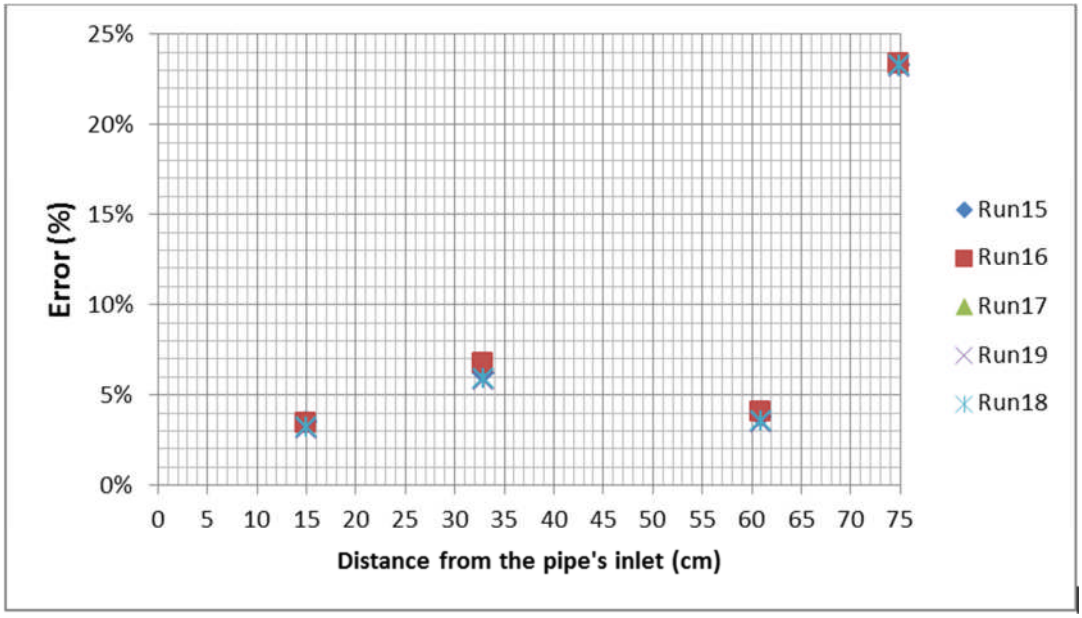

Figure 4-26 HTC error for Horizontal pipe runs

4.2.4 Effects of vapour mass flow rate

Here, the effect of vapour mass fraction on condensation rate and heat transfer in the horizontal pipe is investigated. For this purpose the results of Run 15, Run 18 and Run 21 are investigated. The test conditions for these runs have been averaged between 3 to 12 minutes of test and listed in Table (4-10).

Table 4-10 Test condition for Run15, Run18 and Run2, averaged between 3 to 12 minutes

Pipe Type	Case	Tunnel Speed (m/s)	Tg,in (°C)	Boiler Power (W)	Ma (kg/hr)	Mv (g/min)	Mg (kg/hr)	Wv
Horizontal	Run 15	50	46	63	0.54	0.6	0.58	0.06
Horizontal	Run 18	49	58	157	0.55	3	0.73	0.25
Horizontal	Run 21	49	61	154	0.56	3.1	0.73	0.25

Pipe wall temperatures of these runs have been plotted with their attributed uncertainties, shown as error bars, in Figures (4-27). The experimental heat transfer coefficient is also illustrated in Figure (4-28).

Figures (4-27) and (4-28) show that there are high gradients in all the temperature graphs up to the length of 33cm. The experimental heat transfer coefficients in Figure (4-28) show the similar trend in which the heat transfer coefficients decreasing sharply over the initial length of the pipe and then slowly until they are merged together at the end of the pipe. This indicates that most of the condensation occurs up to length of 33cm of the pipe.

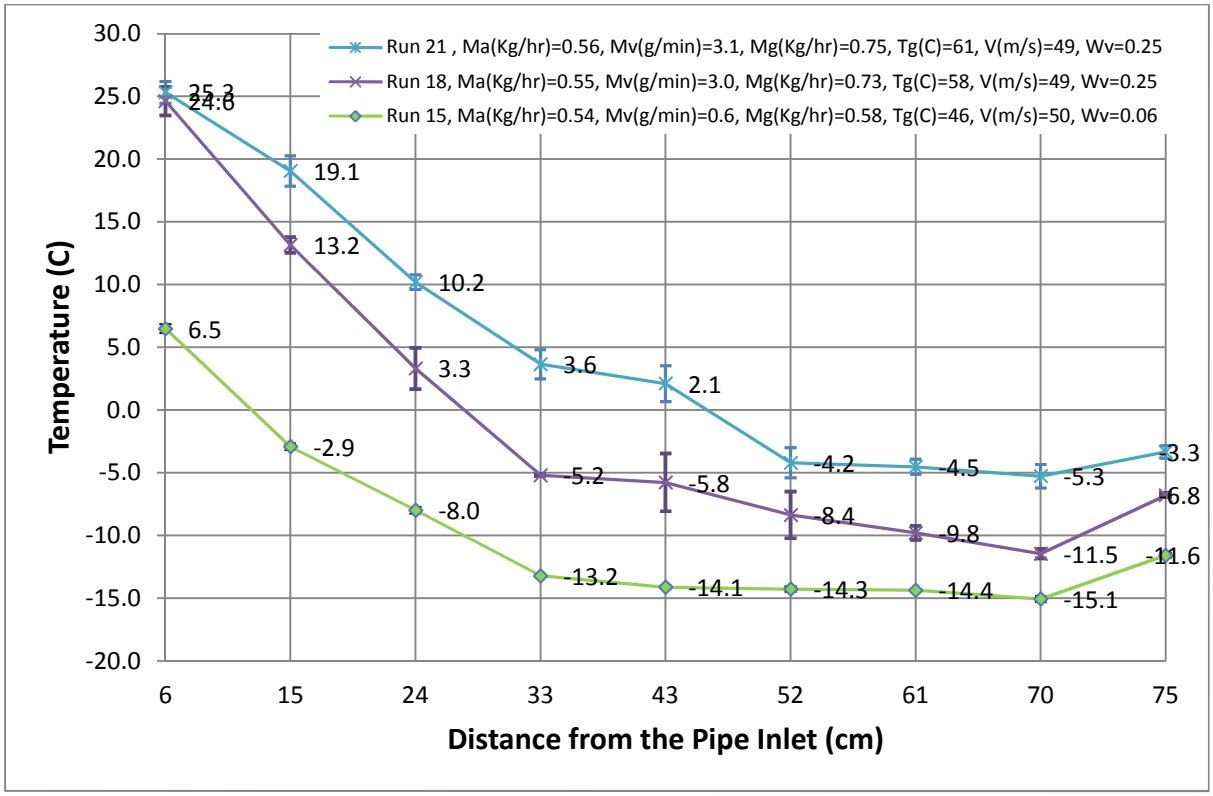

Figure 4-27 Core Temperature in Run 15, Run 18 and Run 21 of horizontal pipe

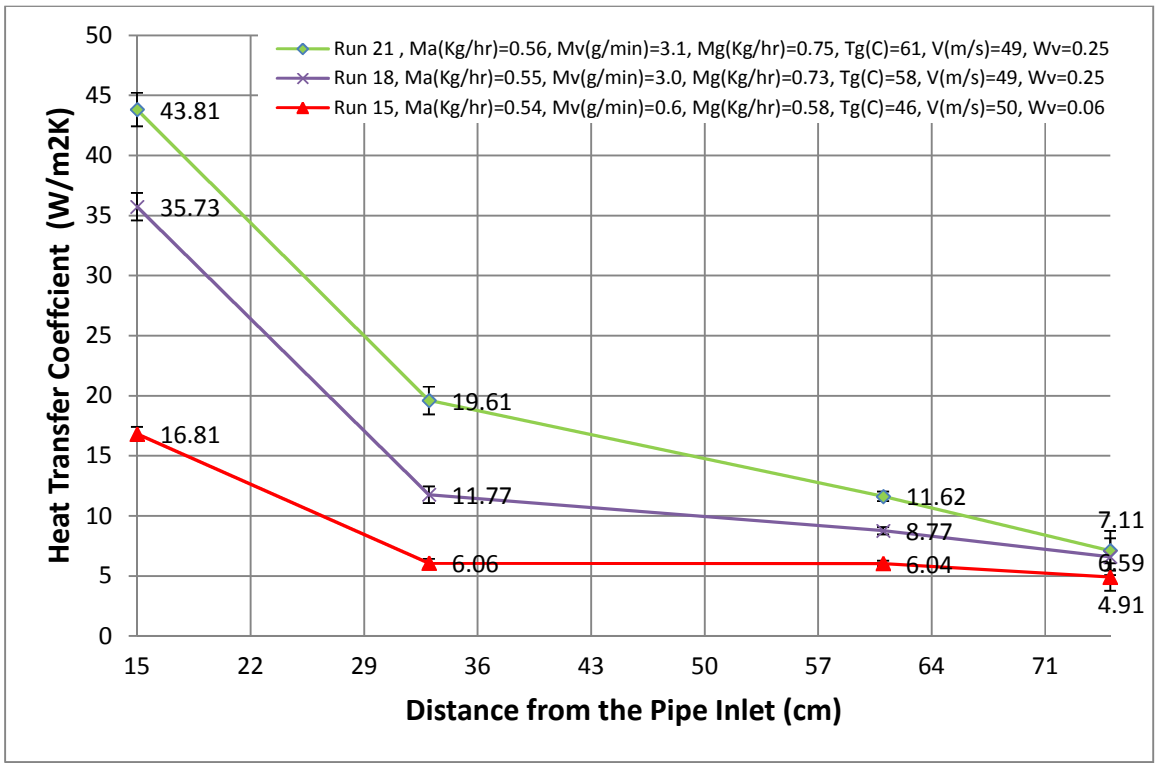

Figure 4-28 Heat Transfer Coefficients in Run 15, Run 18, Run21 of horizontal pipe

It has been discussed in section (4.1.6) that increasing vapour mass flow rate increases latent heat transfer which increases the heat transfer coefficient (HTC). Increasing gas

temperature increases the sensible heat transfer. Run 21 has the highest inlet temperature and vapour mass flow rate and as shown in Figure (4-29) its local heat transfer coefficient is the higher than Run18 and Run15. To investigate this further, the accumulation of condensate water at the bottom of the pipe in each of these runs after 10 minutes is compared in Figure (4-29). From this picture it is clear that condensation in Run 21 is greater than for Runs 18 and 15 and Run 18 is greater than Run15. This means that in the case of higher vapour mass fraction, more water vapour is condensed in the pipe. This would release more latent heat and can increase the heat transfer coefficient and increase the local temperatures.

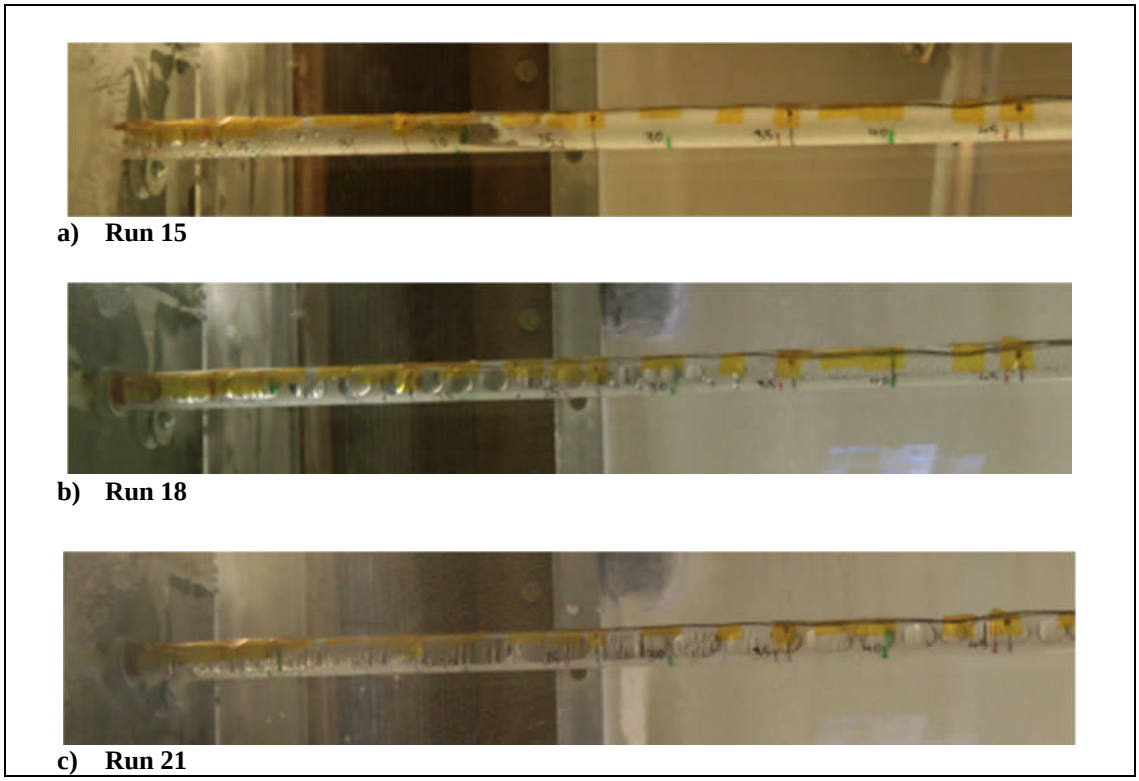

a) Run 15

b) Run 18

c) Run 21

Figure 4-29 Horizontal pipe from bottom view after 10 minutes

To investigate condensation further in each of the cases, videos of the tests have been analysed and condensation rates in each of the cases (Run15, Run18 and Run21) were determined. The time of the droplet departures and their locations from the pipe inlet have been listed in Table (4-8) for Runs 15, 18 and 21.

Table 4-11 Droplet Departure time and their positions in Run15, Run16 and Run 21

Run 15			Run 18			Run 21		
Time of Departure (Minute)	Time of Departure(Seconds)	Location of Departure (cm)	Time of Departure (Minute)	Time of Departure(Seconds)	Location of Departure (cm)	Time of Departure (Minute)	Time of Departure(Seconds)	Location of Departure (cm)
06:35	395	4	02:45	165	3	02:44	164	2
07:48	468	6	02:45	165	4	02:50	170	4
08:30	510	7	04:14	254	6	02:59	179	6
09:59	599	10	04:29	269	7	03:05	185	5
10:23	623	9	04:44	284	7.5	03:15	195	8
11:03	663	12	04:58	298	9	03:31	211	9.5
11:26	686	17	05:05	305	7	03:45	225	9
12:12	732	12.5	05:28	328	12	04:08	248	15
			05:50	350	15	04:08	248	13
			05:50	350	13	04:18	258	12
			06:02	362	10.5	04:18	258	15
			06:14	374	13	04:30	270	16
			06:22	382	24	04:40	280	18
			06:32	392	26	04:53	293	20
			06:43	403	22	04:55	295	22
			07:01	421	29	04:57	297	32
			07:06	426	27	05:03	303	23
			07:18	438	28	05:09	309	25
			07:28	448	33	05:14	314	33
			07:36	456	37	05:19	319	27
						05:25	325	28
						05:27	327	29
						05:34	334	35
						05:44	344	37

In Figure (4-30), the locations of droplet departure versus time are plotted for these three cases. This Figure clearly indicates that increasing the vapour mass flow rate increases condensation rate.

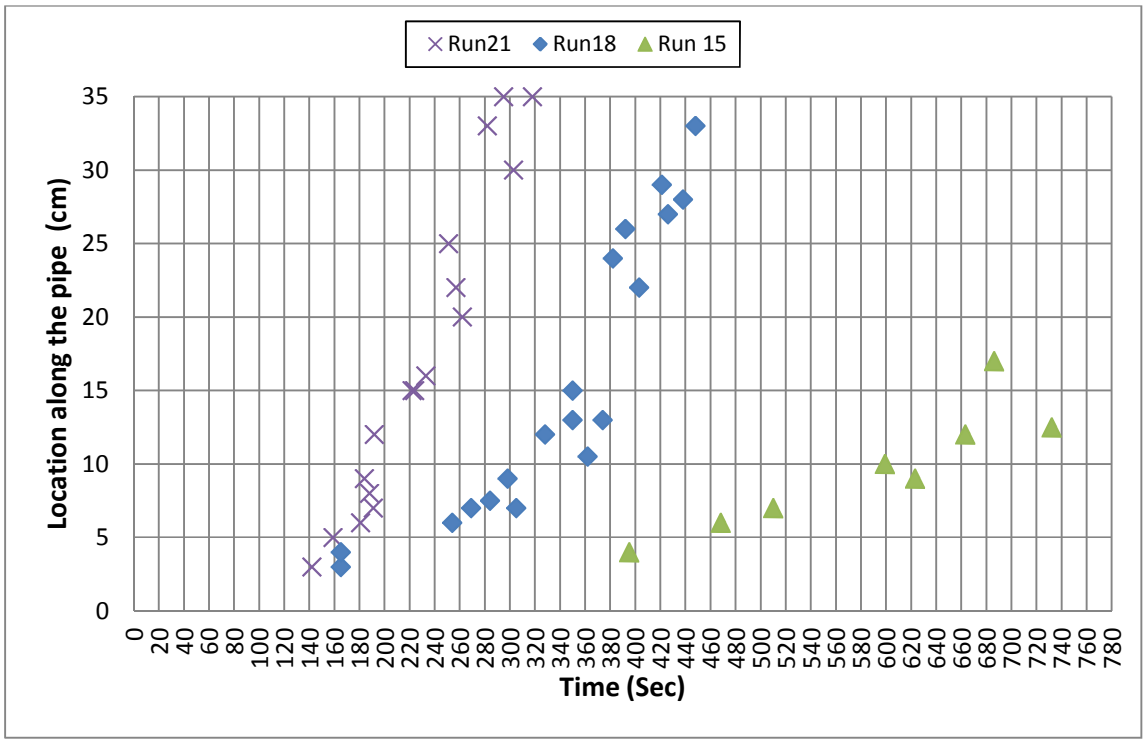

Figure 4-30 Time and location of droplets departure in a horizontal pipe

4.2.5 Temperature and ice formation physics

Measuring pipe temperature helps to recognize freezing in the pipe. Here, the temperature graph for Run 18 is shown in Figure (4-31). As shown, the wall temperature is below 0°C from 28 cm after 37 minutes of the run. The start point of the freezing region can be identified by looking at the pictures. One can identify the freezing region starts from 27cm, as shown in Figure (4-32).

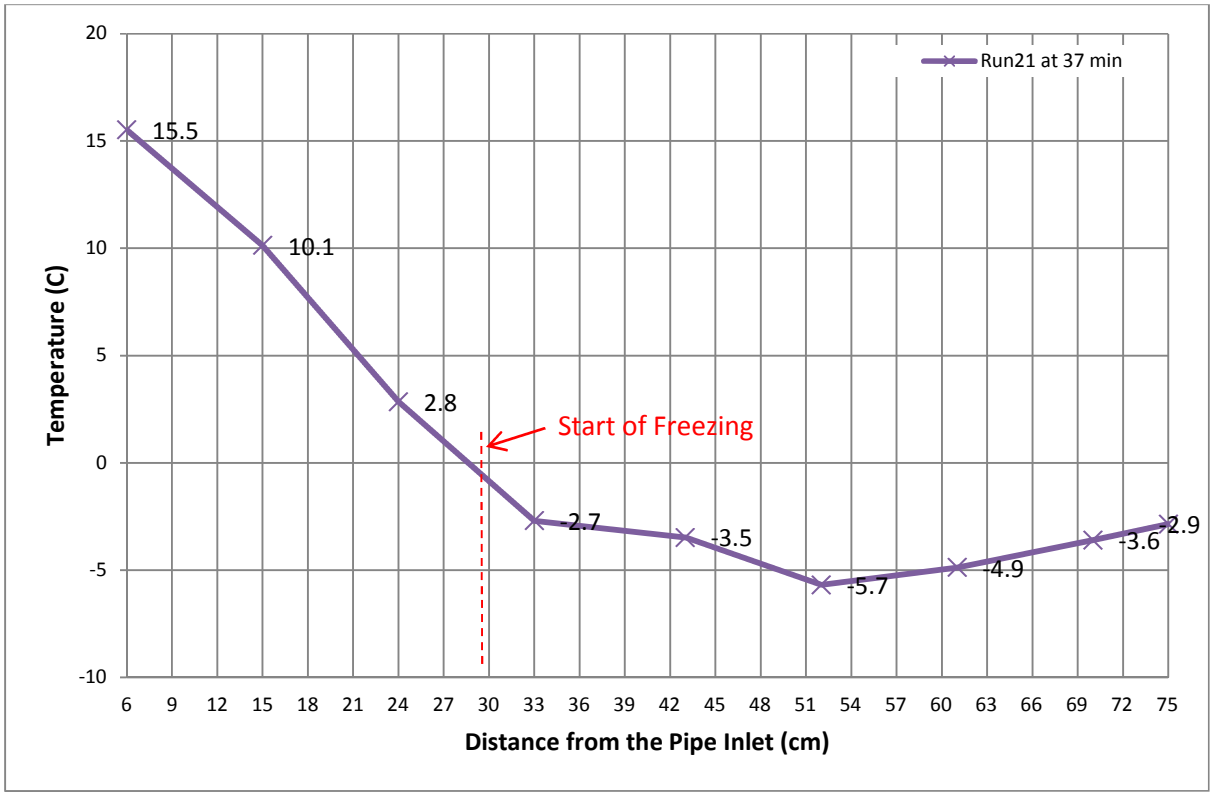

Figure 4-31 Horizontal Pipe Wall Temperature in Run18

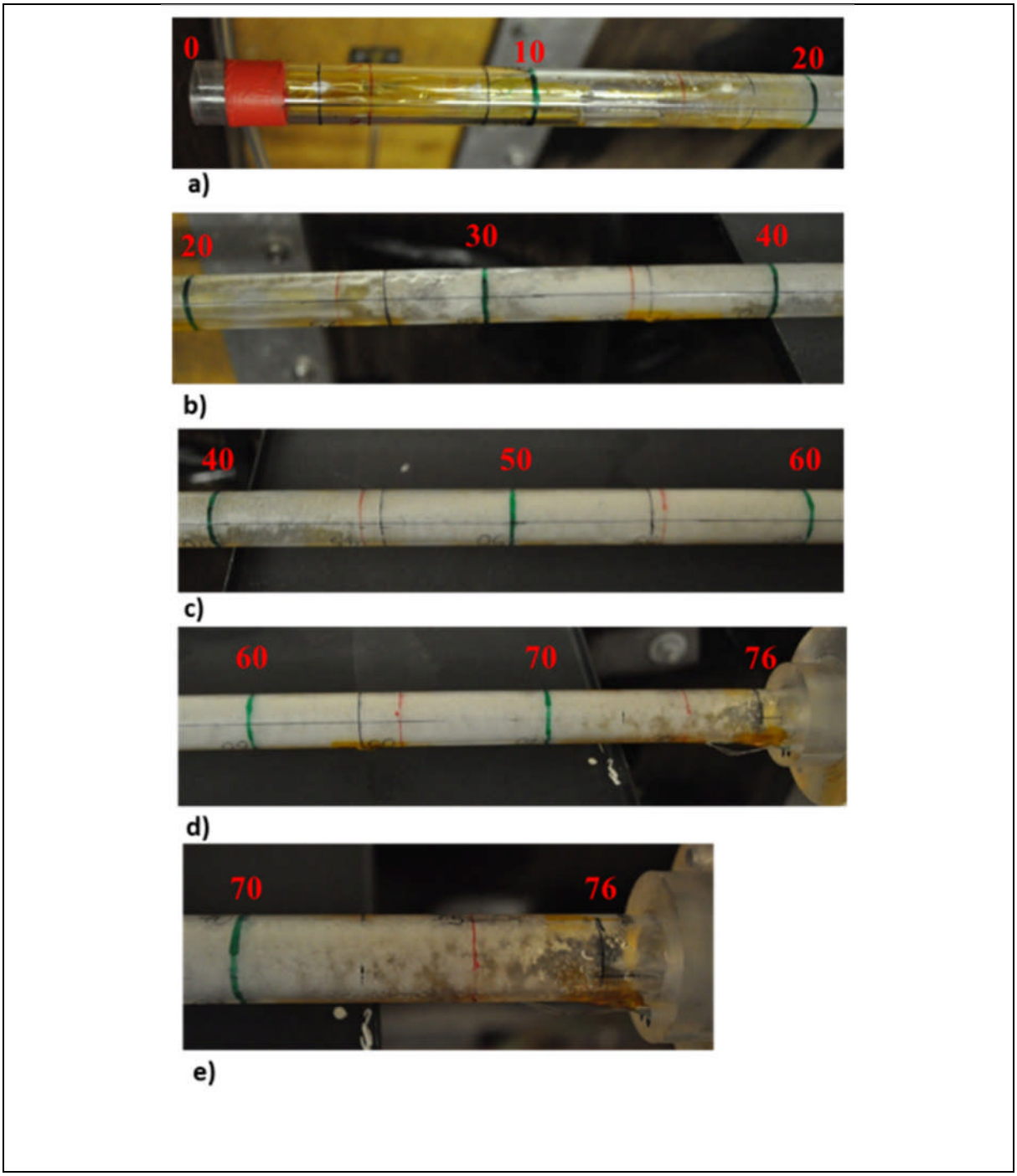

Figure 4-32 Ice formation in Horizontal pipe in Run 18 at 10 minutes

It has been noted earlier about the effects of air which was sucked in to the tunnel from the outside of the test section during the test and increased the pipe temperature. It can be observed in Figure (4-32e) that the ice layers at the end of the pipe were melted due to this effect.

4.3 T-Joint Pipe

The main purpose of conducting test on the T-joint pipe was to evaluate ice formation at the junction of the two pipes, shown in Figure (4-33).

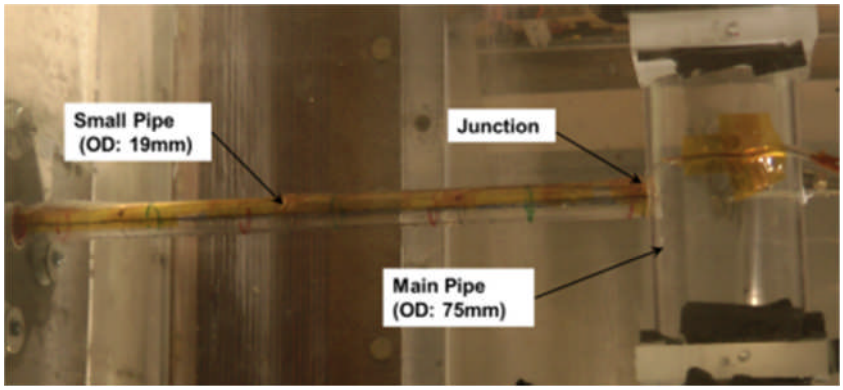

Figure 4-33 Top View of the T-Joint pipe

A total of 14 runs have been conducted on the T-Joint pipe. Four of the runs have been performed in natural external convection, four in forced external convection at tunnel velocity of 40m/s and the rest at the speed of 50m/s. The inlet mixture mass flow rate varies from 0.6 kg/hr to 1.59 kg/hr with an inlet vapour mass fractions of 0.05 to 0.26. The operating pressure was at atmospheric pressure. Test matrix has been shown in Table (4-12).

Table 4-12 T-Joint Pipe Test Matrix

Pipe Type	Case	Tunnel Speed (m/s)	Tg,in (°C)	Boiler Power (W)	Ma (kg/hr)	Mv (g/min)	Mg (kg/hr)	Wv
T-Pipe	Run 1	40	86.1	322	0.9	5.55	1.26	0.26
T-Pipe	Run 2	40	62.0	115	1.0	2.13	1.39	0.11
T-Pipe	Run 3	40	62.2	161	1.0	2.74	1.20	0.14
T-Pipe	Run 4	50	62.0	161	1.0	2.74	1.20	0.14
T-Pipe	Run 5	50	62.1	161	0.8	2.29	0.98	0.14
T-Pipe	Run 6	40	62.4	161	1.2	2.77	1.20	0.14
T-Pipe	Run 7	0	63	165	1.0	2.8	1.22	0.14
T-Pipe	Run 8	0	63	165	1.0	2.8	1.21	0.14
T-Pipe	Run 9	0	62.4	167	1.38	3.46	1.59	0.13
T-Pipe	Run 10	0	48.0	97	1.0	1.5	1.1	0.1
T-Pipe	Run 11	50	52.0	97	1.0	1.6	1.1	0.1
T-Pipe	Run 12	50	61.0	99	0.5	1.4	0.6	0.13
T-Pipe	Run 13	50	44.5	99	1.4	1.2	1.4	0.05
T-Pipe	Run 14	50	43.2	62	0.5	0.6	0.6	0.06

4.3.1 Observing Condensation and Ice Formation physics

Phases of condensation in the T-joint pipe are similar to the horizontal pipe. The difference in the horizontal pipe, however is that the gas mixture is expelled to the atmosphere at the outlet of the pipe. Whereas, in the T-joint pipe the mixture gas is sucked in to the tunnel due to the pressure difference caused by the tunnel air velocity, Figure (4-34).

This pressure difference induces the condensate pool to flow out the small pipe and freeze at the junction of the two pipes.

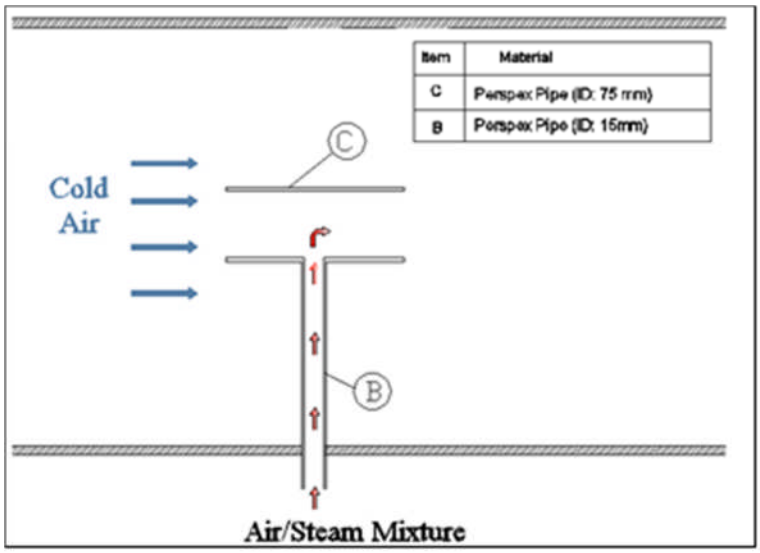

Figure 4-34 schematic of flow direction in T-joint pipe test, (Top view)

In Figure (4-35) four different pictures are shown which have been taken at different times during the Run 7. These pictures were taken from the bottom of the pipe and present the progress of condensation in the T-joint pipe. As illustrated, the flow out phase happened at 6 minutes, Figure (4-35d).

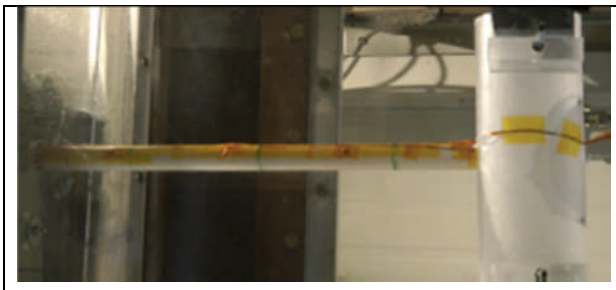

a) at 2 minutes

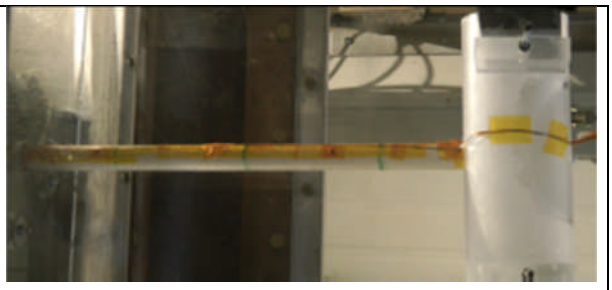

b) after 3 minutes

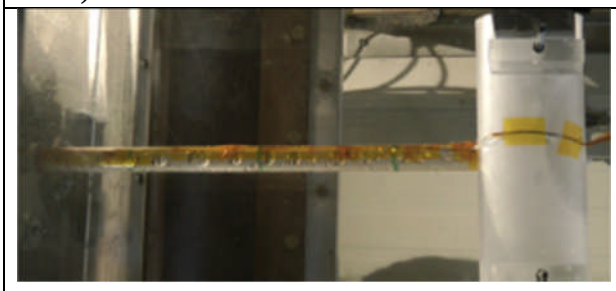

c) at 5 minutes

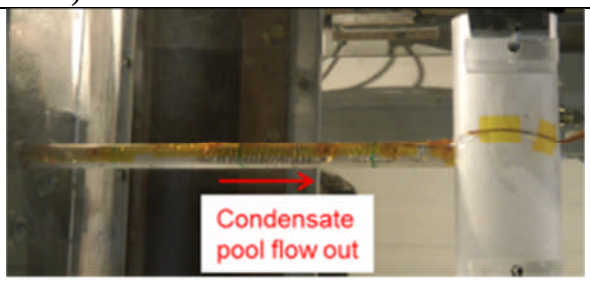

d) at 6 minutes

Figure 4-35 Sequences of condensation at different times in a T-Joint Pipe on Run 7

4.3.2 Condensation Rate

Condensation rate has been studied by examining video recording of Run 5,12 and 13 by for 10 minutes and measuring the time and position of droplets departures.

The time of departure is the time when the droplet reaches the bottom of the pipe, region C, shown in Figure (4-36).

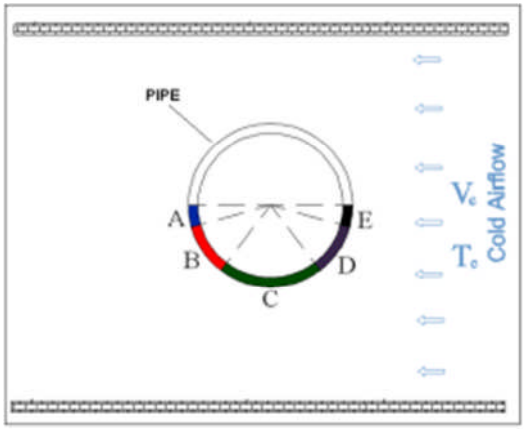

Figure 4-36 Side view of the pipe in the test section

The departure time versus the departure position is illustrated in Figure (4-37). This figure shows that condensation rate in Run 5 with vapour mass flow rate of $\dot{m}_v$ =1.9 g/min is greater than Run 12 with $\dot{m}_v = 1.4\ g/min$, and Run 13 with $\dot{m}_v = 1.2 g/min$.

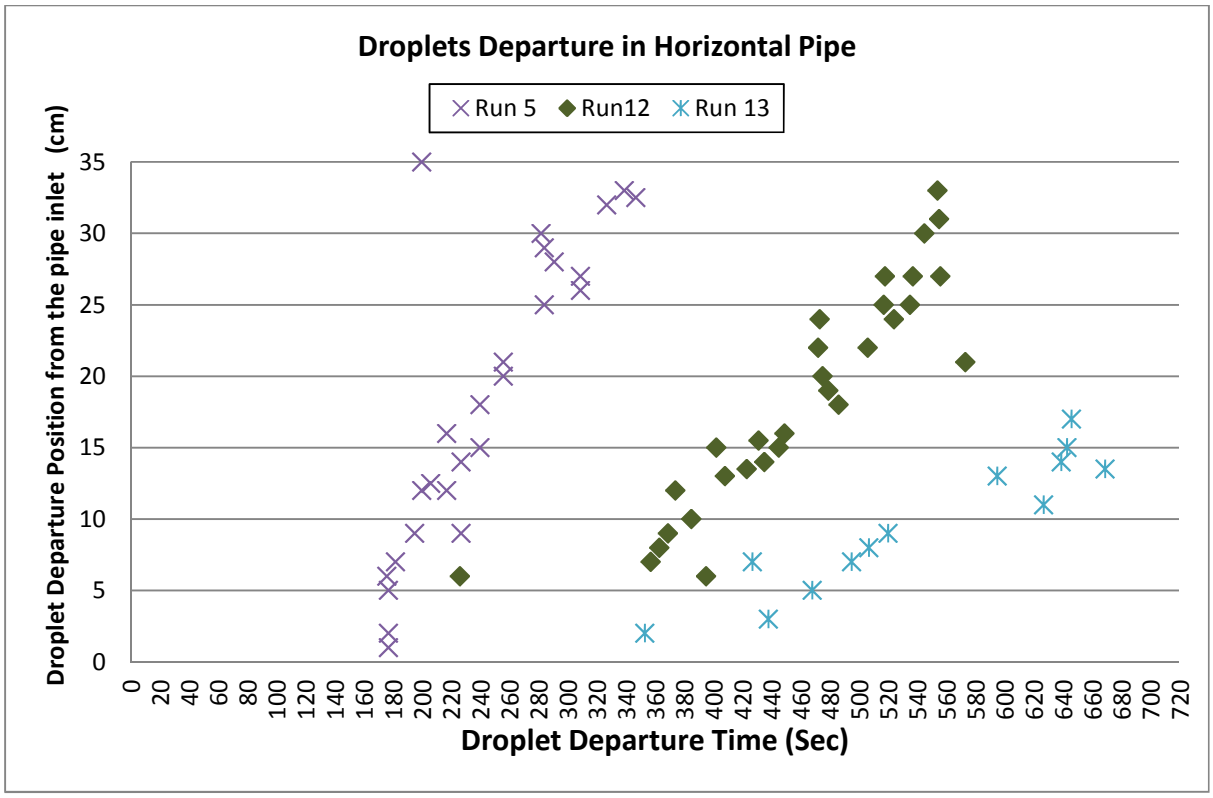

Figure 4-37 Time of droplet departure in T-Joint Pipe

The temperature of the T-joint pipe has been measured at 5 points (T_1 to T_5) and mixture gas core temperature at 3 points ($T_{C,1}$ to $T_{C,3}$), explained in section (3.6).

Figure (4-38) shows the variation of all these temperatures during Run 1 for 35 minutes. The temperature variation indicates that mostly all the temperature become steady after 11 minutes.

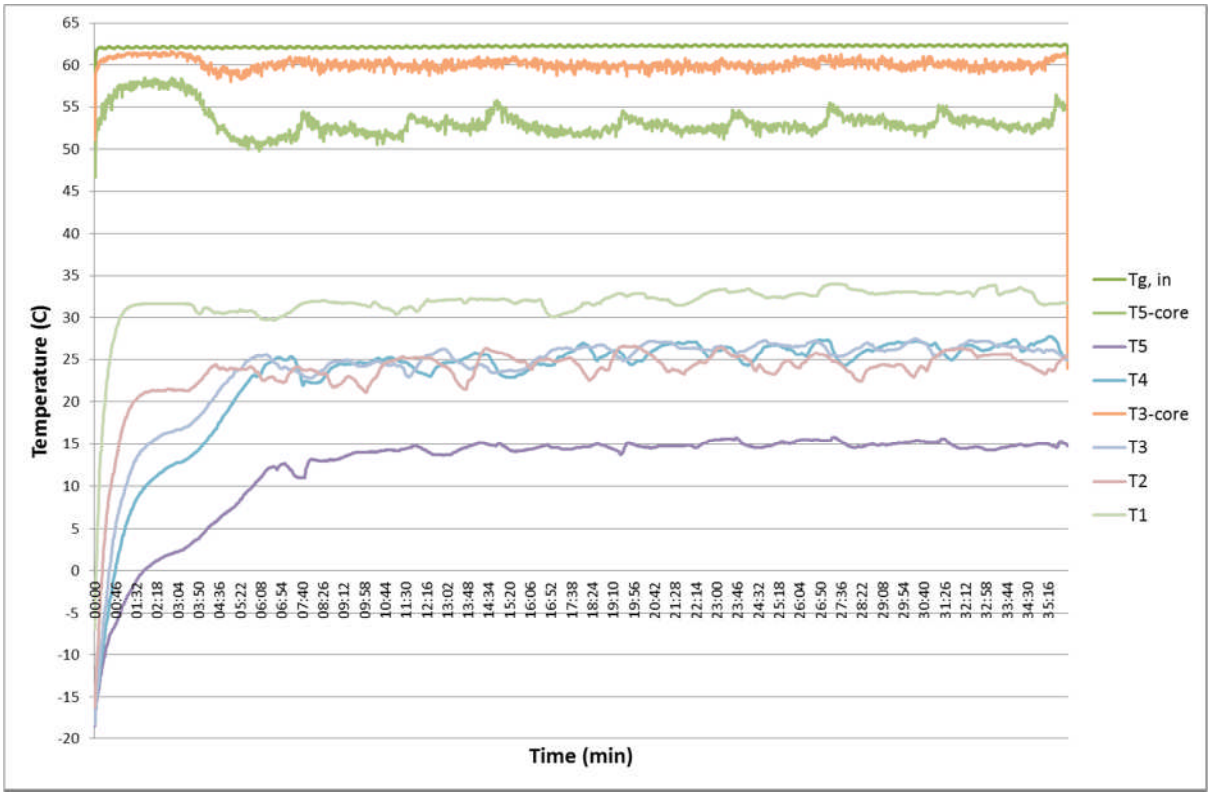

Figure 4-38 Temperature Variation in Run 1

4.3.3 Ice formation at the junction

Ice formation in Run 14 is studied in this section. In this run, gas mixture with mass flow rate of $\dot{m}_g = 0.6\ g/min$ and vapour mass fraction of 0.07 at temperature of 43°C enters the pipe. The icing tunnel is run at -20C and 50m/s. The test has been performed for 40 minutes. Figure (4-39) presents six pictures taken at the end of the test and shows the ice formation at the junction of the pipes, Figures (4-39a,b and c). It also shows that the air/steam mixture turns to ice when it reaches the main pipe, Figure (4-39d,e and f).

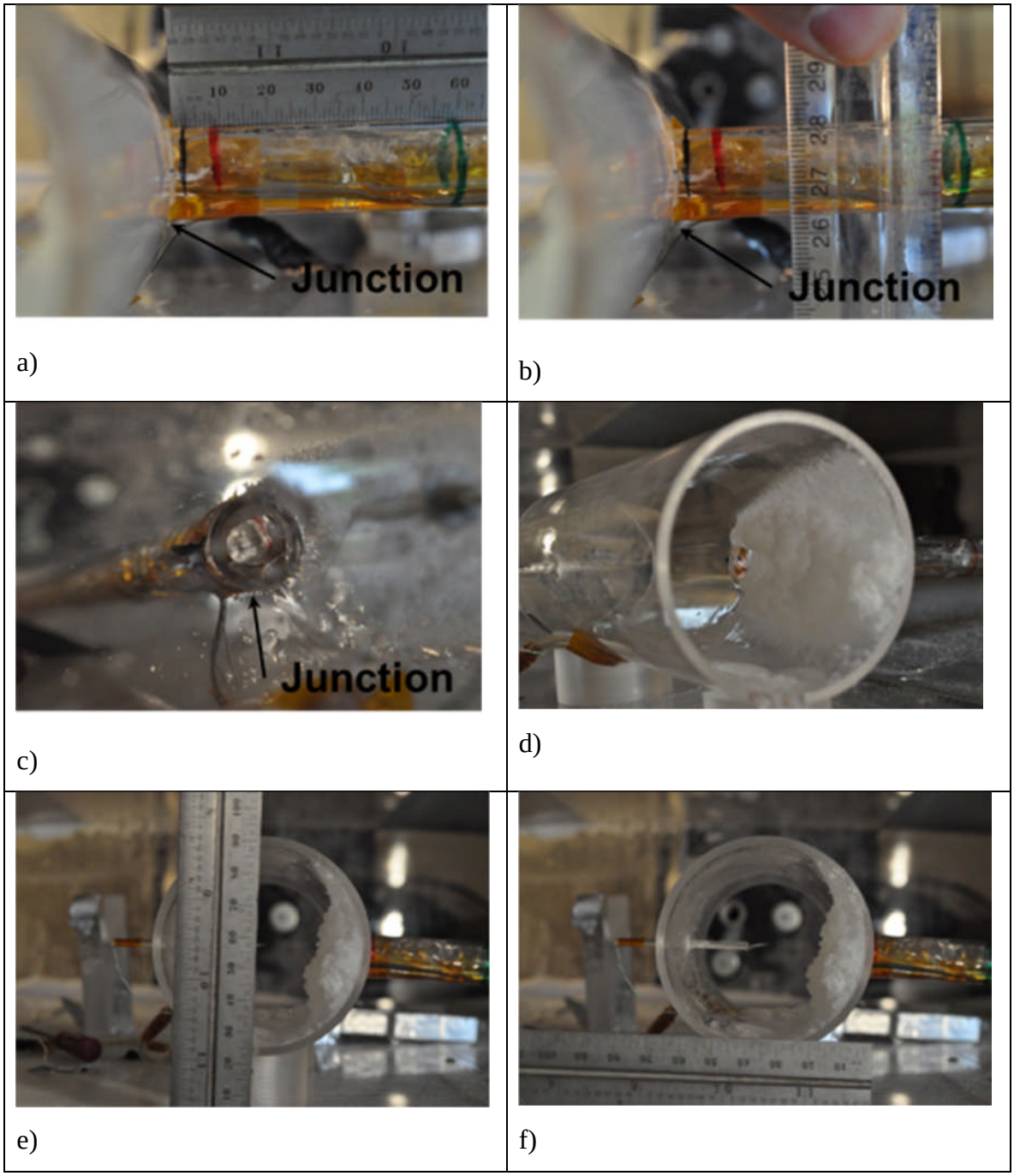

a) b) c) d) e) f)

Figure 4-39 Ice formation in T-Joint Pipe

As explained earlier, in the flow out phase condensate pool flows toward the junction of the pipes. When this water reaches the junction, it turns to ice because of the freezing temperature at this region.

Figure (4-40), indicates the junction of the pipes when the condensate pool is passing by. This figure presents 4 pictures which have been taken in every 15 seconds after 30minute of the Run 14. The eye line view of these pictures are shown in Figure (4-40 a). It is clear from the pictures that some of the condensate water has been turned into ice while it was passing the junction and entering the main pipe.

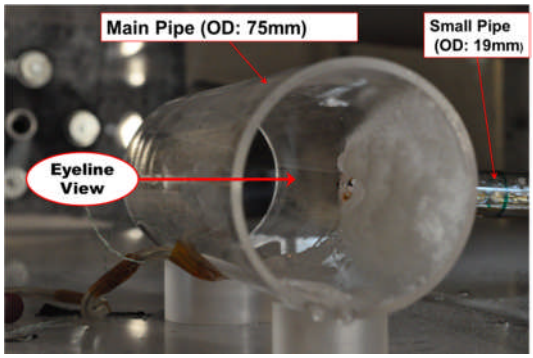

a) Eyline view of the pictures

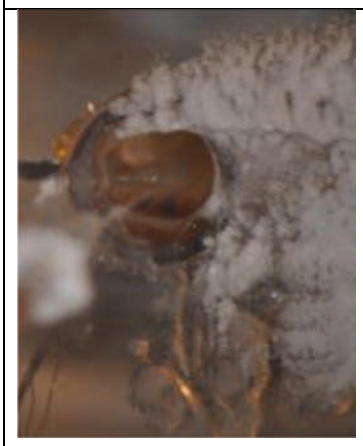

b) 0 sec

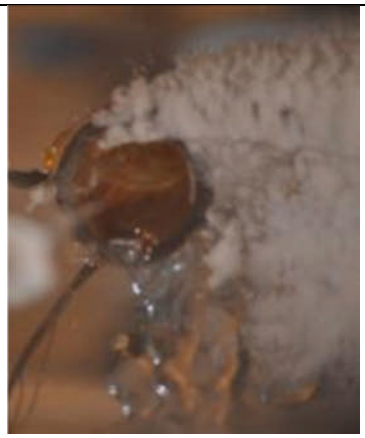

c) After 15 sec

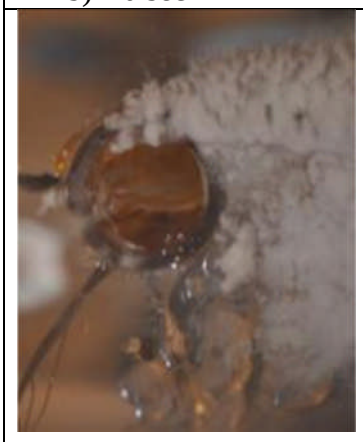

d) After 30 sec

e) After 45sec

Figure 4-40 Condensate pool flow out at the junction of T-Joint pipe, pictures show the junction of the pipes in every 15 seconds after 30 minute (Run 14)

In Figure (4-41), ice formation at the junction of the pipes at two different moment in time (at 30 minutes and 41 minutes) have been compared.

a) After 30 min

b) After 41 min

Figure 4-41 Ice formation at the junction of two pipes in Run 14 at two different time of 30min and 41 minutes

The icing area at the junction has been identified in Figure (4-42). It shows that at 30 minutes the icing area was about 74 mm^2 which had occupied 42% of the total area of the pipe. This has increased to 56% (99 mm^2) after 41 minutes. Comparing the icing blockage areas indicates that ice has been formed at the rate of 2.4 mm^2 per minute which eventually would have blocked the pipe after 73 minutes if it had progressed in the same rate.

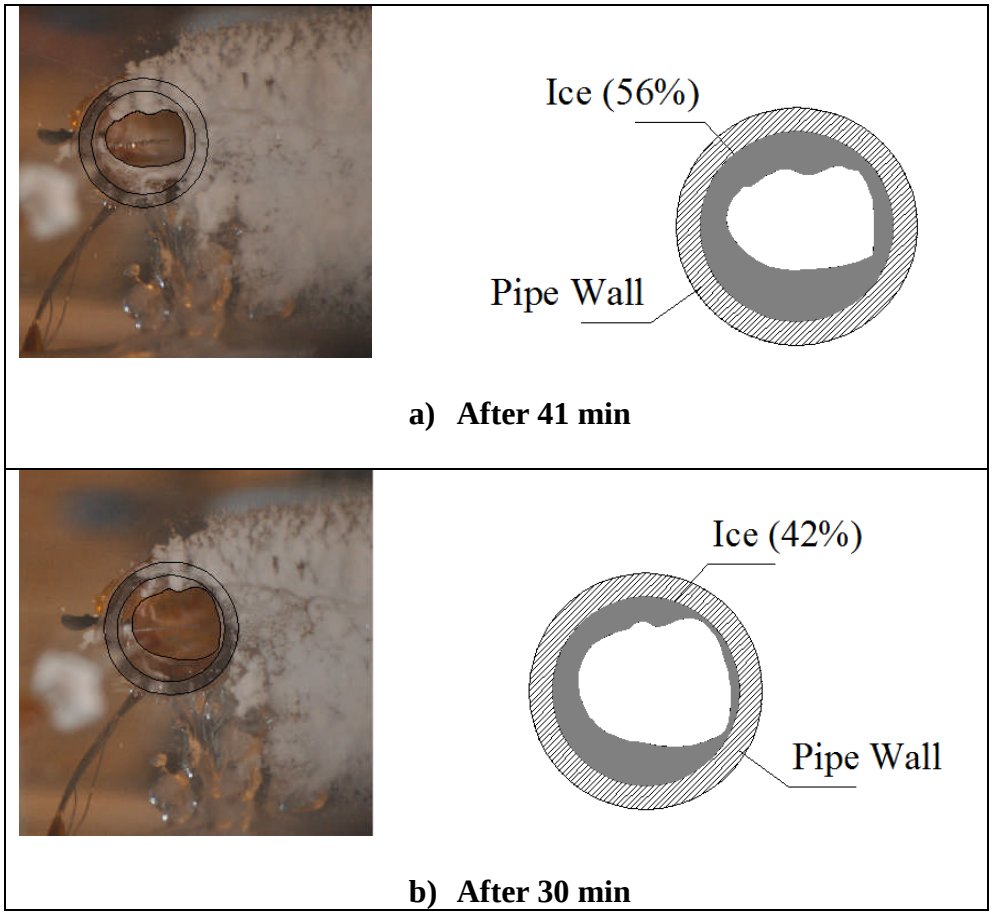

Figure 4-42 Identify Ice region at the junction of two pipes in Run 14 at two different time of 30min and 41 mins

4.3.4 Effect of gas mass flow rate on ice formation

To investigate the influence of the gas mass flow rate on ice formation at the junction, the results of Run13 are compared with Run14. The gas inlet temperatures in both of the runs are nearly 44 °C, but the gas mass flow rate in the Run13 is more than of the Run14. In Table (4-13) the characteristics of the two runs have been presented.

Table 4-13 Flow conditions for Run13 and Run14

Pipe Type	Case	Tunnel Speed (m/s)	Tg,in (°C)	Boiler Power (W)	Ma (kg/hr)	Mv (g/min)	Mg (kg/hr)	Wv
T-Pipe	Run 13	50	44.5	99	1.4	1.2	1.4	0.05
T-Pipe	Run 14	50	43.2	62	0.5	0.6	0.6	0.06

Figure (4-43) shows the junction of the pipes at the end of the tests.

Comparing the pictures of the two runs shows that contrary to Run 14 in Run 13, condensate pool doesn't freezes when it flows out the junction.

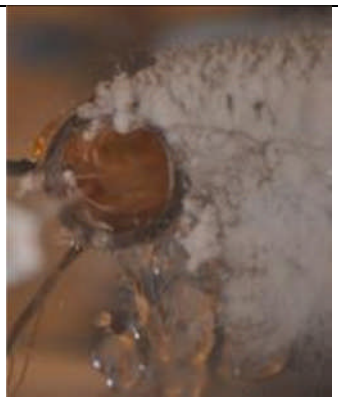

a) Run 14 after 26 min

b) Run 13 after 26 min

Figure 4-43 Ice formation at the junction of T- pipe after 26mins in Run 13 and Run 14

Temperature results of the runs (Figures 4-44 and 4-45) indicates that increasing the mass flow rate from 0.6 (kg/hr) to 1.4 (kg/hr), at nearly a same vapour mass fraction, increases the local temperatures and prevent the condensate pool from freezing at the junction.

Even though the observation may not be fully representative of ice formation in an actual breather pipe, but investigating the ice formation at the junction of the pipes has provided Jaguar engineers information about the effects of condensate film movement and ice growth at the junction of the pipes.

The local gas core temperature and pipe wall temperature distributions of Run 13 and 14 are compared in Figure (4-44) and Figure (4-45), respectively. The results show that the pipe wall temperature in Run 13 is above freezing temperature (0°C) for the whole length of the pipe. In other word, increasing gas mass flow rate can reduce the risk of ice blockage at the junction of the pipes.

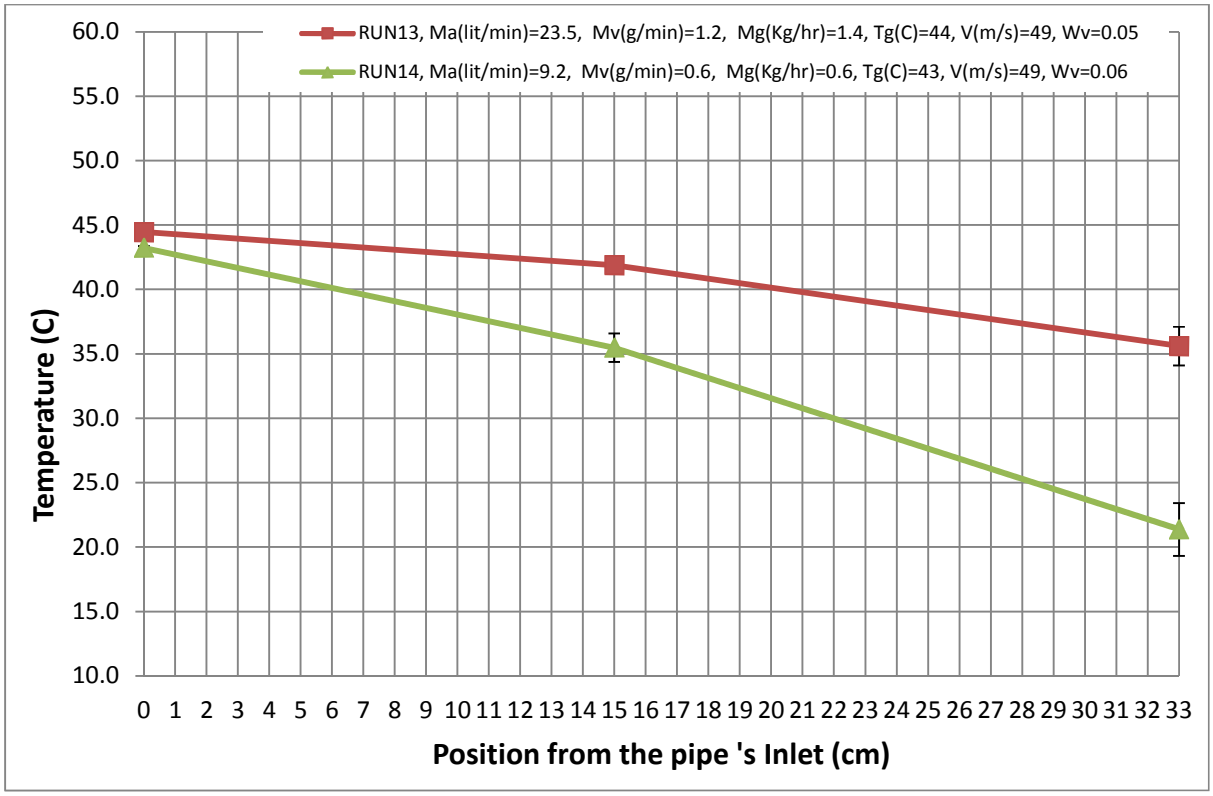

Figure 4-44 Gas Core temperature for Run 13 and Run 14

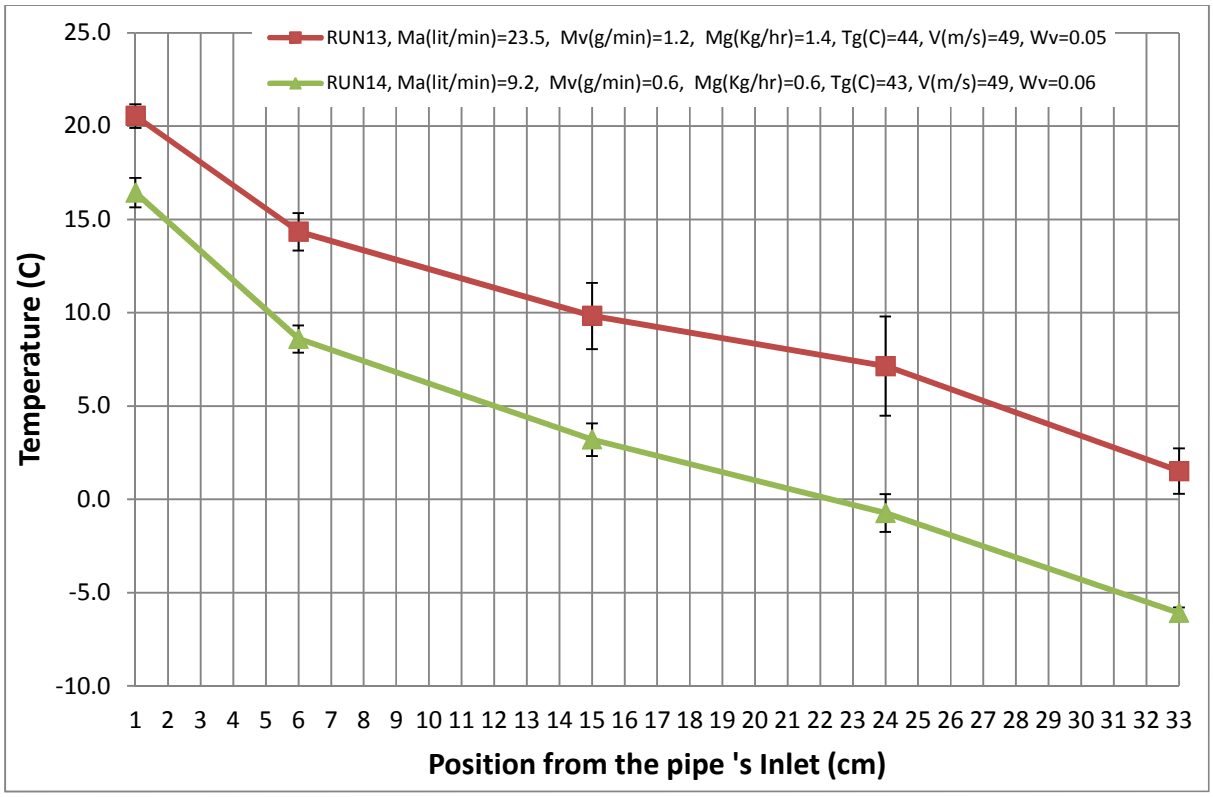

Figure 4-45 Pipe wall temperature for Run 13 & Run 14

4.3.5 Vapour Mass Fraction

Figure (4-46) compares the mixture core temperatures distribution between Run 2 and Run 3. The test conditions for Run2 and Run3 are similar, except the inlet vapour mass flow rate which is15% more in Run3 (2.2 g/min) than Run2 (1.9g/min), as presented in Table (4-14).

Figure (4-46) shows that the inlet gas mixture enters the pipe at 62 °C, in both of the cases, but the core temperature distribution in Run 3 is higher than Run 2 due to greater condensation and higher release of latent heat.

Table 4-14 Run2 and Run3 test conditions

Case	Tunnel Speed (m/s)	Tg,in (°C)	Boiler Power (W)	Ma (kg/hr)	Mv (g/min)	Mg (kg/hr)	Wv
Run 2	50	62	115	1.04	1.9	1.2	0.11
Run 3	50	62	161	1.04	2.2	1.17	0.14

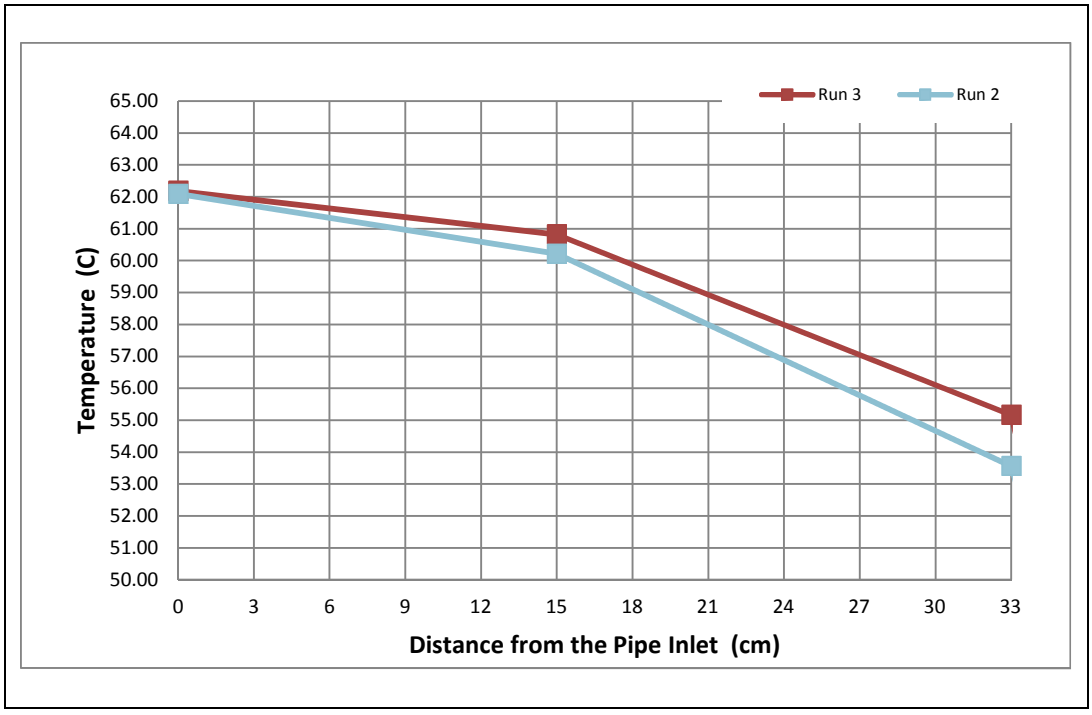

Figure 4-46 Gas core temperature for Run2 and Run3

4.3.6 Effects of external convective cooling (tunnel velocity)

Three runs have been performed at different external air velocities of 0m/s (natural convection), 40m/s and 50 m/s. In Figure (4-47) gas core temperature variations of these runs have been presented. As expected, increasing the external convective cooling increased the heat transfer along the pipe and decreased the local core temperature.

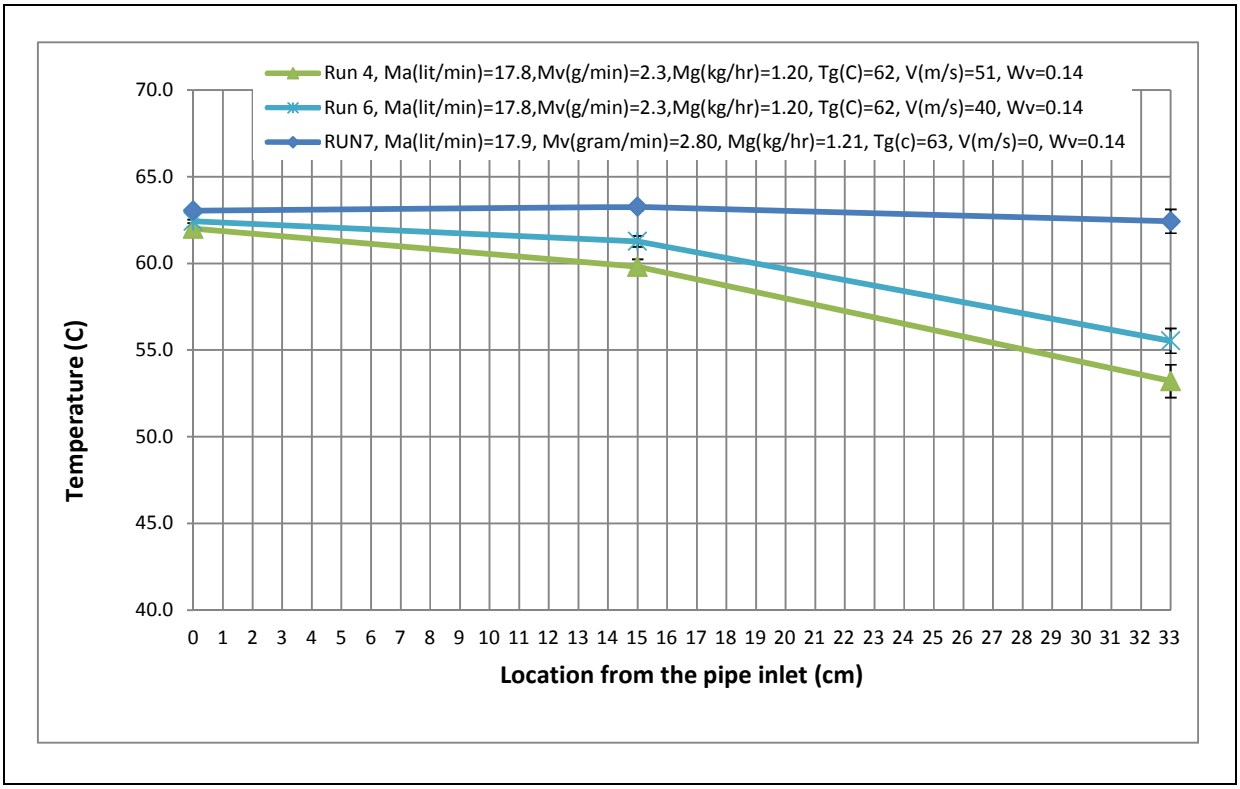

Figure 4-47 Gas core temperature for Run 4, Run6 and Run7

4.4 Conclusion

The observations showed that the process of condensation in the vertical pipe is divided in to three phases such as, “primary droplets”, “droplets coalescences” and “sweeping”. In the horizontal and the T-joint pipe this process is divided in to four phases as “primary droplets”, “droplets coalescences”, “droplets slip down” and “condensate flow out”.

Droplet sweeping can affect the pipe temperature. It can be recognizable by sudden changes in the surface temperature graphs.

Measuring the pipe temperature helped to investigate the heat transfer along the pipe and evaluate the experimental heat transfer coefficient. The results of the experimental heat transfer coefficients showed that the maximum uncertainty occurred at the end of the pipe due to disturbance of the external flow at the walls and suction of outside air in to the tunnel.

The heat transfer from the gas mixture during condensation depends on two interdependent parameters: sensible heat and latent heat. Sensible heat transfer is due to the temperature difference between the gas mixture temperature and the wall. Latent heat transfer is due to vapour mass flow rate. Therefore, increasing the vapour mass flow rate and gas inlet temperature enhances the in-tube experimental heat transfer coefficient. Increasing vapour mass flow also increases the condensation rate in the pipe.

This study suggests that attaching thermocouples does not affect the heat transfer and condensation rate in the vertical pipe. However, hydrophobic coating reduces the droplet departure time.

Increasing the external cooling increased the heat transfer and condensation rate and decreased the local core temperatures.

Even though the observations and the experimental analysis on the vertical, the horizontal and the T-joint pipe may not be fully representative of testing the actual breather pipe, they have provides helpful information about the effects of most dominant parameters like vapour mass fraction, inlet gas temperature, pipe coating on condensation in the pipe and the effects of condensate film movement on ice growth at the junction of the T-joint pipe.

Chapter 5 One Dimensional Code

5-1 Introduction

In section (2.3) the theoretical model of reflux condensation of steam-air in a vertical pipe is explained. In the model, the steam air mixture flows upward in the pipe and the condensate film flows downward as an annular film. The heat and mass transfer equations for liquid and gas phase are balanced with gas mass fraction, temperature and shear stress at the liquid/gas interface. Liao and Vierow's (2007) diffusion model is used to calculate the condensation heat transfer coefficient. The liquid film heat transfer is evaluated by employing liquid film model derived from condensation of vapour co-current to the liquid film used by Chun et al (1971).

In most of the models developed thus far, the temperature of the pipe is known a-priori and external cooling is not taken in to consideration. The present model attempts to address the external cooling heat transfer and be dependent on geometry, external side of the pipe and inlet boundary conditions for the inlet gas mixture. The local pipe temperatures and heat transfer coefficients are unknown and are solved iteratively. These heat transfer coefficients are condensation heat transfer coefficient (h_{cd}), convective heat transfer coefficient (h_{cv}) and film heat transfer coefficient (h_f). The local temperatures are inner wall temperature ($T_{w,i}$) and gas/film interface temperature (T_i). A one dimensional computer code is developed in this study based on this model to predict the heat transfer coefficients and the local temperatures. The iterative solution of the code assumes $T_{w,i}$ and T_i in every iterations and corrects them by balancing mass and energy equations. The freezing heat flux is also applied when $T_{w,i}$ temperature is below 0°C. The solution method of the model is explained in this chapter and the results of gas core temperatures and wall temperatures are compared with experimental data which show satisfactory agreement.

To quantify the parametric effects of nondimensional parameters on the external heat transfer coefficient, a new correlation is developed by using a degradation factor (F) which is explained in this chapter.

Finally at the end of this chapter, the code is used to predict the freezing region in different external cooling condition and different pipe conductivity attributed to actual condition in the Jaguar icing test.

5.2 Solution procedure

The procedure outlined here explains the solution method of the code which calculates the interface temperature (T_i) and inner wall temperature (T_{wi}). This procedure marches from the bottom of the pipe (x=0) to the top of the pipe (x=L). At the pipe inlet, the gas temperature (T_b), vapour mass flow rate and mixture mass flow rate are provided as input data. The interval between the nodes along the tube, Δz is flexible and calculated considering the total energy balance equation (is explained further in this chapter).

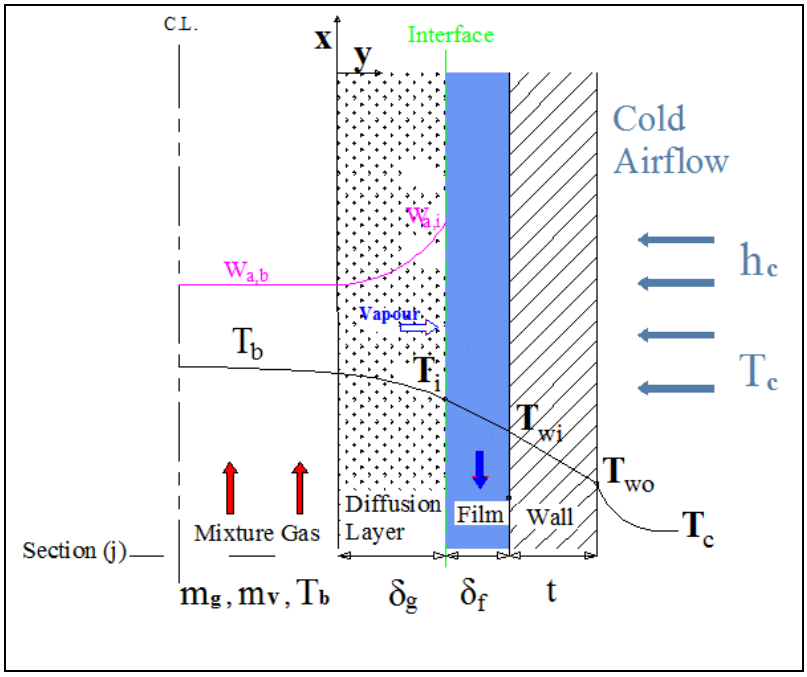

Figure 5-1 Physical model control volume

In the calculation procedure the known parameters are

- Geometric parameters: pipe inner diameter (D_i), pipe thickness (t) and pipe length (L)
- External air flow temperature (T_c) and heat transfer coefficient (h_c) is prescribed from the experimental data (Section 3-8)

- Pipe thermal conductivity, k_w

- Inlet mixture conditions
  - Steam-Air mixture mass flow rate, $\dot{m}_g$
  - Gas mixture temperature, $T_{b,in}$
  - Gas mixture pressure, $P_{b,in}$
  - Vapour mass flow rate, $\dot{m}_v$

The assumptions for this analysis are:

- The gas and condensate flow are laminar
- The motion of the liquid film is specified by neglecting the acceleration terms in the momentum equations.
- The curvature of the condensate film is neglected.
- The bulk gas temperature in radial direction is constant
- When the pipe inner wall temperature becomes zero all the condensate mass turns to ice
- Not all the vapour condenses in the pipe.

Since vapour may not necessarily condense completely inside the pipe, the vapour mass flow rate at the pipe outlet needs to be known a priori. Here, it is assumed that vapour leaves the pipe in saturated condition, the condensation is prohibited at the top of the tube, and the vapour bulk temperature is equal to the tube wall temperature. Hence, the vapour mole fraction at the pipe outlet (x_v) can be calculated as $x_v = P_v\{T_{wi}\}/P$. P_v is the saturated vapour pressure at the pipe wall temperature (T_{wi}) which is known from the test data. Therefore, the vapour mass flow rate at the pipe outlet can be calculated by

$$\dot{m}_{v,out} = \frac{x_v M_v}{(1-x_v)M_g}\dot{m}_g \qquad (5.1)$$

The molecular weight of vapour is $M_v = 0.01802$ (kg/mol) and molecular weight of gas mixture (M_g) is calculated from Eq. (2.58).

The calculation procedure starts at the tube inlet (section j), marked on Figure (5-1). The air and steam mass fraction at the pipe inlet are calculated from Eq. (2-56).

The following procedure is used to calculate the condensation one step upstream the pipe inlet ($z_{j+1} = z_j + \Delta z$).

1- Calculate the core gas temperature, $T_{b,}$ as follows:

$$T_b^{(j+1)} = T_b^{(j)} - \Delta T_b \qquad (5.2)$$

The value of ΔT_b is specified to be (0.05°C) for the first 0.4m of the pipe, because of the rapidly changing the heat transfer coefficient. Thereafter it is kept to be 0.1°C.

2- Determine the air and vapour physical and transport properties at the bulk temperature (T_b) ($\mu_{a,b}$, $k_{a,b}$, $Pr_{a,b}$, $Cp_{a,b}$, $\mu_{v,b}$, $k_{v,b}$, $Pr_{v,b}$, $Cp_{v,b}$, h_{fg} , $\rho_{v,b}$, Re_g, ,$Cp_{v,b}$)

3- Calculate the mixture gas physical properties (M_g , μ_g , k_g) at the bulk temperature (T_b) according to Eqs. (2.58) to (2.60).

4- Calculate the mixture gas Reynolds number (Re_g) as

$$\mathrm{Re}_g = \frac{4\dot{m}_g}{\pi D_i \mu_g} \qquad (5.3)$$

5- Calculate the friction factor as well as the interface shear stress according to the following Eq. (5.4).

$$\tau_I = \frac{1}{2} f_0 \rho_g u_g^2 \quad , \quad f_0 = \frac{0.079}{\mathrm{Re}_g^{1/4}} \qquad (5.4)$$

6- Calculate longitudinal pressure difference, $(\frac{dp}{dx})$

Pressure difference needs to be calculated using gas velocity (u_g) from Eq. (2.12).

7- Guess the inner wall temperature, ($T_{w,i}$)

8- Guess the interface temperature, (T_i)

9- Evaluate the vapour partial pressure ($P_{v,i}$) at the interface temperature, (T_i)

As the condensation occurs at the interface, the vapour partial pressure at the interface can be predicted by defining the saturation pressure at the corresponding temperature (T_i) ($P_{v,i} = P_{sat}\{T_i\}$) from the steam Tables.

10- Define the air mass fraction at the interface given in Eq. (2.56)

11- Calculate the film temperature and the physical properties of liquid water at corresponded temperature (T_f) from Eq (2.49) and determine the condensate film properties (μ_f , k_f , v_f) at this temperature.

12- Calculate the non-dimensional parameters G, L, τ_I^*, according to the Eq. (2.14), Eq. (2.17) and (2.18), respectively.

13- Calculate the nondimensional film thickness (δ^*) and condensate film Reynolds Number (Re_f) according to the Eq. (2.19) and Eq. (2.20), respectively.

14- Calculate the film heat transfer coefficient (h_f) from Eq. (2.23), when the film is laminar and from Eq. (2.24) if the Re_f is greater than 4.

15- Calculate the condensation heat transfer coefficient (h_{cd}) based on equations presented in Section (2.3.4.3)

16- Update the local condensation mass flux as follows which is used to evaluate the flow condition for the next node.

$$\dot{m}_c = \frac{h_{cd}(T_b - T_i)}{h_{fg}} \tag{5.5}$$

17- Calculate convective heat transfer coefficient (h_{cv}) based on equations presented in Section (2.3.4.4)

18- Check the interface temperature using the energy balance at the interface

The initial value of (T_i) can be compared by heat balance at the interface by rearranging equation (2.68) as follows.

$$T_i = \frac{T_{wi}h_f + T_b(h_{cv} + h_{cd})}{h_f + h_{cv} + h_{cd}} \tag{5.6}$$

19- Calculate the outer wall temperature (T_{wo}). This may be calculated by rearranging Eq. (2.67) as follows.

$$T_{wo} = T_{wi} - \left[h_f (T_i - T_{wi}) \frac{d_i \ln(d_o / d_i)/2}{k_W} \right] \tag{5.7}$$

20- Update the inner wall temperature (T_{wi}) by rearranging equation (2.68) as follows.

$$T_{wi} = T_{wo} + \left[h_{cv} (T_{wo} - T_c) \frac{d_o \ln(d_o / d_i)/2}{k_W} \right] \tag{5.8}$$

The Δl can be calculated from the total heat transfer equation from j to j+1 as following.

$$\frac{\pi d \Delta l}{2}\left[(q_w''^{(j)} + q_w''^{(j+1)}\right] = \dot{m}_{cond} h_{fg} + \dot{m}_v Cp_v(\Delta T_b) + \dot{m}_{nc} Cp_{nc}(\Delta T_b) + \dot{m}_a Cp_a(\Delta T_b) \quad (5.9)$$

When the T_{wi} becomes 0C, the freezing heat flux is calculated by multiplying the enthalpy of fusion by condensate mass. This then applied in to right side of the above equation as given:

$$\frac{\pi d \Delta l}{2}\left[(q_w''^{(j)} + q_w''^{(j+1)}\right] = \dot{m}_{cond} h_{fg} + \dot{m}_v Cp_v(\Delta T_b) + \dot{m}_{nc} Cp_{nc}(\Delta T_b) + \dot{m}_a Cp_a(\Delta T_b) + \dot{m}_{cond} h_{fusion} \quad (5.10)$$

The whole iteration is repeated for new axial location ($z_{j+1} = z_j + \Delta z$) until the top of the pipe is reached.

Based on the above procedure the algorithm used in the code is presented in Figure (5-1). The code is written by using Matlab Script File and it is fully presented in Appendix C.

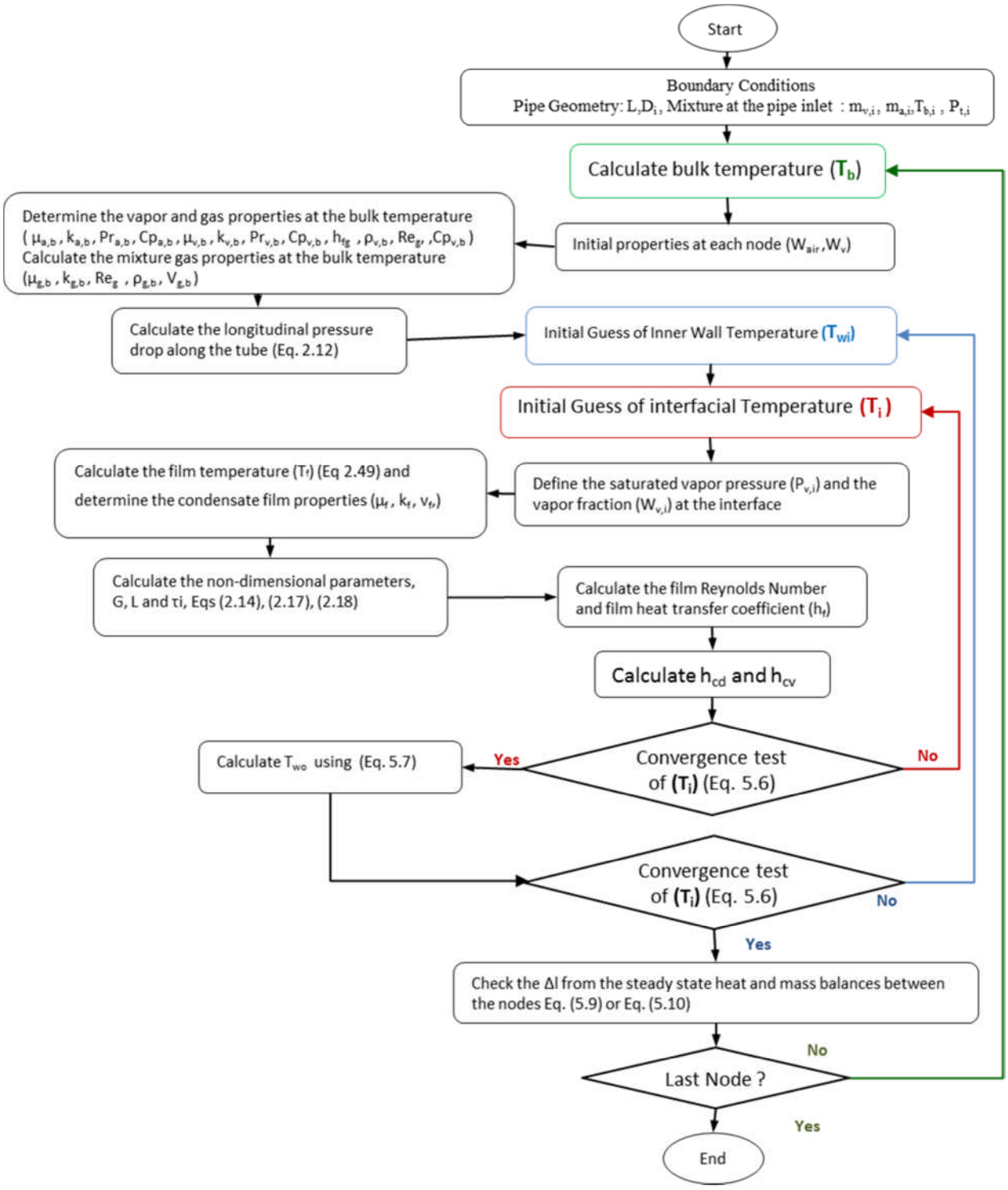

Figure 5-2 Calculation procedure of two iterative simulation of vertical in-tube condensation of steam

5.3 Results

For assessment of the developed model, the experimental results of the vertical pipe (presented in the section 5-1) are employed here. The test conditions are presented in Table (5-1). The pipe properties are also presented in Table (5-2).

Table 5-1 Vertical pipe test Boundary Condition

Pipe Type	Run Number	Tunnel Speed (m/s)	$T_{g,in}$ (°C)	Ma (kg/hr)	Mv (g/min)	Mg (kg/hr)	W_v
Vertical	**Run 22**	50	49.9	1.43	0.38	1.45	0.02
Vertical	**Run 23**	50	49.2	1.39	2.02	1.51	0.08
Vertical	**Run 24**	50	53.4	0.81	1.5	0.90	0.10
Vertical	**Run 25**	50	60.2	0.82	2.22	0.95	0.14
Vertical	**Run 26**	40	54.0	0.62	1.15	0.70	0.10

Table 5-2 Material properties of the pipe

Parameter	Value
Pipe Inner Diameter	15 mm
Pipe Length	750 mm
Pipe thickness	2 mm
Pipe Density (Plexiglass)	1190 kg/m^3
Pipe Specific Heat (Plexiglass)	1450 J/Kg-K
Pipe Thermal Conductivity (Plexiglass)	0.18 W/m-K

In chapter 4, it was shown that increasing the vapour mass flow rate from 0.38(g/min) in Run22 to 2.02 (g/min) in Run23 increases the local heat transfer coefficient. The inlet air mass flow rate for Run 22 and Run 23 are nearly the same.

In Figure (5-3), the variation of air mass fraction (W_{air}), derived numerically, and experimental heat transfer coefficient for Run 22 and Run 23 along the pipe are compared. This figure shows that the air mass fraction increases along the pipe, due to condensation, while the experimental heat transfer coefficient decreases. The gradient of air mass fraction in Run 23 is more than Run 22 which shows more condensation rate occurs in Run 23, their inlet dry air mass flow rates are nearly similar.

Condensation mass flux in Run 22 and Run 23 are compared in Figure (5-4). This figure shows that the condensation in Run 23 is more than Run 22 and in both cases the condensation rate decreases along the pipe.

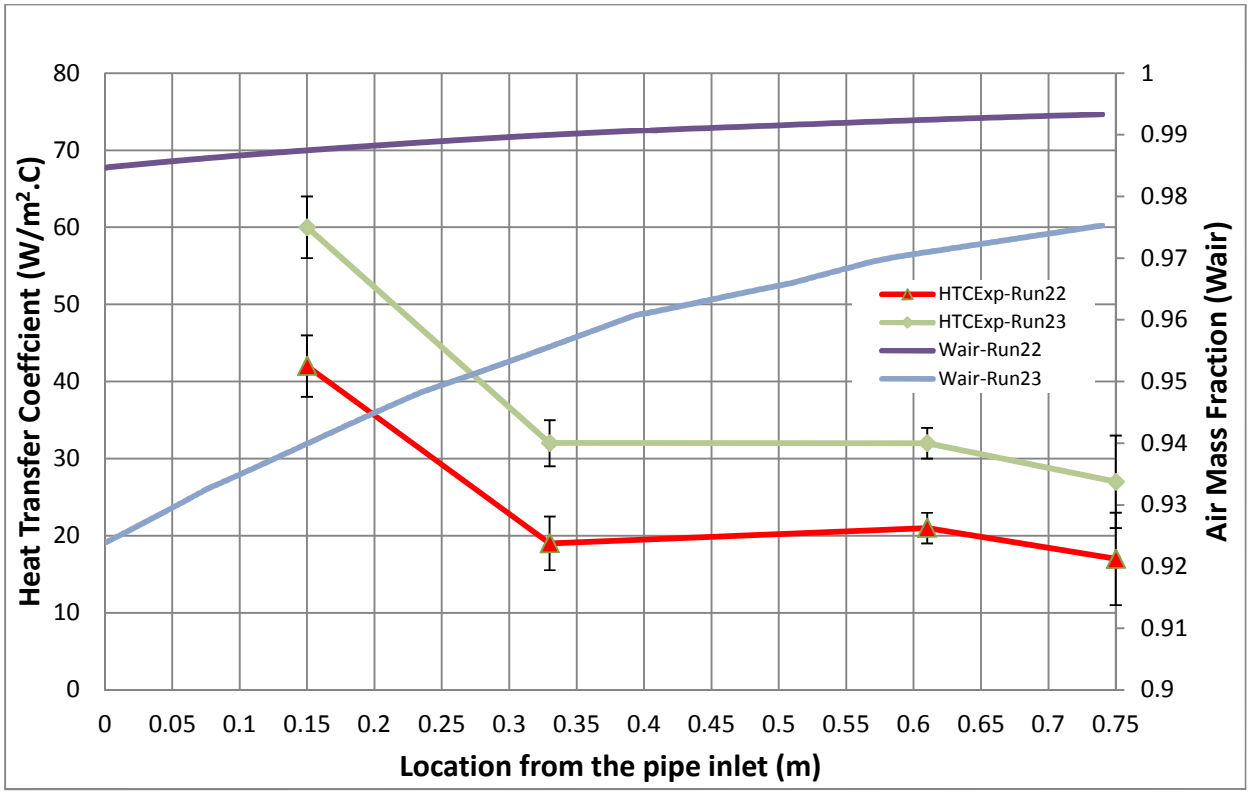

Figure 5-3 Air Mass Fraction along the pipe for Run 25, Run 24 and Run 22

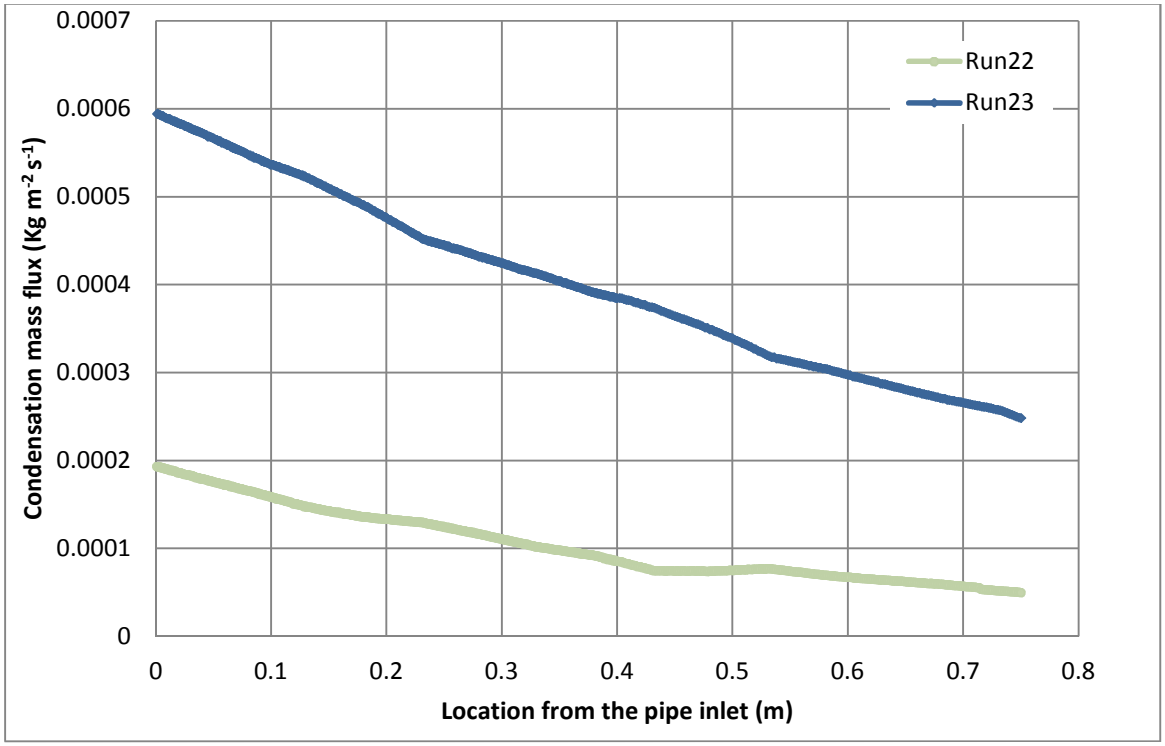

Figure 5-4 Condensation mass flux along the pipe for Run 22 and Run 23

The comparisons of the theoretical local temperatures for 3 different test cases are shown in Figures (5-5) to (5-7). The experimental temperature shown is the averaged value over 12 minutes of the test and the local standard deviations are shown as an error bar in these Figures. As shown, both the magnitude and trend of the local temperatures predicted by the code are in good agreement with the test results.

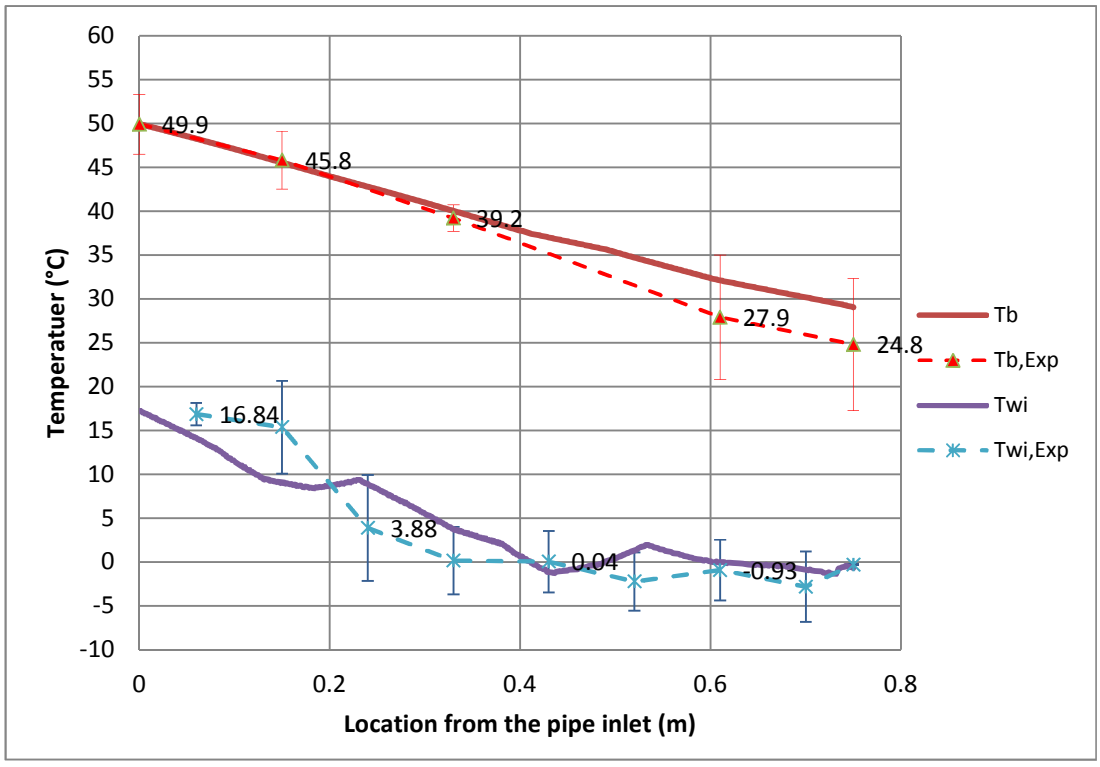

Figure 5-5 Comparison between theoretical and experimental local Temperatures at HTC Gas core temperature for Run 22

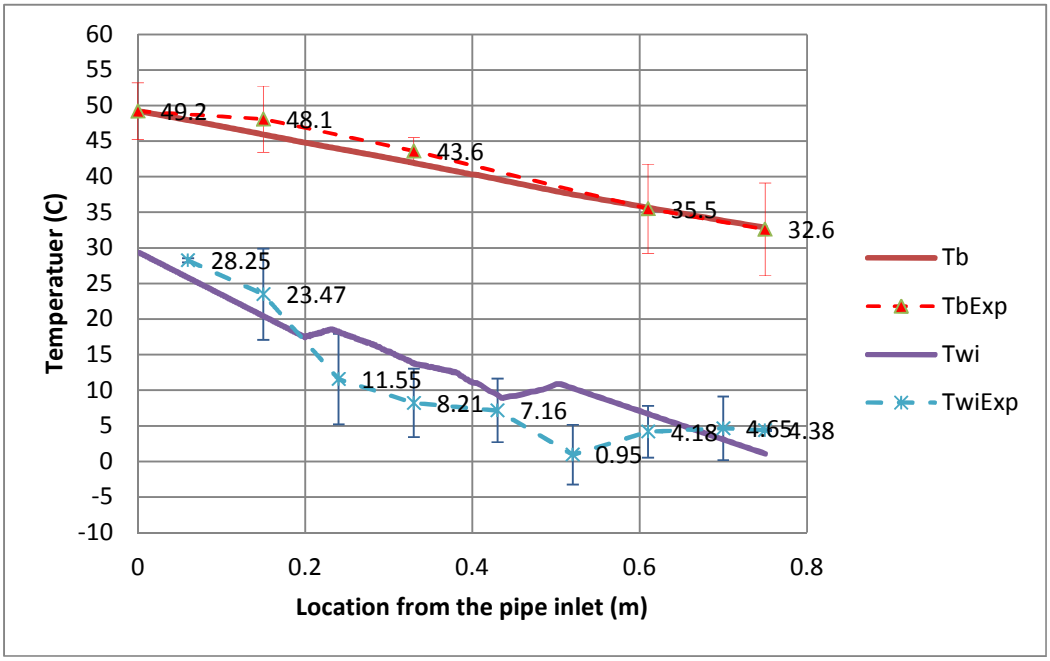

Figure 5-6 Comparison between theoretical and experimental local Temperatures at HTC Gas core temperature for Run 23

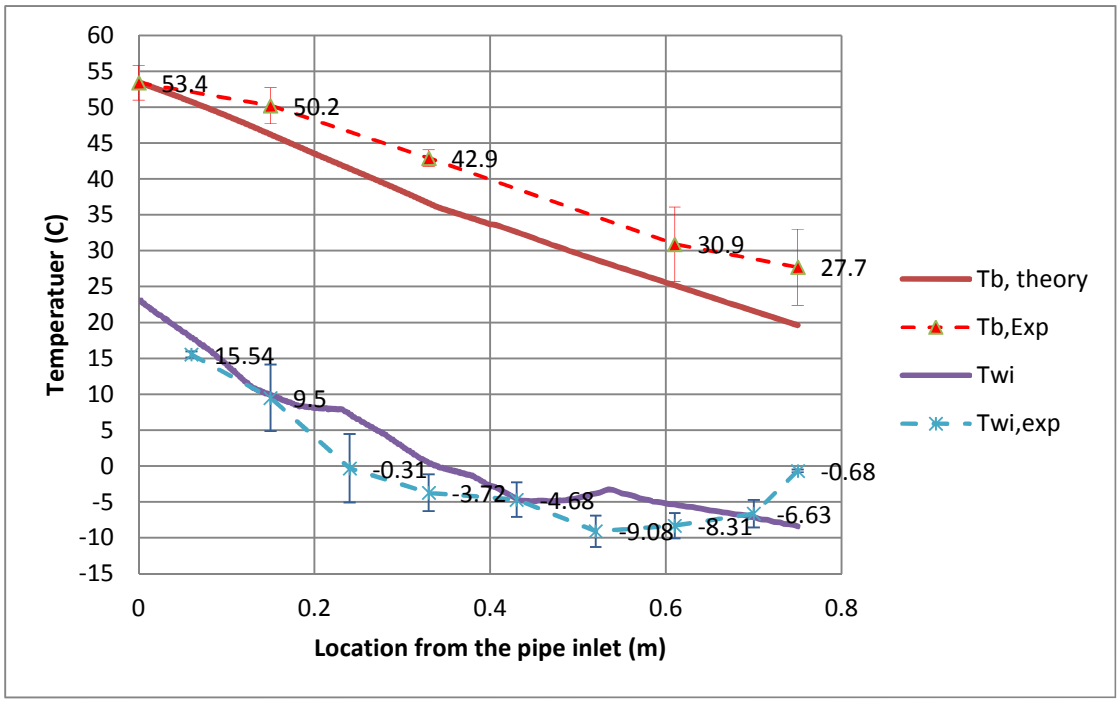

Figure 5-7 Comparison between theoretical and experimental local Temperatures at HTC Gas core temperature for Run 24

To investigate the error in values, root mean square (RMS) error used to evaluate the differences between temperatures predicted by the model and the experimental values. The RMS error is given as:

$$RMS\ Error = \sqrt{\frac{\sum_{i=1}^{N}\left(T_{local,theoritical} - \overline{T}_{local,\exp}\right)^2}{N}} \qquad (5.11)$$

$\overline{T}_{local,\exp}$ is the mean value of the local experimental temperature.

The RMS error of local temperatures is 3.91°C, however considering the standard deviation of the measurement with RMS of 4.31°C, may show that the predictions are in good agreement with the experimental data.

Figure (5-8), shows the comparisons of the predicted values of heat transfer coefficient (HTC) with the measured HTC. This figure shows that most of the data agree with experimental value within $\pm 25\%$ uncertainty. This uncertainty is increased when the heat transfer coefficient is below 30. This is due to the experimental measurement error which increases to 17% at the end of the pipe due to suction of air flow from outside of the Icing Tunnel. (See section 4.1.4 for more details).

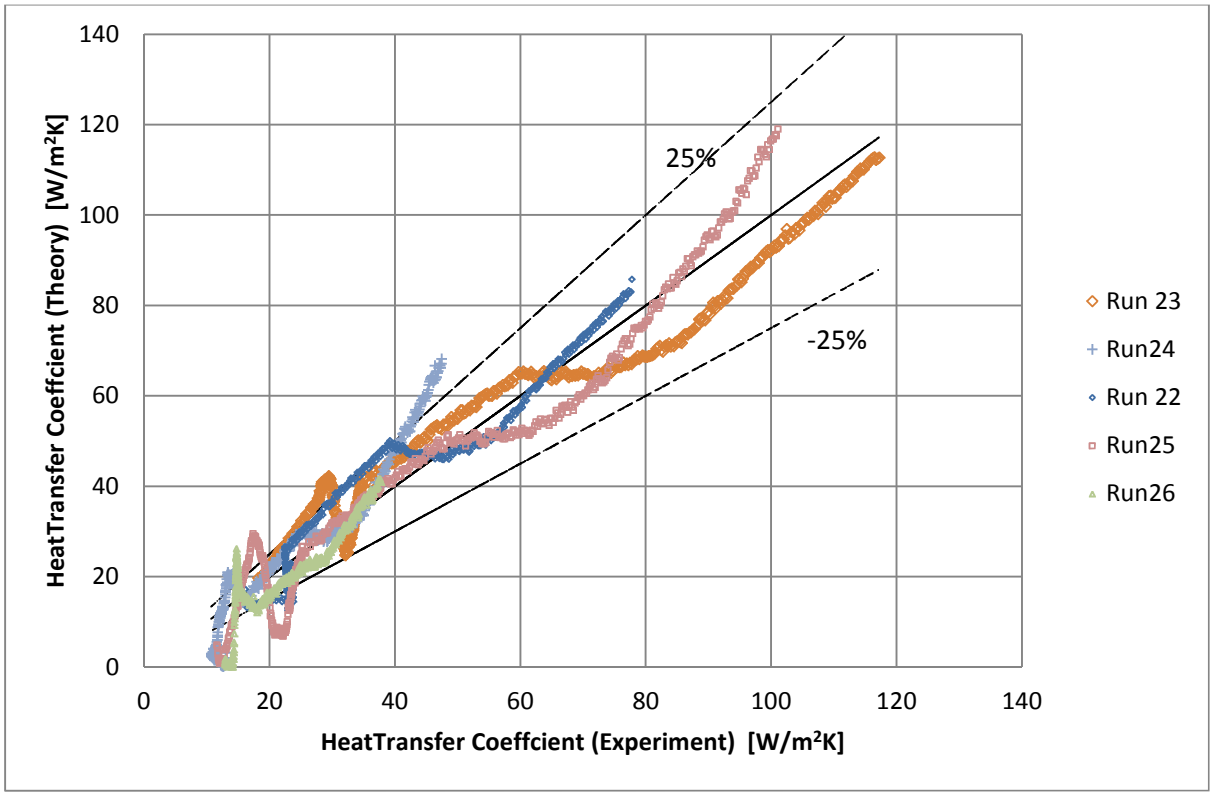

Figure 5-8 Comparions of measured HTCs with predicted HTCs

5.4 Development of a new empirical correlation

In chapter 4, the local experimental heat transfer coefficients are obtained by measuring local temperatures along the vertical pipe. Based on the data of experimental heat transfer coefficients, an empirical correlation is developed here as a function of several nondimensional parameters to define the governing factors on reflux condensation.

Referring to chapter 2, the in-tube heat transfer coefficient (HTC) can be separated in to the film heat transfer coefficient (h_f) and the heat transfer coefficient of the steam-air mixture consisting of convective (h_{cv}) and condensation (h_{cd}) heat transfer coefficients, as given in Eq. (5.12).

$$HTC = \left[\frac{1}{h_{cd} + h_{cv}} + \frac{1}{h_f} \right]^{-1} \tag{5.12}$$

The nondimensional parameters relating to condensation heat transfer (h_{cd}) are Re_g, Re_f, W_{air}, and Jakob number (Ja). The convective heat transfer coefficient (h_{cv}) can be expressed in terms of Re_g and Pr_g, (Moon et. all (2000)).

To quantify the parametric effects of each of these nondimensional parameters on HTC a new correlation is developed in this study. To nondimensionalize the heat transfer coefficient the degradation factor (F) is defined as the ratio of local experimental heat transfer coefficient (HTC_{exp}) to the film heat transfer coefficient (h_f).

The degradation factor (F) is formulated as a function of 4 nondimensional parameters which are the Jakob number (Ja)[10], gas mixture Reynolds (Re_g), and film Reynolds number (Re_f) and Air mass Fraction W_{air} by relationship of the form as follows.

$$F = \frac{HTC_{\exp}}{h_f} = Const + a \times \mathrm{Re}_g + b \times \mathrm{Re}_f + c \times Ja + d \times W_{air} \tag{5.13}$$

By performing a multiple regression analysis the values of the coefficients are obtained and the result is presented in the following equation.

$$F = \frac{HTC_{\exp}}{h_f} = 0.030 + 0.008(\hat{\mathrm{Re}}_g) + 0.053(\hat{\mathrm{Re}}_f) - 0.07(\hat{J}_a) - 0.08(\hat{W}_{air}) \tag{5.14}$$

The $\hat{\mathrm{Re}}_g$, $\hat{\mathrm{Re}}_f$, $\hat{Ja}$, $\hat{W}_{air}$ are normalized parameters and are given as Eq. (5-15).

[10] *Jakob number* is a nondimensional parameter which represents the ratio of *sensible heat to latent heat*

$$\hat{\mathrm{Re}}_g = (\mathrm{Re}_g - 879)/2022 \quad (5.15)$$

$$\hat{\mathrm{Re}}_g = (\mathrm{Re}_f - 0.06)/4.3$$

$$\hat{W}_{air} = (W_{air} - 0.86)/0.99$$

$$\hat{Ja} = (Ja - 0.009)/0.02$$

The variations of the parameters in the above correlation are presented in Table (5-3).

Table 5-3 Variation of parameters included in Eq. (5.14)

Parameter	Range
Re_g	879-2022
Re_f	0.06-4.3
W_{air}	0.86-0.99
Ja	0.009-0.020

Based on this correlation, the most dominant parameter is the air mass fraction (W_{air}). It shows that heat transfer is severely degraded by increasing the air mass fraction. The temperature difference between the tube core temperature and the inner wall temperature affects the heat transfer coefficient and this is presented by the Jakob number which is the second dominant factor in the correlation. The effects of gas Reynolds number on the degradation factor is relatively low based on this correlation.

Figure (5-9) compares the results of the proposed correlation with the experimental data. Using this correlation, the majority of the data agree with experimental value within 15%.

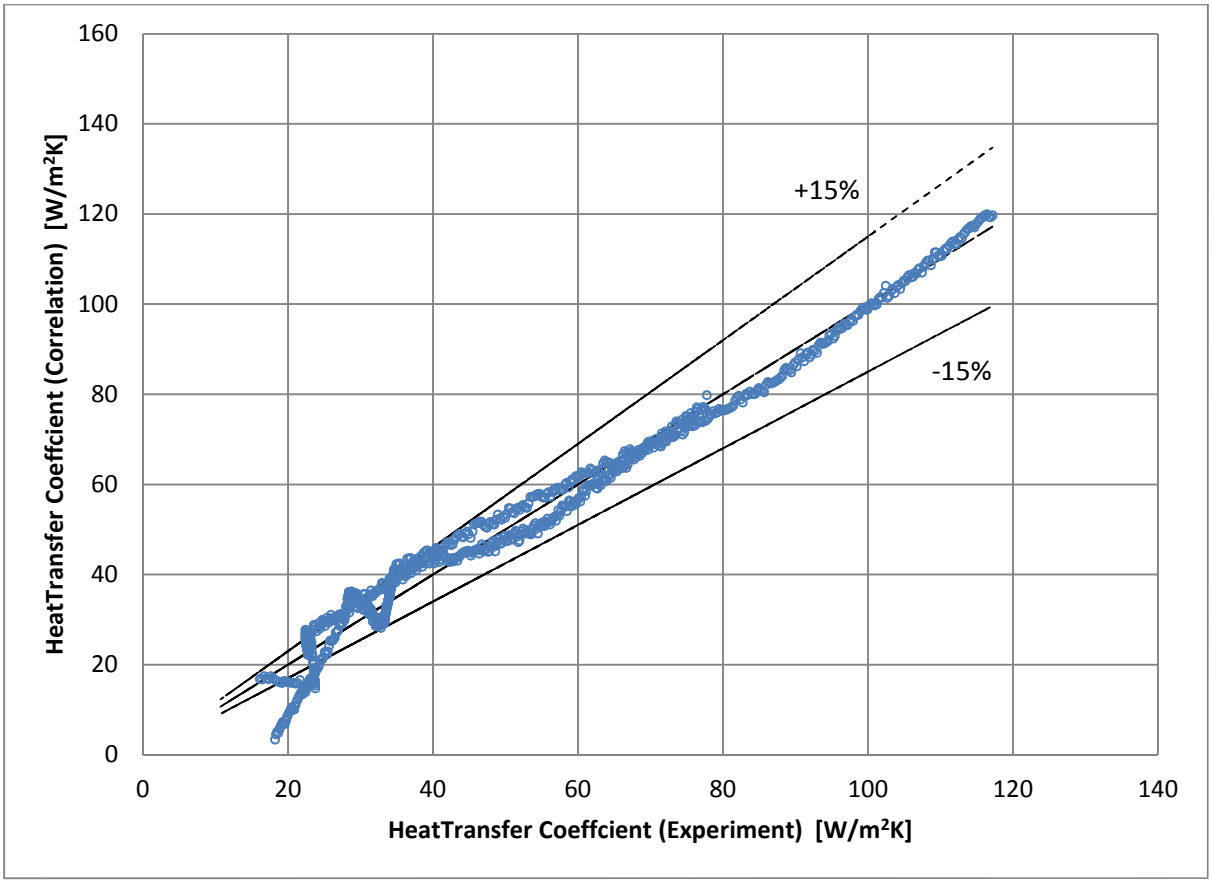

Figure 5-9 Comparisons of correlated HTCs with measured HTCs

5.5 Icing Region Prediction

As explained in chapter 3, the minimum achievable air temperature at the Cranfield icing tunnel is -20C. However in the Jaguar engine icing tests, the engine breather pipe is tested with an external airflow temperature of -40C. The pipe material in the experiments is Perspex with conductivity of 0.18-0.22 W/m.K and is different form the actual breather pipe material which is Polyamide12 with conductivity of 0.24 -0.5 W/m.K.

It is of interest to apply the actual breather pipe material properties, wall thickness and external cooling condition to the code and predict Icing zone at the actual engine test condition.

The new boundary conditions applied to the code are listed as follows.

- External cooling temperature (-40C)
- Pipe conductivity (k_w) of polyamide 0.24 W/m.K to 0.5 W/m.K
- Pipe thickness: 2mm

- External heat transfer coefficient (h_c) 45 W/m.K, 55W/m.K, 65W/m.K and 75W/m.K correspondent to the air flow velocity of 3.5m/s, 4.5 m/s , 5m/s and 5.5m/s

The fixed boundary conditions are: mixture gas mass flow rate (m_g=1.48 kg/hr), inlet gas mixture temperature (T_g=86 C), inlet relative humidity (100%) and external cooling temperature of -40C.

The above boundary conditions have been applied to the code and the results are plotted in Figure (5-10) and Figure (5-11).

In Figure (5-10), the distributions of inner wall temperature along the pipe at different external convective cooling conditions (h_c=45, 55, 65 and 75 (W/m.K)) are plotted. The start locations of freezing zones are highlighted in this figure. Increasing the h_c impose more heat transfer and reduces the inner wall temperature and increase the risk of ice formation in the pipe.

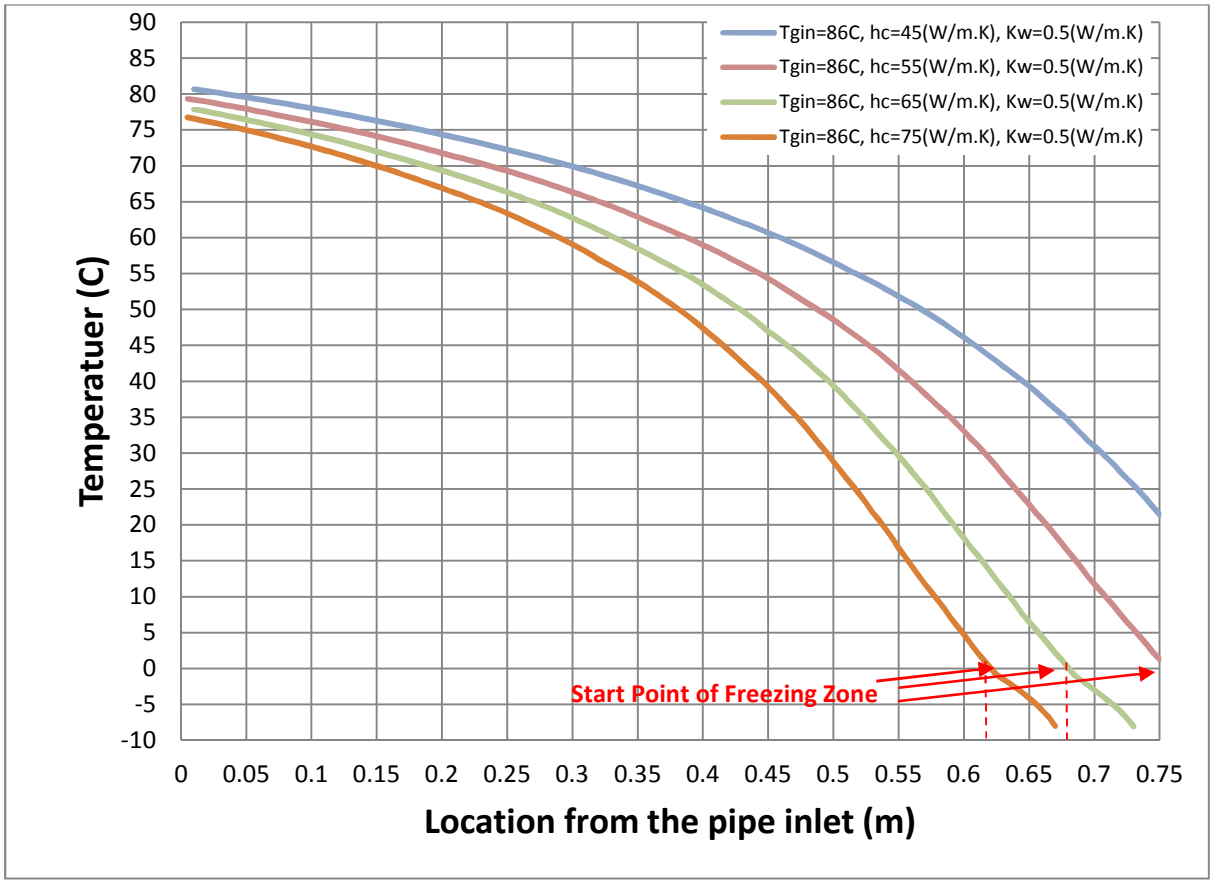

Figure 5-10 Calculated Inner Wall Temperature at different external HTC (Tgin=86C Kw=0.5)

Pipe wall conductivity also plays an important role in shifting the freezing zone along the pipe. Decreasing the wall conductivity will acts as a resistance to the heat transfer. Figure (5-11) shows that decreasing the wall conductivity from 0.5 W/m.K to 0.4 W/m.K shifts the freezing zone start point by nearly 0.1 m.

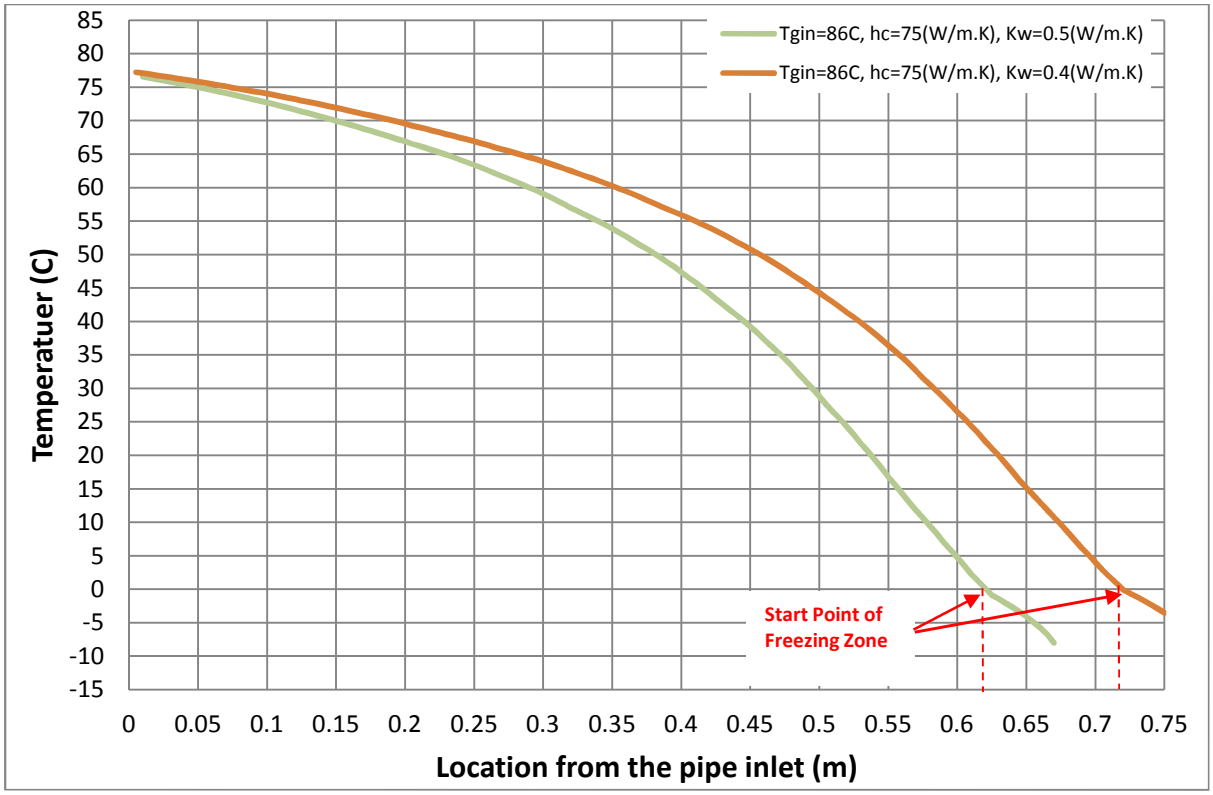

Figure 5-11 Inner Wall Temperature at different pipe wall conductivity (k_w) and at (T_{gin}=86 C h_c=75W/mK)

5.6 Summery and Conclusion

An iterative model is developed in this research which employs heat and mass transfer analogy approach for obtaining local heat transfer coefficient in reflux condensation of steam air mixture counter-current to laminar liquid film. Liao and Vierow's (2007) diffusion model and Chun et al's (1971) liquid film model are used to calculate condensation and film heat transfer coefficients, respectively. External cooling is taken in to consideration and the model is dependent on geometry, inlet boundary condition and external side of the pipe.

This model can satisfactorily predict the trend and magnitude of the local temperatures and heat transfer coefficient along the vertical pipe at the available test conditions within an acceptable uncertainty of $\pm 25\%$.

It also shows that increasing inlet vapour mass flow rate increases the condensation mass flux along the pipe.

To evaluate the effects of gas mixture flow rate on the heat transfer coefficient, a new correlation is developed based on a degradation factor. The empirical correlation is a function of condensate film Reynolds number, gas mixture Reynolds number, gas mass fraction and Jakob number. The correlation showed that air mass fraction and the Jakob number are the most dominant factors. However, the effects of gas Reynolds number on the degradation factor is relatively low.

The model is used to predict start point of freezing region based on the local inner wall temperatures at the boundary conditions attributed to the actual engine icing tests. It shows that at the fixed inlet boundary condition, increasing the external heat transfer coefficient increases the risk of ice formation. Also reducing the pipe thermal conductivity can delay the start of freezing zone in the pipe.

Chapter 6 Computational Fluid Dynamics Simulation

6-1 Introduction

Using CFD analysis helps to predict flow field and heat transfer in the breather pipe. In this study a CFD model is developed for modelling condensation and ice formation in the pipe which is exposed to external convective cooling. StarCCM+ is a CFD package which provides defogging model and helps to simulate condensation in internal and external flows. This software was recommended by Jaguar to be used as a CFD tool for this project. The aim of using the CFD model is to model freezing in the engine breather pipe and to evaluate the pipe blockage time.

As explained in the section (2.4), the “Thin Film Defogging” model is the only available model in StarCCM+ which can be used to model condensation. The model is originally made to simulate condensation in car windshield application. Here in this section this model is modified to be applicable to simulate condensation in horizontal pipes. This model has been developed by implementing a Java script which takes into account freezing heat flux and corrects the heat flux along the pipe.

The simulation was run in a three-dimensional and unsteady mode. To have a quicker convergence just half of the pipe with a symmetry plane is modelled, as shown in Figure (6-1). Most of the parameters are analysed on the symmetry plane and also on the gas/solid interface called “condensation surface”.

The whole pipe was split into two regions namely gas and solid (pipe wall) as shown in Figure (6-2).

The external convective cooling is taken in to account by selecting the external heat transfer coefficient and external temperature on the external surface of the pipe. This method is available in StarCCM+ for modelling external convection in a pipe.

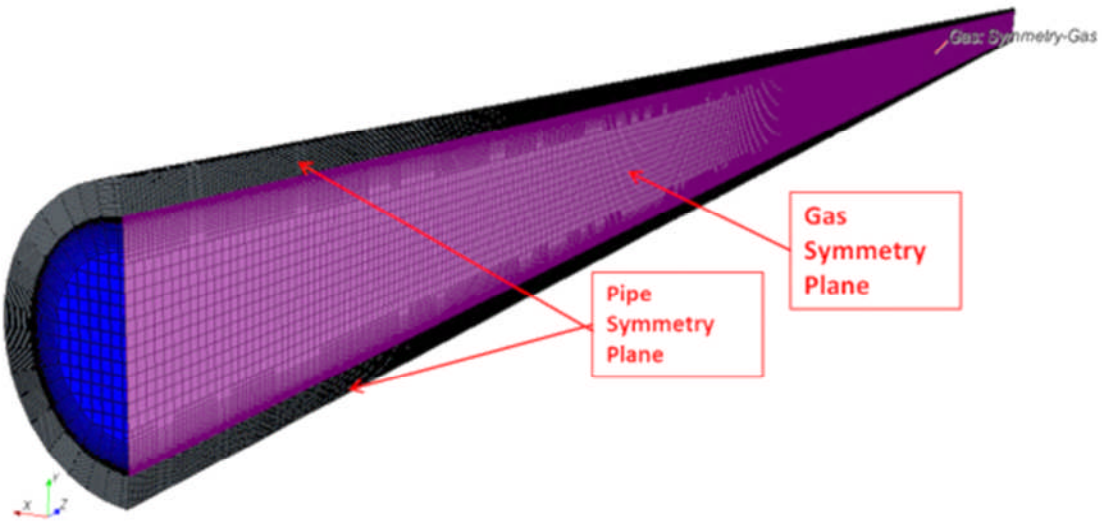

Figure 6-1 Pipe geometry symmetry plane illustration

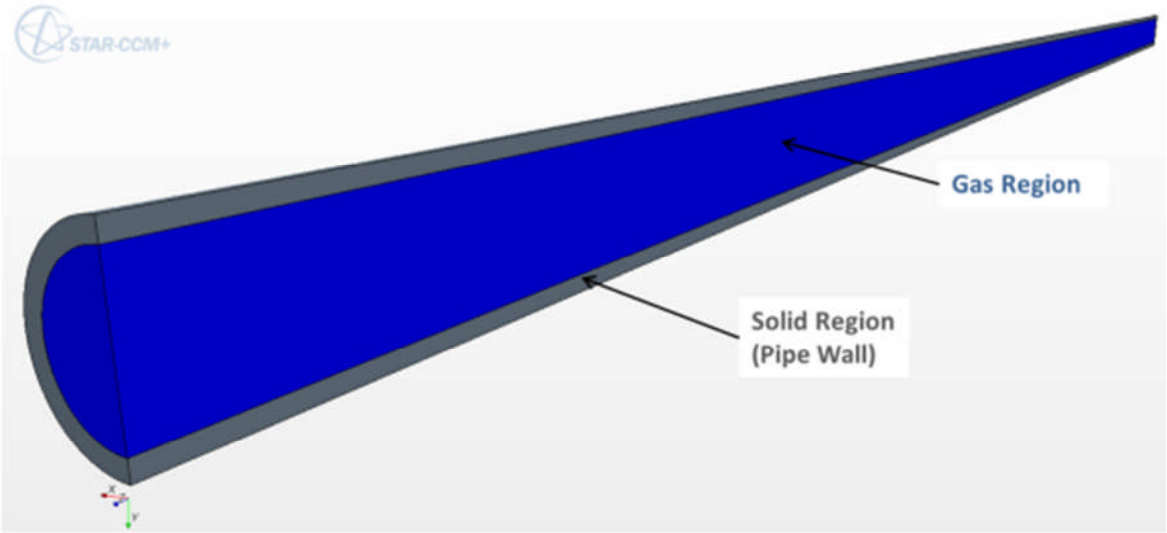

Figure 6-2 Pipes divided in to two regions as gas region and solid region

6.2 CFD boundary settings and materials

The boundary conditions of the model are set at the inlet and outlet of the pipe as inlet mass flow rate and pressure outlet, respectively (as shown in Figure (6-3)).

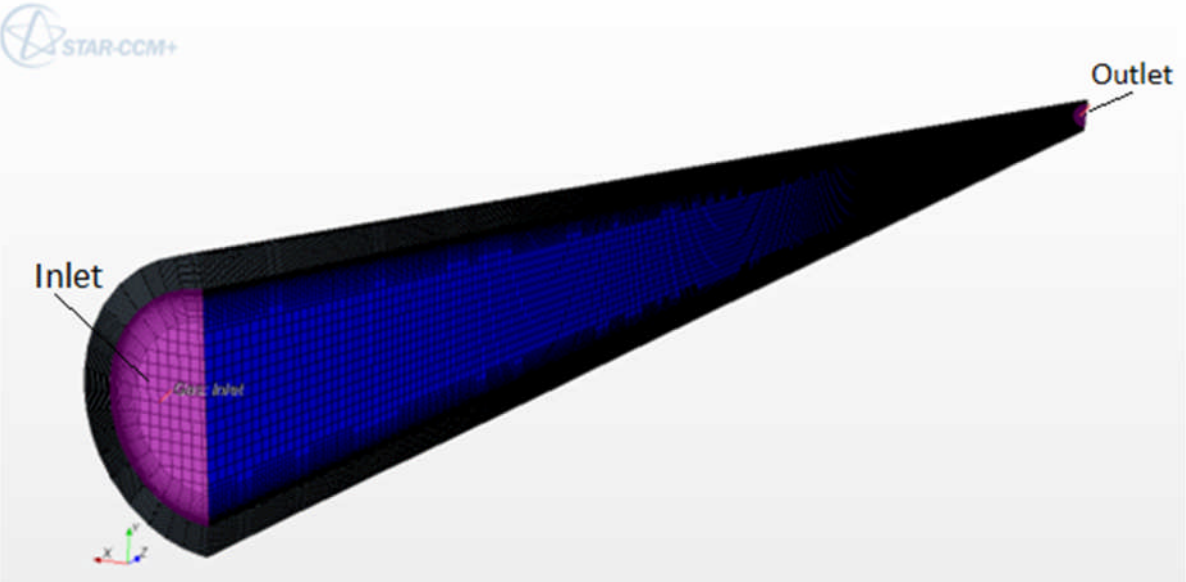

Figure 6-3 Gas Region Boundary Conditions

The values set for the boundary conditions are taken from the test data of the horizontal pipe (Run15 and Run18), explained in chapter 4. Table (6-1) presents the boundary conditions. The values of inlet gas mass flow rate have been divided by 2 as just half of the pipe is modelled

Table 6-1 Boundary Condition

Case	Inlet Boundary				External Flow		Outlet Boundary	
	Mass Flow Rate (kg/hr)	Temp (°C)	Vapour Mass Fraction	Reynolds	Temp (°C)	HTC (W/m2K)	Temp (°C)	Absolute Pressure (Pa)
Run15	0.58	46	0.06	858	-20	Test Data	17.4	101325
Run18	0.71	58	0.12	712	-20	Test Data	30.9	101325

The material of the pipe wall (Solid Region) is set as Plexiglas. The properties of Plexiglas as well as the water film and the mixture gas which have been set in the model are presented in Table (6-2).

Table 6-2 Material properties of water film, Dry Air and Pipe

Parameter	Value
Film Density	1000 kg/m^3
Film Diffusivity	2.556 * 10^(-5) m^2/s
Film Latent Heat	2,500,000 J/kg
C_{emp} (Defogging Empirical Factor)	0.9
Air Dynamic Viscosity	1.855*10^(-5) Pa-s
Air Molecular Diffusivity	Schmidt Number (0.9)
Air Thermal Conductivity	0.0260305 W/m-K
Pipe Density (Plexiglas)	1190 kg/m^3
Pipe Specific Heat (Plexiglas)	1450 J/Kg-K
Pipe Thermal Conductivity (Plexiglas)	0.18 W/m-K

StarCCM+ can compute external heat flux based on the external heat transfer (h_c) and external temperature. In this model the experimental external heat coefficient (h_c), evaluated in section (3.8), is applied to the model as a boundary condition. The distribution of the h_c on the external surface of the pipe is shown as contours in Figure (6-4). The values of h_c are implemented to StarCCM+ by importing the values as a Table. The external temperature is set as (-20°C).

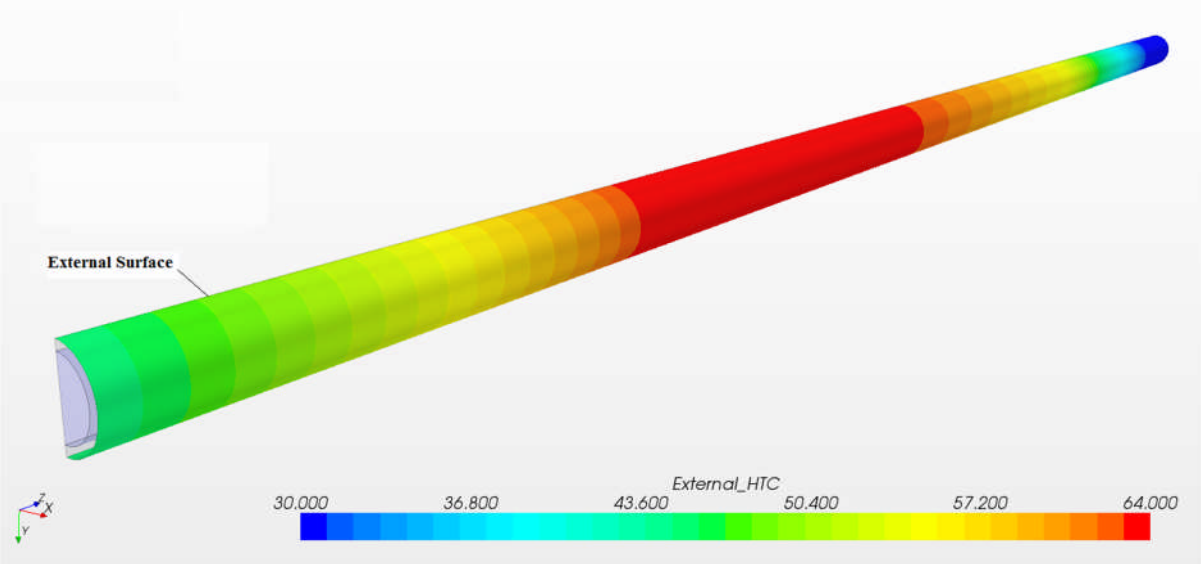

Figure 6-4 Values of external heat transfer coefficient applied at the external wall

6.3 Grid Generation

The gas region was meshed with a structured grid (called a trimmer mesh in StarCCM+).

Due to nature of the conjugate heat transfer[11], it was important to have conformal mesh at the gas/solid interface. Therefore, the mesh in the solid region was generated by extruding the mesh of the gas/pipe interface surface. Considering the pipe wall thickness, which is 2mm, 20 layers of trimmer mesh have been created, 0.1 mm per layer, shown in Figure (6-5).

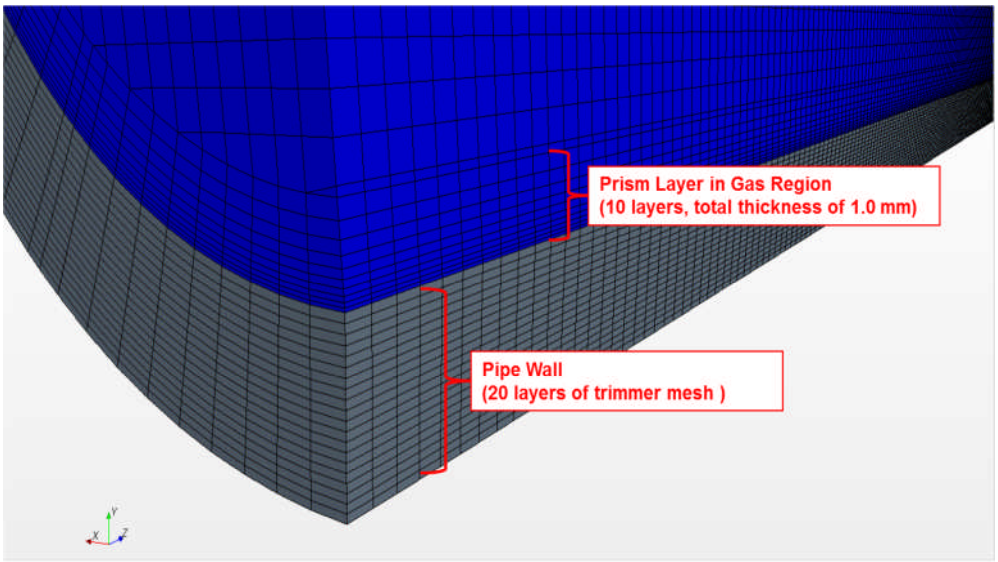

Figure 6-5 Mesh Generated for Gas and Solid regions

As a general rule, a poor quality mesh can impact the accuracy and efficiency of the solution and can even causes the solution to diverge or otherwise produce a bad result. In StarCCM+ these poor quality cells can be checked, identified and removed from the mesh volume region (StarCCM+ Manual).

To evaluate the cell quality, the girds have been diagnosed using the measures listed in Table (6-3). Following this check, no cell has been marked which demonstrate the good quality of the mesh generated.

[11] The term conjugate heat transfer is used to describe processes which involve variations of temperature within solids and fluids, due to thermal interaction between the solids and fluids

Table 6-3 Recommended values for removing invalid cells proposed in Star CCM+ Maual

Parameters	Minimum Value
The cell and boundary Skewness angles	1e-06
Face Validity metric	0.95
Cell quality metric	1e-06
Volume change metric	0.001

In order to capture the flow features near the wall and to have more accurate simulation at the boundary layer, a finer mesh has been used at the region close to the interface.

Considering the maximum gas velocity in the pipe, which is around 2.5m/s, and pipe inner diameter of 15mm, it is chosen to have 50 cells across the pipe width so that the position of each cell correlates to the velocity increment of approximately 0.05m/s. This gives the average cell base size of 0.3mm.

Taking to account the high temperature difference between the gas core flow and the external temperature the first cell height is calculated by dividing the pipe diameter by 200 which gives 0.035 mm. The mesh in the boundary layer is generated by applying prism layer model in StarCCM+. Following the best rule of practice applied for similar pipe flow by Jaguar, 10 layers of prism layer elements is generated which gives a total thickness of 1mm. The thicknesses of prism layer elements are grown with the growth ratio of 1.5, shown in Figure (6-5).

A grid sensitivity study was conducted by reducing the cell base size from 0.8 mm to 0.2 mm and influence of the mesh size was checked by monitoring the values of averaged velocity, averaged vapour mass fraction at the outlet of the pipe and also local temperature at 330 mm from the inlet of the pipe. The results of the grid sensitivity are shown in Table (6-4).

Table 6-4 Mesh Configuration Setting

Case	Base Cell Size	Number of cells across the pipe	Number of Cells	Averaged Velocity at the pipe outlet (m/s)	Averaged Vapour Mass Fraction at the pipe outlet	Temperature at 330 mm (°C)
01	0.8 mm	36	847,400	1.2113	0.07305	33.619
02	0.5 mm	46	2,377,555	1.2096	0.07290	33.7287
03	0.4 mm	52	3,670,920	1.209735	0.072965	33.7914
04	0.3 mm	58	5,080,670	1.209259	0.0729399	33.7898
05	0.2 mm	85	18,521,200	1.20902	0.0729238	33.784

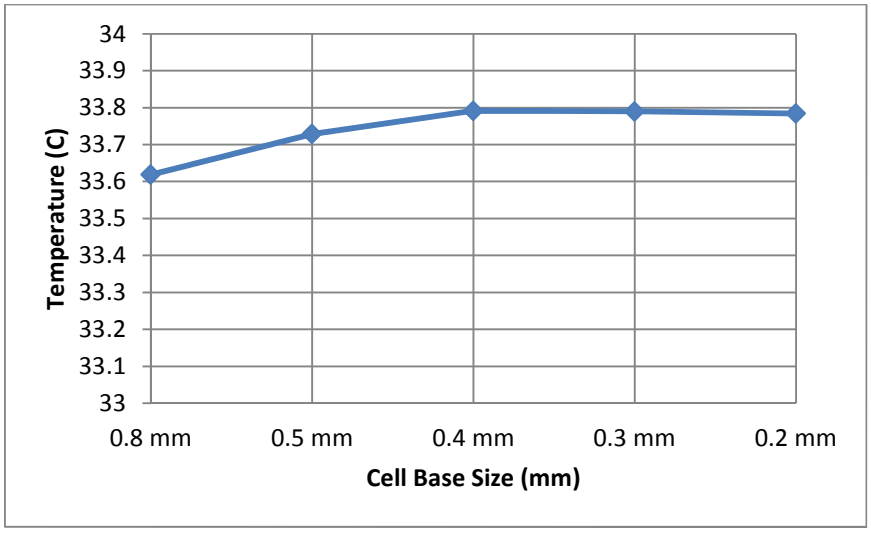

Figure 6-6 Gas Core Temperature at 610 mm from the inlet for different cell base sizes

According to the data presented in Table (6-4) and Figure (6-6), the independency of mesh size to the heat transfer and airflow was achieved with a cell base size of 0.4mm giving 3,670,920 cells which finally used for the analysis.

As a general rule, cell skewness angle of above 85 degree can cause solver difficulties especially in presence of conjugate heat transfer. In Figure (6-7) the cells skewness angles are shown for the gas/solid interface. It shows that the maximum value of 0.82, within the limit for good quality of cells.

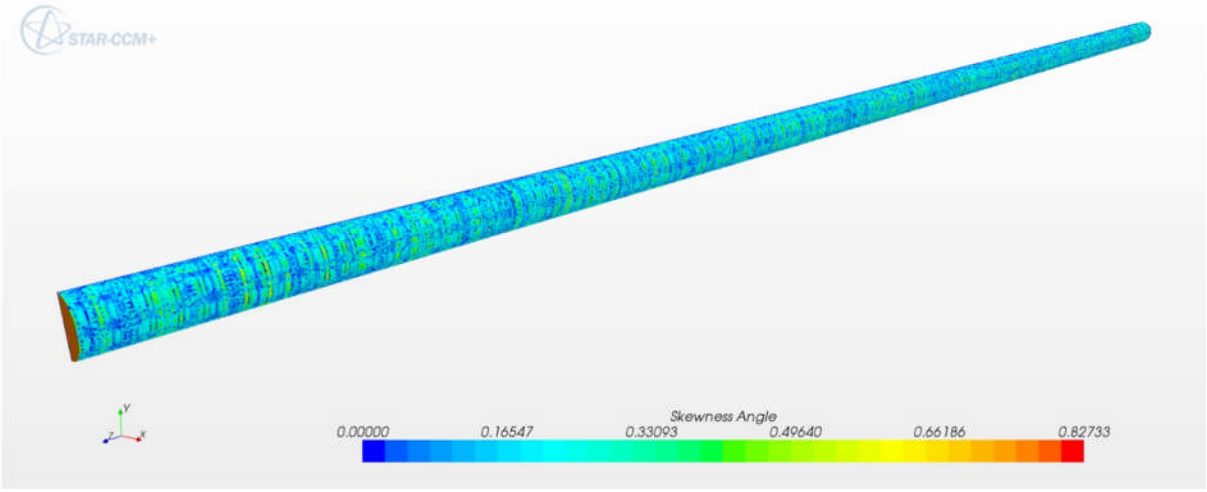

Figure 6-7 Cell skewness angle at the gas/solid interface surface

6.4 Solver Selection and Solution Methods

Segregated flow and energy model is used to solve the flow and energy in the gas and solid regions. The gas mixture is in the laminar regime (Re_g<2300). Thus, laminar model is used to model the flow behaviour and the flow assumed to be incompressible. Thin film defogging model is also used to model condensation.

A second order discretization scheme was used for all the solved quantities. Extra information regarding the numerical solver can be found in the StarCCM+ guide.

To reduce the computation effort and achieve better convergence the following solution procedure is employed:

- Solve for only flow in steady condition (turn off the wall continuum and defogging and energy solvers)
- When the variation of velocity at the outlet boundary is minimized, turn the model to transient unsteady, turn on the wall continuum, energy and defogging solver and run the model.

The time steps are set to the 0.01 second with 20 iterations per time step. This setting made the residuals variation to be monotonic and also the value of velocity to be converged at the end of each time step.

6.5 Modelling freezing

It should be noted that the only available model which can simulate freezing in StarCCM+ was VOF solidification and melting model. However this model is not capable of being linked to the defogging model in order to simulate accumulation of condensation on a bare surface. Therefore, the defogging model is developed in this study to be able to predict the location and extent of the freezing zone and model freezing heat flux in the pipe. This was achieved by developing a Java script and implementing it to the model. The script computes freezing heat flux and corrects the exchanged heat flux at the pipe surface in every iteration.

To take in to account the freezing heat flux, the pipe inner wall temperature is tracked along the pipe in every time step. When the temperature dropped to zero the code assumes that it is a potential location for freezing and calculates the local freezing heat flux by multiplying the enthalpy of fusion by local condensate mass of each cell in the freezing zone. This freezing flux is then applied as a sink term to the exchanged heat flux at the gas/solid

interface. In this methodology it is assumed that all the condensate mass in the freezing zone is converted to ice and there is no splash of water or movement of a liquid film.

It should be noted that defogging model does not compute condensate mass, but it gives the value of vapour mass fraction and also fog layer thickness [12] at each cell as a field function[13]. Employing the average vapour mass fraction at section (j) in the pipe one can calculate the vapour mass flow rate at section (j) by Eq. (6.1).

$$(\dot{m}^{j}_{vapour})_{average} = \dot{m}_{Inlet\ Dry\ Air} \frac{\left(W^{j}_{vapour}\right)_{average}}{1-\left(W^{j}_{vapour}\right)_{average}} \qquad (6.1)$$

$\left(W^{j}_{vapour}\right)_{average}$ is the average vapour mass fraction at section (j) and $\dot{m}_{Inlet\ Dry\ Air}$ is the dry air mass flow rate at the inlet which is constant along the pipe.

Knowing the average vapour mass flow rate $(\dot{m}^{j}_{vapour})_{averaged}$ at two adjacent sections (j and j+1) shown in Figure (6-8), the condensate mass can be evaluated by Eq. (6-2)

$$\dot{m}^{j}_{condensate} = \left(\dot{m}^{j}_{Vapor}\right)_{averaged} - \left(\dot{m}^{j+1}_{Vapor}\right)_{averaged} \qquad (6.2)$$

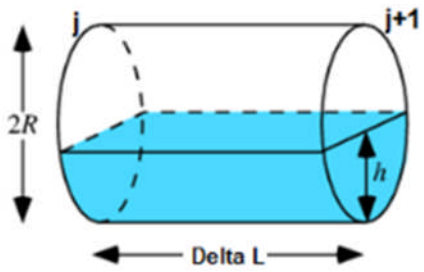

Figure 6-8 Condensate water between section (j) and (j+1)

In order to calculate the averaged value of vapour mass fraction across the pipe at a known interval, the "histogram table" is used in Star CCM+. This histogram table allowed creating a table showing the averaged distribution of selected quantity (like vapour mass fraction) along a defined direction at predetermined intervals.

[12] Fog layer thickness is a term used in StarCCM+ which indicates condensate thickness

[13] Field functions are raw data from the simulation stored in the cells and/or on the boundaries which may be viewed and defined in STAR-CCM+.

6.5.1 Algorithm for Calculating Freezing Heat Flux

The procedure of calculating condensate mass and applying freezing heat flux in the Java code is listed as follows.

1- Compute the local average value of vapour mass fraction every 1 mm along the pipe by employing the histogram table. (as the pipe length is 760mm the number of intervals is 760). Interpolating this histogram table gives the local averaged values of vapour mass fraction along the pipe at any cells in the gas region. The same procedure applies to calculate the local inner wall temperature along the pipe at the inner surface of the pipe.

2- Compute the local average vapour mass flow rate given in Eq. (6.1)

3- Generate a table which presents the local values of vapour mass flow along the pipe This table called "MFR table "

4- Read the local value of vapour mass flow rate at every subsequent interval from the "MFR table and calculate the local condensate mass ($m^{j}_{condensate}$) based on Eq. (6.2).

5- If the local inner wall temperature is below zero the freezing heat flux is calculated by applying:

$$Freezing\ Heat\ Flux = m^{j}_{condensate} \times h_{fusion} \tag{6.3}$$

6- Implement the freezing heat flux as a sink term to the exchanged heat flux at the gas/Solid Interface through User Heat Flux Function.

The above process is executed in every iteration until the end of the simulation. Based on this process a Java script has been written and implemented within the defogging model. The algorithm of this code is shown in Figure (6-9). The code is presented fully in Appendix D.

The results of implementing the code are presented in section (6-6-3).

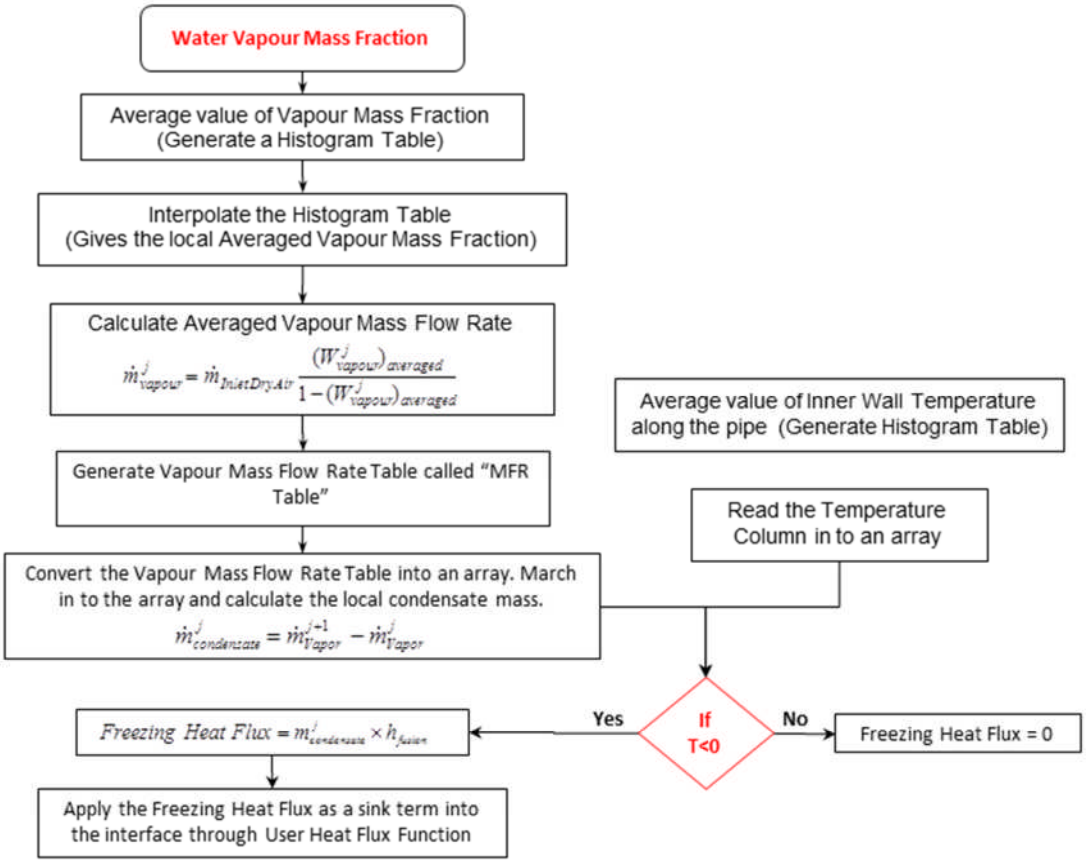

Figure 6-9 Process of computing condensate mass and freezing heat flux

6-6 CFD Results

6-6-1 Convergence Criteria

To evaluate the convergence of the solution the variation of following parameters are monitored during the simulation.

- Vapour mass fraction at the outlet of the pipe
- Difference between the mass flow rate at the inlet and outlet of the pipe
- Maximum Gas Pressure

The simulation was run for 8000 iteration (8seconds) and the results show the vapour mass fraction at the outlet, the difference of mass flow rates and the maximum pressure were become steady from 4000 iteration, (see Figures (6-10), (6-11) and (6-12)).

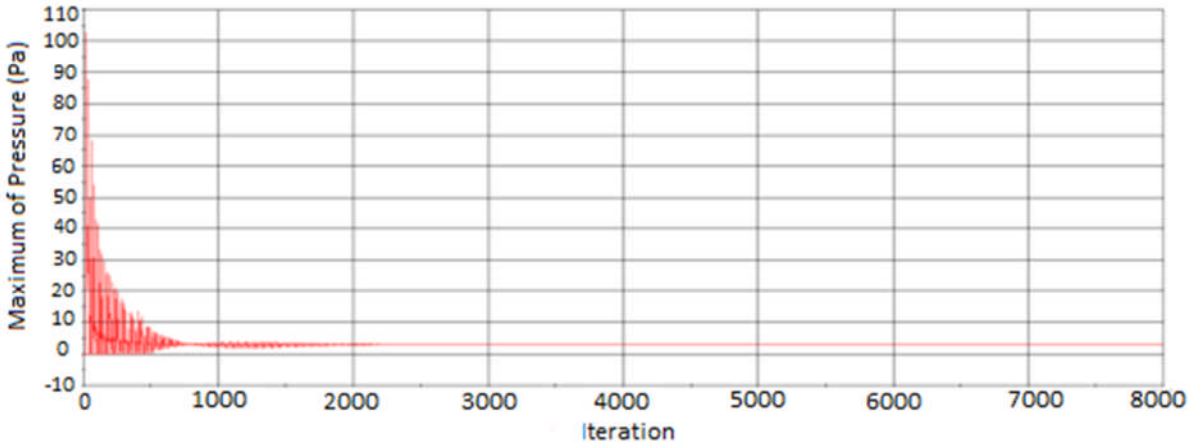

Figure 6-10 Gas Maximum Pressure in Gas Region

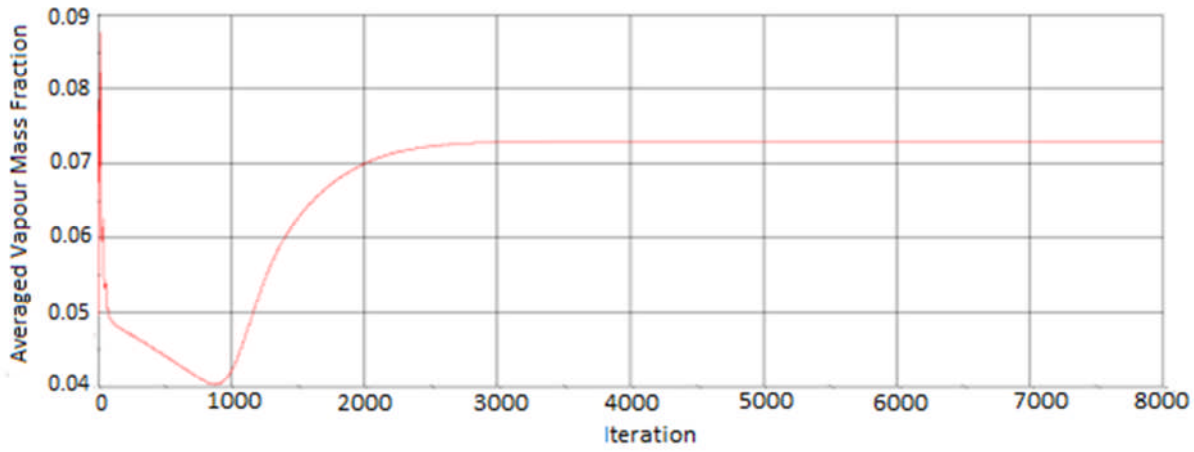

Figure 6-11 Averaged Vapour Mass Fraction at the outlet of the pipe

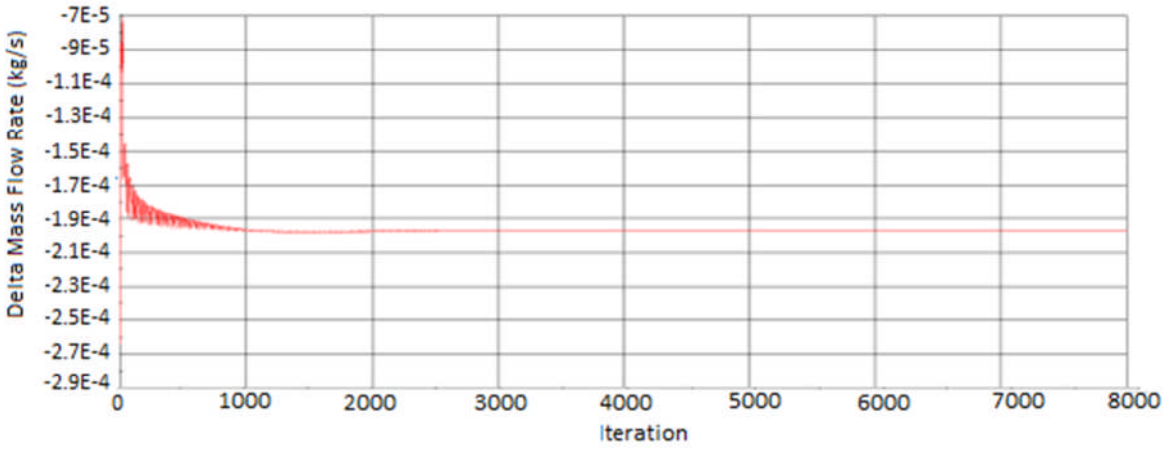

Figure 6-12 Difference between the inlet and outlet mass flow rate

6-6-2 Temperature and Vapour Mass Fraction variation

The distribution of vapour mass fraction and temperature along the pipe are shown in Figure (6-13) and Figure (6-14), respectively. These two Figures show that as the gas travels along the pipe the temperature and vapour mass fraction reduce. This is due to heat transfer to the outside and condensation along the pipe.

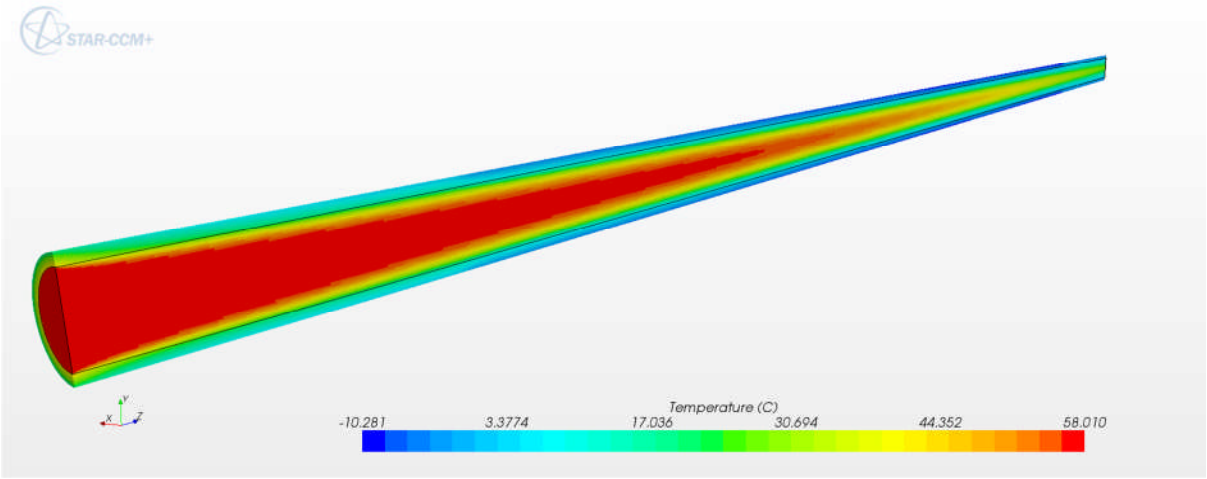

Figure 6-13 Temperature contours for Run 18 after 60 sec

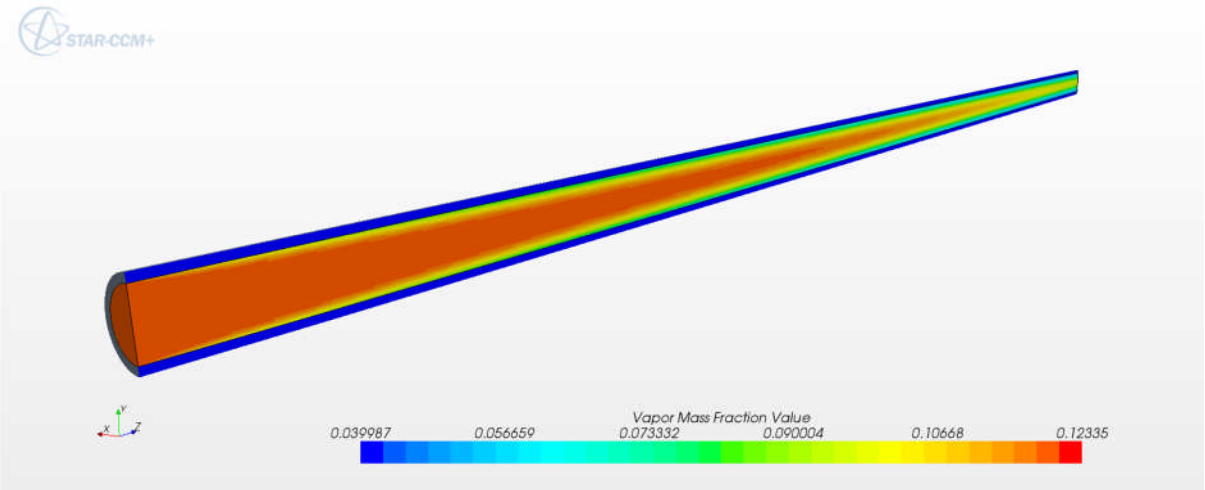

Figure 6-14 Vapour Mass Fraction Contours for Run 18 after 60 sec

In Figure (6-15) the local average value of the fog layer thickness at the gas/solid interface is shown. The contours illustrates that the thickness of the fog layer decreases along the pipe which demonstrate that the rate of condensation reduces along the pipe.

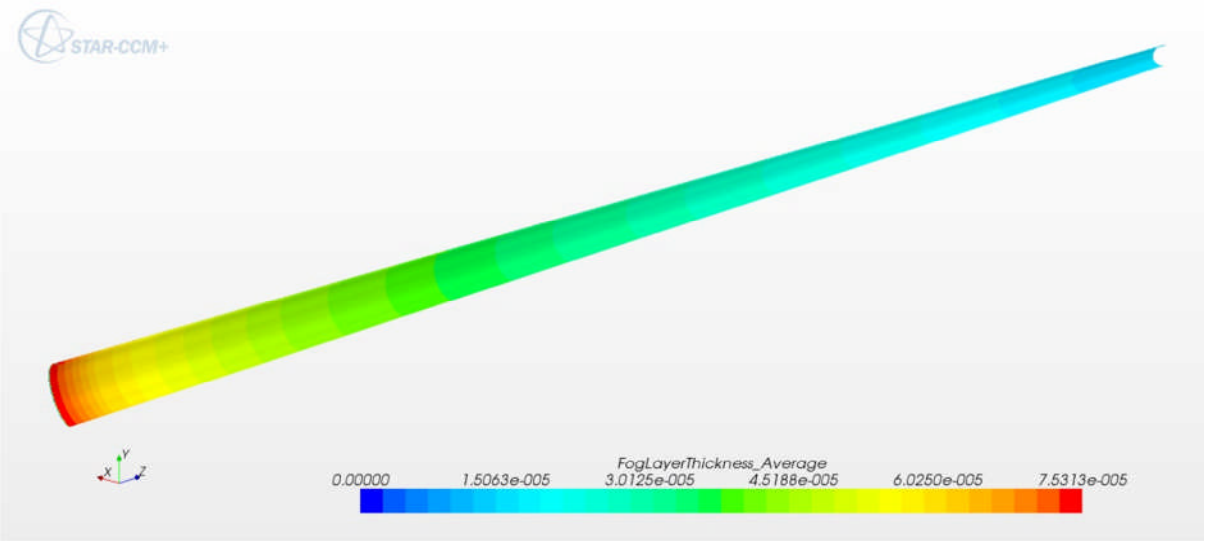

Figure 6-15 Fog layer Thickness Average Value along the pipe for Run 18

For post processing purposes, two separate lines have been defined along the pipe which data is tracked. One was along the core of the pipe and the other at middle of the pipe wall.

Also 4 cross lines were created across the pipe at different distances from the pipe inlet (z=0mm, z=250mm, z=500mm and z= 750mm), as shown in Figure (6-15).

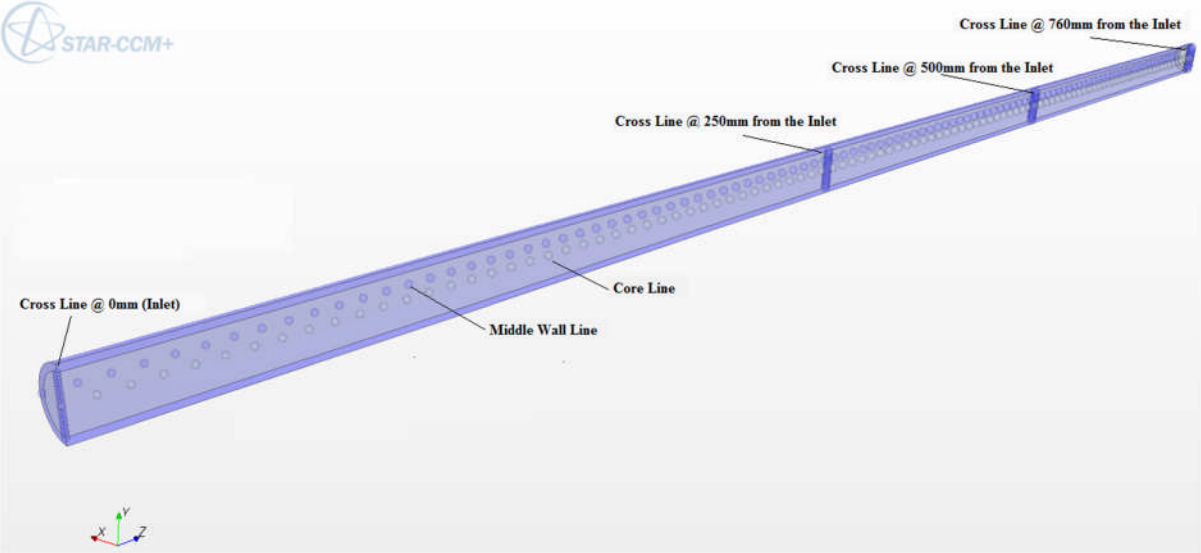

Figure 6-16 Core line and Middle Wall line used for post processing purposes

The variations of air mass fraction across the pipe along the four cross lines are plotted in Figure (6-17). This figure illustrates that air mass fraction at the core of the pipe (y=0) had a minimum value and it increased toward the wall. In fact, the vapour diffused through gas mixture to reach the pipe wall to condense. This enriches the air near the wall and accounted for increasing the air mass fraction. The vapour content of the gas mixture reduces as it travels along the pipe due to condensation. Therefore, the maximum value of air mass is at the outlet of the pipe near the wall.

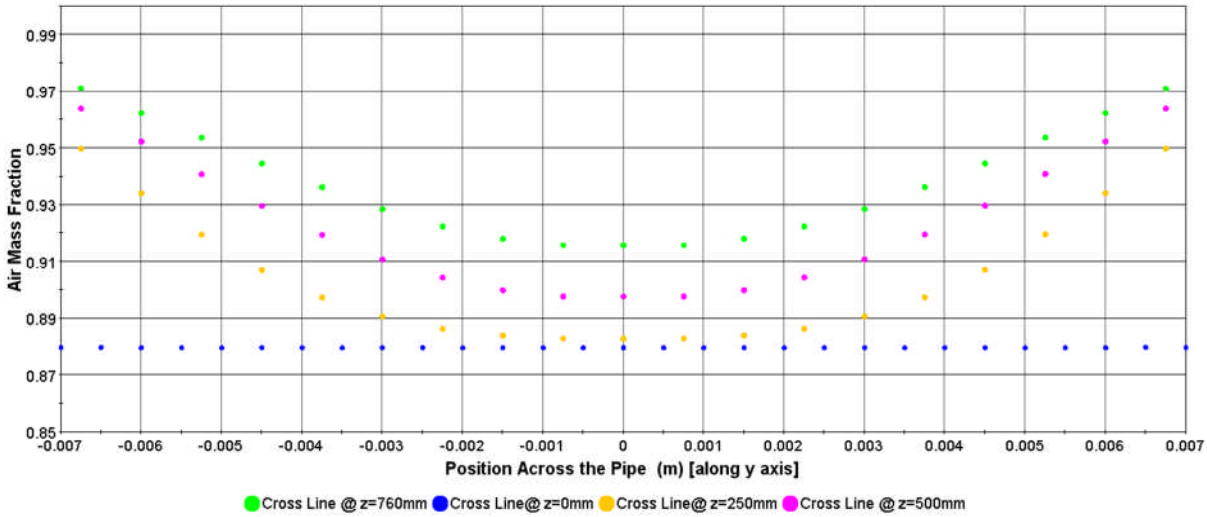

Figure 6-17 Air Mass Fraction Variation across the pipe at 4 different locations (z=0mm, z=250mm, z=500mm and z=760mm)

The local gas core and wall temperatures obtained from the CFD model along the core line and wall middle line are compared with their correspondent experimental values in Figure (6-18), and Figure (6-19) for Runs 18 and Run 15, respectively.

These figures show that the CFD model generally predicts the local wall and core temperatures along the pipe with good accuracy, not only in the magnitude but also in the trend of experimental data.

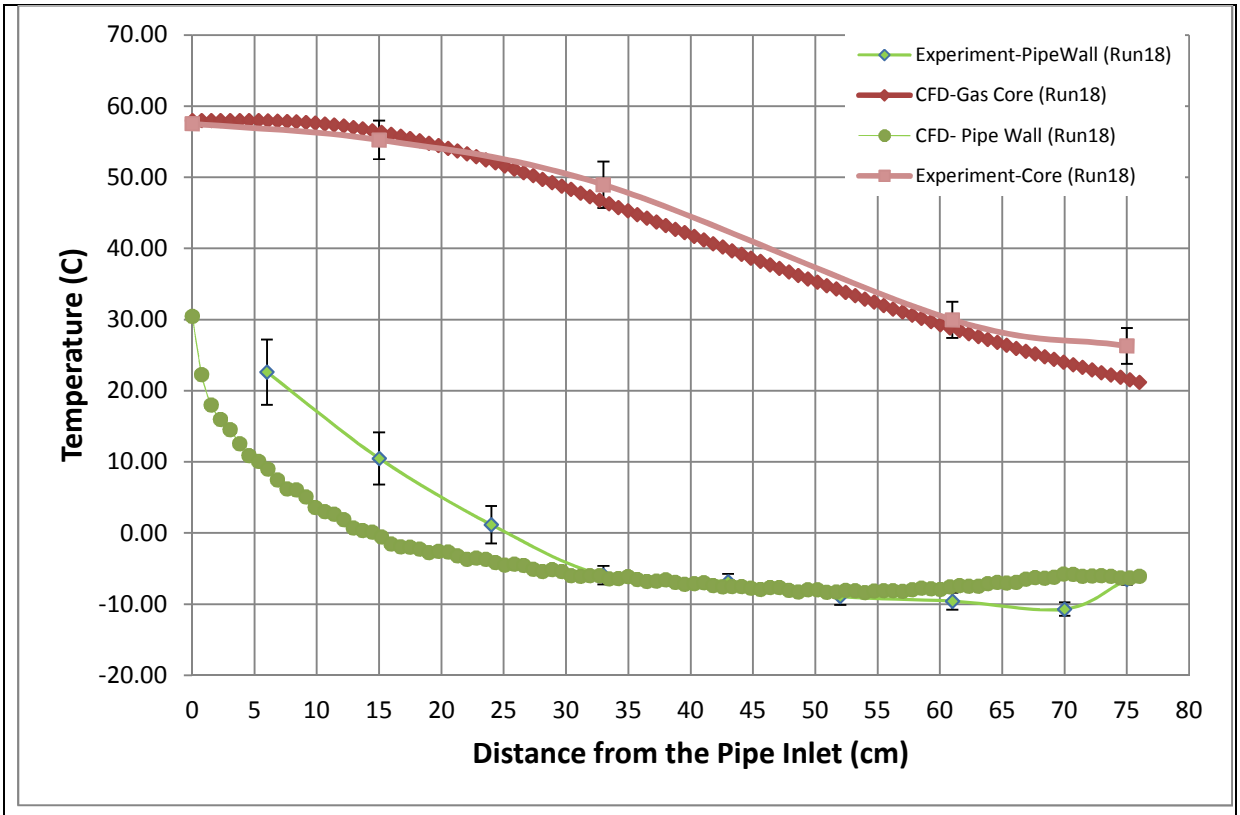

Figure 6-18 Local Temperatures predicted by CFD model compared to experimental value for Run 18

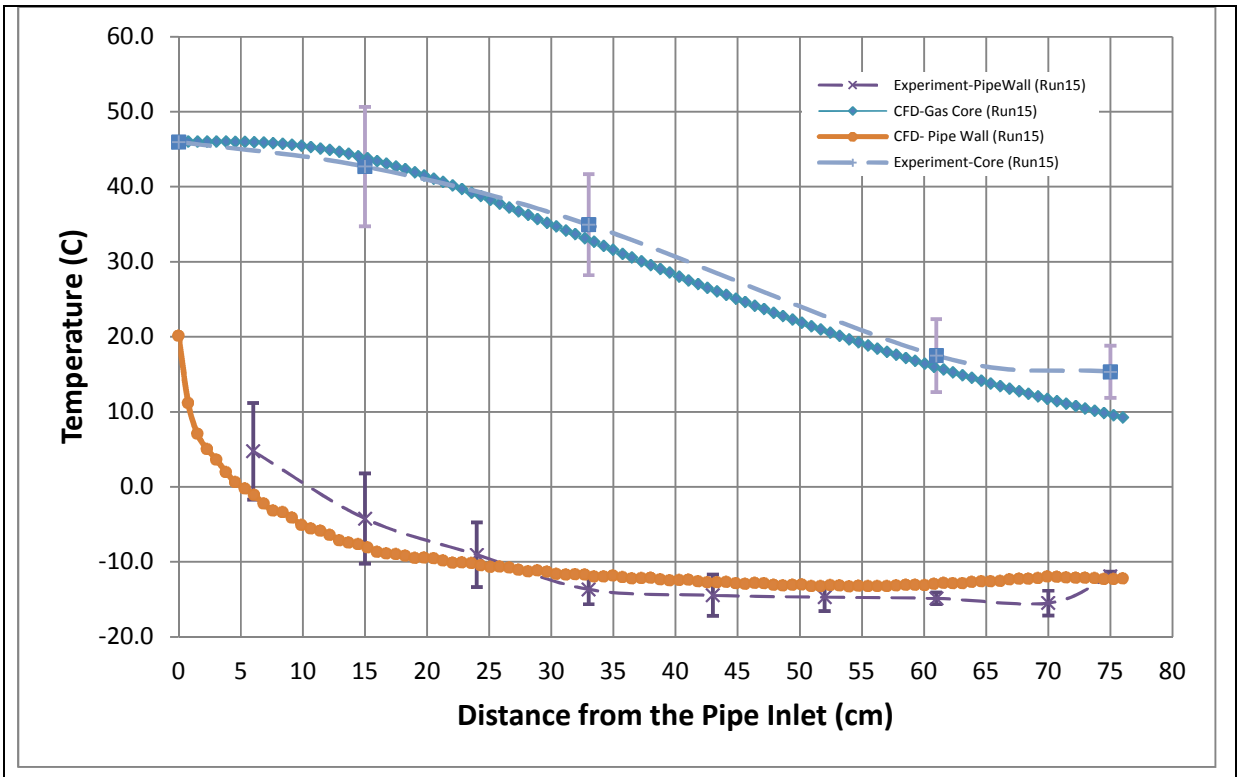

Figure 6-19 Local temperatures predicted by CFD model compared to experimental value for Run 15

In both of the runs, the CFD model under predicted the wall temperature from the beginning of the pipe up to 25 cm. This under prediction is more in Run 18 with vapour mass fraction about double the Run15. This might be attributed to movement of condensate droplets which may affect the temperature measurement which is not taken in to account in the Defogging model.

The RMS Error of the local temperatures is calculated by the Eq. (6.4)

$$RMSError = \sqrt{\frac{\sum_{i=1}^{n}(T_{i,CFD} - T_{i,Exp})^2}{14}} \quad (6.4)$$

$T_{i,CFD}$: Local temperature calculated by CFD model

$T_{i,Exp}$: Local experimental temperature measured in the test

n: is the number of measurement points which is 14 (5 core temperatures and 9 wall temperatures) as explained in chapter 4.

The value of the RMS error for Run 15 and Run 18 are 3.7 °C and 6.7 °C, respectively.

6-6-3 Results of implementing the Java Script

As explained earlier in section (6-5), the Java code developed in this study uses the local average value of vapour mass fraction in a given spatial interval to calculate the average condensate mass along the pipe. Then it goes on to evaluate the freezing heat flux and implement it as a sink term in the energy flux at the gas/solid interface.

The result of the model is presented in Table (6-5). This Table presents the local averaged values of condensate mass, inner wall temperature of the pipe and freezing heat flux along the pipe for the two boundary conditions, Run 15 and Run18.

These results are taken after 10 seconds (in unsteady simulation). For reasons of simplicity, the pipe length is divided in to 20 equal intervals.

Table 6-5 Condensate Mass and Freezing Heat Flux along the pipe for Run 18 and Run15 after 10sec (Freezing Region in highlighted)

Interval	Min. Position [Z] (mm)	Max. Position [Z] (mm)	RUN 15			RUN 18		
			Condensate mass flow (g/s)	Freezing Heat Flux (mW/m^2)	Inner wall Temperature-Average (K)	Condensate mass flow (g/s)	Freezing Heat Flux (mW/m^2)	Temperature - Average (K)
1	0	38	5.24E-04	0	288.08	9.53E-04	0	301.83
2	38	76	2.96E-04	0	277.63	5.38E-04	0	290.52
3	76	114	2.01E-04	67	272.96	3.70E-04	0	284.46
4	114	152	1.40E-04	47	269.96	2.82E-04	0	280.27
5	152	190	1.22E-04	41	267.87	2.33E-04	0	277.19
6	190	228	1.00E-04	33	266.70	1.93E-04	0	275.51
7	228	266	7.97E-05	27	265.66	1.62E-04	54	273.97
8	266	304	7.40E-05	25	264.75	1.40E-04	47	272.57
9	304	342	6.76E-05	23	264.06	1.27E-04	42	271.54
10	342	380	5.79E-05	19	263.54	1.14E-04	38	270.76
11	380	418	5.11E-05	17	263.057	9.89E-05	33	270.02
12	418	456	4.67E-05	16	262.61	9.29E-05	31	269.33
13	456	494	4.71E-05	16	262.24	9.21E-05	31	268.78
14	494	532	4.54E-05	15	261.92	8.40E-05	28	268.32
15	532	570	3.88E-05	13	261.73	7.02E-05	23	268.13
16	570	608	3.35E-05	11	261.75	6.43E-05	21	268.25
17	608	646	3.56E-05	12	261.88	6.41E-05	21	268.504
18	646	684	2.95E-05	10	262.16	5.11E-05	17	269.05
19	684	722	2.32E-05	8	262.46	3.08E-05	10	269.62
20	722	760	1.90E-05	6	262.26	1.28E-05	8	269.35

When the inner wall temperature drops to 0C (273 K) the Java code calculates the freezing heat flux based on Eq. (6.3). Otherwise, it is assumed to be zero, as shown in Table (6-5).

The total condensate mass in the pipe for Run 18 and Run 15 are calculated by adding up the local condensate masses. This can be also calculated by making a surface integral[14], of the fog layer on the inner surface of the pipe where condensation takes place. Both ways of evaluating the total condensate mass led to same result within 2% difference, presented in Table (6-6).

[14] For more details on Surface Integral see Star CCM Manual on Analyzing > Reporting Results > Report Types Reference > Statistical Reports > Surface Integral

Table 6-6 Total Condensate Mass in the pipe after 10 seconds

Case	Total condensate mass flow rate (g/s) (Calculated from vapour mass fraction)	Total condensate mass flow rate (g/s) (Calculated from surface integral of fog layer thickness)
Run15	**2.03E-03**	**2.10E-03**
Run18	**3.78E-03**	**3.71E-03**

The calculated condensate masses showed that condensation in Run 18 is 43% higher than Run 15. This is due to the higher level of vapour mass in Run 18, which has been already discussed in chapter 4, section (4.2.2).

6-6-3-1 Risk of freezing

Based on the data presented in Table (6-5) and Table (6-6), it can be inferred that although the amount of condensate mass in Run 15 is less than Run 18, freezing starts earlier in Run 15 due to lower inlet gas temperature. In order to make a comparison between the two runs in terms of ice blockage, volumes of condensate water in the freezing zone are calculated. To make better comparison, the volume of condensate is divided by the volume of the pipe in the freezing zone. This ratio is called "volume ratio" given as:

$$Volume\ Ratio = \frac{Volume\ of\ Condensate\ Water\ in\ Freezing\ Zone}{Volume\ of\ the\ Pipe\ in\ Freezing\ Zone} \tag{6.4}$$

Volume ratios for both Run 15 and Run 18 are listed in Table (6-7).

Table 6-7 Condensate mass in freezing area in comparison to total condensate mass

	Freezing Surface (m^2)	Total volume of pipe in the freezing zone (mm^3)	Volume of condensate in freezing zone (mm^3)	Volume Ratio
Run15	**0.0161**	**1.14E-04**	**1.21E-09**	**1.06E-05**
Run18	**0.0125**	**8.05E-05**	**2.27E-09**	**2.82E-05**

Table (6-7), compares freezing surface area, total volume of condensate in the pipe, volume of condensate in the freezing zone and volume ratio between Run 15 and Run 18. This comparison shows the freezing zone in Run 18 is less than Run 15 but there is more condensate water in the freezing zone in Run 18 and Run 15. This makes the volume ratio higher in Run 15 and may be more potential for freezing in Run 15. From this comparison it may be inferred that reducing the inlet gas temperature increases the freezing zone in the pipe. However, the amount of condensation in the pipe is another important factor which needs to be considered to evaluate the risk of ice formation.

6-6-3-2 Condensation rate and heat transfer coefficient

In Chapter 4, Section (4-2-4), condensation rate in Run 18 was compared with Run 15 based on the frequency of droplet departures. The accumulations of condensate water at the bottom of the pipe in each of these runs are shown in Figure (6-20). The pictures were taken after 10 minutes.

a) Run 15

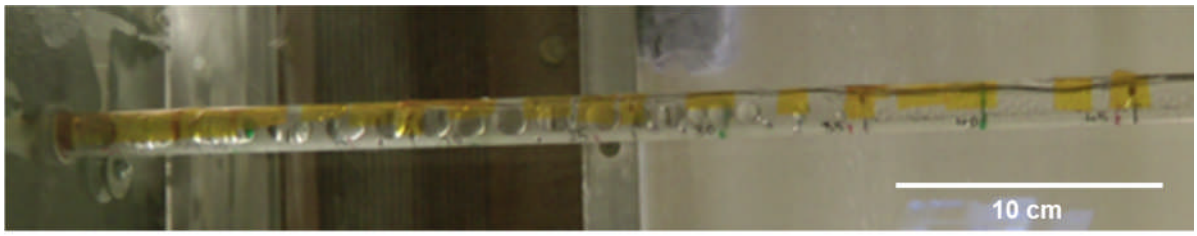

b) Run 18

Figure 6-20 Accumulation of condensate water on the bottom of the pipe for Run 15 and Run 18 after 10 minutes

Here, from the numerical aspect, the local averaged value of the condensation rate along the pipe for both of the Runs is assessed. The CFD results, Figure (6-21), show that the level of condensation in Run 18 is almost double of Run 15 which is a good agreement with the experimental result. (see section (4-2-4) and Figure (4-30) for the attributed experimental results)

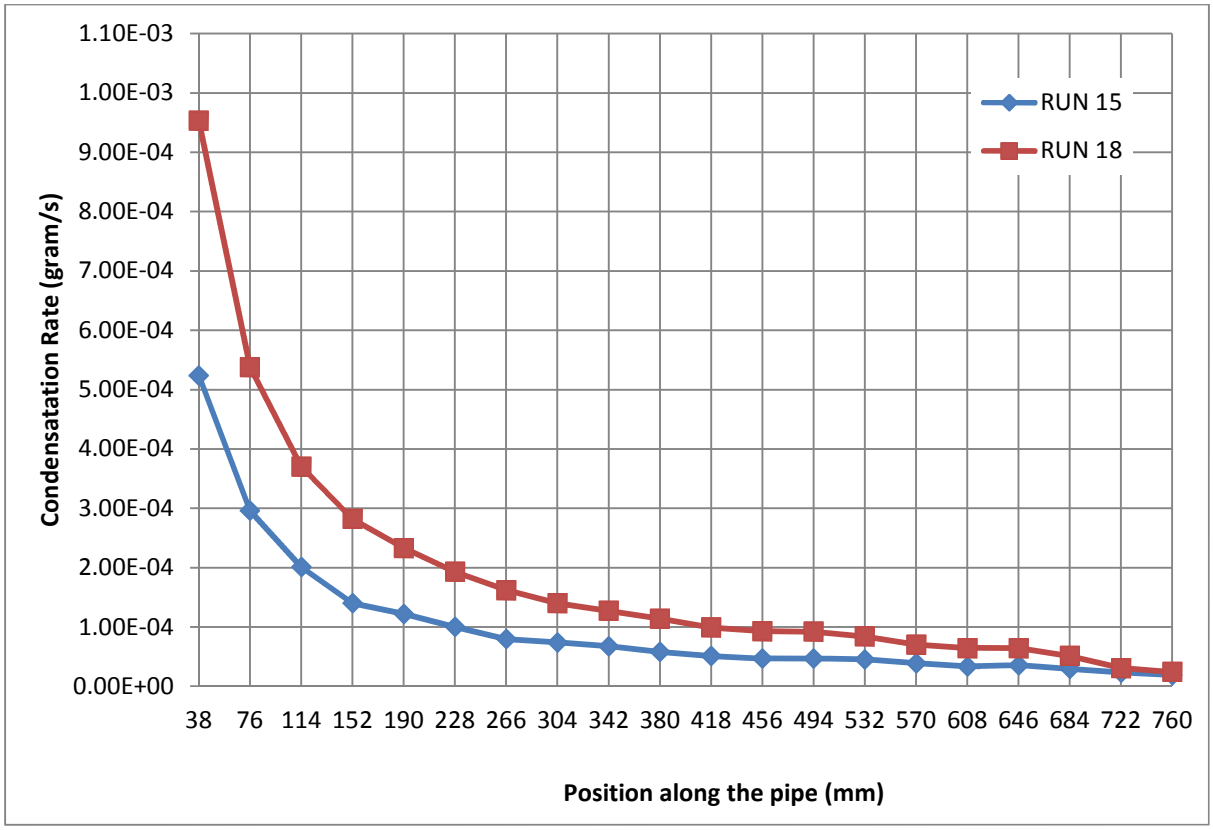

Figure 6-21 Local Condensation rate in the pipe for Run 15 and Run18

In Figure (6-22), the theoretical heat transfer coefficients for Run 18 and Run15 are compared with the experimental values. As shown, the heat transfer coefficient decreases sharply at the start of the pipe and then slowly as the vapour mass fraction decreases along the length. The heat transfer coefficient in Run 18 is more than Run 15 due to its higher level of vapour mass flow rate and higher inlet temperature. Figure (6-22) shows that the CFD model under predicts the heat transfer coefficient at the beginning of the pipe for the both cases. One factor which may be contributing to this might have been the movement of condensate droplets and their accumulation in reality which is not simulated in the CFD model. This under prediction in Run 18, with the higher condensation rate, is more than for Run15.

The heat transfer coefficients are decreasing sharply at the beginning of the pipe and then slowly toward the end of the pipe. This trend is similar to the trend of condensation rate, Figure (6-21).

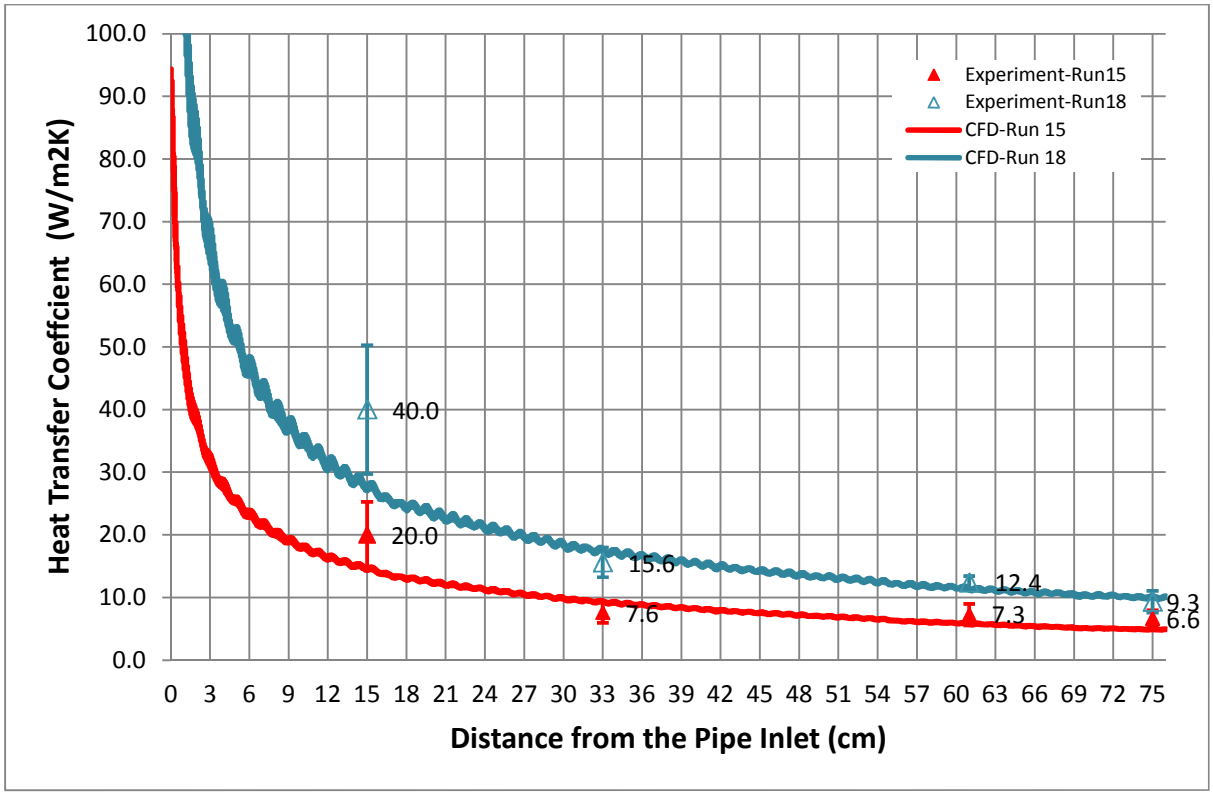

Figure 6-22 Heat Transfer Coefficient along the pipe for Run 18 and Run 15

6.7 Sensitivity of the CFD Model

Star CCM+, calculates the condensation mass based on the diffusion model Eq. (6.5) and (6.6) (Star CCM+ Manual).

$$\dot{m} = \rho_g \beta_g CG \ln \frac{CG(1-C_s)}{CG(1-C_g)} \qquad (6.5)$$

$$\beta_g = C_{emp} \cdot D_v / L \cdot 0.045 \cdot \mathrm{Re}^{0.8} Sc^{0.43} \qquad (6.6)$$

All the coefficients in the above equation were explained in section (2.4.1).

In Eq. (6.5) C_{emp} is an empirical condensation factor which can vary from 0.05 to 0.9. In this section, the sensitivity of the model is evaluated by changing this empirical factor to determine its effect on the RMS error and total condensate mass in the pipe for Runs15 and Run 18. Table (6-8) shows these results for three different values of C_{emp} as 0.05, 0.45and 0.9

Table 6-8 Effects of Changing C_{emp} on RMS Error and Total Condensate Volume

Case	C_{emp}	RMS Error	Total Condensate Volume (mm^3)
Run18	0.05	13.7	31.9
Run18	0.45	7.65	43.3
Run18	0.9	6.7	45.6
Run 15	0.05	7.48	29.6
Run 15	0.45	4.20	36.2
Run 15	0.9	3.73	37.4

The results show that increasing the C_{emp} increases the total condensate volume in the pipe. The optimum value for the C_{emp} is 0.9 which gives the minimum RMS error and is used for the analysis.

6-8 Conclusion

In the CFD model the external convection is taken into account by selecting the external heat transfer coefficient and external temperature on the external surface of the pipe.

Extruding the surface mesh at the gas/solid interface helps to have conformal mesh at the gas/solid interface. Modelling just half of the pipe with a symmetry plane shows shorter convergence time.

The Java code developed in this study is capable of calculating the local condensate mass in a given special interval in the pipe in every time step. It incorporates freezing heat flux as a sink term to the boundary heat flux at the gas/solid interface. Implementing this Java code to Star CCM+ software makes the defogging model to be able to model condensation and predict the location and extend of the freezing zone in the pipe.

The optimum process to achieve convergence is to run the model first in a steady mode and after initial convergence switch it to an unsteady solver.

The results of the CFD model were compared with the test data and showed that the model is capable of predicting condensation rate, local temperatures and heat transfer coefficient with good agreement with experimental results.

The local values of condensation volume can be calculated by the surface integral of fog layer thickness on the freezing surface.

It is presented that in the case of higher vapour mass fraction, more water vapour is condensed and more latent heat can be released. This could increase the heat transfer coefficient and increase the local temperatures.

When the vapour mass flow rate in the pipe is increased, the uncertainty in predicting the local temperatures and the heat transfer coefficient increases. This may be due to the movement of condensate water in practise which cannot be simulated in the current model. The volume ratio is defined in this study as a factor which defines the severity of ice growth in the pipe and shows the potential for ice blockage.

It is presented that the optimum value of the empirical condensation factor (Cemp) for the application of condensation in pipe is 0.9.

Comparing the results of run 15 with run 18 shows that there is more risk of ice formation in run 18. This is due to more condensation in the freezing zone which can cause the ice blockage earlier. From this comparison it can be inferred that reducing the inlet gas temperature increases the freezing zone in the pipe. However, the amount of condensation in

the pipe is another important factor which needs to be considered to evaluate the risk of ice formation. Therefore both the inlet gas temperature and vapour content may affect the risk of ice blockage in the pipe.

Chapter 7 CFD model of actual breather pipe

7-1 Introduction

The Jaguar required the engine breather system to function well in temperature down to -40°C (Jaguar engine design specification, Version 2). The breather system design must prevent the formation of ice that would cause the breather pipe to become blocked or create excessive crankcase pressure. It was of interest for the Jaguar to have a CFD model which can model condensation and freezing in the breather pipe and estimate the total time in which the pipe become blocked by ice. In this chapter the developed CFD model which has been validated in the chapter 6 is applied to the breather pipe, as an example, to predict freezing surface area and estimate the pipe blockage time. Some icing test results were available on one of the Jaguar engines (X250 V8 n/a) which are referred for assessing the CFD model.

In Figure (7-1), the breather pipe assembly is illustrated. The pipe inlet and pipe outlet are connected to the crankcase cover and to the air intake manifold, respectively.

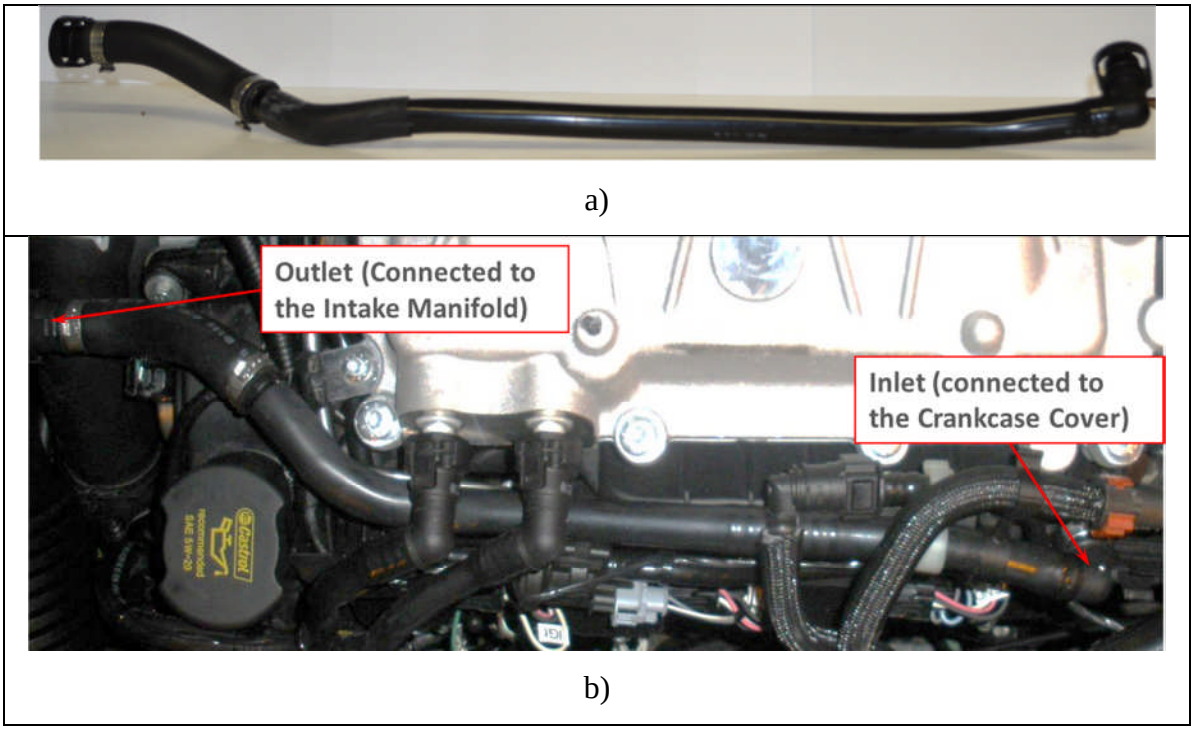

Figure 7-1 Pipe geometry symmetry plane illustration a) Breather Pipe b) Breather pipe connected to the engine

The results of the Jaguar icing tests show that freezing occurs at the outlet of the breather pipe where it is connected to the air intake stub (AIS) as shown in Figure (7-2). The ice blockage can pressurize the crankcase and in extreme conditions blow out the crankcase sealing. The test results on the engine, X250 V8, show that the engine breather pipe become blocked after 90 minutes.

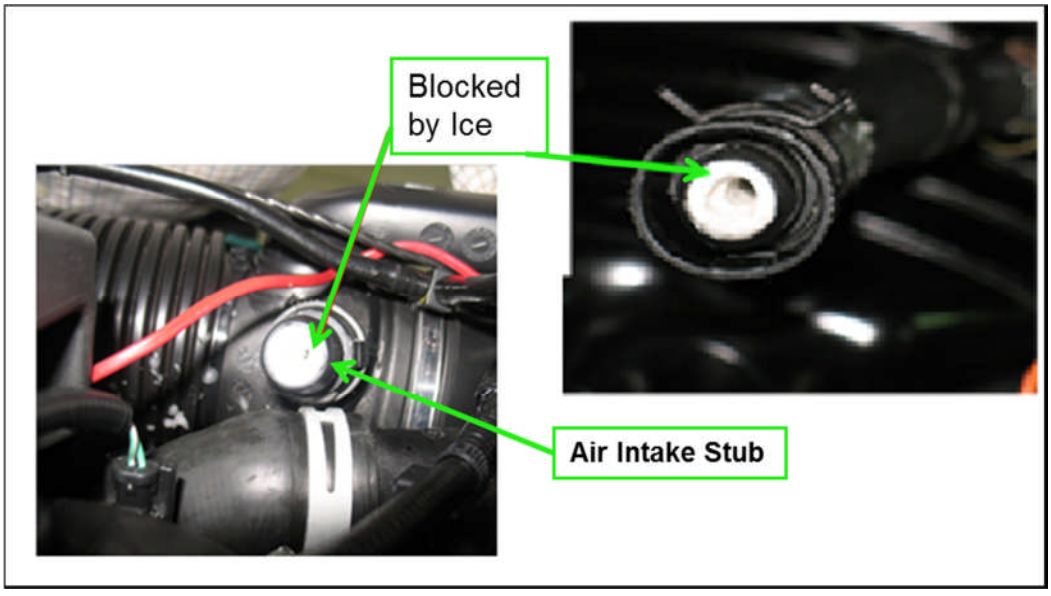

Figure 7-2 Breather pipe is blocked by ice at its connection to the air manifold

The geometry of the breather pipe was simplified for the CFD analysis as shown in Figure (7-3). The inner diameter of the pipe is 15mm with thickness of 1.5mm and the total length of 590 mm. The CFD simulation was run in three-dimensional and unsteady mode.

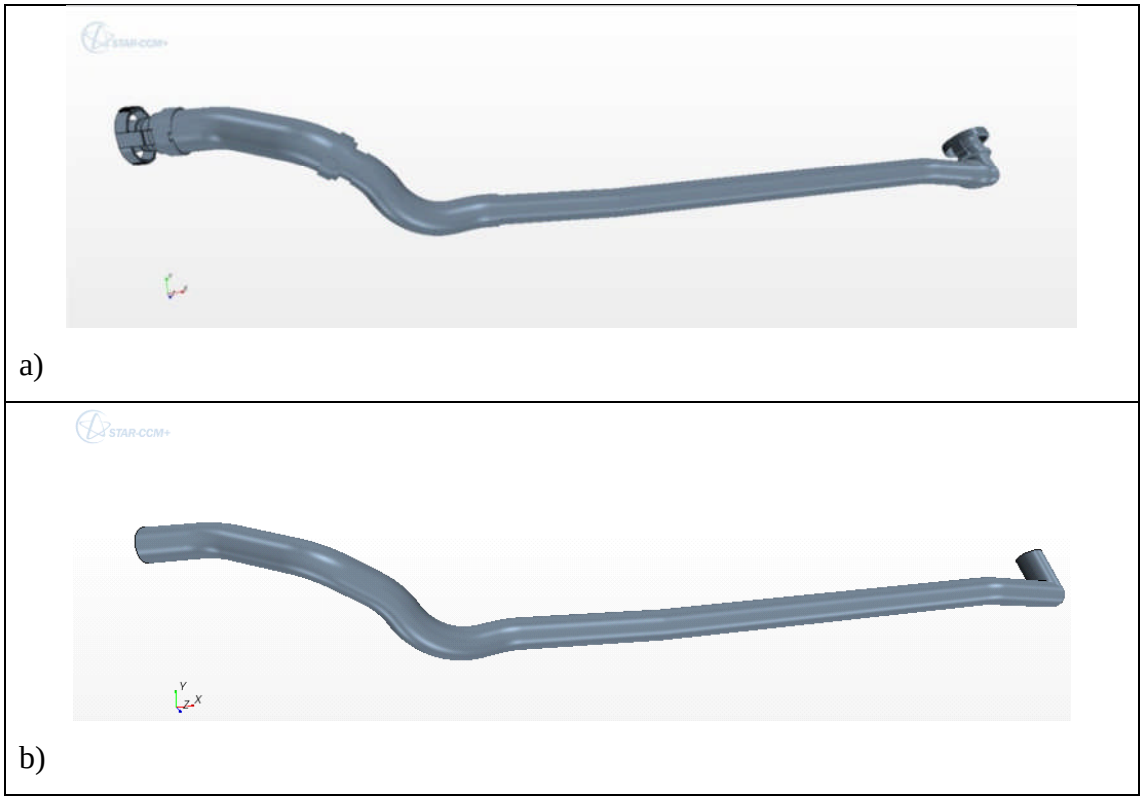

a)

b)

Figure 7-3 a) Breather Pipe Cad model, b) Breather pipe simplified Cad model

7.2 CFD boundary settings

The boundary conditions of the model were set as inlet mass flowrate at the pipe inlet and pressure outlet at the pipe outlet. The values set for the boundary conditions were taken from the test data of the Jaguar icing test as presented in Table (7-1).

Table 7-1 Boundary Conditions

Inlet Boundary			External Flow		Outlet Boundary	
Mass Flow Rate (Kg/hr)	Temp (°C)	RH	Temp (°C)	HTC (W/m^2K)	Temp (°C)	Absolute Pressure (Pa)
1.48	86	100%	-40	45	-40	-25 Pa

The pipe contact surfaces with the crankcase cover at the inlet and the air manifold at the outlet were set as constant temperatures of 86°C and -40°C, respectively as shown in Figure (7-4).

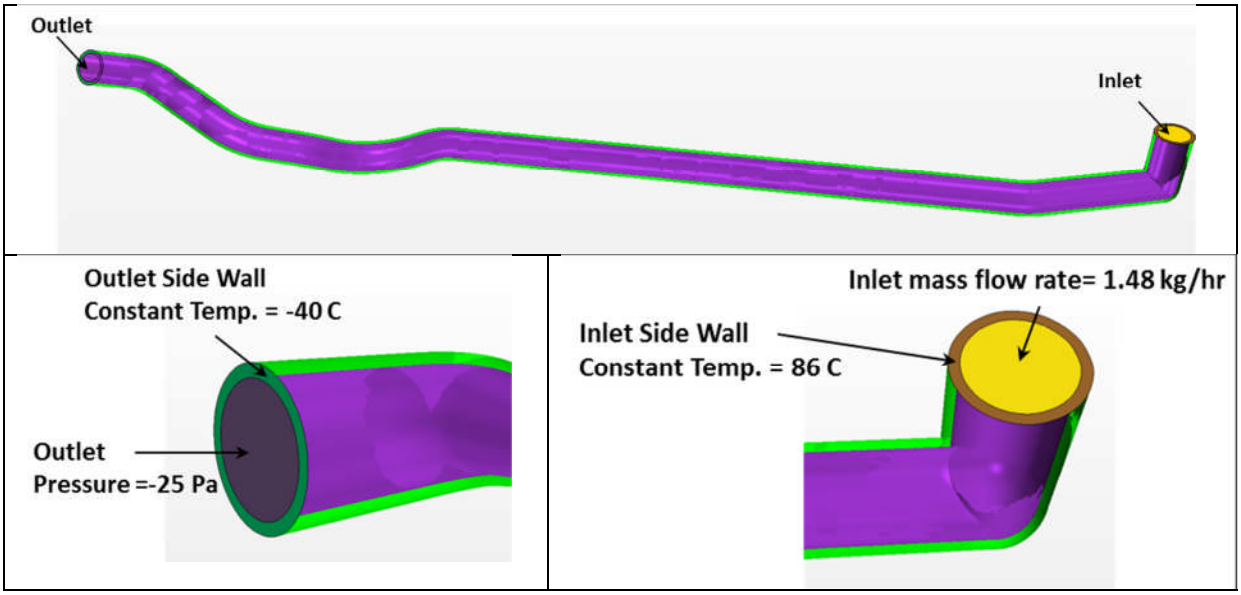

Figure 7-4 Boundary Conditions at the inlet and outlet of the pipe

The external heat transfer was taken in to account by applying the external temperature (-40°C), and external convection heat coefficient, (h_c) on the external surface of the pipe. The applied h_c was 45 [W m^{-2} K^{-1}], taking to account the measured under bonnet air velocity of 3.5m/s. The material of the pipe is Polyamide 12 and its properties are illustrated in Table (7-2).

Table 7-2 Material properties of Polyamid 12

Parameter	Value
Pipe Density	1010 kg/m^3
Pipe Specific Heat	1170 J/Kg-K
Pipe Thermal Conductivity	0.24 W/m-K

7.3 Grid Generation

Since, the breather pipe includes a sharp bend at the beginning, a trimmer mesh couldn't be employed but instead a polyhedral mesh was used for the gas and the solid regions as shown in Figure (7-5a). To achieve a conformal mesh at the gas/solid interface, a prism layer mesh is applied for both of the regions, as shown in Figure (7-5 b)

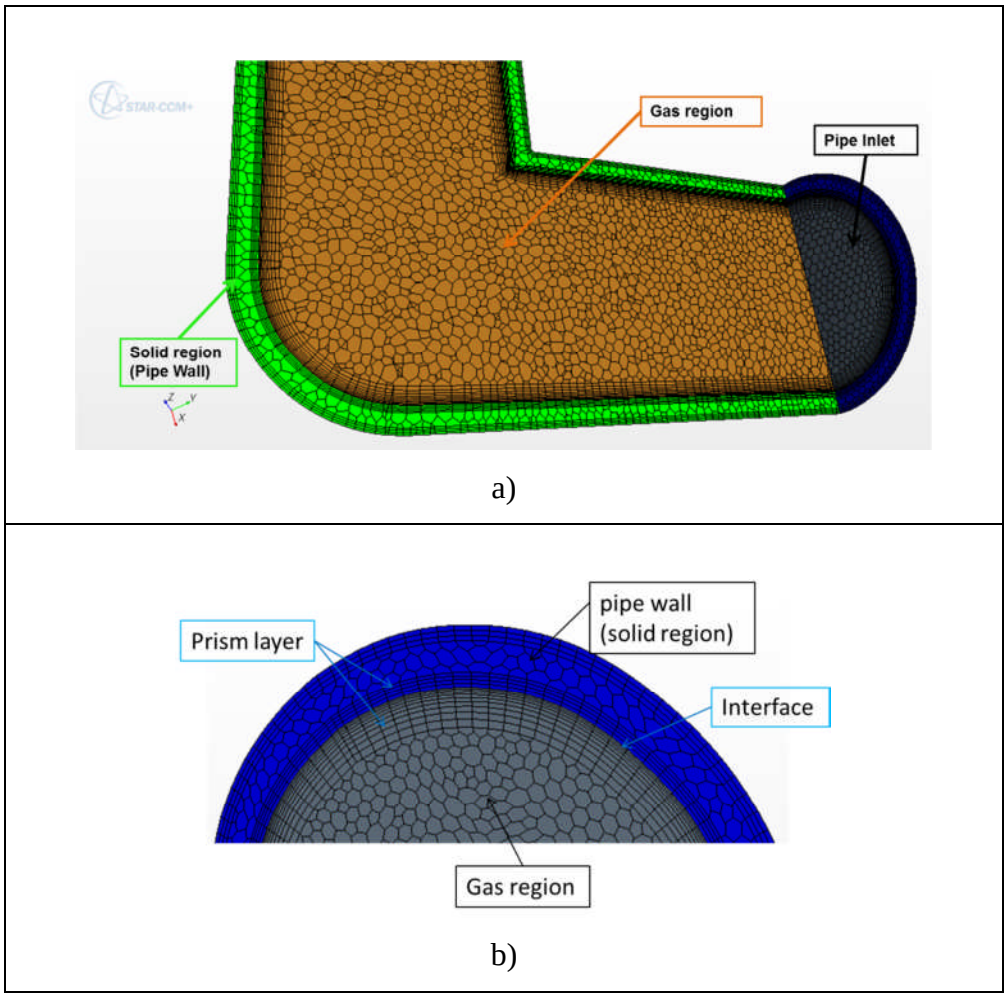

Figure 7-5 Polyhedral mesh applied for gas and solid regions a) Polyhedral mesh shown on a cross plane of the pipe, b) Mesh at the inlet surface of the pipe

To evaluate the cell quality, the girds have been checked using the measures listed in chapter 6, Table (6-3), and no cell has been marked which indicates the good quality of the generated mesh.

In order to capture the boundary layer properly near the wall and resolve the boundary layer in the viscous sublayer, the first cell height is adjusted in such a manner that y plus value to be approximately 1 or less. The y^+ parameter is computed by:

$$y^+ = \frac{\rho u_\tau y_p}{\mu} \quad (7\text{-}1)$$

u_τ : friction velocity at the nearest wall

y_p : distance from point to the wall

μ : dynamic viscosity

For this simulation, the two-layer all y^+ treatment was used in StarCCM+ 7.02 which is a near-wall modelling method employing the high y+ wall treatment for coarse meshes and the low y+ wall treatment for fine meshes. The low y+ wall treatment is suitable only for low-Reynolds number turbulence models and used when the entire mesh is fine enough for y+ to be approximately 1 or less. The high y+ wall treatment implies the wall-function-type approach with the assumption that the near-wall cell lies within the logarithmic region of the boundary layer. It is used when the wall-cell centroid is positioned in the logarithmic region of the boundary layer (y^+ >30).

Different cell sizes were examined as presented in Table (7-3) and mesh independency was achieved after 3 million cells by checking the variations of different parameters such as, the heat flux at the boundaries, the total average surface temperature, the velocity and temperature at 100 millimetres upstream the pipe outlet (Point A). The final grid used for the analysis involved 3,099,775 cells, case “G03” highlighted in Table (7-3).

Table 7-3 Mesh sensitivity study setting

Case	Base Size	Number of Cells	Delta Heat Flux ($W/m^2.K$)	Ave. Surface Temp. (℃)	Velocity at Point A (m/s)	Temp. at Point A (℃)
G01	0.80 mm	1,711,095	0.3394	-10.01	2.005	274.3
G02	0.60 mm	2,8371,04	0.3510	-9.85	2.086	275.9
G03	0.50 mm	3,099,775	0.350	-9.858	2.112	276.7
G04	0.45 mm	3,378,041	0.348	-9.86	2.1105	276.5
G05	0.40 mm	4,777,064	0.346	-9.865	2.110	276.8

7.4 Solver Selection and the CFD results

The segregated flow and energy model was used to solve the flow and energy in the gas and the solid regions. K-ε turbulence model was used to model the flow behaviour following the Jaguar best rule of practise used for similar cases. The Thin Film Defogging model was employed to model the flow behaviour and the flow was assumed to be incompressible.

To reduce the computation effort and achieve better convergence, the solution was run firstly for 1000 iterations in steady state and when the heat flux at the internal and external surfaces of the pipe became steady the solution was switched to unsteady mode. The time steps were set to the 0.01 second with 20 iterations per time step. This setting makes the residuals to be monotonic and allowed the variation of boundary heat flux to become steady at the end of each time step.

To evaluate the convergence of the solution, the variation of the heat flux at the internal and the external surfaces of the pipe were monitored. After 260,000 iterations, equivalent to 128 seconds, the difference between the heat fluxes had fallen to 1% and the convergence was achieved as shown in Figure (7-6). The area of the freezing surface converged to a value of 118.5 mm^2 at the end of the run as shown in Figure (7-7). The freezing surface zone is highlighted in Figure (7-8).

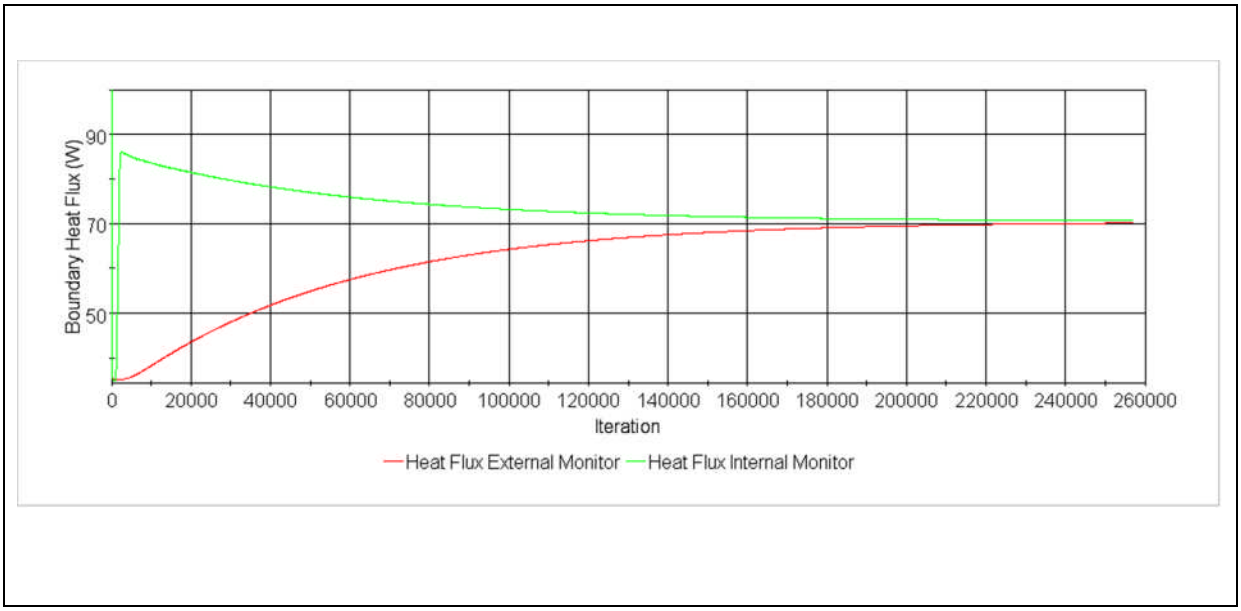

Figure 7-6 Boundary Heat Fluxes at external and internal surfaces of the pipe

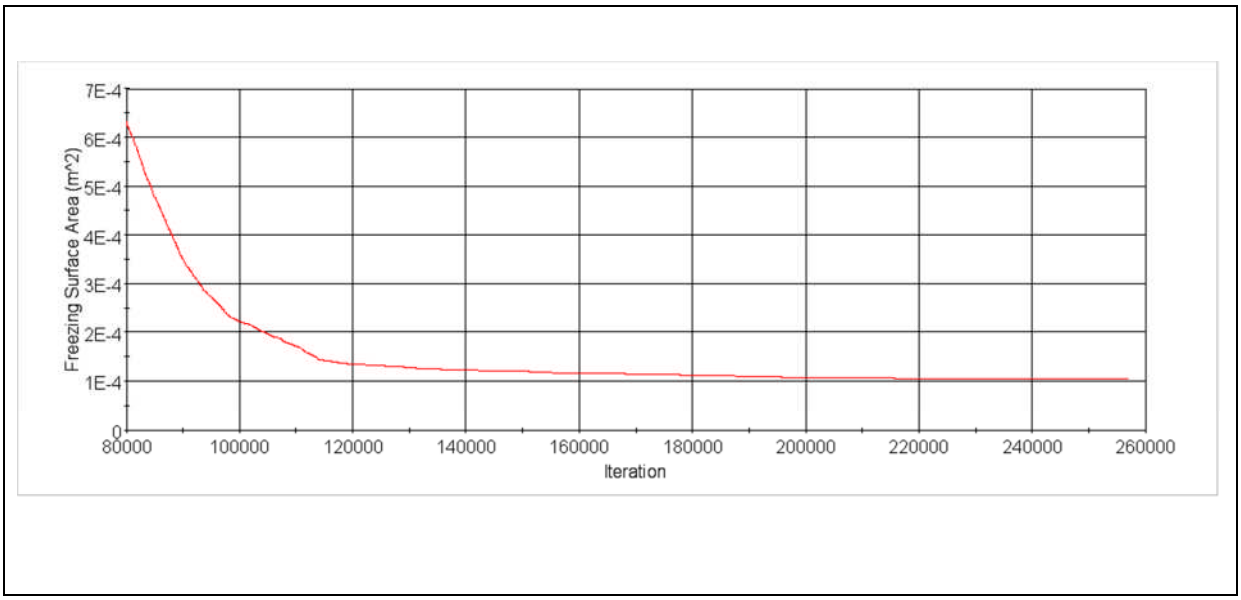

Figure 7-7 Freezing surface area during the run

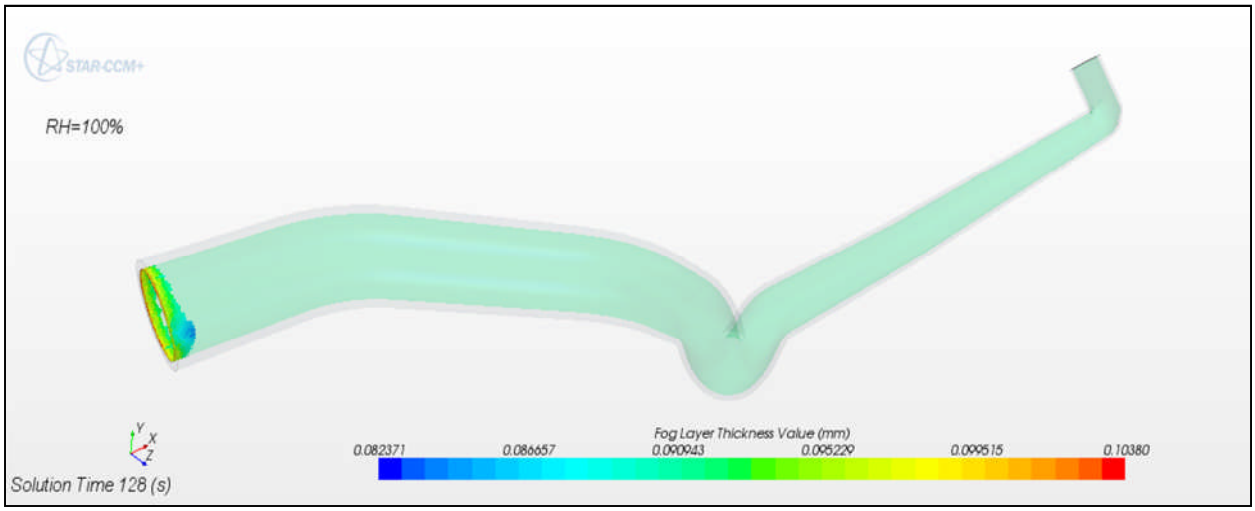

Figure 7-8 Freezing region at the internal surface of the pipe

To estimate the time in which the breather pipe would be blocked by ice, the solution time is divided by blockage ratio as given in Eq. (7-2)

$$\text{Time of Blockage (CFD)} = \frac{\text{Solution Time}}{\text{Blockage Ratio}} \tag{7-2}$$

The Blockage Ratio is defined as the ratio of the maximum fog layer thickness to the pipe radius as given:

$$\text{Blockage Ratio} = \frac{\text{Max Fog layer thickness in Freezing Zone}}{\text{Pipe Radius}} \tag{7-3}$$

It should be noted that fog layer thickness is the thickness of condensate water. The fog layer contours in the freezing zone are illustrated after 128seconds in Figure (7-8).

Table (7-4) presents the results of the CFD model after convergence in terms of the freezing surface area, total condensate volume, the maximum fog layer thickness in the freezing zone, blockage ratio and the estimated pipe blockage time.

Table 7-4 Results of CFD analysis

Parameter	Value
Freezing Surface Area (mm^2)	118.5
Total Condensate Volume (mm^3)	1473
Max Fog Layer Thickness in the freezing zone (mm)	0.1
Blockage Ratio	0.014
Time of Blockage (CFD)	9248 s (154 min)
Time of Blockage (experiments)	5400 s (90 min)
Correction Factor	1.71

Based on the blockage ratio (0.014) and the solution time (128s), the CFD model predicted that the breather pipe would be blocked after 154 minutes. Comparing this with the actual breather pipe blockage time which is 90 minutes, shows that the CFD model over predicts the pipe blockage time. This over prediction can be adjusted by employing a correction factor which in this particular case is 1.7. The size of the breather pipe, its inlet and external conditions and engine size can affect this factor. This factor helps to correct the difference between the predicted blockage time and the actual blockage time. This difference may be due to the disparities between the results of the engine test and the CFD model. These disparities may be caused by:

- Movement of condensate water which is not simulated in the CFD model but happens in the actual engine test. As a result of engine vibration, some of the condensate water in the breather pipe may be pushed toward the pipe outlet and turn to ice. This can speed up the freezing process.

- The complicated and pulsatile nature of breather pipe internal and external flow have not been simulated in the CFD model as there were not any test data available in these terms.

- The inlet relative humidity is not consistent during the Jaguar engine icing test. This would affect condensation and also the extent of freezing.

The effects of inlet relative humidity on the results of the CFD model are taken into consideration in the next section.

7.5 Sensitivity of the CFD Model to relative humidity

The sensitivity of the model is checked in terms of inlet relative humidity. The model is run at three different relative humidity values as 100%, 50% and 0% (dry air). In Figure (7-9) the freezing surface zone at each of the case, at time: 128sec, is highlighted.

a)

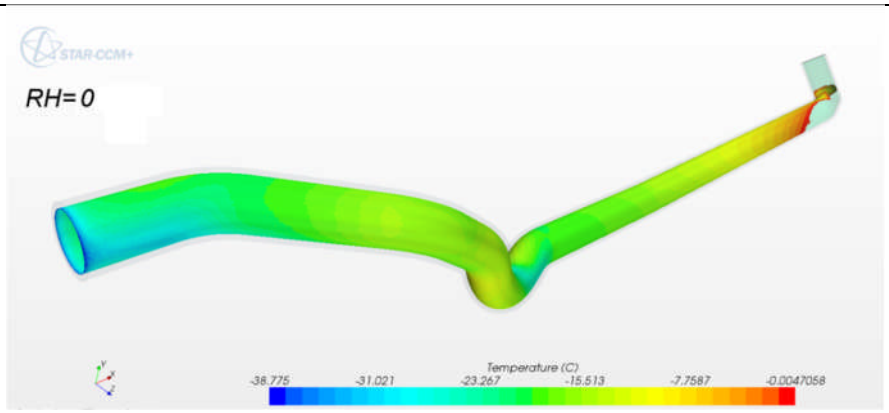

b)

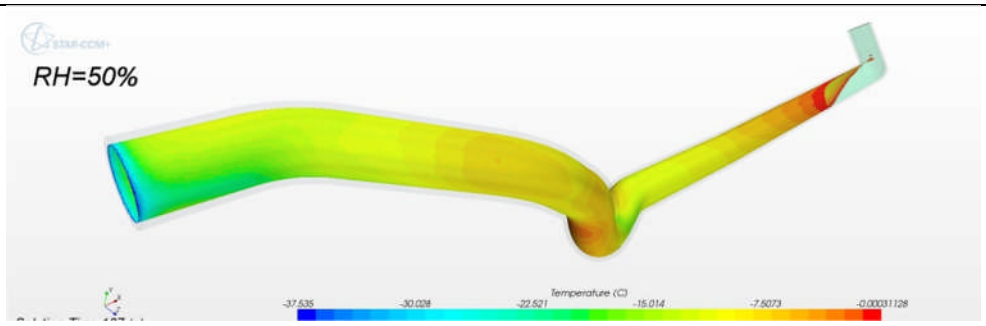

c)

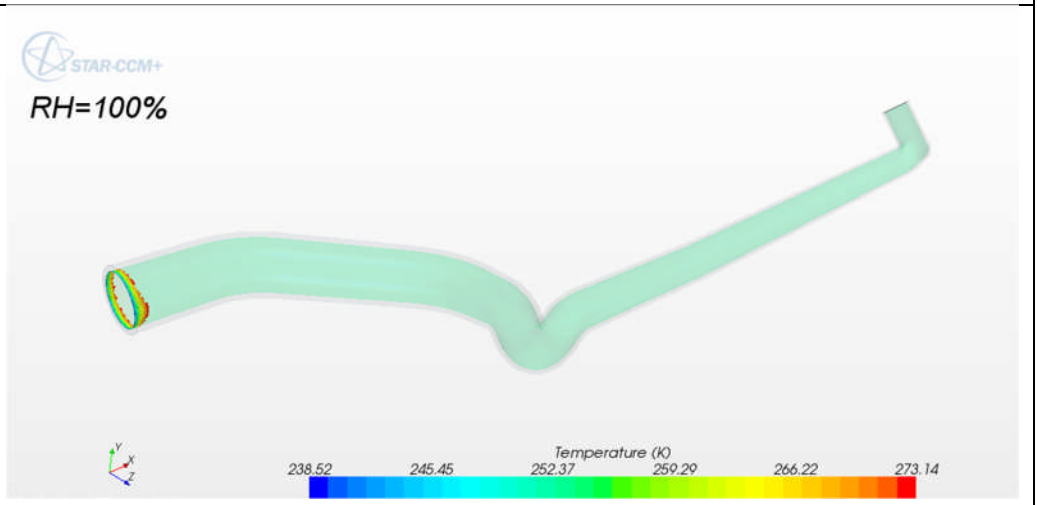

Figure 7-9 Freezing Surface at different inlet relative humidity values a) RH=0% , b) RH=50% , c) RH= 100%

As shown in Figure (7-9), increasing the relative humidity reduces the freezing surface area due to increase of latent heat transfer. However, this may not necessarily mean that the risk of ice blockage reduces as well. To investigate this further, the total condensate volume, the condensate volume in freezing zone, the total volume of the pipe in the freezing zone, the maximum fog layer thickness in the freezing zone, volume ratio and blockage ratio are compared between these cases in Table (7-5).

Table 7-5 Effects of Changing the Inlet Relative humidity on the freezing surface area

Parameter	Case 1	Case 2	Case 3
Inlet Relative Humidity	100%	50%	0%
Freezing Surface Area (mm^2)	118.5	14,523	23,231
Total Condensate Volume (mm^3)	2,598	1,061	-
Condensate Volume in Freezing Surface (mm^3)	10.3	554.5	-
Volume of the pipe in Freezing Zone (mm^3)	388	54461	-
Fog Layer Thickness (mm)	0.11	0.043	-
Volume Ratio	0.026	0.02	-
Blockage Ratio	0.015	0.0057	-

As presented in Table (7-5), increasing the inlet relative humidity from 50% to 100% reduced the freezing surface area from 14,523 mm^2 to 118.5 mm^2. However, the total condensate volume in the pipe increased from 1,061mm^3 to 2,598mm^3. This means that there is more condensate film in the freezing area in the Case 1 but its freezing surface area is less than the Case2. To compare the cases further in terms of the risk of ice formation, the volume ratio and the blockage ratio are considered. Table (7-5) presents that both volume ratio and blockage ratio in Case 1 are higher than Case 2. This comparison shows that risk of ice formation in the pipe with RH=100% may be more than for RH=50%.

7.6 Conclusion

Having the conformal mesh at the gas/solid interface provided quicker convergence. This is achieved by applying polyhedral mesh for both the gas and solid regions and applying prism layer at the gas/solid interface.

To reduce the computation effort and achieve better convergence, the solution was run firstly for 1000 iterations in steady state and when the heat flux at the internal and external surfaces of the pipe became steady the solution was switched to unsteady mode. Setting the time steps to the 0.01 second with 20 iterations per time step allowed the boundary heat fluxes to become steady at the end of each time step.

Due to conjugate heat transfer the boundary heat fluxes at the internal and external surfaces of the pipe were considered as the convergence criterion in this study.

The CFD model predicted the freezing zone at the outlet of the pipe. The results showed that the model over predicted the blockage time. This may be due to disparities between the engine test conditions and CFD model settings. These disparities may be caused by: movements of the condensate water, pulsatile nature of breather gases and external air velocity which are not modelled in the CFD model.

It was shown that the inlet relative humidity is a dominant parameter which affects the freezing surface area in the pipe. Increasing the inlet relative humidity increases the overall condensation and release of latent transfer in the pipe. This would decrease the freezing surface area but may increase the risk of ice formation. Volume ratio and blockage ratio are defined in this study to assess the risk of ice formation in the breather pipe. This study suggested that the risk of ice formation in the pipe in the case of relative humidity of 100% is higher than relative humidity of 50%.

The correction factor of 1.7 is proposed through this study which can be used as a reference parameter for the future simulation.

Chapter 8 Conclusion

The present study has established a framework for evaluation of condensation and freezing in pipes exposed to an external cool airflow. The numerical study, the experimental tests and the CFD analysis helped to highlight the dominant parameters as inlet vapour/air mixture boundary conditions (vapour mass fraction, inlet relative humidity, mixture gas flow rate), external cooling condition (temperature and air velocity) and pipe thermal conductivity on condensation and ice formation in pipes and eventually validate a CFD methodology which can evaluate the risk of ice formation and the blockage time in the actual breather pipe.

The developed one-dimensional numerical model can satisfactoraly predict the trend and magnitude of the local temperatures and heat transfer coefficient along the vertical pipe at the available test conditions within an acceptable uncertainty of $\pm 25\%$. The results of the one dimensional model showed that increasing inlet vapour mass flow rate increases the condensation mass flux along the pipe. This model was used to predict the local inner wall temperatures and starts of the freezing zone at the boundary conditions attributed to the actual engine icing tests. It showed, increasing the external convective cooling, at the fixed inlet boundary condition, increases the heat transfer along the pipe, increases the condensation rate and risk of ice formation. In other words when the external convective cooling is increased vapour is cooled faster and reaches its saturated temperature quicker. Reducing the pipe thermal conductivity has shifted the freezing zone toward the end of the pipe.

To evaluate the effects of gas mixture flow rate on heat transfer coefficient, a new correlation is developed in this study based on a degradation factor. The empirical correlation is a function of condensate film Reynolds number, gas mixture Reynolds number, gas mass fraction and Jakob number. The correlation showed that air mass fraction and the Jakob number are the most dominant factors. However, the effects of gas Reynolds number

on the degradation factor is relatively low. Using this correlation, the majority of the data agree with experimental value within the uncertainty of 15%.

The results of the experimental studies showed that measuring the gas and pipe temperatures can help to:

- Predict the hydrodynamic of condensation
- Estimate icing regions in the pipe
- Evaluate the in-tube experimental heat transfer.

The droplet sweeping can be recognizable by sudden changes in the temperatures graphs.

The condensation rate in the horizontal, the vertical and T-joint pipes have been investigated by evaluating pictures and also by measuring the droplet departure time. Both of the ways have shown that as the gas mixture travels along the pipe its vapour content decreases and this reduces the condensation rate along the pipe.

The results of observation showed that the process of condensation in the vertical pipe follows three phases of “primary droplets”, “droplets coalescences” and “sweeping”. In the horizontal and the T-joint pipe this process is divided in to four phases as “primary droplets”, “droplets coalescences”, “droplets slip down” and “condensate flow out”.

The experimental result in this study showed that the vapour mass fraction and the mixture gas temperature plays an important role on the level of condensation and heat transfer in the pipe. Increasing both of these parameters increased the heat transfer coefficient in the pipe. Increasing vapour mass fraction increases the latent heat and increasing the mixture gas temperature increases sensible heat transfer.

The comparisons of theoretical and experimental heat transfer coefficients showed that the maximum uncertainty occurred at the end of the pipe due to disturbance of the external flow.

This study suggests that attaching thermocouples on the vertical pipe had little effects on the heat transfer and the condensation rate. However hydrophobic coating delays the droplet departure time.

The results of the CFD model were compared with the test data which showed that the model is capable of predicting condensation rate, local temperatures and heat transfer coefficient with good agreement with experimental results.

The java code developed in this study can calculate the local condensate mass in the pipe in every time step and incorporates freezing heat flux as a sink term to the boundary heat flux at the gas/solid interface. Applying this code to Star CCM+ software, enables the Defogging

model to predict local averaged condensate film thickness, freezing surface area, risk of ice blockage and time of ice blockage.

In the CFD model, generating the conformal mesh at the gas/solid interface provided better convergence. This is achieved by extruding the surface mesh at the gas/solid interface for straight pipe. In the event that the pipe includes bends, like the breather pipe, a polyhedral mesh should be applied for the gas and solid regions and a prism layer should be used at the gas/solid interface for both the regions. Modelling just half of the pipe with a symmetry plane shows quicker convergence.

The optimum solution process to achieve a quicker convergence is to run the model first in steady mode and after initial convergence switch it to unsteady solver.

There are two ways to calculate local values of condensation volume in the pipe. The Java code calculates the condensate volume based on local vapour mass fraction. The other method is using surface integral of fog layer thickness on the inner surface of the pipe. It has been shown that both of the methods gives equal results within 2% difference.

The results of the CFD model presented that the gas mixture inlet temperature and vapour mass fraction affect the condensation rate and the extent of freezing in the pipe. It is also presented that increasing vapour mass fraction would increase condensation and release more latent heat. This may increase the heat transfer coefficient and increase the local temperatures.

The CFD results showed that increasing the inlet vapour mass flow rate increases the uncertainty in predicting the local temperatures and the heat transfer coefficient. This may be due to the movement of condensate water in practise which has not been simulated in the CFD model.

The blockage ratio is defined in this study as a factor which defines the severity of ice growth in the pipe and shows the potential for ice blockage. It is presented that the optimum value of the empirical condensation factor (C_{emp}) for the application of condensation in pipe is 0.9.

The validated CFD model has been used to simulate condensation and extent of freezing in one of Jaguar engine breather pipe (X250 V8 n/a) as an example. The boundary heat fluxes at the internal and external surfaces of the pipe were chosen as the convergence criterion. The simulation was run until the difference between the heat fluxes has fallen below 1%.

The CFD model has been used to estimate the icing blockage time in the engine breather pipe. The estimated blockage time is higher than the experimental value. This means the CFD model is over predicting the blockage time. This over prediction can be due to some disparities between the CFD model and the actual conditions of the icing test as follows.

- Movement of the condensate water toward the end of the pipe speed up the freezing process. The movement of water is not simulated in the model.
- The pulsatile nature of internal breather gas flow and external cold flow has not been taken into account in the CFD model.
- The inlet relative humidity during the Jaguar engine icing test is not consistence and it reduces during the Jaguar icing test. This may affect the freezing surface and condensation rate in the breather pipe.

The correction factor of 1.7 is proposed through this study to correct the estimated pipe blockage time. This can be used as a reference parameter for the future simulation.

Inlet relative humidity is one of the most dominant parameter which can affect the freezing surface area in the pipe. Increasing the inlet relative humidity increases the overall condensation in the pipe and increases the latent heat. This would decrease the freezing surface area but may increase the risk of pipe blockage.

This study suggested that the risk of ice formation in the pipe in the case of relative humidity of 100% is higher than relative humidity of 50%. Volume ratio and blockage ratio are defined in this study to address the risk of ice formation in the breather pipe.

Chapter 9 Future Work

Several aspects of this study can be subjected to further investigation and improvement.

In the experimental investigations in this study, the core and pipe wall temperatures have been measured and the movement of the condensate film and the thickness of ice formation were evaluated by observing pictures and videos. However, measuring the thickness of ice and condensate water in the pipe more accurately, can be a challenge which will provide useful data for validating the numerical study.

It is shown that using hydrophobic coating reduces the droplet departure time, it would be useful if the coated pipe temperature can be measured and the effects of coating on experimental heat transfer coefficient is evaluated.

In this study, it has been shown that defogging model doesn't take in to account the movement of condensate film. However, the fluid film model is an independent model available in Star CCM+ which can simulate the movement of a water film due to gravity and shear stress. The fluid film model doesn't simulate condensation and cannot be linked to the defogging model. Therefore, it should be employed separately. In this event, the results of the Defogging model at the end of the run should be exported in to the Fluid Film model as initial conditions. The thickness and temperature of fog layer thickness along the pipe can be exported and defined as initial condition for the water film in the Fluid Film model. Using this model may provide idea about movement of condensate water toward the freezing region.

The inlet relative humidity in the Jaguar engine tests has not been measured yet. It is presented in this study that inlet gas humidity is one of the most dominant parameter which may affect condensation and freezing in the pipe. Decreasing the relative humidity increases the freezing surface area but in the other hand it reduces the amount of condensation in the pipe. Therefore, it is proposed to Jaguar to measure the inlet breather gas humidity in their

next icing tests. The other aspect of improving the icing test is to measure the breather pipe temperature at several locations along the pipe and also make the breather pipe with a transparent material which allows observing the hydrodynamic of condensation and location of freezing region.

Appendix A: Mass Transfer

Mass transfer refers to mass in transit due to a species concentration gradient in a mixture. In fact the, driving potential for mass transfer due to diffusion in a gas mixture is the species concentration gradient.

Let V_v and V_a are the vapor and air velocities with respect to stationary coordinates, respectively. These species velocities results from the gas bulk motion and diffusion of the vapor superimposed on the bulk motion. Hence, the absolute mass flux of vapor with respect to stationary coordinate is defined as $m_v'' = \rho_v V_v$. Specifically, the absolute mass flux of vapour results from the mass flux of vapour bulk motion, $\rho_A V$, and mass flux due to the diffusion superimposed on the bulk motion, J_v, as follows.

$$m_v'' = \rho_v V_v = \rho_v V + J_v \qquad (A.1)$$

V is the local mass average velocity of the gas mixture defined as follows.

$$V = \frac{\rho_a V_a + \rho_v V_v}{\rho_a + \rho_v} = \frac{m_a'' + m_v''}{\rho} = W_a V_a + W_v V_v \qquad (A.2)$$

Substituting Eq. (A.1) into Eq. (A.2)

$$m_v'' = J_v + W_v (m_v'' + m_a'') \qquad (A.3)$$

In the above equations J_A is the diffusive mass flux, mass flux due to diffusion. This is caused by the vapour concentration gradient. The greater the concentration difference , $\frac{dw_v}{dy}$, between the two layer of species is, the more diffusion flux J_A becomes.

The vapour diffusive mass flux, is defined as the vapor transport relative to mass-average velocity of the mixture (V) as follows.

$$J_A = \rho_A (V_A - V) = \rho_A \left(V_A - \left[W_A V_A + W_B V_B\right]\right) \qquad (A.4)$$

Applying the Fick's law of diffusion which is the mass transfer analogous to Fourier's law, the diffusive vapour mass flux is defined as Eq. (A.5)

$$J_A = -\rho D_{AB} \nabla w_A \qquad (A.5)$$

The minus sign in the above equation explains that the diffusion occurs in the direction of decreasing concentration.

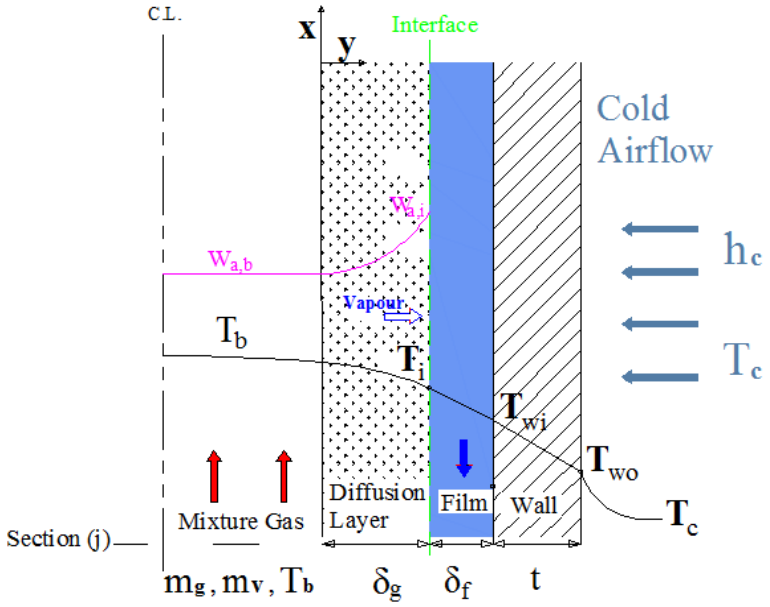

Figure A-1 Physical model control volume

For the air-steam mixture, the steady-state diffusion equations in radial direction, y, obtained by substituting Eq. (A.5) into Eq. (A.3) as follows:

$$m_v'' = -\rho D_v \frac{\partial W_v}{\partial y} + W_v m_t'' \qquad (A.6)$$

$$m_a'' = -\rho D_a \frac{\partial W_a}{\partial y} + W_a m_t''$$

Where D_v and D_a are the diffusion coefficients for the vapour and the air, respectively.

In the vapour condensation in the pipe, the condensate film is impermeable to the air, therefore diffusive mass flux of the air at the film-gas interface is zero, as given in Eq. (A.7)

$$m_a'' = 0 \qquad m_t'' = m_v'' \qquad (A.7)$$

In other word, the air molecular are motionless in the radial direction relative to the stationary coordinate and the vapour molecular diffuses through the diffusion layer. Therefore, the Eq. (A.6) reduced to

$$m_v'' = -\rho D_v \frac{\partial W_v}{\partial y} + W_v m_v'' \qquad (A.8)$$

$$0 = -\rho D_a \frac{\partial W_a}{\partial y} + W_a m_v''$$

Considering the assumption that the mixture density and diffusion coefficient are not a function of radial position, y, the vapour diffusive mass flux can be evaluated by rearranging and integrating the above equation.

$$\int_{W_{v,i}}^{W_{v,b}} \frac{d(1-W_v)}{(1-W_v)} = \frac{m_v''}{\rho D}\int_0^{\delta_g} dy \qquad (A.9)$$

$$m_v'' = \frac{\rho D}{\delta_g}\ln\left(\frac{1-W_{v,i}}{1-W_{v,b}}\right) \qquad (A.10)$$

Appendix B: Diffusion Coefficient of water vapour in air

There are different methods for calculating the diffusion coefficient of water vapor in air. Hasanein (1991), evaluate the vapour diffusion coefficient as follows.

$$D_v = \left(\frac{D_{va}}{x_a} \right) \qquad (B.1)$$

Where D_{va} is the binary diffusion coefficient and is obtained from the following equation.

$$D_{va} = \frac{6.6 \times 10^{-4} T^{1.83}}{P\left[\left(\frac{T}{P} \right)_v^{1/3} + \left(\frac{T}{P} \right)_a^{1/3} \right]^3} \sqrt{\frac{1}{M_a} + \frac{1}{M_v}} \qquad (B.2)$$

The empirical diffusion coefficient of water vapour diffusing in air is 0.282 (cm^2/s) at one atmosphere.

Fuller (1966) developed an empirical relation as follows.

$$D_{va} = 10^{-3} \frac{T^{1.75}}{P\left[V_v^{1/3} + V_a^{1/3} \right]^2} \sqrt{\frac{1}{M_a} + \frac{1}{M_v}} \qquad (B.3)$$

Where P is in atmosphere pressure, T is in Kelvin and V_a and V_v are the volumes of parts of the air molecule and vapour molecule, respectively.

Figure (B-1) illustrates the calculated diffusion coefficient of water vapour in air as a function of temperature, provided by Bolz and Tuve (1976).

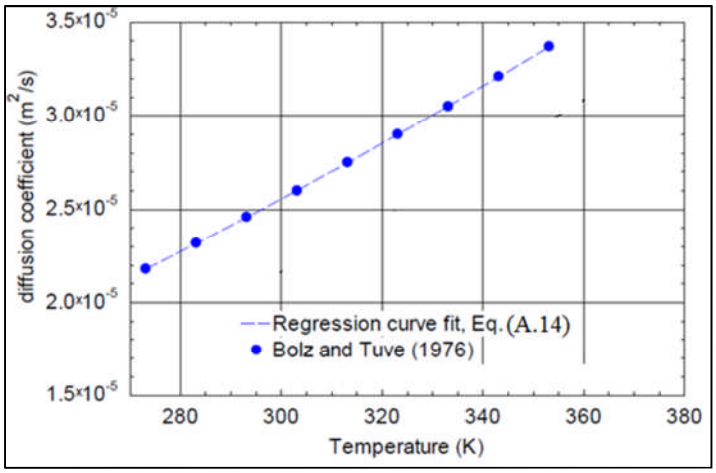

Figure B-1: The air-water vapour diffusion coefficient as a function of temperature, estimated using the method provided by Bolz and Tuve (1976).

The diffusion coefficient of water vapor in air can be obtained by a more accurate equation using a regression curve fit to the data from Bolz and Tuve (1976) as presented in Eq. (B-4) which is used in this study.

$$D_{va} = -2.775\times10^{-6} + 4.479\times10^{-8}T + 1.656\times10^{-10}T^2 \qquad (B.4)$$

Appendix C: Matlab Code

This appendix presents the Matlab code developed in this study. The names of variables are self-explanatory. If additional clarifications are required, comments are inserted. All the thermodynamic tables required to look up are listed in the code.

```
clc
clear all


%% Geometry conditions
Di=0.015; ri=Di/2; Ai=3.14/4*Di^2;    % pipe inside diameter (m)
t=0.002; Pi=2*3.14*ri                  % Wall thickness (m)
Do=Di+2*t; ro=Do/2;Ao=3.14/4*Do^2;   % pipe inside diameter (m)
Dm=0.017; rm=Dm/2; Am=3.14/4*Dm^2;    % pipe inside diameter (m)
Po=2*3.14*ro
Kw=0.25;                             % Thermal conductivity of Nylon (W/mK)

%% Properties Library

% Air properties at different temperature at atmospheric pressure
Taref=[100,150,200,250,300,350,400]-273;
Mua=[71.1,103.4,132.5,159.6,184.6,208.2,230.1]*10^(-7); % N.s/m2
Ka=[0.009246,0.013735,0.01809,0.02227,0.02624,0.030030,0.03365]; %W/m.K
Cpa=[1.0266,1.0099,1.0061,1.0053,1.0057,1.0090,1.0140]*1000; % J/kgK;
Pra=[0.770,0.753,0.739,0.722,0.708,0.697,0.689];

Ma=0.028966;                          % kg/mol

% saturated water properties at different temperature and pressure

Tlref=[273.15,275,280,285,290,295,300,305,310,315,320,325,330,335,340,345,350,355,3
60,365,370]-273;
Psat=[0.00611,0.00697,0.00990,0.01387,0.01917,0.02617,0.03531,0.04712,0.06221,0.081
32,0.1053,0.1351,0.1719,0.2167,0.2713,0.3372,0.4163,0.51,0.6209,0.7514,0.9040]*10^5
; % Pa
Vf=[1,1,1,1,1.001,1.002,1.003,1.005,1.007,1.009,1.011,1.013,1.016,1.018,1.021,1.024
,1.027,1.030,1.034,1.038,1.041]*0.001; % m3/kg
Vv=[206.3,181.7,130.4,99.4,69.7,51.94,39.13,28.74,22.93,17.82,13.98,11.06,8.82,7.09
,5.74,4.683,3.846,3.180,2.645,2.212,1.861]; % m3/kg
Hfg=[2502,2497,2485,2473,2461,2449,2438,2426,2414,2402,2390,2378,2366,2354,2342,232
9,2317,2304,2291,2278,2265]*1000; %j/kg
Cpf=[4.217,4.211,4.198,4.189,4.184,4.181,4.179,4.178,4.178,4.179,4.180,4.182,4.184,
4.186,4.188,4.191,4.195,4.199,4.203,4.209,4.214]*1000; % j/kgK
Cpv=[1.854,1.855,1.858,1.861,1.864,1.868,1.872,1.877,1.882,1.888,1.895,1.903,1.911,
1.920,1.930,1.941,1.954,1.968,1.983,1.999,2.017]*1000; % j/kgK
Muf=[1750,1652,1422,1225,1080,959,855,769,695,631,577,528,489,453,420,389,365,343,3
24,306,289]*10^(-6); %Ns/m2
Muv=[8.02,8.09,8.29,8.49,8.69,8.89,9.09,8.29,9.49,9.69,9.89,10.09,10.29,10.49,10.69
,10.89,11.09,11.29,11.49,11.69,11.89]*10^(-6); %Ns/m2
Kf=[569,574,582,590,598,606,613,620,628,634,640,645,650,656,660,668,668,671,674,677
,679]*0.001; %W/mk
Kv=[18.2,18.3,18.6,18.9,19.3,19.5,19.6,20.1,20.4,20.7,21,21.3,21.7,22,22.3,22.6,23,
23.3,23.7,24.1,24.5]*0.001; %W/mk
Prv=[12.99,12.22,10.26,8.81,7.56,6.62,5.83,5.20,4.62,4.16,3.77,6.42,3.15,2.88,2.66,
2.45,2.29,2.14,2.02,1.91,1.80];
Prf=[0.815,0.817,0.825,0.833,0.841,0.849,0.857,0.865,0.873,0.883,0.894,0.901,0.908,
0.916,0.925,0.933,0.942,0.951,0.960,0.969,0.978];

Mv=0.01802;                           % kg/mol
```

```
%% Experimental Library
Vcb=[50,50,50,50,40];
Lcb=[0.03,0.08,0.13,0.18,0.23,0.28,0.33,0.38,0.43,0.48,0.53,0.58,0.63,0.68,0.73,0.7
6];
hc50b=[58,60,66,62,51,54,60,60,72,60,44,45,43,41,41,8];
hc40b=[41,41,47,42,42,42,54,49,59,39,38,31,42,32,37,8];

%% Averaged 4 to 12 min
LTwmb=[0.06,0.15,0.24,0.33,0.43,0.52,0.61,0.7,0.75];
TwmExpb(1,:)=[11.0,10.4,1.0,-2.5,-3.4,-4.0,-2.4,-4.0,-1.5];
TwmExpb(2,:)=[19.8,15.6,7.1,3.7,2.1,-1.8,1.6,2.6,2.8];
TwmExpb(3,:)=[9.6,4.9,-3.3,-6.3,-7.7,-10.5,-9.7,-7.7,-2.1];
TwmExpb(4,:)=[23.4,19.2,9.0,2.6,1.9,-3.2,-1.7,0.9,0.9];
TwmExpb(5,:)=[9.5,4.3,-1.4,-6.7,-7.9,-9.5,-7.3,-5.6,-2.7];

TwmExpErrorb(1,:)=[0.966    0.555   0.769   0.450   0.564   0.876   0.010   0.585
0.432]';
TwmExpErrorb(2,:)=[1.027    0.360   0.258   0.577   0.565   0.328   0.008   0.375
0.175]';
TwmExpErrorb(3,:)=[2.358    0.779   0.515   0.191   0.147   0.096   0.005   0.958
0.138]';
TwmExpErrorb(4,:)=[1.674    1.332   0.583   0.614   0.615   0.540   0.004   0.674
0.717]';
TwmExpErrorb(5,:)=[0.599    0.837   0.505   0.434   0.674   0.921   0.005   0.599
0.198]';

TwiExpMb(1,:)=[13.71    13.16   2.64    -1.02   -1.71   -2.89   -1.13   -2.95   -
0.24]';
TwiExpMb(2,:)=[23.27    18.81   9.23    5.76    4.36    -0.57   3.15    4.11
4.35]';
TwiExpMb(3,:)=[12.16    7.23    -1.95   -5.07   -6.42   -9.87   -9.02   -6.89   -
0.89]';
TwiExpMb(4,:)=[27.25    22.82   11.29   4.62    4.14    -2.02   -0.47   2.24
2.26]';
TwiExpMb(5,:)=[12.11    6.49    0.04    -5.57   -6.67   -8.72   -6.43   -4.66   -
1.53]';

LTb=[0,0.15,0.33,0.61,0.75];
TbExpb(1,:)=[86,46.0,39.0,27.6,24.3];
TbExpb(2,:)=[48.4,48.7,44.3,36.5,33.5];
TbExpb(3,:)=[53.9,50.8,43.7,31.7,27.9];
TbExpb(4,:)=[60.2,57.6,52.2,44.3,40.7];
TbExpb(5,:)=[53.7,50.4,42.1,31.8,27.3];
TbExpErrorb(1,:)=[0.27  0.68    0.60    0.71    0.80]';
TbExpErrorb(2,:)=[0.85  0.36    0.42    0.56    0.67]';
TbExpErrorb(3,:)=[0.35  0.84    1.22    0.75    0.52]';
TbExpErrorb(4,:)=[0.34  0.73    0.90    0.75    0.89]';
TbExpErrorb(5,:)=[0.46  0.93    0.98    0.56    0.94]';

LHTCb=[0.15,0.33,0.61,0.75];
HTCExpb(1,:)=[42.2  18.9    21.3    17.4]*1.27';
HTCExpb(2,:)=[59.7  30.9    30.6    26.2]*1.27';
HTCExpb(3,:)=[26.1  12.2    8.7     14.4]*1.27';
HTCExpb(4,:)=[51.4  20.6    14.1    12.5]*1.27';
HTCExpb(5,:)=[19.0  11.3    9.9     9.7]*1.27';
HTCExpErrorb(1,:)=[1.92 1.76    1.15    5.15]';
HTCExpErrorb(2,:)=[2.63 2.62    1.55    7.72]';
HTCExpErrorb(3,:)=[1.48 1.08    0.43    4.26]';
HTCExpErrorb(4,:)=[3.00 1.67    0.86    3.71]';
HTCExpErrorb(5,:)=[1.18 0.66    1.35    1.55]';

mainb=[1.43,1.39,0.81,0.82,0.62]; % kg/hr
mvinputb=[0.023,0.187,0.187,0.277,0.220]; % kg/hr

%% Average 12 min

LTwmb=[0.06,0.15,0.24,0.33,0.43,0.52,0.61,0.7,0.75];
```

```
TwmExpb(1,:)=[8.6   7.0 -1.1    -4.4    -5.0    -5.7    -4.5    -5.9    -2.3]';
TwmExpb(2,:)=[17.4  13.2    5.0 1.8 0.4 -3.2    -0.3    0.2 1.9]';
TwmExpb(3,:)=[7.5   2.5 -4.4    -7.4    -8.5    -11.2   -10.5   -9.0    -2.6]';
TwmExpb(4,:)=[20.6  15.2    6.4 0.3 -0.1    -4.9    -3.7    -1.5    -0.4]';
TwmExpb(5,:)=[9.4   4.4 -1.5    -6.8    -7.8    -9.6    -7.9    -5.9    -2.8]';
TwmExpErrorb(1,:)=[1.278    5.290   6.028   3.842   3.510   3.324   3.464   4.004
0.013]';
TwmExpErrorb(2,:)=[0.291    6.413   6.361   4.820   4.493   4.211   3.633   4.477
0.013]';
TwmExpErrorb(3,:)=[0.434    4.642   4.757   2.570   2.400   2.183   1.752   1.907
0.191]';
TwmExpErrorb(4,:)=[0.283    6.912   7.565   5.464   4.462   4.328   3.448   3.849
0.070]';
TwmExpErrorb(5,:)=[0.137    0.674   0.682   0.806   0.529   0.569   0.665   1.106
0.113]';

TwoExpMb(1,:)=[1.19 -0.39   -5.47   -8.48   -9.44   -8.82   -7.67   -8.64   -
4.08]';
TwoExpMb(2,:)=[7.75 4.10    -0.80   -3.86   -5.69   -6.81   -4.36   -3.69   -
0.29]';
TwoExpMb(3,:)=[0.44 -3.64   -8.02   -10.69  -11.93  -13.13  -12.44  -11.15  -
4.39]';
TwoExpMb(4,:)=[10.14    5.57    0.23    -4.96   -5.99   -8.14   -7.06   -5.09   -
2.39]';
TwoExpMb(5,:)=[3.69 -0.68   -5.17   -9.96   -10.95  -11.50  -10.06  -8.23   -
4.41]';

TwiExpMb(1,:)=[16.84    15.37   3.88    0.15    0.04    -2.23   -0.93   -2.82   -
0.31]';
TwiExpMb(2,:)=[28.25    23.47   11.55   8.21    7.16    0.95    4.18    4.65
4.38]';
TwiExpMb(3,:)=[15.54    9.50    -0.31   -3.72   -4.68   -9.08   -8.31   -6.63   -
0.68]';
TwiExpMb(4,:)=[32.40    26.12   13.25   6.30    6.59    -1.16   0.01    2.53
1.78]';
TwiExpMb(5,:)=[15.81    10.17   2.60    -3.20   -4.29   -7.45   -5.39   -3.24   -
0.97]';

LTbb=[0,0.15,0.33,0.61,0.75];
TbExpb(1,:)=[49.9   45.8    39.2    27.9    24.8]';
TbExpb(2,:)=[49.2   48.1    43.6    35.5    32.6]';
TbExpb(3,:)=[53.4   50.2    42.9    30.9    27.7]';
TbExpb(4,:)=[60.3   57.4    51.4    43.3    40.0]';
TbExpb(5,:)=[53.5   50.5    42.2    31.9    27.4]';
TbExpErrorb(1,:)=[3.42  3.31    1.51    7.10    7.53]';
TbExpErrorb(2,:)=[3.98  4.66    1.89    6.27    6.53]';
TbExpErrorb(3,:)=[2.45  2.52    1.16    5.20    5.30]';
TbExpErrorb(4,:)=[2.54  4.04    2.09    4.71    4.14]';
TbExpErrorb(5,:)=[1.51  0.69    0.27    1.26    0.82]';

LHTCb=[0.15,0.33,0.61,0.75];

HTCExpb(1,:)=[52.6  22.4    23.8    15.2];
HTCExpb(2,:)=[79.7  34.7    27.7    16.8];
HTCExpb(3,:)=[32.8  15.2    10.7    13.3];
HTCExpb(4,:)=[66.6  25.3    16.6    11.1];
HTCExpb(5,:)=[27.5  15.1    12.7    12.3];

HTCExpErrorb(1,:)=[10.66    8.80    6.23    4.4];
HTCExpErrorb(2,:)=[13.92    9.86    5.80    4.3];
HTCExpErrorb(3,:)=[6.89 5.80    2.93    3.09];
HTCExpErrorb(4,:)=[13.93    9.57    5.62    3.23];
HTCExpErrorb(5,:)=[1.23 0.88    1.54    1.6];

mainb=[1.42,1.39,0.83,0.81,0.64]; % kg/hr
mainb=[1.48,1.45,0.86,0.84,0.66];
mvinputb=[0.023,0.187,0.187,0.277,0.220]; % kg/hr
```

```
%%

Ra=287;                              % Dry air constant
Rv=462;
R=8.3144;                            % Universal gas constant
g=9.81;

for j=1:2


    %% Coolant Gas Properties    ***************

    Tc=-20;                              % C
    Vc=Vcb(1,j);
    Pc=101325;
    kc=interp1(Taref,Ka,Tc,'linear','extrap');
    muc=interp1(Taref,Mua,Tc,'linear','extrap');
    prc=interp1(Taref,Pra,Tc,'linear','extrap');

    pc=Pc/(Ra*(Tc+273));
    Rec=pc*Vc*Do/muc;
    %% Inlet Conditions       ***************

    main=mainb(1,j);        % kg/hr
    mvin=mvinputb(1,j);     % kg/hr

    main=main/3600;         % kg/s
    mvin=mvin/3600;         % kg/s

    T=TbExpb(j,1); Tk=273+T;               % Gas mixture Temperature (C)


    P=101325;

    %% Correct Vapour Mass flow to Get the Gas Saturated

    Psatvb=interp1(Tlref,Psat,T,'linear','extrap');
    Pv=Psatvb;
    sH=0.622*Pv/(P-Pv);
    mvsat=sH*main;
    mvsatkghr=mvsat*3600;

    %% Vapor mass flow rate at the outlet

    Psatvout=interp1(Tlref,Psat,TwiExpMb(j,9),'linear','extrap');
    Pvout=Psatvout;
    sHout=0.622*Pvout/(P-Pvout);
    mvout=sHout*main;
    mvoutkghr=mvout*3600;


    %% Inlet Mass Flow rate      $$$$$$$$$$$$$$$$$$$$$$$$$$$$$$$$$$$$$$$$$$$$

    ma=main;
    mv=mvsat;

    if j==1
        mv=mvin;
    end

    %% Initial Conditions

    mf=mv-mvout;
    mc=0;
    i=0;
    L1=0;
    deltaL=0.001; %m
    deltaT=0;
```

```
%% Main Code

while L1<0.75

    if L1>0.4
        deltaL=0.002
    end

    i=i+1;
    L1

    T=T-deltaT;
    Tb(1,i)=T;

    PsatT=interp1(Tlref,Psat,T,'linear','extrap');
    Pasat=P-PsatT;
    sHsat=0.622*PsatT/(P-PsatT);
    mvsatb=sHsat*ma;

    mv=mv-mc;

    sH=mv/ma;
    Pv=P*sH/(0.622+sH);
    Pa=P-Pv;
    RH=Pv/PsatT;

    mvb(1,i)=mv;
    RHb(1,i)=RH;
    mf=mf-mc

    P=(0.622*Pv+sH*Pv)/sH;              % Gas mixture pressure (pa)
    xvb=Pv/P;
    xab=1-xvb;
    Wvb=Mv*xvb/(Ma*(1-xvb)+Mv*xvb);
    Wab=(P-Pv)/(P-(1-Mv/Ma)*Pv);

    M=xvb*Mv+(1-xvb)*Ma;

    if Vc==50
        hc=interp1(Lcb,hc50b,L1,'linear','extrap');

    else
        hc=interp1(Lcb,hc40b,L1,'linear','extrap');
    end

    % Dry Air Physical Properties        ****************************

    mua=interp1(Taref,Mua,T,'linear','extrap');
    ka=interp1(Taref,Ka,T,'linear','extrap');
    pra=interp1(Taref,Pra,T,'linear','extrap');
    cpa=interp1(Taref,Cpa,T,'linear','extrap');

    % Vapour physical properties          ****************************

    muv=interp1(Tlref,Muv,T,'linear','extrap');
    kv=interp1(Tlref,Kv,T,'linear','extrap');
    prv=interp1(Tlref,Prv,T,'linear','extrap');
    cpv=interp1(Tlref,Cpv,T,'linear','extrap');

    pa=(Pa)/(Ra*(T+273));                           % air density
    pv=Pv/(Rv*(T+273)) ;                            % Vapour density

    % Mixture Gas Conductive (kg) and Viscosity (mug)  ***************

    phav=1/sqrt(8)*(1+(Ma/Mv))^(-0.5)*(1+(mua/muv)^0.5*(Mv/Ma)^0.25 )^2;
    phva=1/sqrt(8)*(1+(Mv/Ma))^(-0.5)*(1+ (muv/mua)^0.5*(Ma/Mv)^0.25 )^2;
    mug=(xab*mua)/(xab+xvb*phav)+(xvb*muv)/(xab*phva+xvb);
```

```
kg=(xab*ka)/(xab+xvb*phav)+(xvb*kv)/(xab*phva+xvb);

% Mixture Gas Velocity and Reynolds       ************************

Reg=4*(ma+mv)/(3.14*Di*mug);                % Coolant air Reynolds
pg=pa+pv;                                   % gas mixture density
ug=(ma+mv)/(pg*3.14*ri^2);                  % gas mixture velocity

% Mixture Gas pressure drop  ************************************

f0=0.079/(Reg^(0.25));
dP=0.5*f0*(0.5*pg*ug^2)/ri;
P=P-dP;

% Experimental Temperatures >>>>>>>>>>>>>>>>>>>>>>>>>>>>>>>>>>>>>>>

TbExp=interp1(LTbb,TbExpb(j,:),L1,'linear','extrap');
TwmExp=interp1(LTwmb,TwmExpb(j,:),L1,'linear','extrap');
HTCExp=interp1(LHTCb,HTCExpb(j,:),L1,'linear','extrap');
U=(log(ro/rm)*ro/Kw+1/hc)^(-1);

QfluxExp=U*(TwmExp-Tc);
TwoExp=QfluxExp/hc+Tc;
TwiExp2=TwmExp+QfluxExp*ro*log(rm/ri)/Kw;

TwiExp=interp1(LTwmb,TwiExpMb(j,:),L1,'linear','extrap');

%% Code 2 Calculate Wall Temperature (Twi)

% Initial Condition

deltaTwi=10;
Twi=(T-20);

if i>=2
    Twi=Twib(1,i-1)+2;
end

while deltaTwi>0.2

    Twi=Twi-0.1;

    %%  Core Code Calculate Interface Temperature (Ti)

    % Initial Condition

    deltaTi=100;

    Ti=(T+Twi)/2;

    if i>=2
        Ti=Tib(1,i-1)+4;
    end

    while deltaTi>0.05

        Ti=Ti-0.1;

        % Air and Vapor mass fraction at the interface ***********

        Psatvi=interp1(Tlref,Psat,Ti,'linear','extrap');
        Pai=P-Psatvi;
        xvi=Psatvi/P; xai=1-xvi;
        Wvi=Mv*xvi/(Ma*(1-xvi)+Mv*xvi);
        Wai=1-Wvi;
        M=xvi*Mv+xai*Ma;

        % Film heat transfer coefficient ( hf )*******************
```

```
                Tf=Twi+0.31*(Ti-Twi);                % film temp (Tf)

                % film properties

                vf=interp1(Tlref,Vf,Tf,'linear','extrap');
                muf=interp1(Tlref,Muf,Tf,'linear','extrap');
                kf=interp1(Tlref,Kf,Tf,'linear','extrap');
                cpf=interp1(Tlref,Cpf,Tf,'linear','extrap');

                nuf=muf*vf;

                pl=1/vf;
                Rel=4*mf/(3.14*Di*muf);

                % Interfacial Shear stress and Nondimensional parameters

                ti=0.5*f0*pg*ug^2;
                L=((nuf^2)/g)^(1/3) ;          % Dimensionless length
                td=ti/(pl*g*L) ;               % Dimensionless shear stress
                G=1+(1/(pl*g))*dP;

                % Film thickness

                delFd=0.5*(24*Rel/G)^(1/3)+0.5*(td/G)+0.5*(24*Rel/G)^(-
1/3)*(td/G)^2+1/3*(24*Rel/G)^(-2/3)*(td/G)^(3);
                delF=delFd*L;
                hfd=kf/delF;

                delFNU2=0.5*(24*Rel/1)^(1/3)+0.5*(0/1)+0.5*(24*Rel/1)^(-
1/3)*(0/1)^2+1/3*(24*Rel/1)^(-2/3)*(0/1)^(3);
                hfNU2=kf/delFNU2;

                % Nusselt Film Solution

                delFNU=(3*muf^2*Rel/(4*pl*(pl-pg)*g))^(1/3);
                delF3=(3*nuf*mf/(3.14*Di*(pl-pg)*g))^(1/3);
                hfNU=kf/delFNU;

                if Rel>4
                    hf=hfd/(1.33*(4*Rel)^(-0.11));
                else
                    hf=hfd;
                end


                % Convective heat trasfer ( hcv )************************

                if Reg<2300;
                    hcv=(48/11)*(kg/Di);
                else
                    hcv=0.023*Reg^(0.8)*pra^(0.35)*(kg/Di);
                end

                % Condensive heat trasfer ( hcd ) ***********************

                Tbar=(T+Ti)/2;

                hfg=interp1(Tlref,Hfg,Tbar,'linear','extrap');

                hfg2=hfg+cpv*(T-Ti);
                xvbar=(xvb-xvi)/log(xvb-xvi);
                Mbar=xvbar*Mv+(1-xvbar)*Ma;
                cpg=xvbar*cpv+(1-xvbar)*cpa;

                Mi=xvi*Mv+xai*Ma;
                Mb=xvb*Mv+xab*Ma;
```

```
                pbar=Mbar*P/(R*Tbar);

                phi1=log((1-Wab)/(1-Wai))/log(Wai/Wab);

                phi2=Mbar^2/(Mb*Mi);

                %D=0.24*0.0001*(1.013/(P*10^(-5))*((Ti+273)/273)^(1.75))*(1-
0.3*(P*10^(-5))/200);

                D=-2.775*10^(-6)+4.479*10^(-8)*(Ti+273)+1.656*10^(-10)*(Ti+273)^2;

                Sc=mug/(pg*D);

                kc=phi2/phi1*(hfg*hfg2*P*D*Mv*Ma)/(R^2*(Tbar+273)^3);

                if Reg<2300
                    hcd=(48/11)*kc/Di;
                else
                    hcd=0.023*Reg^(0.8)*Sc^(0.35)*kc/Di;
                end

                % diffusion layer thickness    ***************

                delg=hfg2*pg*D/(hcv*(T-Ti))*log((1-Wvi)/(1-Wvb));

                % Update the interface temperature (Ti)  *****************

                Qf=hf*(Ti-Twi);
                Qb=(hcv+hcd)*(T-Ti);

                Ti2=( T*(hcd+hcv)+Twi*hf )/(hf+hcd+hcv);

                deltaTi=abs(Ti2-Ti);

            end

            Ti=Ti2;

            % Compute the Outer wall temperature (Two)

            Two=Twi-( hf*(Ti-Twi)*( Di*log(Do/Di)/(2*Kw) ) );

            % Update the Inner wall temperature (Twi)

            Twi2=Two+( hc*(Two-Tc)*(Do*log(Do/Di)/(2*Kw)));
            deltaTwi=abs(Twi2-Twi);
            deltaTwib(1,i)=deltaTwi;

        end

        %% Compute the Outer wall temperature (Two)

        Twi=Twi2;

        mvbi=ma*(1-Wai)/Wai;
        mvib(1,i)=mvbi;
        hcdnew=mvbi*hfg/(T-Ti);

        HTCExp
        HTC=(1/(hcv+hcd)+1/hf)^(-1);
        HTCnew=(1/(hcv+hcdnew)+1/hf)^(-1);
        F1=HTCExp/HTC;
        F2=HTCExp/hf;
        F3=HTCExp/hcd;

        F1b(1,i)=F1;
        F2b(1,i)=F2;
        F3b(1,i)=F3;
```

```
        Ja=cpg*(T-Twi)/hfg;
        Jab(1,i)=Ja;
        mcflux=hcd*(T-Ti)/hfg;
        mc=hcd*(T-Ti)/hfg*Pi*deltaL;              % local condensate mass
        mcb(1,i)=mc;
        mvb(1,i)=mv;

        if i>=2
            mc2=mvb(1,i-1)-mvb(1,i)
            mc2b(1,i)=mc2;
            mcb(1,i-1);
            deviationmc=(mc2b(1,i)-mcb(1,i-1))/mc2b(1,i-1);
            mcbi=mvib(1,i-1)-mvib(1,i)
        end

        %% Calculate the delta L

        Qwi=(2*Kw)/(Di*log(Do/Di))*(Twi-Two)
        Qwo=(2*Kw)/(Do*log(Do/Di))*(Twi-Two)

        Qf=hf*(Ti-Twi)
        Qb=(hcv+hcd)*(T-Ti)
        QHTC=(HTC)*(T-Twi)
        Qc=hc*(Two-Tc)
        %         deltaTiha=abs(Ti3-Ti2);
        deltaKIR=Qf-Qwi;

        delWvbWvi=(Wvb-Wvi);
        HTC2=Qwi/(T-Twi);

        hice=334000;  % Enthaply of freezing
        Ql=2*3.14*Kw*(Twi-Two)/log(ro/ri)*deltaL
        Qt(1,i)=Ql;

        if i>=2
            mvave=(mvb(1,i)+mvb(1,i-1)-mc)/2;
            deltaT2=(Ql-mc*hfg)/(ma*cpa+mvave*cpv);
            Ql=(Qt(1,i)+Qt(1,i-1))/2;

            if Twi<0
                deltaT=(Ql-(mc*hfg+mc*hice))/(ma*cpa+mvave*cpv);
            else
                deltaT=(Ql-mc*hfg)/(ma*cpa+mv*cpv);
            end

        end
        DelQ=Ql*deltaL;
        L1=deltaL+L1;
        DelQb(1,i)=DelQ;
        Qvb=mv*cpv*(deltaT);
        Qvb2=mv*cpv*(deltaT);
        Qab=ma*cpa*(deltaT);
        delWvbWvi=(Wvb-Wvi);

        L1b(1,i)=L1;
        deltaLb(1,i)=deltaL;
        Tcb(1,i)=Tc; Tib(1,i)=Ti; Twib(1,i)=Twi; Twob(1,i)=Two; Ubb(1,i)=ug;
        TwiExpb(1,i)=TwiExp; TwoExpb(1,i)=TwoExp;
        TbExpbextrapolate(1,i)=TbExp; HTCExpbextrapolate(1,i)=HTCExp;

        Wabb(1,i)=Wab;Waib(1,i)=Wai;Wvbb(1,i)=Wvb;Wvib(1,i)=Wvi;
        mufb(1,i)=muf;plb(1,i)=pl;pgb(1,i)=pg;Relb(1,i)=Rel;
        mvb(1,i)=mv;mab(1,i)=ma;mfb(1,i)=mf; mcfluxb(1,i)=mcflux; pab(1,i)=pa;
delFb(1,i)=delF*1000;delFNUb(1,i)=delFNU*1000;delF3b(1,i)=delF3*1000;delgb(1,i)=del
g*1000;
        mvsatbb(1,i)=mvsatb;
        delTiTw(1,i)=(Ti-Twi); kfb(1,i)=kf;
```

```
        Pvb(1,i)=Pv; xvbb(1,i)=xvb; xvib(1,i)=xvi; delWvbWvib(1,i)=delWvbWvi;
        Pb(1,i)=P;
dPb(1,i)=dP;mvb2(1,i)=mv*1000;mcb2(1,i)=mc*1000;mfb2(1,i)=mf*1000;
        Regb(1,i)=Reg;Recb(1,i)=Rec;Relb(1,i)=Rel;
        hcdb(1,i)=hcd; hfb(1,i)=hf
;hfNUb(1,i)=hfNU;hfNU2b(1,i)=hfNU2;hcvb(1,i)=hcv;hcb(1,i)=hc;
        HTCb(1,i)=HTC;
        Scb(1,i)=Sc;
        HTCExpbb(1,i)=HTCExp;

        Limitation=i;

        ErrorT=T-TbExp
        ErrorTWi=Twi-TwiExp

    end

    for gg=1:i
        RHbinv(gg,1)=RHb(1,gg);
        L1binv(gg,1)=L1b(1,gg);
        HTCbinv(gg,1)=HTCb(1,gg);
        Tbinv(gg,1)=Tb(1,gg);
        Twibinv(gg,1)=Twib(1,gg);

        hfbinv(gg,1)=hfb(1,gg);
        hcvbinv(gg,1)=hcvb(1,gg);
        hcdbinv(gg,1)=hcdb(1,gg);
        HTCbinv(gg,1)=HTCb(1,gg);
        HTCExpbbinv(gg,1)=HTCExpbb(1,gg);

        F1binv(gg,1)=F1b(1,gg);
        F2binv(gg,1)=F2b(1,gg);
        F3binv(gg,1)=F3b(1,gg);

        Regbinv(gg,1)=Regb(1,gg);
        Relbinv(gg,1)=Relb(1,gg);
        Jabinv(gg,1)=Jab(1,gg);
        Wabbinv(gg,1)=Wabb(1,gg);
        Scbinv(gg,1)=Scb(1,gg);
        hfNUbinv(gg,1)=hfNUb(1,gg);
        hfNU2binv(gg,1)=hfNU2b(1,gg);
        mcfluxbinv(gg,1)=mcfluxb(1,gg);
    end

    Numerical01=[L1binv,Tbinv,Twibinv,HTCbinv,RHbinv];

Numerical02=[hfbinv,hcvbinv,hcdbinv,HTCbinv,HTCExpbbinv,F1binv,F2binv,F3binv,Regbin
v,Relbinv,Jabinv,Wabbinv,Scbinv,hfNUbinv,hfNU2binv,mcfluxbinv];

    Experimenal01=[LTwmb(1,:);TwiExpMb(j,:);TwmExpErrorb(j,:)];
    Experimenal02=[LTb(1,:);TbExpb(j,:);TbExpErrorb(j,:)];
    Experimenal03=[LHTCb(1,:);HTCExpb(j,:);HTCExpErrorb(j,:)];

    if j==1

        xlswrite('1DCodeResults-deltaT-Twi-mvin-mvsat-Correlation2case1.xls',
Numerical01, 'R1', 'B3');
        xlswrite('1DCodeResults-deltaT-Twi-mvin-mvsat-Correlation2case1.xls',
Numerical02, 'R1', 'R3');
        xlswrite('1DCodeResults-deltaT-Twi-mvin-mvsat-Correlation2case1.xls',
Experimenal01, 'R1', 'H2');
        xlswrite('1DCodeResults-deltaT-Twi-mvin-mvsat-Correlation2case1.xls',
Experimenal02, 'R1', 'H6');
        xlswrite('1DCodeResults-deltaT-Twi-mvin-mvsat-Correlation2case1.xls',
Experimenal03, 'R1', 'H10');

    end
```

```
    if j==2

        xlswrite('1DCodeResults-deltaT-Twi-mvin-mvsat-Correlation2case1.xls',
Numerical01, 'R2', 'B3');
        xlswrite('1DCodeResults-deltaT-Twi-mvin-mvsat-Correlation2case1.xls',
Numerical02, 'R2', 'R3');
        xlswrite('1DCodeResults-deltaT-Twi-mvin-mvsat-Correlation2case1.xls',
Experimenal01, 'R2', 'H2');
        xlswrite('1DCodeResults-deltaT-Twi-mvin-mvsat-Correlation2case1.xls',
Experimenal02, 'R2', 'H6');
        xlswrite('1DCodeResults-deltaT-Twi-mvin-mvsat-Correlation2case1.xls',
Experimenal03, 'R2', 'H10');

    end

    if j==3

        xlswrite('1DCodeResults-deltaT-Twi-mvin-mvsat-Correlation2case1.xls',
Numerical01, 'R3', 'B3');
        xlswrite('1DCodeResults-deltaT-Twi-mvin-mvsat-Correlation2case1.xls',
Numerical02, 'R3', 'R3');
        xlswrite('1DCodeResults-deltaT-Twi-mvin-mvsat-Correlation2case1.xls',
Experimenal01, 'R3', 'H2');
        xlswrite('1DCodeResults-deltaT-Twi-mvin-mvsat-Correlation2case1.xls',
Experimenal02, 'R3', 'H6');
        xlswrite('1DCodeResults-deltaT-Twi-mvin-mvsat-Correlation2case1.xls',
Experimenal03, 'R3', 'H10');

    end

    if j==4

        xlswrite('1DCodeResults-deltaT-Twi-mvin-mvsat-Correlation2case1.xls',
Numerical01, 'R4', 'B3');
        xlswrite('1DCodeResults-deltaT-Twi-mvin-mvsat-Correlation2case1.xls',
Numerical02, 'R4', 'R3');
        xlswrite('1DCodeResults-deltaT-Twi-mvin-mvsat-Correlation2case1.xls',
Experimenal01, 'R4', 'H2');
        xlswrite('1DCodeResults-deltaT-Twi-mvin-mvsat-Correlation2case1.xls',
Experimenal02, 'R4', 'H6');
        xlswrite('1DCodeResults-deltaT-Twi-mvin-mvsat-Correlation2case1.xls',
Experimenal03, 'R4', 'H10');

    end

    if j==5

        xlswrite('1DCodeResults-deltaT-Twi-mvin-mvsat-Correlation2case1.xls',
Numerical01, 'R5', 'B3');
        xlswrite('1DCodeResults-deltaT-Twi-mvin-mvsat-Correlation2case1.xls',
Numerical02, 'R5', 'R3');
        xlswrite('1DCodeResults-deltaT-Twi-mvin-mvsat-Correlation2case1.xls',
Experimenal01, 'R5', 'H2');
        xlswrite('1DCodeResults-deltaT-Twi-mvin-mvsat-Correlation2case1.xls',
Experimenal02, 'R5', 'H6');
        xlswrite('1DCodeResults-deltaT-Twi-mvin-mvsat-Correlation2case1.xls',
Experimenal03, 'R5', 'H10');

    end


    %%  Plots

    if j==1
        figure(1)
        hold on
        plot (L1b,Tb)
        errorbar(LTbb,TbExpb(1,:),TbExpErrorb(1,:),'-.or')
```

```
    h1 = legend('Numerical (Run1)','Experiments (Run1)');
    xlabel('Distance from Pipe Inlet (cm)')
    ylabel('Temperature (c)')
    title('Gas Core Temperature')
    plot (L1b,Twib,L1b,TwiExpb)
    hold off

    figure (2)
    hold on
    plot(L1b,HTCb)
    errorbar(LHTCb,HTCExpb(1,:),HTCExpErrorb(1,:),'-.or')
    h1 = legend('Numerical (Run1)','Experiments (Run1)');
    xlabel('Distance from Pipe Inlet (cm)')
    ylabel('Total Heat Transfer Coefficient (C)')
    title('Total Heat Transfer Coefficient')
    hold off

    figure (3)

    plot(L1b,mvsatbb,mvb,mcb);

end

if j==2

    figure(3)
    hold on
    plot (L1b,Tb)
    errorbar(LTbb,TbExpb(2,:),TbExpErrorb(2,:),'-.or')
    h1 = legend('Numerical (Run1)','Experiments (Run1)');
    xlabel('Distance from Pipe Inlet (cm)')
    ylabel('Temperature (c)')
    title('Gas Core Temperature')
    plot (L1b,Twib,L1b,TwiExpb)
    hold off

    figure (4)
    hold on
    plot(L1b,HTCb)
    errorbar(LHTCb,HTCExpb(2,:),HTCExpErrorb(2,:),'-.or')
    h1 = legend('Numerical (Run1)','Experiments (Run1)');
    xlabel('Distance from Pipe Inlet (cm)')
    ylabel('Total Heat Transfer Coefficient (C)')
    title('Total Heat Transfer Coefficient')
    hold off
end

if j==3
    figure(5)
    hold on
    plot (L1b,Tb)
    errorbar(LTbb,TbExpb(3,:),TbExpErrorb(2,:),'-.or')
    h1 = legend('Numerical (Run1)','Experiments (Run1)');
    xlabel('Distance from Pipe Inlet (cm)')
    ylabel('Temperature (c)')
    title('Gas Core Temperature')
    plot (L1b,Twib,L1b,TwiExpb)
    hold off

    figure (6)
    hold on
    plot(L1b,HTCb)
    errorbar(LHTCb,HTCExpb(3,:),HTCExpErrorb(2,:),'-.or')
    h1 = legend('Numerical (Run1)','Experiments (Run1)');
    xlabel('Distance from Pipe Inlet (cm)')
    ylabel('Total Heat Transfer Coefficient (C)')
    title('Total Heat Transfer Coefficient')
    hold off
```

```
    end

    if j==4

        figure(7)
        hold on
        plot (L1b,Tb)
        errorbar(LTbb,TbExpb(4,:),TbExpErrorb(4,:),'-.or')
        h1 = legend('Numerical (Run1)','Experiments (Run1)');
        xlabel('Distance from Pipe Inlet (cm)')
        ylabel('Temperature (c)')
        title('Gas Core Temperature')
        plot (L1b,Twib,L1b,TwiExpb)
        hold off

        figure (8)
        hold on
        plot(L1b,HTCb)
        errorbar(LHTCb,HTCExpb(4,:),HTCExpErrorb(4,:),'-.or')
        h1 = legend('Numerical (Run1)','Experiments (Run1)');
        xlabel('Distance from Pipe Inlet (cm)')
        ylabel('Total Heat Transfer Coefficient (C)')
        title('Total Heat Transfer Coefficient')
        hold off

        figure (11)
        hold on
        plot(L1b,mvb)
        hold off

    end

    if j==5

        figure(9)
        hold on
        plot (L1b,Tb)
        errorbar(LTbb,TbExpb(5,:),TbExpErrorb(5,:),'-.or')
        h1 = legend('Numerical (Run1)','Experiments (Run1)');
        xlabel('Distance from Pipe Inlet (cm)')
        ylabel('Temperature (c)')
        title('Gas Core Temperature')
        plot (L1b,Twib,L1b,TwiExpb)
        hold off

        figure (10)
        hold on
        plot(L1b,HTCb)
        errorbar(LHTCb,HTCExpb(5,:),HTCExpErrorb(5,:),'-.or')
        h1 = legend('Numerical (Run1)','Experiments (Run1)');
        xlabel('Distance from Pipe Inlet (cm)')
        ylabel('Total Heat Transfer Coefficient (C)')
        title('Total Heat Transfer Coefficient')
        hold off
    end

end
```

Appendix D: Java Code

This appendix presents the Java code developed in this study.

```
// STAR-CCM+ macro: test005.java
package macro;

import java.util.*;
import java.util.logging.Level;
import java.util.logging.Logger;
import star.common.*;
import java.io.*;
import java.util.*;
import java.io.File;
import java.io.FileNotFoundException;
import java.io.PrintWriter;
import java.util.ArrayList;
import java.util.Scanner;
import star.base.neo.*;



public class test005 extends StarMacro {
  public void execute() {
        try {
            execute0();
        } catch (FileNotFoundException ex) {

Logger.getLogger(test005.class.getName()).log(Level.SEVERE, null,
ex);
        }
  }

private void execute0() throws FileNotFoundException {

    Simulation simulation_0 =
      getActiveSimulation();

// Generate Histogram Vapour Mass Fraction **********************

    HistogramTable histogramTable_0 =

simulation_0.getTableManager().createTable(HistogramTable.class);


histogramTable_0.setPresentationName("HistogramVapourMassFraction");

    Region region_0 =
      simulation_0.getRegionManager().getRegion("Gas");

    Boundary boundary_0 =
      region_0.getBoundaryManager().getBoundary("Outlet");
```

```
    Boundary boundary_1 =
      region_0.getBoundaryManager().getBoundary("Symmetry-Gas");

    DirectBoundaryInterfaceBoundary
directBoundaryInterfaceBoundary_0 =
      ((DirectBoundaryInterfaceBoundary)
region_0.getBoundaryManager().getBoundary("Condensation
[Gas/Pipe]"));

    Boundary boundary_2 =
      region_0.getBoundaryManager().getBoundary("Inlet");

    Boundary boundary_3 =
      region_0.getBoundaryManager().getBoundary("Condensation");

    histogramTable_0.getParts().setObjects(region_0, boundary_0,
boundary_1, directBoundaryInterfaceBoundary_0, boundary_2,
boundary_3);

    HistogramBase histogramBase_0 =
      histogramTable_0.getHistogram();

    histogramBase_0.setWeightingMode(1);

histogramBase_0.setNumberOfBin(50);

    FieldFunctionUnits fieldFunctionUnits_0 =
      histogramBase_0.getWeightingFunction();


    PrimitiveFieldFunction primitiveFieldFunction_0 =
      ((PrimitiveFieldFunction)
simulation_0.getFieldFunctionManager().getFunction("VaporMassFractio
n"));

    fieldFunctionUnits_0.setFieldFunction(primitiveFieldFunction_0);

    FieldFunctionUnits fieldFunctionUnits_1 =
      histogramBase_0.getBinFunction();

    PrimitiveFieldFunction primitiveFieldFunction_1 =
      ((PrimitiveFieldFunction)
simulation_0.getFieldFunctionManager().getFunction("Position"));

    VectorComponentFieldFunction vectorComponentFieldFunction_0 =
      ((VectorComponentFieldFunction)
primitiveFieldFunction_1.getComponentFunction(2));


fieldFunctionUnits_1.setFieldFunction(vectorComponentFieldFunction_0
);

    XYPlot xYPlot_0 =
      ((XYPlot) simulation_0.getPlotManager().getObject("XY-
VelocityCoreline"));
```

```
    Axes axes_0 =
      xYPlot_0.getAxes();

    Axis axis_0 =
      axes_0.getYAxis();

    AxisTitle axisTitle_0 =
      axis_0.getTitle();

    axisTitle_0.setText("Velocity: Magnitude (m/s)");

    axisTitle_0.setText("Velocity: Magnitude (m/s)");

// Field function Histogram Vapour Mass
Fraction(Interpolation)******


    UserFieldFunction userFieldFunction_0 =
      simulation_0.getFieldFunctionManager().createFieldFunction();


userFieldFunction_0.setPresentationName("Hist_Vapour_Mass_Frac");

    userFieldFunction_0.setFunctionName("Hist_Vapour_Mass_Frac");


userFieldFunction_0.setDefinition("interpolateTable(@Table(\"Histogr
amVapourMassFraction\"), \"Position[Z] - Min Extent\",LINEAR,
\"Vapor Mass Fraction Value - Average\", $$Position[2]) ");


// Field function Histogram Vapour Mass Flow Rate
*******************

    UserFieldFunction userFieldFunction_2 =
      simulation_0.getFieldFunctionManager().createFieldFunction();

    userFieldFunction_2.setPresentationName("MFR_Dry_Inlet(Kg/s)");

    userFieldFunction_2.setFunctionName("MFR_Dry_Inlet(Kg/s)");

    userFieldFunction_2.setDefinition("0.00015\n");

    UserFieldFunction userFieldFunction_1 =
      simulation_0.getFieldFunctionManager().createFieldFunction();

    userFieldFunction_1.setPresentationName("VapourMassFlowRate");

    userFieldFunction_1.setFunctionName("VapourMassFlowRate");


userFieldFunction_1.setDefinition("${MFR_Dry_Inlet(Kg/s)}*(${Hist_Va
pour_Mass_Frac})/(1-${Hist_Vapour_Mass_Frac}) ");
```

```
// Generate HistogramTable Vapour Mass Flow Rate
********************

    HistogramTable histogramTable_1 =

simulation_0.getTableManager().createTable(HistogramTable.class);


histogramTable_1.setPresentationName("HistogramVapourMassFlowRate");

    histogramTable_1.getParts().setObjects(region_0, boundary_0,
boundary_1, directBoundaryInterfaceBoundary_0, boundary_2,
boundary_3);

    HistogramBase histogramBase_1 =
      histogramTable_1.getHistogram();

    histogramBase_1.setWeightingMode(1);

     histogramBase_1.setNumberOfBin(50);


    FieldFunctionUnits fieldFunctionUnits_2 =
      histogramBase_1.getWeightingFunction();

    fieldFunctionUnits_2.setFieldFunction(userFieldFunction_1);

    FieldFunctionUnits fieldFunctionUnits_3 =
      histogramBase_1.getBinFunction();


fieldFunctionUnits_3.setFieldFunction(vectorComponentFieldFunction_0
);


// Export File HistogramTable Vapour Mass Flow Rate
*****************

    histogramTable_1.export(resolvePath("H:\\Work\\Java
Scripts\\Final\\ccm04.csv"), ",");


// Open the Histogram Vapor Mass Flow Rate File
*********************

      File file = new File("H:\\Work\\Java
Scripts\\Final\\ccm04.csv");

File fileTemp = new File("H:\\Work\\Java
Scripts\\Final\\Temperature.csv");

      Scanner inputFile = new Scanner(file);

      Scanner inputFileTemp = new Scanner(fileTemp);
```

```
      PrintWriter out = new PrintWriter("H:\\Work\\Java
Scripts\\Final\\BibiJende.csv");


// Declaration

     int index = 0;
     ArrayList<Double> numbers = new ArrayList<Double>();
     ArrayList<Double> subtract = new ArrayList<Double>();
     ArrayList<Double> firstColumn = new ArrayList<Double>();
     ArrayList<Double> secondColumn = new ArrayList<Double>();
     ArrayList<Double> thirdColumn = new ArrayList<Double>();
     ArrayList<Double> TempColumn = new ArrayList<Double>();
     ArrayList<Double> HeatFlux = new ArrayList<Double>();



// Read the Temperature Column

     String lineTemp;

     inputFileTemp.nextLine();
      while ( inputFileTemp.hasNextLine())
            {

       lineTemp = inputFileTemp.nextLine();
        String[] digit = lineTemp.split(",");
        TempColumn.add(Double.parseDouble(digit[3]));
      }

// Read the file contents into an array and create a New Table for
Condensate Mass Called Output

     String line;

     inputFile.nextLine();
     while ( inputFile.hasNextLine())
     {
      line = inputFile.nextLine();
       String[] digit = line.split(",");
       firstColumn.add(Double.parseDouble(digit[1]));
       numbers.add(Double.parseDouble(digit[3]));
     }

     for ( int i = 0; i < numbers.size()-1; i++)
     {
       subtract.add(numbers.get(i) - numbers.get(i+1));

      if (TempColumn.get(i)<273)
      {
       HeatFlux.add(subtract.get(i)*287000/(2*3.14*0.0075*(0.76/50))
);
           } else {
            HeatFlux.add(subtract.get(i)*0);
      }
      }
```

```
     out.println("Position[Z]" + "," + "CondensateMass" + "," +
"Temperature" + "," + "HeatFlux" );

out.println(firstColumn.get(0) + "," + "0" + "," + TempColumn.get(0)
+ "," + "0");


     for ( int i = 0; i < subtract.size(); i++)
     {
       out.println(firstColumn.get(i+1) + "," + subtract.get(i) +
"," + TempColumn.get(i) + "," + HeatFlux.get(i) );
}

//Close the file
     inputFile.close();
     out.close();

File condFile = new File("H:\\Work\\Java
Scripts\\Final\\BibiJende.csv");


     Scanner tempIn = new Scanner(condFile);
     Scanner condIn = new Scanner(condFile);
     Scanner condIn2 = new Scanner(condFile);

     String line1;
     String line2;
     String line3;

     int counter = 0;
     double temp;

     double mass = 0;
     double totalmass = 0;

     final double TEMPERATURE = 273;

     tempIn.nextLine();

      do
     {
       line1 = tempIn.nextLine();
       String[] row1 = line1.split(",");
       temp = Double.parseDouble(row1[2]);
      simulation_0.println("Temp is = " + temp);
       counter++;
     }
       while ( temp > TEMPERATURE);

     simulation_0.println("counter= " + counter);

       condIn.nextLine();
     for(int i = 0; i <counter; i++ )
      {
```

```
       line2 = condIn.nextLine();
       String[] row2 = line2.split(",");
       simulation_0.println("mass is = " +
Double.parseDouble(row2[1]));
       mass += Double.parseDouble(row2[1]);
     }

      condIn2.nextLine();

       while ( condIn2.hasNextLine())
     {
       line3 = condIn2.nextLine();
      String[] row3 = line3.split(",");
      totalmass += Double.parseDouble(row3[1]);
      }

     Double MassFreezing = totalmass - mass;

     Double Risk = (MassFreezing / totalmass)*100 ;

     simulation_0.println
("----------------------------------------");

simulation_0.println("");
     simulation_0.println("Total Mass of Condensate in the pipe = "
+ totalmass);
     simulation_0.println("");
     simulation_0.println("Mass of Condensate in Freezing Region is
= " + MassFreezing);
   simulation_0.println("Mass of Condensate in NonFreezing Region is
= " + mass);
     simulation_0.println("");
     simulation_0.println("");

 simulation_0.println("Risk of Ice formation is = " + Risk + "%");

simulation_0.println("");

if (Risk <30)
{
simulation_0.println(" -->  As the Risk is Less than 30% The Design
is Acceptable <-- ");
} else {
simulation_0.println(" -->  As the Risk is Above 30% The Design is
Not Acceptable <-- ");
}

     simulation_0.println("");
     simulation_0.println("----------------------------------------
");

     condIn.close();

  }
}
```

References

Avergard P., Lindstrom F. (2003), “Modelling of Crankcase Gas Behaviour in a Heavy-Duty Diesel Engine”, thesis (Master), Department of Automatic Control, Lund Institute of Technology

Bunn A.R. (2009) “Bunn Motorcycle Crankcase Breathing and Tuning”, http://bunnbreather.bigblog.com.au/index.do Marty (2000)

Batram, Bernhard, Brunsmann, Ingo, Knickmann, Kai-Uwe (2000), “Oil Mist Separators– The Next Generation; Hengst Filterwerke, Münster”

Barris, Marty, Closed Crankcase Filtration, http://www.meca.org/crankcasearticle.html (January 2003)

Chapman, Gilbert E. (1946) “Laboratory investigation of icing in the Carburettor and supercharger inlet elbow of an aircraft engine VI: effect of modifications to fuel-spray nozzle on icing characteristics”, naca-wr-e-175

Churchill, S. W., and H. H. S. Chu. (1975), “Correlating Equations for Laminar and Turbulent Free Convection from a horizontal Cylinder”, Int. J. Heat Mass Transfer, vol. 18, p. 1049

Colburn A.P., Hougen O.A., (1934), Design of cooler condensers from mixtures of vapours with noncondensing gases, Industry and Engineering Chemistry, 26 (1934), pp. 1178 – 1182

Dharma Rao V, Murali K.V, Sharma K.V., Mohana Rao, P.V.J. ,(2008). “Convective condensation of vapor in the presence of a non-condensable gas of high concentration in laminar flow in a vertical pipe”, International Journal of Heat and Mass Transfer, Volume 51, Issues 25-26, Pages 6090-6101

Dehbi, A. Guentay S. (1997), “A model for the performance of a vertical tube condenser in the presence of noncondensable gases“, Nuclear Engineering and Design 177, 41-52

Dalkilic, A.S., and Wongwises, S., (2009), “Intensive Literature Review of Condensation Inside Smooth and Enhanced Tubes”, *International Journal of Heat and Mass Transfer*, Vol. 52, pp. 3409-3426.

Edward W K., Walter O. S. and Stephen G. R., (1997) “Effects of fuel dissolved in crankcase oil on engine-out hydrocarbon emissions from a spark –ignited engine”, SAE International Conferrence, 972891

F. Dobran, R.S. Thorsen, (1980), “Forced flow laminar filmwise condensation of a pure saturated vapor in a vertical tube” Int. J. Heat Mass Transfer, Vol. 23, pp. 161-177

Farooq Saeed, (2002), “State-of-the-Art Aircraft Icing and Anti-Icing Simulation” ARA Journal, Vol. 2000-2002, No. 25-27

G.F. Hewitt, G.L. Shires and T.R. Bott, (1994), Process Heat Transfer, CRC Press, Chapter 10

Gardner,L., Moon,G. (1998), “Aircraft Carburettor Icing Studies”, National Research Council of Canada Ottawa (Ontario), Div. of Mechanical Engineering

Hasanein H. A, Kazimi M. S., Golay M. W. (1995), “Forced Convection in-tube steam condensation in the presence of noncondensable gases”, Int J. Heat Mass Transfer Vol. 39, No. 13, pp. 2625-2639

Hee C. N., Hyun S.P., (2002), “Non-iterative condensation modelling of steam condensation with non-condensable gas in a vertical tube”, International Journal of Heat and Mass Transfer, 45 845-854

Heinz H. (1995), “Advanced engine technology”, Edward Arnold, London

Heinz W. Ebner, Alfred J. (1998) "The Importance of Blow-By Measurements, Measuring Equipment Required and Implementation", 1998, International Congress & Exposition Technical Papers,

Holman J.P. (2002), Heat Transfer, (8th Edition), McGraw-Hill, New York

Jaguar Landrover System Design Specification, Positive Crankcase Ventilation, Version 2, Released 28-02-2011

John J. B., Eric W. Curtis, Marc M. (2006), “Modelling the Evaporative Emissions of Oil-Fuel Mixtures”, SAE, 2006-01-3402

Kim J.W., Lee Y.G (2009), “Condensation heat transfer characteristic in the presence of noncondensable gas on natural convection at high pressure”, Nuclear Engineering and Design, Vol. 239, pp 688-698

Kim S.J., No H.C. (2000) “Turbulent film condensation of high pressure steam in a vertical tube”, Int. J. Heat Mass Transfer, Vol. 43, pp. 4031-4042

Kim M.H., Corradini M.L, (1990) “Modeling of condensation heat transfer in a reactor containment”, Nuclear Engineering and Design, Vol. 118, pp. 193-212

Kuhn S.Z., V.E. Schrock, P.F. Peterson, (1997), “An investigation of condensation from steam–gas mixtures flowing downward inside a vertical tube”, Nuclear Engineering and Design, Vol. 177, pp. 53–69

Tallio K. V., B. J Torbis, A. Selamet, (1993) “The Application of Steady-Flow Loss Correlation to Intake Manifold Design” SAE International Conferrence.

Luxford, G. (2005), “Experimental and Modelling Investigation of the Deformation, Drag and Break-up of Drizzle Droplets Subjected to trong Aerodynamic Forces in Relation to SLD Aircraft Icing”, PhD Thesis, Cranfield University

Liao Y., Guentay S. Suckow D., Dehbi A., (2009) “Reflux condensation of flowing vapor and non-condensable gases counter-current to laminar liquid film in a vertical tube”, Nuclear Engineering and Design, Vol 239, pp. 2409-2416

Liao Y., Vierow K, (2007) “A generalized diffusion layer model for condensation of vapor with noncondensable gases”, ASME Journal of Heat Transfer, 129 (2007), pp. 988 – 994

Lee, KY., and Kim, M.H. (2008), “Experimental and empirical study of steam condensation heat transfer with a noncondensable gas in a small diameter vertical tube”, Nuclear Engineering and Design, Vol. 238, pp. 207-216.

Lopez O. (2004), “Experimental study of lube oil characteristics in the PCV system and effects on engine oil consumption”, (unpublished PhD thesis), Massachusetts Institute of Technology. Dept. of Mechanical Engineering,.

McCann, D. W. (2005), "NNICE - a neural network aircraft icing algorithm", Environmental Modelling and Software, vol. 20, no. 10, pp. 1335-1342.

Moon Y.M., No. K. C. Kaist, Park H. S. (2000), “ Assessment of RELAP5/MOD3.2 for Reflux Condensation Experiment” Office of Nuclear Regulatory Research, U.S. Nuclear Regulatory Commission, Washington, DC 20555-0001

Maheshwari, N.K., Saha, D., Sinha, R.K., Aritomi, M., (2004).” Investigation on condensation in presence of a noncondensable gas for a wide range of Reynolds number.”, Nuclear Engineering and Design 227, 219 – 238.

Messinger, B. L. (1953), "Equilibrium Temperature of an Unheated Icing Surface as a Function of Air Speed", Journal of the Aeronautical Sciences, vol. 20, no. 1, pp. 29-42.

Marty, Barris (2003) “Closed Crankcase Filtration”, http://www.meca.org/crankcasearticle.html

Nan Da H., Anuvat S., Kitipat S., James O. W. (2007), “Vertical two-phase flow regimes and pressure gradients: Effect of viscosity” Experimental Thermal and Fluid Science, Volume 31, Issue 6, pp 566-577

Narain, A., Phan, L. A., Wang, X., Kurita, J. H., Siemionko, A., Ng, T. W. and Kulkarni, S. D. (2006), "Direct computational simulations and experiments for film condensation inside tubes and channels", Annals of the New York Academy of Sciences, vol. 1077, pp. 471-506.

Nusselt, W., (1916) “Die Oberflachenkondensation des Wasserdampfes”, *Z. Ver. Deut. Ing.*, Vol. 2, 69.

No, H.C., and Park, S.H., 2002, “Non-Iterative Condensation Modeling for Steam Condensation with Non-Condensable Gas in a Vertical Tube”, International Journal of Heat and Mass Transfer, Vol. 45, pp. 845-854.

Park, S.H., and No, H.C., (1999), "A Condensation Experiment in the Presence of Noncondensables in a Vertical Tube of a Passive Containment Cooling System and Its Assessment with RELAP5/MOD3.2", *Nuclear Technology*, Vol. 127, pp. 160-169.

Peterson, P. F., Schrock, V. E., Kageyama, T., 1992, Diffusion layer theory for turbulent vapor condensation with noncondensable gases, ASME J. Heat Transfer Vol 115, pp 998-1003

Prapainop, R. and Maneeratana, "Simulation of ice formation by the finite volume method"

Quang Tan Le, (2012), "Physically based closed-form solutions from film condensation of pure vapors in vertical tubes", Msc Thesis, Manitoba University

Racor Technical Report (2006), Restrictions on Environmental Pollutants (www.parker.com/racor)

Revankar, S., Oh, S., and Zhou, W., 2010, "Condensation Correlation for a Vertical Passive Condenser System", *Nuclear Technology*, Vol. 170, pp. 28-39.

Reitze, A (2001), "Air Pollution Control Law Published", Environmental law Institute, ISBN: 9781585760275

Ra Y., Reitz R. D., Jarrett M. W., (2006) "Effects of piston crevice flows and lubricant oil vaporization on diesel engine deposits" SAE, 2006-01-1149

Shayler P. J., Winborn L. D., A. Scarisbrick (2000) "Fuel Transport to the Crankcase, Oil Dilution and HC return with breather flow during cold operation of SI Engine" SAE World Congress, Detroit, Michigan, 2000-01-1235

Sleezer R., Elder J., Mendezaceves E., Qureshi A., (2004), "Carburettor icing risk detection system", ECEN 4023 Senior Design II

Siddique M. (1992)**,** "The effects of non-condensable gases on steam condensation under forced convection conditions", Thesis (Ph. D.), Massachusetts Institute of Technology, Dept. of Nuclear Engineering

Siddique M., Alhazmy M. (2008) "Experimental study of turbulent single-phase flow and heat transfer inside a micro-finned tube", Int. J. of Refrigeration, Vol. 31 pp 234-241

Seban R., Hodgson J., (1982), "Laminar film condensation in a tube with upward vapor flow", International Journal of Heat and Mass Transfer, Vol. 25, pp. 1291 – 1300

Sparrow E. M., Lin S H, (1964) "Condensation Heat Transfer in the Presence of a Noncondensable Gas" J. Heat Transfer, 76 (1964) 430 436

Shah M. M. (1979), "A GENERAL CORRELATION FOR HEAT TRANSFER DURING FILM CONDENSATION INSIDE PIPES", Int. J. Heat Mass Transfer, Vol. 22, pp 547-556.

Steffen S., Gabriele G., Manfred P. (2007), "CFD-Based Development of Oil Droplet Separators in Crankcase Ventilation Systems" Institute of Mechanical Process Engineering, University of Stuttgart, Germany

Tanrikut A., (2000) “In-Tube Steam Condensation in the Presence of Air”, International Agreement Report, Turkish Atomic Energy Authority, Eskisehir Yolu 06530 Ankara, Turkey, Middle East Technical University, 06531 Ankara, Turkey

Tallio K. V., Tobris B. J, Selamet A., (1993) “The Application of Steady-Floe Loss Correlation to Intake Manifold Design”, SAE International Conference

Thumm, Ch. Philipp, U. Gross (2001), “Film condensation of water in a vertical tube with counter-current vapor flow”, International Journal of Heat and Mass Transfer, Vol. 44, pp. 4245 – 4256

Thomas D., Naji Z. (2007), “Crankcase flow modelling for racing motorcycle Engine”, SAE 2007 World Congress, Detroit, Michigan

Vierow, K.M., and Schrock, V.E., 1991, “Condensation in a natural circulation loop with noncondensable gases: Part 1 – Heat transfer”, *Proceeding of the International Conference on Multiphase Flow*, Tsukuba, Japan, pp. 183-186.

Whalen, E. A., Broeren, A. P., Bragg, M. B. and Lee, S. (2005), "Characteristics of Runback Ice Accretions on Airfoils and their Aerodynamic Effects", 43rd AIAA Aerospace Sciences Meeting and Exhibit; Reno, NV; USA; 10-13 Ja. 2005, Vol. AIAA Paper 2005-1065, American Institute of Aeronautics and Astronautics, 1801 Alexander Bell Drive, Suite 500, Reston, VA, 20191-4344, USA, [URL:http://www.aiaa.org],

Whalen, E. A., Broeren, A. P., Bragg, M. B. and Lee, S. (2005), "Characteristics of Runback Ice Accretions on Airfoils and their Aerodynamic Effects", 43rd AIAA Aerospace Sciences Meeting and Exhibit; Reno, NV; USA; 10-13 Ja. 2005, Vol. AIAA Paper 2005-1065, American Institute of Aeronautics and Astronautics, 1801 Alexander Bell Drive, Suite 500, Reston, VA, 20191-4344, USA, [URL:http://www.aiaa.org],

Yongbin L., Defu C., Yanbin K. (2007), “Effect of vapor condensation on forced convection heat transfer of moistened gas”, Heat Mass Transfer 43:676-686